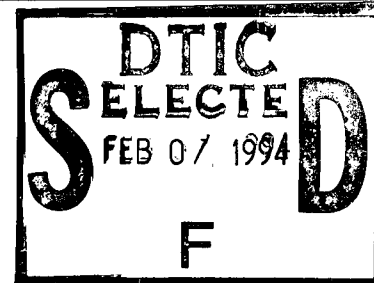


ARD 32826.1-PH-CF

# LASER APPLICATIONS TO CHEMICAL ANALYSIS



POSTCONFERENCE EDITION

This document has been approved  
for public release and sale; its  
distribution is unlimited.

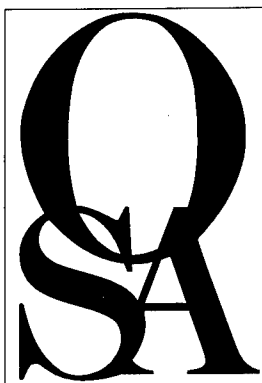
*Sponsored by*  
Optical Society of America

19950203 137

1994 TECHNICAL DIGEST  
SERIES VOLUME 5

MARCH 8-11, 1994  
JACKSON HOLE, WYOMING

REPORT DOCUMENTATION PAGE			Form Approved OMB No. 0704-0188	
<small>Public reporting burden for this collection of information is estimated to average 1 hour per response, including the time for reviewing instructions, searching existing data sources, gathering and maintaining the data needed, and completing and reviewing the collection of information. Send comments regarding this burden estimate or any other aspect of this collection of information, including suggestions for reducing this burden, to Washington Headquarters Services, Directorate for Information Operations and Reports, 1215 Jefferson Davis Highway, Suite 1204, Arlington, VA 22202-4302, and to the Office of Management and Budget, Paperwork Reduction Project (0704-0188), Washington, DC 20503.</small>				
1. AGENCY USE ONLY (Leave blank)	2. REPORT DATE December 1994	3. REPORT TYPE AND DATES COVERED Final 7 Mar 94-6 Mar 95		
4. TITLE AND SUBTITLE Laser Applications to Chemical Analysis		5. FUNDING NUMBERS  DAAH04-94-G-0046		
6. AUTHOR(S)  David W. Hennage (principal investigator)				
7. PERFORMING ORGANIZATION NAME(S) AND ADDRESS(ES) Optical Society of America 2010 Massachusetts Avenue NW Washington, DC 20036-1023		8. PERFORMING ORGANIZATION REPORT NUMBER		
9. SPONSORING/MONITORING AGENCY NAME(S) AND ADDRESS(ES) U.S. Army Research Office P.O. Box 12211 Research Triangle Park, NC 27709-2211		10. SPONSORING/MONITORING AGENCY REPORT NUMBER  ARO 32826.1-PH-CF		
11. SUPPLEMENTARY NOTES The views, opinions and/or findings contained in this report are those of the author(s) and should not be construed as an official Department of the Army position, policy, or decision, unless so designated by other documentation.				
12a. DISTRIBUTION/AVAILABILITY STATEMENT  Approved for public release; distribution unlimited.		12b. DISTRIBUTION CODE		
13. ABSTRACT (Maximum 200 words)  Summaries of papers presented at the Laser Applications to Chemical Analysis Topical Meeting, March 8-11, 1994, Jackson Hole, Wyoming.				
14. SUBJECT TERMS Solid State Lasers, Nonlinear Optics, Condensed Phase, Diode Lasers, Lidar, Aerosols, Biological Materials, Detection, Molecules, Spectroscopy, Laser Applications			15. NUMBER OF PAGES 274	
			16. PRICE CODE	
17. SECURITY CLASSIFICATION OF REPORT UNCLASSIFIED	18. SECURITY CLASSIFICATION OF THIS PAGE UNCLASSIFIED	19. SECURITY CLASSIFICATION OF ABSTRACT UNCLASSIFIED	20. LIMITATION OF ABSTRACT UL	



# Laser Applications to Chemical Analysis

*Summaries of papers presented at the  
Laser Applications to Chemical Analysis  
Topical Meeting*

March 8–11, 1994  
Jackson Hole, Wyoming

1994 Technical Digest Series  
Volume 5

POSTCONFERENCE EDITION

*Sponsored by*  
Optical Society of America

Optical Society of America  
2010 Massachusetts Avenue NW  
Washington DC 20036–1023

Accession For	
NTIS CRA&I	<input checked="checked" type="checkbox"/>
DTIC TAB	<input type="checkbox"/>
Unannounced	<input type="checkbox"/>
Justification _____	
By _____	
Distribution /	
Availability Codes	
Dist	Avail and/or Special
A-1	

## TECHNICAL PROGRAM COMMITTEE

**Mary Wirth, Chair**  
*University of Delaware*

**Alan C. Eckbreth, Chair**  
*United Technologies Research Center*

**Jay B. Jeffries, Program Chair**  
*SRI International*

**J. Michael Ramsey, Program Chair**  
*Oak Ridge National Laboratory*

**Sarah Cohn**  
*Potomac Photonics*

**Alan Fried**  
*National Center for Atmospheric Research*

**James H. Jett**  
*Los Alamos National Laboratory*

**Murray V. Johnston**  
*University of Delaware*

**Robert P. Lucht**  
*University of Illinois*

**Ulrich E. Meier**  
*DLR EN-CV, Germany*

**Andrzej W. Miziolek**  
*U.S. Army Ballistic Research Laboratory*

**Kay Niemax**  
*Institute für Spektrochemie und Angewandte Spektroskopie, Germany*

**Andy Sappey**  
*Los Alamos National Laboratory*

**Colin Seaton**  
*Coherent Laser Group*



## LOBBY

3:00 pm–10:00 pm REGISTRATION

## GRAND ROOM

7:00 pm–8:40 pm

**TuA, SOLID STATE LASER TECHNOLOGY AND SURFACE NONLINEAR OPTICS**J. Michael Ramsey, *Oak Ridge National Laboratory, Presider*

7:00 pm (Invited)

**TuA1 New horizons for solid-state lasers**, William K. Bischel, *Deacon Research*. There has been an explosion of new products introduced during the past year in the area of pulsed solid state lasers and their tunable accessories. The capabilities of existing commercial systems will be reviewed, and new technologies that may lead to improved specifications for beam quality, linewidth, repetition rate, and conversion efficiency will be discussed. (p. 2)

7:40 pm

**TuA2 Tunable diode-pumped mid-infrared lasers**, P. A. Budni, M. G. Knights, P. G. Schunemann, J. C. McCarthy, T. M. Pollak, E. P. Chicklis, *Lockheed Sanders*. Tunable diode-end-pumped mid-infrared lasers using 2  $\mu\text{m}$  Tm:Ho:YLF pumping ZnGeP<sub>2</sub> OPOs are described; outputs > 800 mW (4 KHz) between 3 and 5  $\mu\text{m}$ , pulse-diode-pumped > 1.25 MW (60 Hz) at 2  $\mu\text{m}$  were achieved. (p. 5)

8:00 pm (Invited)

**TuA3 Surface chemical analysis on diamond C(111) by IR sum frequency generation and second harmonic generation spectroscopy**, R. P. Chin, J. Y. Huang, Y. R. Shen, *Lawrence Berkeley Laboratory*; T. J. Chuang, H. Seki, *Almaden Research Center*. The adsorption of H and CH<sub>x</sub> on the diamond surface is studied by infrared sum frequency generation and second harmonic generation spectroscopy. (p. 9)

8:40 pm–8:50 pm BREAK

## TETON ROOM

8:50 pm–10:30 pm

**TuB, POSTER SESSION: 1**

**TuB1 Hook spectroscopy as a single-shot OH density and temperature diagnostic**, David K. Zerkle, Andrew D. Sappey, *Los Alamos National Laboratory*. Hook spectroscopy is used in an atmospheric pressure flame to determine absolute OH density and rotational temperature. Advantages and limitations of this technique are discussed. (p. 14)

**TuB2 C<sub>2</sub> Swan band spectral measurements of temperatures in a decaying laser-induced plasma**, Christian Parigger, David H. Plemmons, James O. Hornkohl, J. W. L. Lewis, *Univ. Tennessee Space Institute*. Spontaneous emission spectra of C<sub>2</sub> Swan bands were recorded well after laser-induced optical breakdown of carbon monoxide to yield molecular temperatures in excess of 6000 K. (p. 16)

**TuB3 Spatially and temporally resolved electron number densities in a decaying laser-induced hydrogen plasma**, Christian Parigger, David H. Plemmons, J. W. L. Lewis, *Univ. Tennessee Space Institute*. Spatially and temporally resolved spectral measurements of the hydrogen alpha line emissions from laser-induced optical breakdown plasmas yield a high electron number density profile. (p. 20)

**TuB4 Vacuum ultraviolet photoionization time-of-flight mass spectrometry for the investigation of products of benzene oxidation**, German Bermudez, Lisa Pfefferle, *Yale Univ.* Quantitative analysis of products of ultra-lean benzene oxidation using vacuum ultraviolet photoionization mass spectrometry including theoretical means for estimating relative ionization and detection efficiencies is described. (p. 24)

**TuB5 Trace organic chemical detection using an ultraviolet excitation molecular beam fluorometer**, B. L. Prep-ernau, P. J. Hargis, *Sandia National Laboratories*. Operation is demonstrated for an ultraviolet laser-excited pulsed supersonic molecular beam fluorometer, which simultaneously detects vibrationally resolved integrated fluorescence, photoionization, and dispersed fluorescence spectra. (p. 28)

**TuB6 Chemical species from tritium-breeding compacts by Raman spectroscopy**, David J. Taylor, Fred J. Steinkruger, David E. Christiansen, Donald J. Gettemy, *Los Alamos National Laboratories*. Laser-Raman spectroscopy was used to detect chemical species (HT, CO, etc.) released from neutron-irradiated tritium-breeding compacts at conditions simulating nuclear reactor accidents. (p. 32)

**TuB7 Absorption spectra of propylene at CO<sub>2</sub> laser wavelengths**, Mohammad A. Rob, Larry H. Mack, Jr., *Univ. Houston–Clear Lake*. Absorption coefficients of pure propylene at about 50 CO<sub>2</sub> laser lines are measured and presented. Results will be useful for laser spectroscopy of propylene and for air pollution measurement. (p. 36)

**TuB8 Unimolecular photochemistry studied by photodissociation-photoionization mass spectrometry**, M. V. Johnston, P. L. Ross, S. E. Van Bramer, E. D. Leavitt, *Univ. Delaware*. Photodissociation mechanisms of large aliphatic molecules are studied by photoionization mass spectrometry. In several cases, molecular dissociation from the excited state yields unexpected products and nonstatistical energy partitioning. (p. 40)

**TUESDAY, MARCH 8, 1994—Continued**

**TuB9 Wavelength modulation spectroscopy of oxygen A band transitions for nonintrusive concentration measurements**, A. D. Jackson, A. N. Dharamsi, S. K. Chaturvedi, *Old Dominion Univ.* Wavelength modulation spectroscopy in the oxygen A band is described and shown to provide a sensitive, nonintrusive method for monitoring concentrations of oxygen. (p. 43)

**TuB10 Silicon processing chemical diagnostics and control using diode lasers**, Edward A. Whittaker, H. C. Sun, C. K. Ng, *Stevens Institute of Technology*; B. Singh, V. Patel, *David Sarnoff Research Center*. We describe chemically selective measurements of polysilicon and oxide plasma etch processes using diode laser absorption spectroscopy and demonstrate very sensitive etch endpoint detection. (p. 47)

**TuB11 Detection of chlorine and oxygen in a microwave-induced plasma using frequency modulation spectroscopy**, Ring-Ling Chien, E. L. Ginzton *Research Center*. Diode laser FM spectroscopy is used as an elemental selective detector for trace amounts of O, S, and Cl in a microwave-induced plasma. (p. 51)

**WEDNESDAY, MARCH 9, 1994**

**GRAND ROOM**

**8:15 am–10:15 am**

**WA, CONDENSED PHASE STUDIES**

Alan C. Eckbreth, *United Technologies Research Center, Presider*

**8:15 am (Invited)**

**WA1 Optical diagnostics of single liquid droplets**, Michael Winter, *United Technologies Research Center*. Measurements of heat and mass transfer into droplets characteristic of a spray, illustrate flow patterns using LIF, vaporization using morphology-dependent resonances, and flame-fronts in microgravity. (p. 56)

**8:55 am**

**WA2 Suppression of scattering resonances in inhomogeneous microdroplets**, Dat Ngo, *New Mexico State Univ.*; R. G. Pinnick, *U.S. Army Research Laboratory*. The addition of nanometer-sized polystyrene latex particles to micro-sized glycerol droplets causes suppression of elastic scattering resonances. (p. 60)

**9:15 am**

**WA3 Near-field optical measurements at the liquid/air interface**, Mark Seaver, A. E. Frost, M. D. Duncan, *U.S. Naval Research Laboratory*. We measure evanescent decay lengths above the liquid/air interface for glycerol, mineral oil, and water. Shear force detection allows submicron height stabilization. (p. 64)

**9:35 am**

**WA4 Structure and extended electronic states in molecular assemblies of hemicyanine amphiphiles**, Q. Song, Z. Xu, W. Lu, P. W. Bohn, *Univ. Illinois*; G. J. Blanchard, *Michigan State Univ.* Extended electronic states in Langmuir-Blodgett molecular assemblies of a set of structurally related hemicyanines have been characterized by resonance second-harmonic generation and picosecond fluorescence measurements. (p. 67)

**9:55 am**

**WA5 Multichannel time-resolved Raman spectroscopy for photophysical and photochemical studies**, Julius C. Fister, Joel M. Harris, *Univ. Utah*. Raman spectra of intermediates in photoinitiated reactions, isolated by multidimensional analysis, have been used to elucidate structures and kinetics of triplet state sensitizers and photoproducts. (p. 71)

**10:15 am–10:30 am COFFEE BREAK**

WEDNESDAY, MARCH 9, 1994—Continued

GRAND ROOM

10:30 am–12:10 pm

**WB, DIODE-LASER BASED MEASUREMENTS**

Ulrich E. Meier, *DLR EN-CV, Germany, Presider*

10:30 am (Invited)

**WB1 Application of diode lasers to atmospheric diagnostics**, Joel A. Silver, D. Christian Hovde, David S. Bomse, Daniel B. Oh, Daniel J. Kane, Alan C. Stanton, *Southwest Sciences, Inc.* The applications of near-infrared diode lasers for measurement of trace gases, including uses as hygrometers, perimeter monitors, fluxmeters, and gas sensors, are discussed. (p. 76)

11:10 am

**WB2 New field-tunable diode laser absorption spectrometer for highly sensitive measurements of atmospheric gases**, Alan Fried, Scott Sewell, Bruce Henry, *National Center for Atmospheric Research*; James R. Drummond, *Univ. Toronto, Canada*. A new field tunable diode laser absorption spectrometer developed at NCAR for ground-based measurements of trace atmospheric constituents is described. (p. 80)

11:30 am

**WB3 Laser spectroscopy for practical isotope ratio measurements**, Robert W. Shaw, C. M. Barshick, J. P. Young, J. M. Ramsey, *Oak Ridge National Laboratory*. Glow discharge analyte sputtering and laser-excited, high resolution opticalgalvanic spectroscopy have been combined to begin development of a fieldable method for isotope ratio measurements. (p. 83)

11:50 am

**WB4 Wavelength modulation atomic absorption spectrometry with semiconductor diode lasers**, K. Niemax, *Univ. Hohenheim, Germany*; C. Schnürer-Patschan, H. Groll, *Institute for Spectrochemistry and Applied Spectroscopy, Germany*; A. Zybin, Y. Kuritsyn, *Institute of Spectroscopy, Russia*. Significant reductions of element detection limits by application of wavelength modulation absorption spectrometry with diode lasers in well-known spectrochemical sources are reported. (p. 87)

12:10 pm–7:00 pm AFTERNOON FREE

WEDNESDAY, MARCH 9, 1994—Continued

GRAND ROOM

7:00 pm–9:00 pm

**WC, DIODE-LASER TECHNOLOGY AND LIDAR**

Colin Seaton, *Coherent Laser Group, Presider*

7:00 pm (Invited)

**WC1 Advances in tunable semiconductor diode lasers**, David G. Mehuys, *SDL, Inc.* Semiconductor diode lasers are capable of generating tunable radiation with any of narrow-linewidth, high-power, or short-pulse output. Fundamental concepts, laser characteristics, and applications will be discussed. (p. 90)

7:40 pm (Invited)

**WC2 Raman lidar profiling of atmospheric water vapor**, J. E. M. Goldsmith, Scott E. Bisson, *Sandia National Laboratories*. We describe measurements of atmospheric water vapor using Raman lidar. The dual-field-of-view design of the system provides advanced daytime capabilities without sacrificing nighttime performance. (p. 91)

8:20 pm

**WC3 Differential absorption lidar measurements of tropospheric ozone**, Andrew O. Langford, Michael H. Profitt, *NOAA Aeronomy Laboratory*. We describe the NOAA differential absorption lidar that can profile atmospheric ozone from 4 to 14 km in one-minute day or night. (p. 94)

8:40 pm–8:50 pm BREAK

TETON ROOM

8:50 pm–10:30 pm

**WD, POSTER SESSION: 2**

**WD1 Dual Fabry-Perot optical fiber sensor**, Qi Wang, *Huazhong Univ. of Science and Technology, China*. An optical fiber sensing system consisting of two Fabry-Perot cavities and white light source is presented in this paper. A multimode optical fiber provides a link to the sensing cavity. A relative simple control electronics is used to adjust the reference cavity gap and make the system lock in the central coherent peak when the power turns on. (p. 98)

**WD2 Fiber-optic sensor based on dye-doped porous polymer: detecting ammonia in liquid media**, D. B. Bondarenko, S. M. Dolotov, M. F. Koldunov, E. P. Ponomarenko, N. M. Sitnikov, A. V. Startsev, T. V. Tulaikova, *Institute of General Physics, Russia*. In this paper the development of optical fiber sensors used for detection of ammonia and sulphurated hydrogen, gases or liquids is presented. (p. 104)

**WEDNESDAY, MARCH 9, 1994—Continued**

**WD3 Infrared heterodyne receiver for high-resolution measurements of molecular species in the stratosphere,** P. K. Cheo, Y. Zhou, *Univ. Connecticut*. A ground-base heterodyne spectrometer for remote sensing of ozone,  $\text{HNO}_3$  and some minor molecular species in the stratosphere will be reported. The spectrometer consists of a tunable  $\text{CO}_2$  sideband laser, solar tracker, photomixer, post electronics, and data acquisition. (p. 112)

**WD4 Population and thermal grating contributions to degenerate four-wave mixing line shapes,** Paul M. Danehy, *Stanford Univ.*; Ernest J. Friedman-Hill, Roger L. Farrow, *Sandia National Laboratories*. Degenerate four-wave mixing (DFWM) line shapes are analyzed for conditions dominated by population and thermal gratings. Relative contributions are estimated from nearly-DFWM spectra. (p. 115)

**WD5 Laser diagnostics by electrostrictive gratings in the gas phase,** A. Stampanoni-Panariello, W. Hubschmid, B. Hemmerling, *Paul Scherrer Institute, Switzerland*. The dissipation of acoustic waves and their velocity has been measured in the gas phase employing an electrostrictive laser-induced grating. Furthermore, the imaging capabilities of this novel technique have been demonstrated. (p. 119)

**WD6 Measuring CO concentration and temperature in a  $\text{CH}_4$ /air premixed flame with broadband coherent anti-Stokes Raman spectroscopy,** J. W. Hahn, S. N. Park, *Korea Research Institute of Standards and Science*; K. T. Kang, S. H. Chung, *Seoul National Univ., Korea*. The profile of CO concentration in a  $\text{CH}_4$ /air premixed flame of a counterflow burner was measured from the modulation dip of nonresonant background of broadband coherent anti-Stokes Raman spectrum. (p. 124)

**WD7 Species identification and conversion measurements in a carbon tetrachloride radio frequency plasma using coherent Raman techniques,** R. Rodriguez, F. V. Wells, *Idaho State Univ.* Coherent Stokes Raman scattering provided conversion information and allowed identification of chemical species present in a low pressure radio frequency plasma of carbon tetrachloride. (p. 128)

**WD8 Laser light-scattering interferometry for real-time diagnostic studies of aerosol produced by a new high-efficiency nebulizer,** Akbar Montaser, Huiying Liu, *George Washington Univ.* Laser light-scattering interferometry reveals that the aerosols produced by a new high-efficiency nebulizer exhibit droplet size and span much smaller than those of the conventional devices. The new nebulizer is useful for plasma spectrochemical analysis at solution uptake rates down to  $10 \mu\text{L}/\text{min}$ . (p. 131)

**WEDNESDAY, MARCH 9, 1994—Continued**

**WD9 Trapping of laser-desorbed ions in an ion trap mass spectrometer using a gated RF field,** G. C. Eiden, A. W. Garrett, M. E. Cisper, N. S. Nogar, P. H. Hemberger, *Los Alamos National Laboratory*. We describe a new method for trapping laser desorbed ions in an ion trap. Effects of laser-to-RF phase and delay, and buffer gas pressure and mass are qualitatively explained by an effective potential barrier model. (p. 135)

**WD10 Potential application of three laser-based bacteria detection techniques to the meat processing plants—a review,** Nee-Yin Chou, *CW Optics, Inc.*; Yud-Ren Chen, *USDA/ARS*. Potential application of three laser-based spectroscopic techniques for rapid detection of bacteria in meat processing plants is reviewed. Estimated signal levels are presented. (p. 139)

**WD11 Fluorescence lifetime measurements in a flow cytometer by amplitude demodulation using digital data acquisition technique,** C. Deka, J. A. Steinkamp, *Los Alamos National Laboratory*; Larry A. Sklar, *Univ. New Mexico*. Fluorescence lifetime measurements by amplitude demodulation of fluorescence signals are reported, for the first time, in a flow cytometer using digital data acquisition technique. (p. 143)

THURSDAY, MARCH 10, 1994

GRAND ROOM

8:15 am–10:15 am

**ThA, AEROSOL STUDIES**

Kay Niemax, *Institute für Spektrochemie und Angewandte, Germany, Presider*

8:15 am (Invited)

**ThA1 Chemical analysis of single aerosol particles using laser ionization**, D. M. Murphy, *NOAA Aeronomy Laboratory*. We have developed a portable instrument to make in situ measurements of the composition of individual, sized particles with diameters between 0.3 and 10  $\mu\text{m}$ . The beam from a miniature excimer laser strikes the particles, producing ions that are analyzed in a time of flight mass spectrometer to provide a complete mass spectrum for each aerosol particle. (p. 148)

8:55 am

**ThA2 On-line analysis of single microparticles by laser mass spectrometry**, M. V. Johnston, P. G. Carson, K. R. Neubauer, B. A. Mansoori, A. S. Wexler, *Univ. Delaware*. Single microparticles are sampled and analyzed in real time. Applications include elemental analysis and chemical speciation of inorganic materials, organic molecular analysis, and determination of surface vs bulk composition. (p. 152)

9:15 am

**ThA3 Mass spectrometry of individual microparticles in an ion trap**, J. M. Ramsey, J. M. Dale, M. Yang, W. B. Whitten, *Oak Ridge National Laboratory*. We are developing techniques for laser desorption/ablation sampling of microparticles inside the quadrupole electrodes of an ion trap mass spectrometer with subsequent mass analysis. (p. 156)

9:35 am

**ThA4 Raman spectroscopy measurements of single reacting aerosol microparticles**, Scot D. Rassat, E. James Davis, *Univ. Washington*. Raman spectra were obtained for chemical reactions between single levitated microparticles and a reactive gas. Temperatures were determined from anti-Stokes and Stokes Raman measurements. (p. 159)

9:55 am

**ThA5 Laser ionization of biomolecules in solution**, Kermit K. Murray, Michelle D. Beeson, David H. Russell, *Texas A&M Univ.* We have developed a method for laser ionization of biomolecules in solution by applying the technique of matrix-assisted laser desorption ionization to liquid aerosols. (p. 163)

10:15 am–10:30 am **COFFEE BREAK**

THURSDAY, MARCH 10, 1994—Continued

GRAND ROOM

10:30 am–12:10 pm

**ThB, LASER DESORPTION/ABLATION AND CONDENSED PHASE PROBES**

Andrew Sappey, *Los Alamos National Laboratory, Presider*

10:30 am

**ThB1 Fundamental investigations of the mechanism of laser desorption and ionization in matrix assisted laser desorption/ionization**, Gary R. Kinsel, Kent Gillig, Ricky Edmondson, David H. Russell, *Texas A&M Univ.* Translation energies of matrix assisted laser desorbed ions are determined by signal profile and electrostatic energy analysis. The results implicate both surface and gas-phase ionization. (p. 168)

10:50 am

**ThB2 Time-resolved thermometry in a condensing laser-ablated copper plasma plume by Doppler-resolved laser-induced fluorescence**, David K. Zerkle, Andrew D. Sappey, *Los Alamos National Laboratory*. Laser-induced fluorescence of Cu atom is used for thermometry in copper plasma plumes. Voigt profiles are fit to determine the Doppler width of the transition. (p. 172)

11:10 am

**ThB3 Resonant laser ablation: threshold behavior and semiquantitative aspects**, J. E. Anderson, G. C. Eiden, N. S. Nogar, *Los Alamos National Laboratory*. Resonant laser ablation (RLA) uses a single tunable laser to enhance the ablation/ionization yield of a selected sample component(s). We report on RLA for low level detection and semiquantitative analysis. Threshold behavior and power dependence are discussed. (p. 175)

11:30 am

**ThB4 New fiber optic LIF-sensor for the detection of environmental pollutants**, W. Schade, J. Bublitz, M. Dickenhausen, M. Grätz, *Univ. Kiel, Germany*. Multiwavelength laser excitation and time-integrated fluorescence detection is applied to measure poly- and monocyclic aromatic hydrocarbon contaminations in water and soil samples. (p. 179)

11:50 am

**ThB5 Zeeman laser interferometry for detection and chemical analysis**, Roger G. Johnston, *Los Alamos National Laboratory*. Zeeman interferometry has a number of applications for ultrasensitive detection and chemical analysis, including refractive index detection, micro-thermometry, thermo-optic spectroscopy, and light scattering. (p. 183)

12:10 pm–7:00 pm **AFTERNOON FREE**

THURSDAY, MARCH 10, 1994—Continued

GRAND ROOM

7:00 pm–8:40 pm

**ThC, LASER APPLICATIONS TO DETECTION AND ANALYSIS OF BIOLOGICAL MATERIAL**

James Jett, *Los Alamos National Laboratory, Presider*

7:00 pm (Invited)

**ThC1 Cellular and biological applications of laser-induced fluorescence**, Larry A. Sklar, *Los Alamos National Laboratory*; Gregory M. Jones, Terri Gilbert Houghton, *Univ. New Mexico*. Lasers are widely used in biological applications to detect fluorescent molecules that probe the structure and activities of cells, cellular components, and biomolecules. This presentation introduces measurements on molecules in solution, and cells in suspension and adhered to surfaces. The detection systems emphasized are spectrofluorometry, flow cytometry, and microscopy. (p. 188)

7:40 pm

**ThC2 Phase sensitive flow cytometry: new technology for analyzing biochemical, functional, and structural features in fluorochrome-labeled cells and particles**, John A. Steinkamp, *Los Alamos National Laboratory*. A phase-sensitive flow cytometer has been developed that provides unique capabilities for making laser-excited, phase-resolved measurements on fluorochrome-labeled cells and particles. (p. 192)

8:00 pm

**ThC3 Recent developments in DNA fragment sizing by flow cytometry**, Mitchell E. Johnson, Jeffrey T. Petty, Peter M. Goodwin, John C. Martin, W. Patrick Ambrose, Babetta L. Marrone, James H. Jett, Richard A. Keller, *Los Alamos National Laboratory*. Fragments of fluorescently stained DNA are sized and counted rapidly and accurately using flow cytometry and sensitive laser-induced fluorescence detection. (p. 196)

8:20 pm

**ThC4 Morphological resonances for multicomponent immunoassays**, W. B. Whitten, M. J. Shapiro, J. M. Ramsey, *Oak Ridge National Laboratory*; Burt V. Bronk, *U.S. Army Edgewood RDEC*. We have been studying a multicomponent immunoassay technique for microorganisms based on microsphere size discrimination. (p. 198)

8:40 pm–9:00 pm COFFEE BREAK

GRAND ROOM

9:00 pm–10:20 pm

**ThD, SINGLE MOLECULE DETECTION**

Robert P. Lucht, *University of Illinois at Urbana-Champaign, Presider*

9:00 pm

**ThD1 Single-molecule detection in microdroplets**, Michael D. Barnes, William B. Whitten, J. Michael Ramsey, *Oak Ridge National Laboratory*. Detection of single dye molecules (R6G) has been demonstrated with high signal-to-noise ratios ( $\approx 40$ ) using levitated microdroplets as the sample medium. (p. 202)

THURSDAY, MARCH 10, 1994—Continued

9:20 pm

**ThD2 Monte Carlo model of a single molecule counting experiment**, Lloyd M. Davis, Li-Qiang Li, *Univ. Tennessee Space Institute*. Monte Carlo simulations of our experiment to efficiently count single molecules in solution are used to select operating conditions and signal processing procedures. (p. 206)

9:40 pm

**ThD3 Electrophoresis of single fluorescent molecules**, Alonso Castro, Brooks Shera, *Los Alamos National Laboratory*. A new method for the detection and identification of molecular species at extremely low concentrations by measuring electrophoretic velocities of individual molecules in solution is discussed. (p. 210)

10:00 pm

**ThD4 Fluorescence spectroscopy on a single molecule basis with a near-field spectrometer**, X. Sunney Xie, Robert C. Dunn, *Molecular Science Research Center*. Steady state and time-resolved fluorescence spectroscopy on single chromophores and single proteins in an ambient environment with nanometer spatial resolution using a near-field fluorescence spectrometer are reported. (p. 214)

FRIDAY, MARCH 11, 1994

GRAND ROOM

8:15 am–10:15 am

**FA, GAS PHASE SPECTROSCOPY**

Andrzej W. Miziolek, *U. S. Army Ballistic Research Laboratory, Presider*

8:15 am (Invited)

**FA1 Diagnostics for emission monitoring for hazardous waste incineration**, Terrill A. Cool, *Cornell Univ.* Measurements are presented of the limits for detection of 20 aliphatic and aromatic compounds by resonance ionization spectroscopy. The implications of these measurements on the selection of surrogates and the prospects for repetitive on-line hazardous emissions monitoring are discussed. (p. 220)

8:55 am

**FA2 Tunable diode laser study of premixed methane/oxygen flames inhibited by halogenated compounds**, Robert G. Daniel, Kevin L. McNesby, Andrzej W. Miziolek, *U.S. Army Research Laboratory*. Temperature and CO concentration profiles of premixed methane/oxygen low pressure flames doped with halogenated compounds have been measured using infrared absorption spectroscopy. The primary goal of this study is to provide much needed experimental results for comparison with developing chemical kinetic models of inhibited premixed flames. (p. 223)

9:15 am

**FA3 Laser-induced fluorescence measurements of CH and C<sub>2</sub> during diamond CVD**, George A. Raiche, Michael S. Brown, Jay B. Jeffries, *SRI International*. CH and C<sub>2</sub> radicals are observed in the effluent of a dc-arc-jet plasma during the growth of diamond films. Several LIF strategies for CH are evaluated and the gas temperature is inferred from the rotational distribution. (p. 227)

9:35 am

**FA4 Structure matters: detection of difluoromethyl and difluoroethyl radicals by resonance-enhanced multiphoton ionization spectroscopy**, Jeffrey W. Hudgens, Jeffrey L. Brum, Russell D. Johnson III, David V. Dearden, *NIST-Gaithersburg*. The REMPI spectra of CHF<sub>2</sub>, CF<sub>2</sub>CH<sub>3</sub>, and CHF<sub>2</sub>CH<sub>2</sub> radicals reflect the structural changes caused by the photoionization process. These changes limit detection selectivity. (p. 231)

9:55 am

**FA5 Computation of synthetic diatomic spectra**, J. O. Hornkohl, C. Parigger, J. W. L. Lewis, *Univ. Tennessee Space Institute*. Methods for the computation of synthetic diatomic spectra are discussed. Only methods applicable to all types of diatomic spectra are considered. (p. 234)

10:15 am–10:20 am COFFEE BREAK

FRIDAY, MARCH 11, 1994—Continued

GRAND ROOM

10:30 am–12:10 pm

**FB, FOUR WAVE MIXING SPECTROSCOPY**

Jay B. Jeffries, *SRI International, Presider*

10:30 am (Invited)

**FB1 Degenerate four-wave mixing for quantitative diagnostic measurements**, R. L. Farrow, P. H. Paul, E. J. Friedman-Hill, *Sandia National Laboratories*; P. M. Danehy, *Stanford Univ.* We report investigations of the effects of collisional quenching and thermal-grating formation in degenerate four-wave mixing and discuss their significance for diagnostic measurements. (p. 240)

11:10 am

**FB2 Effects of Doppler broadening and unequal pump intensities in saturated degenerate four-wave mixing spectroscopy**, Robert P. Lucht, *Univ. Illinois*; Michael S. Brown, *MetroLaser*; Larry A. Rahn, *Sandia National Laboratories*. The effects of Doppler broadening on quantitative degenerate four-wave mixing concentration measurements and the influence of unequal pump intensities on line shapes are investigated. (p. 244)

11:30 am

**FB3 Degenerate four-wave mixing in a methane/air flame using a regeneratively mode-locked Ti:sapphire laser**, M. A. Linne, *Colorado School of Mines*; G. J. Fiechtner, *Univ. Colorado*. Results of experimental picosecond degenerate four-wave mixing on potassium in a methane-air flame, using a regeneratively mode-locked Ti:sapphire laser, are presented. (p. 248)

11:50 am

**FB4 A 30-Hz CARS system for concentration and temperature measurements in supersonic turbulent, H<sub>2</sub>/air combustion**, M. W. Smith, A. D. Cutler, G. B. Northam, *NASA Langley Research Center*; M. W. Millard, *MetroLaser*. A 30-Hz broadband CARS system was designed to measure single-shot N<sub>2</sub> temperature and relative concentration and single-shot H<sub>2</sub> temperature in a hydrogen-fueled scramjet combustor. (p. 252)





Tuesday, March 8, 1994

# Solid-State Laser Technology and Surface Nonlinear Optics

**TuA** 7:00pm–8:40pm  
Grand Room

J. Michael Ramsey, *Presider*  
*Oak, Ridge National Laboratory*

## New Horizons for Solid-State Lasers

William K. Bischel  
Deacon Research  
2440 Embarcadero Way  
Palo Alto, CA 94303

There has been an explosion of new products introduced during the past year in the area of pulsed solid state lasers and their tunable accessories. In this talk I will discuss two emerging new technologies that may have a significant impact on laser development for applications in chemical analysis: high repetition rate YAG lasers and new "quasi-phase matched" periodically poled nonlinear materials.

### High Repetition Rate Pulsed YAG Lasers

The user of pulsed YAG lasers has seen a variety of new products introduced during the last year, many of which are aimed at providing the user with higher repetition rate. There are many experiments that could greatly benefit from an increase in repetition rate. However, the specifications for other laser parameters (e.g. beam quality and laser linewidth) must also improve or at least remain the same as the repetition rate increases. A user survey by the author has indicated that the ideal YAG laser for many applications in chemical analysis would simultaneously have the following specifications: (1) repetition rates exceeding 100 Hz, (2) single pulse energies at 532 nm greater than 200 mJ (20 W average power), (3) a transform limited linewidth to facilitate the pumping of narrow linewidth optical parametric oscillators (OPO), (4) diffraction-limited beam quality to enhance OPO operation and other nonlinear optical process, and (5) pulse lengths of 1-5 ns to allow time resolved measurements while maintaining transform limited linewidths that are smaller than typical gas-phase Doppler-limited linewidths of atoms and molecules.

There has been good progress toward achieving these specifications at several companies and government laboratories during the past few years. Although there have been several government funded projects that have achieved these specifications using an all-diode-pumped laser system, the cost of such diode pumped lasers is currently prohibitive for most users. These cost constraints limit the development of high average power commercial lasers to a hybrid approach where the oscillator could be diode pumped while the power amplifier would continue to be flashlamp pumped for the foreseeable future.

Since the oscillator is the starting point for any new laser system, the first technology I will first discuss the development of a diode-pumped Q-switched ring oscillator that can either form the input to an amplifier system, or operate as a stand alone oscillator for low power experiments. A schematic of this oscillator is given in Figure 1. Laser diode arrays with 500 mW output power were used to pump a simple two mirror laser cavity. The ring geometry is formed with a standard 10 mm long AR coated acousto-optic Q-switch and a prism of laser material, Nd:YAG or Nd:YLF, placed directly on top of the Q-switch side face. The cavity round trip time in such a compact cavity is less than 0.2 ns. The laser mode runs unidirectionally<sup>1</sup> thus allowing single-

longitudinal-mode (SLM) Q-switched operation with pulse widths as short as 6 ns pulsewidth.

Single-longitudinal-mode Q-switched operation requires a low level of cw prelude to be running in the cavity. Q-switched operation can be achieved with less than 2 mW of prelude. The extraction efficiency is very good and we have demonstrated energies in excess of 25  $\mu$ J from YAG lasers and 35  $\mu$ J from YLF lasers. The entire laser is actively temperature controlled by a single TE cooler beneath the Q-switch. This ensures long term SLM operation without mode hops, with RMS pulse energy stabilities of less than 0.5%. This laser technology should be commercially available in the near future.

The second part of any laser system is the laser amplifier. Amplifying 25  $\mu$ J of SLM laser energy to 500 mJ (approximately  $2 \times 10^4$  gain) at high repetition rate while maintaining the beam quality specification is not an easy problem to solve in a cost effective manner. Cost effective amplifier concepts for simultaneously achieving the system specifications will be discussed.

### Periodically Poled Nonlinear Materials

There is great interest in developing new nonlinear materials that would allow the development of high efficiency optical parametric oscillators in the wavelength region of 2-5  $\mu$ m for applications in chemical analysis. The interest in "quasi-phase-matched" periodically poled lithium niobate (PPLN) derives mainly from the ability to tailor the phase-matching wavelength anywhere within the transparency range that extends out to 5 microns. The walkoff can thereby be completely eliminated, thus improving both the conversion efficiency and the mode characteristics of the output beam. System stability is improved due to the expanded acceptances in terms of temperature, crystal tilt angle, and beam divergence. The highest nonlinear coefficient of the material ( $d_{\text{eff}} = 2 * d_{33} / \pi = 22 \text{ pm/V}$ )<sup>2</sup> can be used for the nonlinear process since birefringent phase matching is not necessary. Since all beams are polarized in the same plane, simpler optical design approaches are possible. Finally, LiNbO<sub>3</sub> combines excellent transmission with a good optical damage performance. Both waveguide and bulk fabrication techniques are currently being studied in a number of laboratories. I will review the current work in the field and give my view of what the future holds for this interesting nonlinear material.

### References

1. M. K. Reed and W. K. Bischel, "Acousto-optic modulators as unidirectional devices in ring lasers," Opt. Lett. 17, 691 (1992).
2. S. K. Kurtz, J. Jerphagnon, M. M. Choy, "Nonlinear dielectric susceptibilities" in Landolt-Bornstein, New Series, (K. H. Hellwege, ed.), Springer-Verlag, Berlin, V11, 682 (1979).

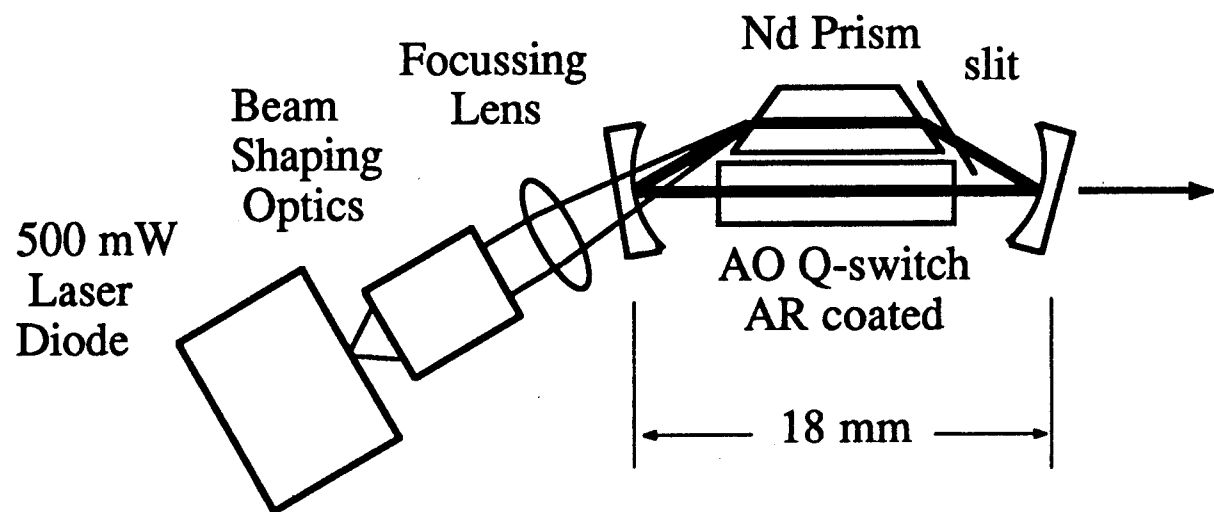


Figure 1. Single-longitudinal-mode Q-switched diode pumped laser cavity design.

## Tunable Diode-Pumped Mid-infrared Lasers

P.A. Budni, M.G. Knights, P.G. Schunemann,

J.C. McCarthy, T.M. Pollak, E.P. Chicklis

Lockheed Sanders, P.O. Box 868, Nashua, N.H. 03060-0868 (603)-885-3010

Recent advances in Mid-Infrared (MIR) tunable lasers open new possibilities for detection / analysis of chemical species in the laboratory and by the use of remote sensing techniques in the field. Lasers for these applications vary by system defined operating parameters such as: energy output, pulse repetition rate, spectral emission / tunability, linewidth, and compact reliable platform mounted architectures. Solid-state lasers comprising of optical parametric oscillators (OPO) using  $\text{ZnGeP}_2$  and  $\text{AgGaSe}_2$  non-linear optical crystals driven by 2-micron  $\text{Tm,Ho:YLF}$  pump lasers, are an attractive method for the generation of efficient tunable MIR radiation spanning the wavelength ranges of 2.6 to 12 microns. Providing systems which can operate at high repetition rates (4-20kHz), high average power (2.4W, 3-to-5 microns) [1], or low repetition rate (<60Hz) systems with capabilities of energy output in the 15mJ region (2 microns). We describe two MIR diode-end-pumped laser systems: one a high repetition rate OPO / 2-micron laser, and the other a laser-diode pulse-pumped 2-micron laser operating at low repetition rate / high peak power per pulse (60Hz / 1.25MW) designed to drive an OPO for >500KW of pulsed output.

Two-micron laser pumped OPO in the semiconductor chalcopyrites  $\text{ZnGeP}_2$  (ZGP) and  $\text{AgGaSe}_2$  (SGS) permits MIR tunable output spanning from 2.6 to 12 microns using a fixed pump laser wavelength of 2.05 microns. Tuning the OPO wavelength is accomplished by taking advantage of the anisotropy in the refractive index of the crystals by pumping along directions and polarizations which allow a coherent growth of waves (phasematching) generated by the non-linear polarization in the presence of a strong laser pump field. The phasematched condition for a three wave interaction is,

$$n_p \omega_p = n_s \omega_s + n_i \omega_i$$

where  $n$  is the refractive index,  $\omega$  is the radian frequency and the subscripts  $p$ ,  $s$ , and  $i$  refer to pump, signal and idler waves respectively. From the above expression we see that pairs of signal and idler waves satisfy the phasematching condition. The resultant output from an OPO produces signal and idler waves whose energy content is proportional to the ratio of their photon energies to the pump energy, with the signal possessing the higher energy content. Figure 1 shows calculated angular tuning curves for type I and type II phasematching for a fixed pump wavelength of 2.05 microns in ZGP. Figure 2 shows detail of the type I curve in ZGP near degeneracy (signal = idler = 2 X pump wavelength), data was taken at high repetition rate with OPO mirrors which by design operated between 3.5 and 5 microns [2]. From the curves we can see that type I operation provides continuous tuning throughout the angular range, while type II possesses discontinuities. The rate of change in wavelength vs. angle for type II however, is much smaller than type I, this feature can allow precise fine tuning in wavelength. Single wavelength operation can be achieved by resonating only one branch on either side of degeneracy (signal or idler), further linewidth narrowing can be achieved by intracavity wavelength selective elements such as etalons or gratings [3].

Figure 3 shows a schematic of a MIR diode-pumped high repetition rate laser. The laser system consists of three stages: a multiplexed array of small area emitting CW laser diodes, a Tm,Ho:YLF crystal (2 micron laser), and a ZGP OPO. The CW laser diodes end-pump the 2-micron stage, this stage consists of a Tm,Ho:YLF crystal which is cooled to LN<sub>2</sub> temperatures in a compact detector type dewar, and an acousto-optic Q-switch. The output of the 2 micron stage is in the form of short pulses (7 nsec.), at 4KHz with >3W (TEM<sub>00</sub>) of average power. The output of the 2 micron stage is focused to a spot of 0.5mm diameter into a ZGP OPO consisting of an 11mm. long crystal in a 15mm. long resonator. Figure 4 shows data of slope and conversion efficiencies from 2 microns to the 3-to-5 micron region (doubly resonant OPO), the highest conversion point was 29% (100MW/cm<sup>2</sup> pump drive intensity) with a slope efficiency of 53%, yielding >800mW of average power into both signal and idler, this corresponds to approximately 40KW of peak power. The two other curves depict data with various OPO output coupler mirror reflectivities. Best slope performance was obtained with a mirror which provided 40% feedback.

Requirements for higher peak power output in the MIR can be achieved by Q-switched low repetition rate lasers which are end-pumped by Quasi-CW commercially available pulsed laser diode arrays. The architecture for such an OPO / pump laser consists of a laser diode-array coupled to pump a 2 micron  $\text{Tm,Ho:YLF}$  laser in a manner similar in principle to the high repetition laser described above with the distinction that a pulsed laser diode array of broad emitting dimensions is used. The OPO is similar to the high repetition rate case except that the 2 micron pump spot size has to be increased in order to avoid optical damage to the OPO crystal. Using the pulse-pumped scheme pumping  $\text{Tm,Ho:YLF}$  we have obtained 2 micron Q-switched pulse outputs exceeding 1.25 MW of peak power (15mJ in <12nsec.) at 60 Hz,  $\text{TEM}_{00}$  in a compact  $\text{LN}_2$  dewared laser head (thermoelectrically cooled experiments have yielded >50mJ of non-Q-switched output). The output from this laser is sufficient to drive a nonlinear stage such as an OPO in ZGP or SGS with approximately  $140\text{MW}/\text{cm}^2$  of peak power intensity, well below the single pulse damage threshold of  $3\text{ J}/\text{cm}^2$  [4,5] for estimated conversion efficiencies exceeding 40% (compared to the high repetition rate drive of  $100\text{MW}/\text{cm}^2$  which yields 30% efficiency) this translates to >5mJ or approximately >500KW of peak MIR power output.

In summary, we have demonstrated tunable MIR output from high repetition rate CW diode-pumped 2 micron lasers driving OPO's at average powers > 800mW, and have developed a 2 micron pulse-diode-pumped laser providing sufficient peak power to drive OPO's for estimated outputs exceeding 500KW of peak power.

## REFERENCES

- [1] M.G. Knights, et al., Advanced Solid State Lasers Conference (ASSL), (OSA, 1994), paper to be presented in Salt Lake City, Utah Feb. 1994.
- [2] P.A. Budni, et al., OSA Proceedings on Advanced Solid State Lasers, (Optical Society of America, Washington DC 1992), Vol.13, p. 380.
- [3] W. R. Bosenberg, et al., OSA Proceedings on Advanced Solid State Lasers, (Optical Society of America, Washington DC 1992), Vol.13, p. 343.
- [4] B.C. Ziegler and K.L. Schepler, Appl. Opt. 30, 5077 (1991).
- [5] K.L. Vodopyanov, J. Opt. Soc. Am. B, Vol. 10, No. 9, September 1993, p. 1723.

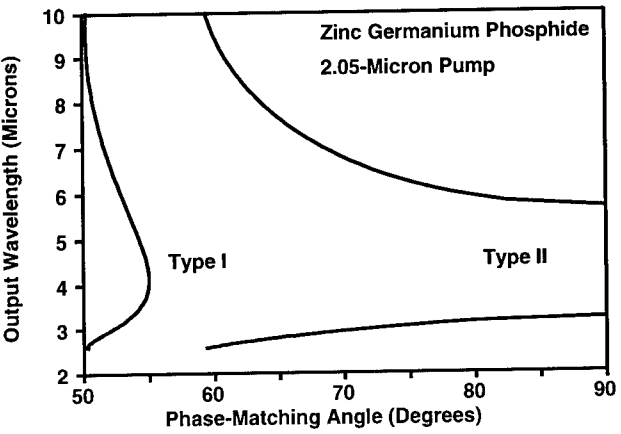


Fig. 1. ZnGeP<sub>2</sub> tuning curves for Type I and Type II, 2.05-micron laser pump.

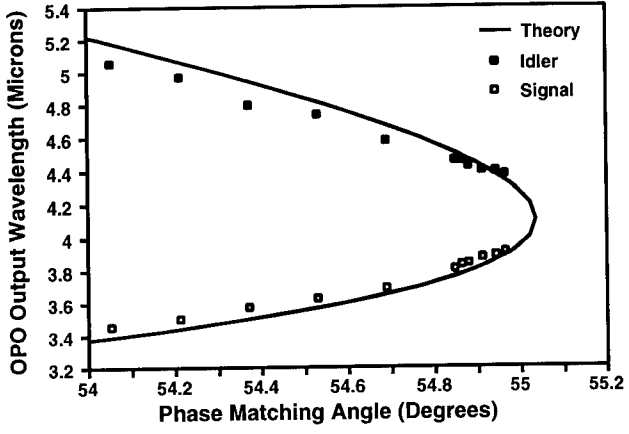


Fig. 2. Measured vs. Theoretical Type I tuning in ZnGeP<sub>2</sub> near degeneracy.

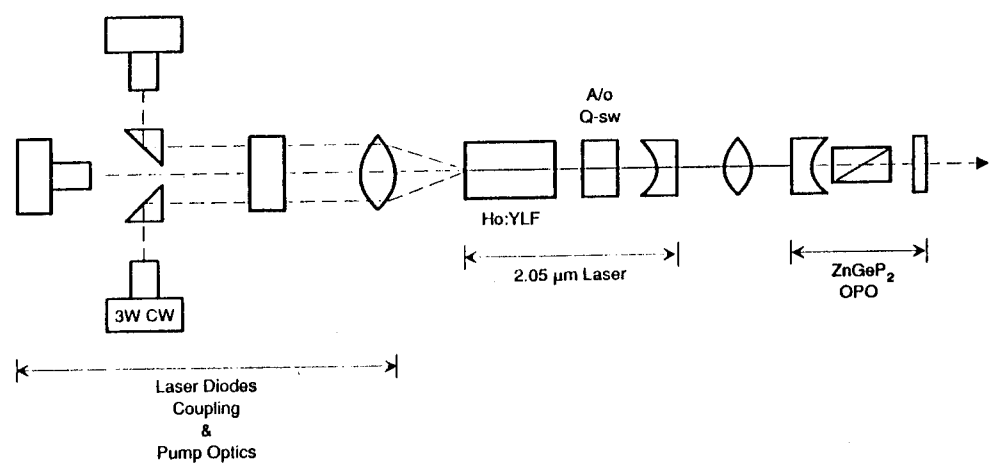


Fig. 3. Optical Schematic of a high repetition rate solid-state Mid-IR laser.

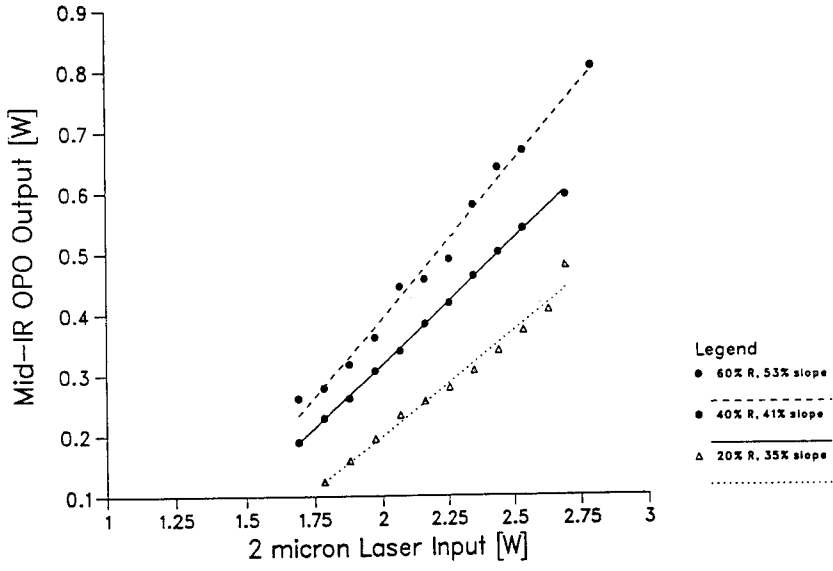


Fig. 4. Slope efficiency data for a 4kHz Mid-IR solid-state laser.



## Surface Chemical Analysis on Diamond C(111) by IR Sum Frequency Generation and Second Harmonic Generation Spectroscopy

R.P. Chin, J.Y. Huang, & Y.R. Shen

Material Science Division, Lawrence Berkeley Laboratory, Berkeley, CA 94720  
Dept. of Physics, University of California at Berkeley, Berkeley, CA 94720

T.J. Chuang & H.Seki

IBM Research Division, Almaden Research Center  
650 Harry Rd., San Jose, CA 95120-6099

Infrared sum frequency generation (SFG) and second harmonic generation (SHG) has found widespread use as surface sensitive probes [1]. As second order nonlinear processes, SFG and SHG are forbidden in the bulk of centrosymmetric media but allowed at its interface where the symmetry is broken. We have used the techniques to study adsorption of H and  $\text{CH}_x$  on diamond. In particular, with the help of a tunable infrared laser, the infrared-visible SFG allows us to measure in-situ surface vibrational spectra and hence identify the adsorbed species. The results provide us with useful insight about possible mechanisms governing the chemical vapor deposition (CVD) process for diamond growth.

In our experiments [3-5], a natural type IIa diamond oriented in the (111) direction is used. The diamond is placed on a high temperature heater capable of reaching  $1200^\circ\text{C}$ . Activated species from a hydrogen or methane ambient are produced by a tungsten hot filament at  $\sim 2000^\circ\text{C}$ . The UHV chamber has a base pressure of  $\sim 10^{-9}$  torr. Dosing is at a pressure of  $\sim 10^{-5}$  torr, with the diamond sample kept near the room temperature.

A SFG spectrum (p-polarized infrared) of the as-polished diamond clearly shows a single C-H feature at  $2828\text{ cm}^{-1}$ . For s-polarized infrared light very little signal is seen. This polarization dependence suggests the C-H bond to be normally oriented since only p-polarized IR can excite the C-H stretch mode. An upper limit to the bond tilt spread angle is  $\theta = 30^\circ$  agreeing with electron stimulated desorption ion angular distribution (ESDIAD) results [6]. This orientation is expected from the bulk terminated geometry of the (1x1) surface with the  $\text{sp}^3$  bonds normal to the surface.

Adsorption of atomic hydrogen by dosing onto a reconstructed (2x1)/(2x2) "clean" diamond (111) surface can be followed with SHG. The signal responds with coverage dependence and the surface structure. At ~5% ML coverage, a transition to the unreconstructed (1x1) surface is observed. Such a small amount of hydrogen is sufficient to cause the transition is certainly surprising. The SHG signal saturates at near full coverage of H.

The spectrum at low H coverage (<40% ML) is dominated by the appearance of a distinct peak at  $2860\text{ cm}^{-1}$ . With increasing H coverage, this peak gradually diminishes while a new peak at  $2830\text{ cm}^{-1}$  gains strength and becomes dominant. Conversion of the  $2860\text{ cm}^{-1}$  peak to the  $2830\text{ cm}^{-1}$  peak also occurs with a mild ( $700^\circ\text{C}$ ) anneal of the substrate. This indicates the presence of a metastable (1x1) surface as an intermediate stage during the (2x1)→(1x1) surface phase transformation. As more hydrogen chemisorbs to the surface or with annealing, the surface relaxes fully to the equilibrium (1x1) structure.

We also use SFG spectroscopy to study adsorption of H and methane radicals produced by passing methane over the hot filament. The spectra of the dosed C(111) surface show mainly the presence of H and  $\text{CH}_3$ . Aside from the C-H peak at  $2830\text{ cm}^{-1}$ , we can identify  $\text{CH}_3(\nu_s)$  symmetric stretch at  $\sim 2860\text{ cm}^{-1}$ , and  $\text{CH}_3(\nu_{as})$  and Fermi resonance at  $\sim 2985\text{ cm}^{-1}$ . With increasing dosing (~30-60 min.), the C-H peak decreases with a corresponding increase of the  $\text{CH}_3(\nu_s)$  peak at  $2863\text{ cm}^{-1}$ . This behavior suggests the abstraction of hydrogen in favor of the methyl terminated surface.

The  $\text{CH}_3$  orientation can be determined by the intensity ratio of the  $\text{CH}_3(\nu_s)$  peak to the  $\text{CH}_3(\nu_{as})$  peaks. As in the C-H case, the symmetric stretch mode along the symmetric  $\text{CH}_3$  axis is excited most by p-polarized infrared light if the  $\text{CH}_3$  group is normally oriented. For the asymmetric modes, these are excited least for normal orientation. With greater exposure, the asymmetric peaks decrease with a corresponding increase of the symmetric peak. This behavior can be explained by an increasing normal orientation due to the steric interaction with neighboring sites. For the saturated surface, the  $\text{CH}_3$  tilt spread is found to be  $8^\circ$ , much less than the C-H case above. A comparison of signal strengths of the peaks for the  $\text{CH}_3$  saturated case to the H saturated case yields a  $\text{CH}_3$  coverage of ~70% ML. The fact that the saturation coverage is less than unity implies a strong steric interaction.

Kinetic parameters relating to the bond energy can be found by thermal desorption. By exposing the H terminated diamond to a heating cycle in the range of 600°C to 750°C for a period of a few tens of seconds to half an hour, some hydrogen can be desorbed. The partial coverage is determined from the strength of the C-H peak since the surface nonlinear susceptibility is proportional to the surface density, neglecting any orientation changes. The results yield close to first order desorption kinetics with an activation energy,  $E_d = 3.4 \pm 0.2$  eV and pre-exponential factor of  $10^{13 \pm 1} \text{ s}^{-1}$ .

The study of relevant reactive species for CVD diamond growth by SFG and SHG gives insight to the surface species and reaction mechanisms involved. It has been shown that atomic hydrogen plays an important role for holding the (1x1) diamond structure; for abstraction of species not contributing to diamond growth; and for opening new reaction sites. Methyl radical adsorption appears to be preferential than for atomic hydrogen with strong steric interaction at high  $\text{CH}_3$  coverage. Future work is expected to yield greater information about the reactions involving  $\text{CH}_3$  and with conditions closer to those for CVD diamond film growth. Other principal growth planes, (100) and (110) can be studied similarly.

### Acknowledgment

This work was supported by the Director, Office of Energy Research, Office of Basic Energy Sciences, Material Sciences Division of the U.S. Department of Energy under Contract No. DE-AC03-765F00098.

### References

1. Y.R. Shen, *Nature (London)* **337**, 519 (1989) ; X.D. Zhu, H. Suhr, and Y.R. Shen, *Phys. Rev. B*, **35**, 3047 (1987) and references therein.
2. R.C. DeVries, *Ann. Rev. Mater. Sci.* **17**, 161 (1987);  
K.E. Spear, *J. Am. Ceram. Soc.* **72**, 171 (1989);  
J.C. Angus and C.C. Hayman, *Sci.* **241**, 913 (1988).

3. R.P. Chin, J.Y. Huang, Y.R. Shen, T.J. Chuang, H. Seki and M. Buck, Phys. Rev. B, **45**, 1522 (1992) and references therein.
4. Yoshitaka Mitsuda, Taro Yamada, T.J. Chuang, H. Seki, R.P. Chin, J.Y. Huang, and Y.R. Shen, Surf. Sci. Lett., **257**, L633 (1991) and references therein.
5. R.P. Chin, J.Y. Huang, Y.R. Shen, T.J. Chuang, and H. Seki, (to be published)
6. A.V. Hamza, G.D. Kubiak, and R.H. Stullen, Surf. Sci. **206**, L833 (1988).
7. B.B. Pate, Surf. Sci. **165**, 83 (1986).

Tuesday, March 8, 1994

## Poster Session 1

**TuB** 8:50pm–10:30pm  
Teton Room

## Hook Spectroscopy as a Single-Shot OH Density and Temperature Diagnostic

David K. Zerkle and Andrew D. Sappey  
 Los Alamos National Laboratory  
 Chemical and Laser Sciences Division  
 MS J565, CLS-2  
 Los Alamos, NM 87545  
 (505) 665-7101

Hook spectroscopy is being implemented to measure OH density and temperature in a premixed, CH<sub>4</sub>/air, atmospheric pressure flame on a single shot basis. The hook method makes use of the region of anomalous dispersion surrounding electronic transitions, typically in atoms<sup>1</sup>. In this region, the refractive index of the sample experiences dramatic shifts from its non-resonant values as shown in Figure 1. As seen in the figure, the solid curve has a minimum on the blue side of  $\lambda_0$  and a maximum to the red. The dashed curve represents the Sellmeier approximation to the refractivity which assumes that the linewidth is infinitely narrow. This approximation is normally quite valid in the wings of electronic transitions and is used to simplify the mathematics involved in determining number density from hook spectra.

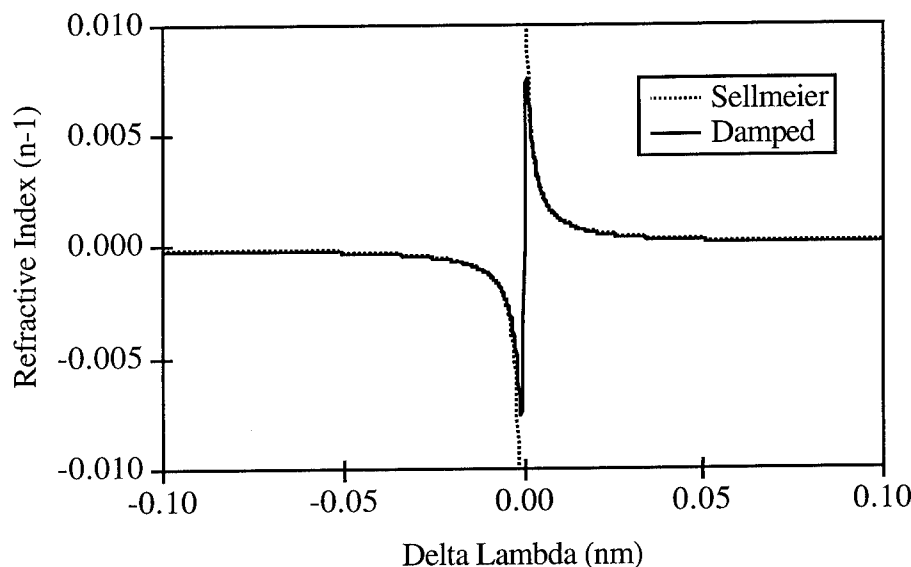


FIG. 1. Variation of index of refraction with wavelength near the 324.754 nm resonance.

The basic laboratory apparatus for this experiment has been described in earlier papers<sup>2,3</sup>, and is very similar to that employed by Molander<sup>4</sup>. The method requires a light source with a bandwidth large compared to the linewidth of the electronic transition. This source illuminates a Mach-Zehnder interferometer. In one arm of the interferometer is placed the dispersive sample while a compensating optic is placed in the other arm. The sample introduces a wavelength dependent phase shift, the size of which depends on the product of  $NfL$ , where  $N$  is the average density of the dispersive species,  $f$  is the oscillator strength of the electronic transition, and  $L$  is the path length through the sample<sup>1</sup>. If  $f$  and  $L$  are known, the interferogram can be used to determine average density. Each wavelength increment in the sample beam has a different phase relative to the beam in the reference arm. When the beams are recombined, the interference pattern created contains the wavelength dependent phase shift information, but the interferogram must be dispersed in a monochromator to recover it. The wavelength dispersed interferogram has hooks on either side of  $\lambda_0$  which have the characteristic shape of the anomalous dispersion curve of Figure

1. The wavelength separation between the hooks is given by Equation 1, where  $K$  is the interferometer constant,  $\Delta\lambda$  is the wavelength separation between hooks,  $r_0$  is the classical electron radius, and  $\lambda_0$  is the center wavelength of the transition.

$$\bar{N} = \frac{\pi K \Delta\lambda^2}{f L r_0 \lambda_0^3} \quad (1)$$

The hook method has been used for nearly 100 years to determine oscillator strengths of electronic transitions in atoms. Recently, we have used hook spectroscopy to determine Cu atom number density in optically thick laser-ablated copper plumes<sup>3</sup>. As a diagnostic technique, hook spectroscopy has the advantage of being insensitive to the collisional environment which means that absolute density can be determined *exactly* in optically thick plasmas and flames without recourse to quenching corrections which plague laser-induced fluorescence (LIF) measurements. The disadvantage is that it is a line of sight technique, like absorption spectroscopy; however, 1-dimensional spatial resolution is available in a plane normal to the beam propagation direction<sup>5</sup>.

Hook spectroscopy has typically been used for measurements on atomic species; however, there is no theoretical reason to prevent its use on molecular systems. In practice, to our knowledge, the OH radical is the only molecule to which the technique has been applied<sup>6</sup>. In that work, Anketell and Pery-Thorne used the hook method to (incorrectly) determine the oscillator strengths of the A-X (0,0) and (1,0) bands of OH. We are implementing the method to measure single shot OH density and temperatures. Our experimental hook method setup has been described in detail previously. Only the aspects unique to OH detection are discussed here. The light source consists of a broadband KrF laser equipped with unstable resonator optics (Lambda Physik, 105i) Raman shifted in H<sub>2</sub> and HD (first Stokes in each) to produce broadband output encompassing the OH A-X (0,0) Q<sub>1</sub>(1-7) rotational features. The interferometer optics consist of two 308 nm 50% beamsplitters at 45° incidence and two 308 nm 99.5% full reflectors at 45° incidence. The OH is produced in an atmospheric pressure, premixed, methane/air flame. The linear configuration Maxon burner provides a flame approximately 12 inches in path length for our measurements.

Temperature can be determined from a rotationally-resolved molecular hook spectrum with knowledge of the rotational line strengths, since the hook separation will depend upon the product of the oscillator strength for the A-X (0,0) band, the rotational line strengths, and the population of the ground state rotational level involved in the transition, which is a known function of temperature. Experimentally, difficulties can arise analyzing data from interferograms in which hooks from neighboring transitions overlap. This can be mitigated by limiting the path length which is easily accomplished and/or increasing the linear dispersion of the monochromator, which is not so easily accomplished. Unfortunately, one can not decrease the path length arbitrarily, because the hook separation must be sufficiently large for the hooks to occur in a region of the transition wing for which the Sellmeier approximation is valid; thus the minimum allowable hook separation (or  $NfL$  product) will depend on the collisional environment. In any case, methods of determining hook separations from overlapping transitions have been developed and used effectively in atomic spectra<sup>1</sup>. Finally, hook spectroscopy has the potential to be used for other light molecular hydrides such as CH, NH, and SH. In addition, heavy molecules with unresolvable rotational structure may also prove amenable to the technique, although temperature could not be determined for such species.

### References

- 1 W.C. Marlow, Appl. Opt. **6**, 1715 (1967).
- 2 A.D. Sappey, T.K. Gamble, and D.K. Zerkle, Appl. Phys. Lett. **62**, 564 (1992).
- 3 D.K. Zerkle, A.D. Sappey, and T.K. Gamble, AIAA Paper No. 93-3227, (1993).
- 4 W.A. Molander, SPIE Conference on Metal Vapor, Deep Blue, and Ultraviolet Lasers, **1041** 11 (1989).
- 5 R.J. Sandeman, Proceedings of the 15th International Symposium on Shock Waves and Shock Tubes, Berkeley, California, July 28-August 2, 1985, Stanford University Press, Stanford, California, page 3.
- 6 J. Anketell, A. Pery-Thorne, Proc. Roy. Soc. A. **301**, 343 (1967).

# C<sub>2</sub> Swan Band Spectral Measurements of Temperatures in a Decaying Laser-Induced Plasma

*Christian Parigger, David H. Plemmons, James O. Hornkohl, and J. W. L. Lewis*

*University of Tennessee Space Institute*

*Center for Laser Applications*

*Tullahoma, Tennessee 37388*

*Phone: 615-393-7338*

## 1. INTRODUCTION

It is of interest to characterize temperature fields from laser-induced breakdown plasmas in a temporal regime well separated from the breakdown initiating laser pulse. The post-breakdown emission spectra are predominantly recombination molecular spectra. The use of such spectra has been previously demonstrated to yield high temperatures for CN.<sup>1</sup>

Diatomic recombination spectra of C<sub>2</sub> are recognizable within the first microsecond after laser plasma creation. However, atomic carbon lines are superposed. At delays of typically 30  $\mu$ s, the well marked, single-headed and degraded to the violet progression<sup>2</sup> of the C<sub>2</sub> Swan system  $\Delta\nu = 0$ ,  $\Delta\nu = \pm 1$  sequences become prominent, corresponding to the  $A^3\Pi_g \rightarrow X^3\Pi_u$  molecular transition. Individual measurements of the sequences with the 1800 g/mm grating yield the temperature subsequent to molecular recombination. Monitoring the  $\Delta\nu = 0$  sequence of the CN violet system, corresponding to  $B^2\Sigma^+ \rightarrow X^2\Sigma^+$  molecular transition, serves as an additional temperature diagnostic. Comparing the observed rotation-vibrational structures of the individual sequences with synthetic spectra shows temperatures in excess of 6000 K some 30  $\mu$ s after the initial optical breakdown event.

## 2. SPECTRAL MEASUREMENTS

Laser-induced optical breakdown was accomplished inside a laboratory cell containing CO by focusing of 7.5 nanosecond pulse-width Nd:YAG 1064-nm radiation. Typically 300-mJ pulse energies produced strong breakdown plasmas in the focal volume. Observation of individual breakdown events shows that the laser-induced plasma consists of a set of individual plasmas.

The Continuum YG680S-10 Nd:Yag laser is operated at an internal frequency of 10 Hz. 1064-nm laser radiation is focused into the cell containing 3.25 psi above atmospheric pressure CO gas of 99.97% purity, with at most 0.02% N<sub>2</sub> gas. An electrical pre-trigger pulse drives the delay generator which externally synchronizes the optical multichannel analyzer (OMA) and controls the hardware for the gate pulser. Using personal computer control via GPIB, a delay of 30  $\mu$ s from the laser pulse and a gate-width of 1  $\mu$ s is selected with the OMA2000 program to control the pulser which applies the gate pulse to the intensifier in front of the linear diode array. Data are transferred from the diode array to the OMA memory and are available for further processing in the computer. The spectra were obtained using the MonoSpec 27 Thermo Jarrel-Ash 0.275 m monochromator. The 1800 g/mm holographic grating has a reciprocal linear dispersion of 2 nm/mm; this grating and the diode array give  $\sim 40$  nm of coverage in a spectrum. Wavelength calibrations were performed using standard light sources; the sensitivity correction was accomplished with a tungsten lamp, and data have been detector-noise background subtracted.



The recorded spectrum of the  $\Delta\nu = -1$  sequence of the  $C_2$  Swan System is shown in Fig. 1. The measured average OMA counts show an average over 200 individual data scans of the linear diode array.

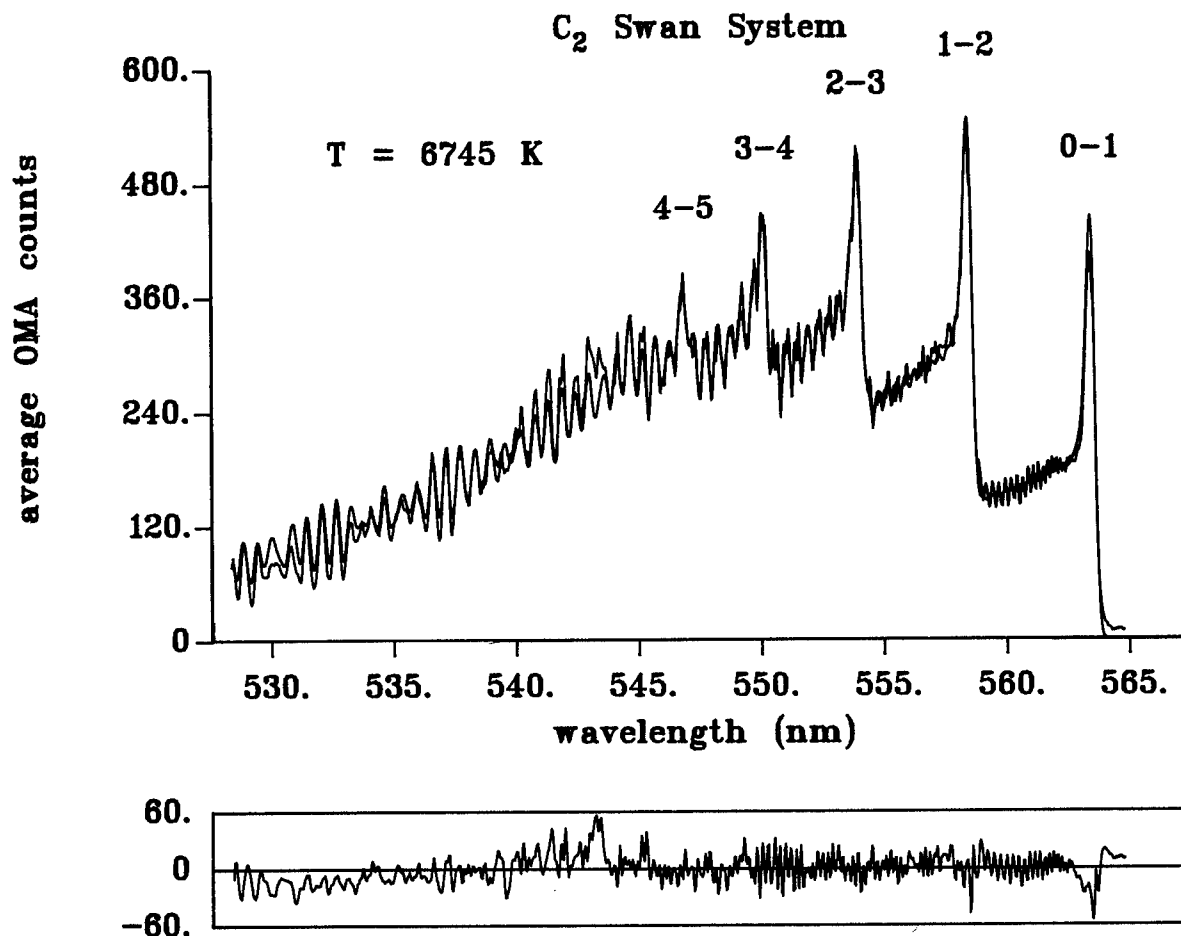


Fig. 1:  $\Delta\nu = -1$  sequence of the  $C_2$  Swan System at a delay of 30  $\mu s$ .

Also shown in Fig. 1 is the residual of a synthetic spectrum fitted to the experimental spectrum. The synthetic spectrum was obtained by applying the downhill simplex method<sup>3</sup> to minimize the squared-residuals between the measured and computed spectral intensities by varying both temperature  $T$  and the spectral resolution. The difference between experimental and synthetic spectrum shows discrepancies near the band edges of the 0-1, 1-2, and 2-3 bands. Also, near 543 nm, the behavior of the residual indicates the presence of the 6-7 band of the so called High Pressure Band of  $C_2$ .<sup>2</sup> Although the high pressure bands are known to be an intensity anomaly in the  $C_2$  Swan system corresponding to  $\nu' = 6$ , the theoretical fitting procedure does not include bands for which  $\nu' = 6$ . The temperature of  $T=6745$  K and FWHM (full width at half maximum) of  $11.5\text{ cm}^{-1}$  yields the best agreement between the experimental and synthetic spectrum. Experiments using a slightly higher resolution spectrometer with a cryogenically cooled CCD detector confirm the above temperature but also typically show the High Pressure Band.

The observed spectrum of the  $\Delta\nu = 0$  sequence and the residual of the fit are shown in Fig. 2. Apart from the disparities near the 0-0 band, the residual shows some "offset" variation at the low and high wavelength sides.

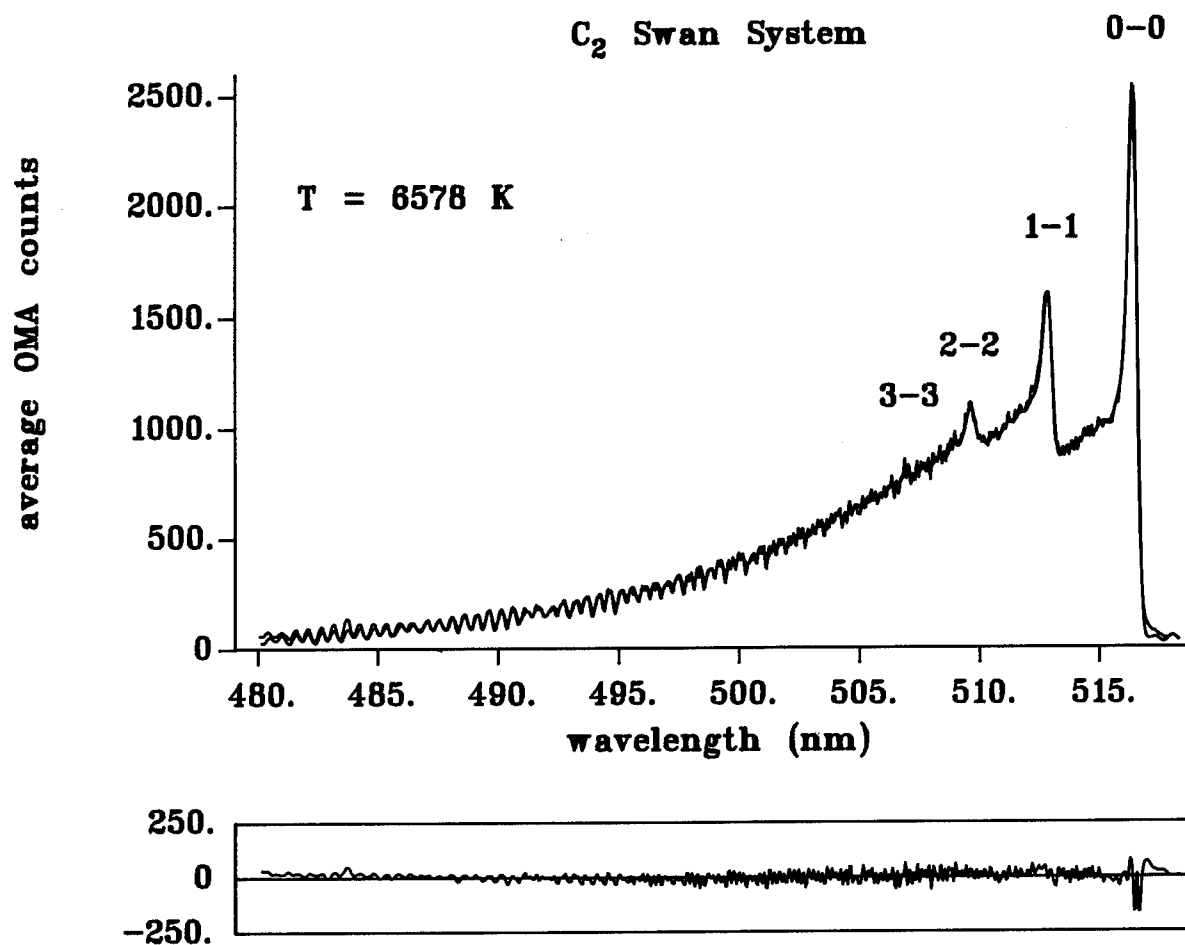


Fig. 2:  $\Delta\nu = 0$  sequence of the  $C_2$  Swan System at a delay of  $30 \mu\text{s}$ .

A temperature of  $T=6578 \text{ K}$ , and a FWHM of  $14 \text{ cm}^{-1}$ , was obtained from the fitting procedure. Note the smooth residual near the spectral contribution of the 3-3 band and the mainly rotational spectral features at the low wavelength side.

The  $\Delta\nu = +1$  sequence gives 3 times higher standard deviations than were obtained for the  $\Delta\nu = -1$  and 0 sequences. The Franck-Condon factor for the 6-5 band is  $\sim 6$  times larger than for the 6-7 band. Thus, the intensity anomaly which constitutes the High Pressure Bands is stronger for the  $\Delta\nu = +1$  sequence. We attribute a discrepancy near 468-nm to the 6-5 High Pressure Band of  $C_2$ . The 6-5 High Pressure Band is listed<sup>2</sup> to be 3 times stronger than the 6-7 High Pressure Band, therefore, more strongly affecting the  $C_2$  Swan System in the  $\Delta\nu = +1$  region. Differences near the band edges are larger than for the other two sequences. Without accounting for High Pressure Band spectral features, we find a temperature of  $T=6548 \text{ K}$  and a resolution of FWHM  $17.5 \text{ cm}^{-1}$  from the  $\Delta\nu = +1$  sequence.

In addition to the C<sub>2</sub> Swan System, we observed CN spectra originating from at most 0.02% N<sub>2</sub> in the 99.97% pure CO gas. The  $\Delta\nu = 0$  sequence of the CN Violet System was measured. Applying the fitting procedure<sup>1</sup> yields a temperature of  $T = 6349$  K; the residual typically shows differences near the band edges and near the minima. Such differences, however, result in a similar least-square residual as obtained from the  $\Delta\nu = -1, 0$  sequences of C<sub>2</sub>.

An estimate of the accuracy of the temperatures was obtained by varying the baseline correction that is applied to the experimental spectrum. For constant resolutions of the C<sub>2</sub> spectral sequences, the temperature was found using the Nelder-Mead iteration scheme. We obtain an accuracy of  $\pm 5\%$ , or  $\pm 300$  K. Therefore, the C<sub>2</sub> and CN molecular temperatures agree within experimental errors.

### 3. SYNTHETIC SPECTRA

The molecular constants that are required for the computation of the synthetic spectra were determined from fitting of the line position data of Phillips and Davis.<sup>4</sup> The method of Zare *et al.*,<sup>5</sup> was used in the analysis of the reported bands. The fitted molecular constants are not reported here. It is believed that the determination of the molecular constants is of sufficient accuracy for fitting of the low-resolution experimental spectra.

The line strengths that were employed in this work contain the variations of the electronic transition moments with internuclear distance. The variation of the Franck-Condon factors with rotational quantum numbers was ignored despite the high molecular temperatures and, hence, high rotational quantum numbers ( $N=150$  for the  $0' - 0$  band).

Modifications due to the High Pressure Bands of C<sub>2</sub> are expected to improve the overall fit to the experimental data, yet the effects on temperature are believed to be negligible.

### 4. SUMMARY

Molecular C<sub>2</sub> Swan system and molecular CN violet system recombination spectra have been observed to yield temperatures in excess of 6000 K. Well after the initial breakdown process, both CN and C<sub>2</sub> spectra have been analyzed to yield approximately equal temperatures. The presence of the C<sub>2</sub> High Pressure System limits the accuracy of the temperature determination. The  $\Delta\nu = +1$  sequence appears more affected than the  $\Delta\nu = -1$  sequence, therefore, we conclude that the  $\Delta\nu = -1, 0$  sequences yield more accurate temperatures.

### REFERENCES

1. J. O. Hornkohl, C. Parigger, and J. W. L. Lewis, *J. Quant. Spectrosc. Radiat. Transfer* **46**, 405 (1991).
2. R. W. B. Pearse and A. G. Gaydon, *The Identification of Molecular Spectra*, pp. 95-96, Chapman & Hall, London (1963).
3. J. A. Nelder and R. Mead, *Comput. J.* **7**, 308 (1965).
4. J. G. Phillips and S. P. Davis, *The Berkley Analysis of Molecular Spectra*, Vol. 2 (a), The Swan System ( $A^3\Pi - X^3\Pi$ ) of the C<sub>2</sub> Molecule (Univ. California Press, Berkley 1968).
5. R. N. Zare, A. L. Schmeltekopf, W. J. Harrop, and D L. Albritton, *J. Mol. Spectrosc.* **46**, 37-66 (1973).

# Spatially and Temporally Resolved Electron Number Densities in a Decaying Laser-Induced Hydrogen Plasma

*Christian Parigger, David H. Plemmons, and J. W. L. Lewis*

*University of Tennessee Space Institute*

*Center for Laser Applications*

*Tullahoma, Tennessee 37388*

*Phone: 615-393-7338*

## 1. INTRODUCTION

Measurements of the widths of Stark broadened hydrogen Balmer Series lines can be used to infer electron number densities of optically created plasmas. A typical optical breakdown plasma is transient and shows spatial structure. For example, self-focusing effects may induce density variations which may be measured using diffraction techniques.<sup>1</sup> The expanding plasma induces number density variations that in fact may form a light pipe for high intensity laser pulses.<sup>2</sup>

Spectral measurements, spatially resolved along the slit dimension of a spectrometer, of the hydrogen alpha line allow us to characterize the spatial and temporal evolution of the plasma. The electron number density can be determined by fitting the experimentally recorded spectra to tabulated profiles.<sup>3</sup> Early in the plasma decay the  $H_\alpha$  lines are very wide: number densities of typically  $10^{19} \text{ cm}^{-3}$  are found. A series of measurements was performed with delays of up to a few microseconds after creation of the optical breakdown plasma in hydrogen gas.

## 2. SPECTRAL MEASUREMENTS

Laser-induced optical breakdown is accomplished inside a laboratory cell containing  $H_2$  by focusing of 6 nanosecond pulse-width Nd:YAG 1064-nm radiation. Typically 220-mJ pulse energies produce strong breakdown plasmas in the focal volume. The peak intensity is estimated to be  $10^{12} \text{ W/cm}^2$  in the focal volume.

The Continuum YG680S-10 Nd:YAG laser is operated externally at a frequency of 10 Hz. The laser pulse is passed through a 3X beam expander focused into the cell containing research grade  $H_2$  gas 150 torr above atmospheric pressure. An electrical pre-trigger pulse drives the delay generator which externally synchronizes the lens-coupled intensifier in front of a cryogenically cooled CCD camera.

Using personal computer control and a gate width of 6 ns, delays in increments of 6 ns are selected to monitor the early plasma emissions, while larger gate widths were applied for longer delays from the laser spark. Data are transferred from the CCD camera to the computer hard disk and are available for further processing in the computer.

The spectra were resolved using the Jobin Yvon 0.64 meter Czerny-Turner monochromator. A 1200 g/mm grating was employed to disperse the plasma emission. This grating and the CCD chip cover the emission over a spectral range of 15 nm. The plasma emission from the optical breakdown is imaged one-to-one onto the spectrometer slit in such a way that the direction of propagation of the laser pulse is parallel to the slit. This allows us to spatially resolve spectra across the length of the breakdown. Wavelength calibrations were performed using standard light sources, the sensitivity correction was accomplished

with a tungsten lamp, and data have been detector dark-noise background subtracted. The accumulative CCD counts (z-axis) resulting from 1000 laser shots are displayed versus slit dimension (x-axis) and versus wavelength (y-axis). The breakdown laser pulse propagated to the positive x direction.

The recorded  $H_\alpha$  spectra at a delay of 12 ns are shown in Fig. 1. The 3-dimensional plot visualizes the wavelength-spatial characteristics – the  $H_\alpha$  line is embedded in the broad continuum spectra produced by the sea of dense, free electrons.

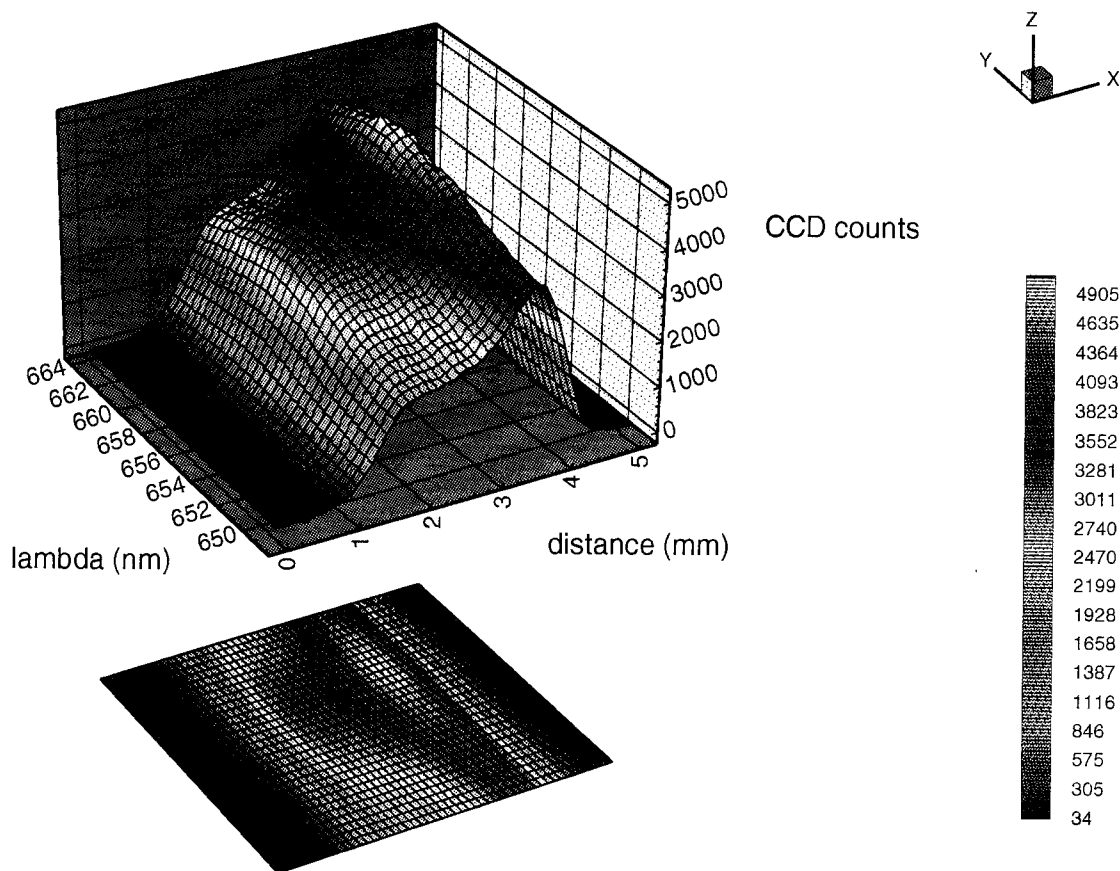


Fig. 1:  $H_\alpha$  spectra recorded with a 6 ns gate at a delay of 12 ns.

Also shown in Fig. 1 is the pseudocolor projection displaying the intensity variation of the  $H_\alpha$  emission along the length of the plasma. From individual widths we infer an electron number density gradient along the length of the plasma. The emission is more intense in the forward direction, density gradients are apparent.

At early times in the plasma decay note the substantial red shift of the  $H_\alpha$  line profile from its neutral position. Larger shifts occur in the forward region of the breakdown plasma. The red shifts are related to temperature,<sup>4</sup> i.e., larger shifts correspond to higher temperatures, therefore, we conclude that there is also an electron (or excitation) temperature gradient across the length of the plasma.

The recorded spectra at a delay of 30 ns are shown in Fig. 2. The spatial two-peak appearance is typical for plasma decay. Initially, the plasma emission is most intense at the position of the forward peak without a second peak. As the plasma decays, a second peak appears. The analysis of the individual spectra shows that in the area between the peaks the electron number density is higher despite lower spectral intensity.

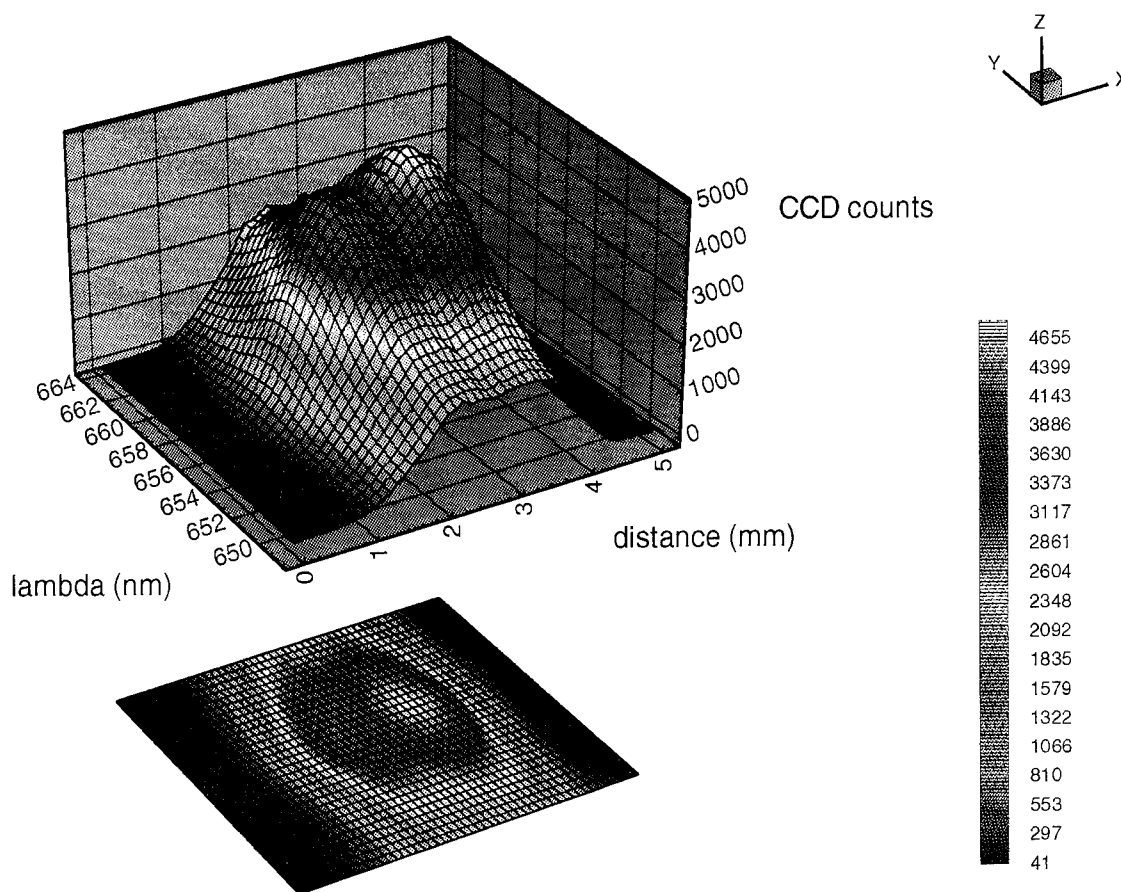


Fig. 2:  $H_\alpha$  spectra recorded with a 6 ns gate at a delay of 30 ns.

The experimental result for a delay of 300 ns is displayed in Fig. 3 (see next page). For longer delays only spatial single-peaked emission was observed.

### 3. SUMMARY

The temporally and spatially resolved hydrogen alpha spectra allows us to visualize the internal characteristics of the optical breakdown process. A detailed analysis of the individual images should yield a precise distribution of the electron number density along the excitation direction.

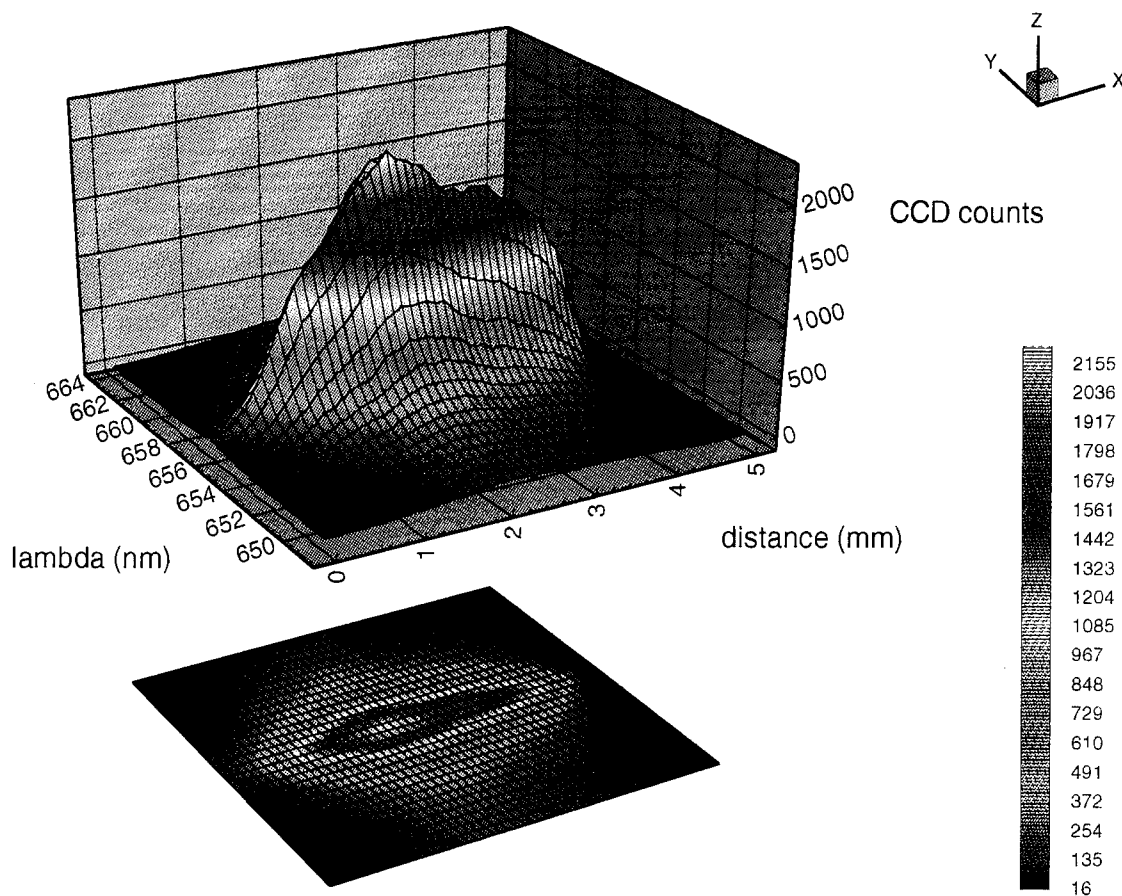


Fig. 3:  $H_\alpha$  spectra recorded with a 6 ns gate at a delay of 300 ns.

## REFERENCES

1. I. A. Bufetova, G. A. Bufetova, A. M. Prokhorov, and V. B. Fedorov, *Pis'ma. Zh. Eksp. Teor. Fiz.* **58**, 73 (1993).
2. C. G. Dufree III and H. M. Milchberg, *Phys. Rev. Letts.* **71**, 2409 (1993).
3. C. Parigger, D. H. Plemmons, and J. W. L. Lewis, *Technical Digest of 1993 OSA Annual Meeting*, Toronto, Oct 3-8 (1993) paper THXX4.
4. H. R. Griem, *Phys. Rev. A* **28**, 1596 (1983).

## Vacuum Ultra-Violet Photoionization Time-of-Flight Mass Spectrometry for the Investigation of Products of Benzene Oxidation

German Bermudez and Lisa Pfefferle  
Yale University, Department of Chemical Engineering  
New Haven, CT 06520-2159  
(203) 432-4059; (203) 432-4377

### 1.0 Summary

A serious limitation for direct, routine mass spectrometric analysis of complex mixtures arises from the destructive nature of electron ionization methods employed in commercial instrumentation. Parent species fragmentation limits mixture analysis because the mass spectrum must be deconvoluted into its single species contributions within the overall mass range examined. In most cases the overlap of the many fragments, multiple charge ions, and parent species precludes interpretation in real instruments having finite mass resolution and signal to noise ratios. The alternative approach of lowering the electron ionizing energy may minimize fragmentation, but it decreases the sensitivity. Separation/detection procedures have become the standard for analysis of complex mixtures however the inherent advantages of mass spectrometry are lost, in terms of rapid analysis and universality. Our approach addresses these difficulties by using non-fragmenting laser ionization time-of-flight mass analysis at 10.5 eV with simultaneous electron ionization quadrupole analysis for cross calibration. Most species relevant to large hydrocarbon processing and combustion (aromatics, C<sub>3</sub> or larger species, and hydrocarbon radicals) have ionization potentials below 10.5 eV and thus are accessible to "soft ionization" at this photon energy.

### 2.0. Instrumentation

#### 2.1. Laser Photoionization Time -of-Flight Mass Spectrometer

The VUV photoionization mass spectrometer (VUV-MS) is equipped with Wiley-McLaren type acceleration for higher resolution and an Einzel lens to compensate for the normal component of kinetic energy so that the probability of reaching the detector is relatively independent of mass. Sample introduction, which is normal to the flight tube axis of the mass spectrometer, minimizes detector fouling from neutral species generated in the reactor, and decreases the width of the ion velocity distribution along the time-of-flight axis, resulting in higher resolution as compared with the on-axis arrangement. The detector is also protected by a liquid nitrogen cryotrap. The detector sensitivity (microchannel plus type with wide linearity range) is not decreased after many months of operation. Overall detector gain after linear amplification is estimated to be  $10^8$  and the response linear over three orders of magnitude. Ion signals are averaged (2000 traces of 50  $\mu$ s record length at 10 Hz rate) in real time and recorded directly onto a 100 MHz digital storage oscilloscope interfaced with a PC. The overall mass resolution for these experiments was measured as 470 at 78 amu.

VUV photons were generated by the non-linear optical mixing technique of third harmonic generation (THG) in Xe. 335 nm radiation from a Nd:YAG laser (Quanta Ray DCR-3G system) operating at 10 Hz was focused into a Xenon cell at 7.5 Torr. Maximum 118 nm production as determined from benzene one photon ionization was found at approximately 40 mJ of energy in a 6 ns pulse at 354.6 nm, corresponding to a peak power of approximately  $8.7 \times 10^6$  W for THG generation in the Xe gas cell. Our data, however, is taken with 10 mJ of 355 power, for which any multi-photon processes or spurious effects from electrons generated at the vacuum chamber surfaces (through 355 and/or 118 nm radiation) are absent. This points out the advantage of using a high sensitivity detector. Multiphoton processes (118 + 355 nm) at the ionization region are



minimized through differential focusing and the slightly off-axis entrance angle of the 355 fundamental. Positioning of the 118 focal point is controlled with an XYZ translation stage.

## 2.2 Reactor and MS Coupling Systems and Residual Gas Analyzer

The reactor is a closed end alumina tube with an exit orifice of 5 to 100 mm to accommodate the overall pumping speed of the vacuum system at the desired reactor pressures. The tube is directly coupled to the ionization region of the two stage time-of-flight mass spectrometer (TOF). The hot reacting mixture expands through the pinhole into the vacuum, achieving rapid cooling and quenching reactions. Under the expansion conditions used in this study, hydrocarbon radicals survive the gas mixture expansion and are detected by the soft laser ionization method. The reactor/analyzer arrangement used is analogous to the molecular beam sampling methods employed in many combustion studies, which address stable and radical species. The reacting mixture enters the analysis chamber and becomes "residual" gas whose composition can be related to the reactor species concentration. To analyze this residual gas we use a Transpector C100M Residual Gas Analyzer (Leybold Inficon) attached to the ionization chamber of the TOF-MS. Five spectra were taken at the slowest scanning rate for each experimental condition and later averaged and background subtracted. This procedure gave a S/N level of 2 at  $1 \times 10^{-12}$  amps output level from the Faraday Cup detector.

Premixed gases were delivered to the reactor via a mass flow controller. Before its use in mixture preparation, benzene (Baker Analyzed, Reagent Grade) was outgassed by three consecutive freeze-pump-thaw cycles. Orifice sizes from the reactor to the analysis chamber were chosen to provide adequate signal to noise in the mass spectra. During all the experiments reported here, the analysis chamber pressure was maintained below  $5 \times 10^{-5}$  torr and in the TOF tube below  $2 \times 10^{-6}$  torr.

## 2.3 Data Analysis

In this study mass spectral intensities from both the VUV-MS and RGA are used to cross-calibrate concentration measurements taking the following issues into consideration. At the same concentration, a given species will produce different signal levels in the residual gas analyzer (RGA) spectra than any other species due to their differences in electron ionization cross sections and instrumental ion detection efficiencies. In the TOF spectra, a similar situation is encountered, due to differences in photoionization cross sections at 10.5 eV, ion collection efficiencies, and detector sensitivities to ions of different velocities and chemical characteristics. In addition, the decrease in the total gas throughput to the analysis chamber, caused by decreases in gas density and discharge coefficient through the nozzle as the temperature is increased at constant pressure, must also be considered. Quantitative connection between RGA and TOF data can be established through these relationships as shown in equations 1-4 below for selected specie/s that are detectable with both techniques (benzene in this study).

In the RGA spectra the relationship between the partial pressure of a particular component in the mixture and the signal intensity at a given mass is given by:  $P_i = (I_{i,m}/S_{i,m})f_{\text{nozzle}}(T)$  (1) where  $P_i$  is the partial pressure of species  $i$  at the reactor,  $I_i$  is the RGA intensity (current in amps) measured at a selected mass used for species  $i$ ,  $S_{i,m}$  is an experimentally determined sensitivity factor (amps/torr) for species  $i$  at mass  $m$ , and  $f_{\text{nozzle}}$  takes into account the variations in nozzle throughput at different temperatures. The sensitivity factors ( $S_{i,m}$ ) at room temperature are determined by measuring pressures at the microburner (MKS Baratron). The mass selected for analysis of a particular species is chosen such that there is unambiguous assignment (no overlap exists) with respect to any other fragments of parent species in the mixture.

Peak intensities corrected for temporal broadening in the time of flight configuration are given by:

$$I_{(m,T,Wd,g)}^{TOF} = W_d g [c]_{(m,T)}^{TOF} (\bar{\sigma}_m / \bar{\sigma}_{benzene})^2 \quad (2)$$

where  $W_d$  (Watts/m<sup>2</sup>) is the laser radiant flux density and  $g$  is detector gain.  $c_{(m,T)}^{TOF}$  is the concentration of the neutral species in the ionization volume with mass  $m$  at temperature  $T$ , and  $\bar{\sigma}_m$  and  $\bar{\sigma}_{benzene}$  are the temporal width of the time of flight peaks corresponding to mass  $m$  and benzene respectively. The concentration in the microreactor can then be obtained from:

$$C_{(m,T)}^{TOF} = (C_{(benzene,T)}^{RGA} / I_{(78,T,Wd,g)}^{TOF}) R_{(m,V_{io})} I_{(m,T,Wd,g)}^{TOF} \quad (3)$$

Here  $C_{(benzene,T)}^{RGA}$  is the benzene concentration (ppm) found with RGA analysis and  $I_{(78,T,Wd,g)}^{TOF}$  and  $I_{(m,T,Wd,g)}^{TOF}$  are the observed integrated intensities of benzene and mass  $m$  peaks. Since all mass peaks detected (with the exception of acetone) correspond to one photon ionization, the  $I$  dependence on radiant flux density cancels out in Equation (3).

$R_{(m,V_{io})}$  is an instrumental response factor given by:

$$R_{(m,V_{io})} = (VUV_{(m)} C_{eff}(V_{io}, m, d) D_{eff}(m))^{-1} \quad (4)$$

All factors in this equation are normalized relative to benzene.  $VUV_m$  is the ionization efficiency at 118 nm of species of mass  $m$ . Values of  $VUV_{(m)}$  at 118 nm reported in the literature (eg. Persons et al.) were used when available. For species larger than mass 78 amu  $VUV_{(m)}$  can be estimated as equal to benzene. For a range of species, this assumption is only introduces an error of less than 30% in the estimated concentrations. Theoretically-based methods for estimating VUV photoionization efficiencies are discussed below in section 3.0.  $C_{eff}(m, V_{io})$  is the instrumental ion collection efficiency. In general, ion trajectories for different masses introduced normal to the time-of-flight axis are not the same due to the unequal kinetic energy component in this direction. Even though molecular velocities in the thermalized reactor are distributed so that kinetic energies of species with different mass are the same, during the expansion this velocity distribution sharpens, and ions of different mass acquire different kinetic energies in the axial direction of the TOF tube. Modeling of ion trajectories for masses between 10 and 600 amu with the perpendicular sample introduction and the Einzel lens at the front end of the acceleration region of the TOF, showed that ions in this mass range can reach the detector with equal probability. Experimentally, after proper tuning of ion optics and ionization volume position, a range of conditions is reached within which no variations of the ion intensities in a wide mass range (>400 amu) are observed, therefore  $C_{eff}(m, V_{io}) = 1$  for this mass range.  $D_{eff}(m)$  is the plate detector secondary electron efficiency generation at mass  $m$ . Studies of secondary electron emission probabilities for ions of the same kinetic energy but different mass striking various detector surfaces provide guidelines for assessing relative detection efficiency. Using the correlations for peptides ( $m/z = 86$  to 1059) from Geno and MacFarland, the probability of detection of an ion once it reaches the surface of the plate would be unity for ions smaller than biphenyl (mass 154).

### 3.0 Method to Estimate Ionization Efficiencies

Photoabsorption data and ion yields (Koizumi et al., Person and Nicole and others) allow accurate absolute determination of the photoionization coefficients by simultaneously measuring the absorption cross sections ( $\sigma_a$ ) and ionization cross sections ( $\sigma_i$ ) as functions of the incident photon energy. This data is in all cases, photons with an energy from 0-0.3 eV above the first ionization potential (IP) give rise to rapidly changing ion yields. For photons above approximately 0.3 eV over the first IP the ion yields for the majority of species reported remain fairly constant, varying by less than 30% from the first IP to (IP + 2 eV). Strategies for estimating VUV photoionization efficiencies of hydrocarbons using both absorption techniques and photoelectron spectroscopy (PES) measurements have been

developed to augment experimentally-based calibrations. To a first approximation, Eland, 1984 found that the areas of the individual bands in a photoelectron spectrum are sufficient to determine the relative probability of ionization to the different ionic states. From this PES analysis, and our relative ionization efficiency data at 118 nm, we have observed that the ionization efficiencies using 118 nm photoionization are high and relatively constant ( $\pm 30\%$ ) for many hydrocarbon compounds containing six or more carbon atoms. These compounds have IPs a full 1-2 eV below the photon energy ( $1182 \text{ \AA} = 10.49 \text{ eV}$ ). The simultaneously-obtained peak ratios can thus approximate relative concentrations. However for smaller hydrocarbons with ionization potentials lying closer to the single-photon energy and for some larger alkynes, absorption cross sections and ionization efficiencies vary considerably necessitating experimental calibrations and/or more detailed theoretical analysis.

We have developed a method for correlating VUV photoionization yields, similar to one recently proposed by Koizumi (1991), making use of simultaneously obtained photoabsorption and photoionization cross section of alkanes, alkenes, alcohols and ethers (over the range of C1 to C6). Koizumi summarizes a wide survey of experimental studies on the decay of superexcited states (states above the ionization potential) of organic molecules and shows that for most alkanes, alkenes, ethers and alcohols examined in the photoabsorption and decay scheme neutral fragmentation, not autoionization, is the primary channel for decay of the superexcited states. This observation is rationalized by noticing that the high energy states in these species are formed by excitation of an electron in a  $\sigma$  bonding molecular orbital, which is likely to leave the molecule in a repulsive part of the highly excited state potential energy curve. Fast dissociation of the neutral excited species then competes efficiently with autoionization processes. Due to the fact that most high energy states,  $AB'$ , are Rydberg in nature, the photoabsorption cross section  $\sigma_t$  in regions of the spectrum above the first ionization potential becomes the sum of the direct photoionization cross sections  $\sigma_i$  and the Rydberg excitation cross sections. Since the excited Rydberg electron feels a Coulombic field similar to the one in an excited hydrogen atom, Koizumi uses its smoothly decreasing (with increasing principal quantum number) photoabsorption cross sections to model approaching each ionization continuum for each molecular IP. The separate contributions from each Rydberg series converging to every molecular IP at a given energy are summed with values from the curves fitted using hydrogen atom data. The Koizumi algorithm can be modified by adding an onset function fitted using PES data where available. This gives better agreement with experimental ionization efficiencies for compounds where IPs are more broadly spaced. For alkanes and alkenes this provides a good estimate of photoionization efficiency ( $\pm 20\text{-}30\%$ ).

#### 4. Summary of Results

Results will be presented for fuel lean oxidation of benzene at temperatures from 800-1100K. Major species detected from the low equivalence ratio runs are consistent with GC/MS flow reactor studies of Glassman and coworkers (Venkat et al.). In addition in our study using VUV photoionization MS, hydrocarbon radicals such as  $C_3H_3$  and  $C_5H_5$  were detected semi-quantitatively along with low concentration higher hydrocarbon products. We will emphasize both calibration methodology and error analysis in the talk. In summary the technique has provided a powerful "soft-ionization" method for detection of hydrocarbons and hydrocarbon radicals.

- Geno, P., and MacFarlane, R., *Int. J. Mass Spectrom. Ion Proc.*, **92**, 195, (1989).  
 Koizumi, H., *J. Chem. Phys.*, **95**(8), 5846, 1991.  
 Person, J.C., and Nicole, P.P., *J. Chem. Phys.*, **53**, 1767, (1990), *J. Chem. Phys.*, **49**, 5421, (1968), *J. Chem. Phys.*, **55**, 3390, (1971).  
 Venkat, C. Brezinsky, K. and Glassman I., 19th Symp. Intl'on Comb., 143, (1982).

Trace Organic Chemical Detection Using an Ultraviolet Excitation Molecular Beam Fluorometer, B.L. Preppernau and P.J. Hargis, Sandia National Laboratories, Dept. 1128, P.O. Box 5800, Albuquerque, NM 87185, (505) 844-9425.

Detection of air-borne environmental contaminants, such as organic solvents, requires unambiguous compound identification and sensitivity to concentrations below those permitted by regulating agencies. One promising detection approach uses a pulsed supersonic molecular beam vacuum expansion in combination with fluorescence signal spectral analysis to identify species in a chemical mixture. Expanding a contaminated atmospheric sample through a supersonic molecular beam expansion acts to cool the sample and greatly reduce the spectral density in a fluorescence or photoionization spectrum. Most organic contaminants of interest have electronic transitions in the ultraviolet with near-featureless broad band fluorescence spectra when recorded at atmospheric pressure and room temperature. By using a supersonic vacuum expansion, cooling to within a few degrees of absolute zero can reduce the effective rotational and translational temperatures of the sample molecules and provide a sharply defined spectra which can be used to unambiguously identify specific molecules and their concentrations.

We have constructed a pulsed supersonic molecular beam apparatus which can be synchronously probed with a pulsed ultraviolet laser source. The atmospheric pressure inlet to a commercial pulsed valve assembly is comprised of a high pressure mixing sample plenum and a mixing manifold. The mixture ratio of compounds in the carrier gas is monitored by high accuracy baratron pressure transducers. This mixing system allows us to generate calibrated mixtures of compounds with mixture ratios down to ten parts-per-billion (ppb). A high sensitivity 200 amu residual gas analyzer (RGA) is also coupled to the mixing manifold. The RGA can be used to determine the stability of a gas mix in the sample plenum, monitor system contamination, and ultimately to determine mixture compositions below one ppb.

The ultraviolet laser excitation source consists of a moderately high resolution dye laser (2 GHz linewidth) pumped by a pulsed Nd:YAG laser operated at 355 nanometers and a pulse repetition rate of 10 Hz. The output of the dye laser is doubled using either BBO or KDP nonlinear crystals and passed through Suprasil fused silica windows into the molecular beam expansion chamber. The ultraviolet wavelength tuning range used extends from 210 to 400 nanometers with output pulse energies up to 1 millijoule.

Spectra can be recorded simultaneously using three techniques. At right angles to the molecular beam axis and the laser probe axis are collection optics for wavelength integrated laser-induced fluorescence (LIF) detection using a photomultiplier tube. Also in the expansion chamber is a DC biased plate (-100 V) for collecting charge generated by photoionization. The photoionization signal is detected using a high gain charge sensitive amplifier. Finally, a quartz fiber optic vacuum feedthrough collects fluorescence from the laser-probe/molecular-beam-interaction region and couples the light into a 1/4-meter spectrometer (1200 groove/mm, 250-nm blaze) equipped with an intensified thermoelectrically cooled

charge coupled device (CCD) camera for dispersed wavelength fluorescence measurements.

Figure 1 demonstrates the effect of supersonic expansion cooling on a portion of the LIF spectrum of acetone vapor seeded into a helium carrier gas. The upper trace shows the laser-induced fluorescence (LIF) spectra obtained near normal atmospheric conditions (100 Torr). As the expansion to vacuum base pressure is reduced, the LIF spectra become progressively more sharply defined as broad band structures narrow due to the cooling effect of the expansion. The middle trace was acquired at a base pressure of  $2 \times 10^{-3}$  Torr and the bottom trace was acquired at  $6 \times 10^{-6}$  Torr. Though the absolute signal level in the bottom trace is reduced due to a

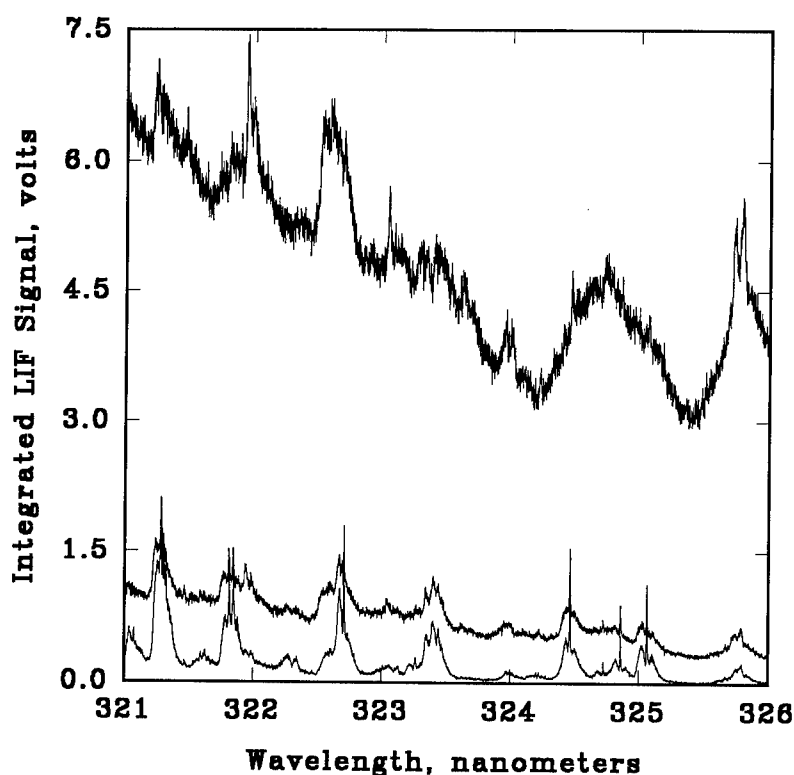


Figure 1. Supersonic Beam Expansion Base Pressure Dependence for Acetone LIF Spectra.

lower concentration of background acetone molecules in the expansion chamber, the signal to noise ratio of the spectra has improved by nearly two orders of magnitude since the incident laser pulse energy is distributed among fewer rovibrational transitions. The approximate rotational manifold temperatures are 5 Kelvin.

Figure 2 shows a comparison of LIF and photoionization spectra for toluene recorded at a concentration of 10 parts-per-million in 1000 Torr of helium carrier gas. This figure demonstrates the complementary value of recording simultaneous spectral signatures by different methods. In many cases the LIF and

photoionization spectra for organic species are nearly identical in certain wavelength regions. However, some vibrational bands at other wavelengths may show dramatically different spectral profiles. In some cases there may be no identifiable spectral structures from the LIF signal, but a well defined photoionization spectra can be recorded.

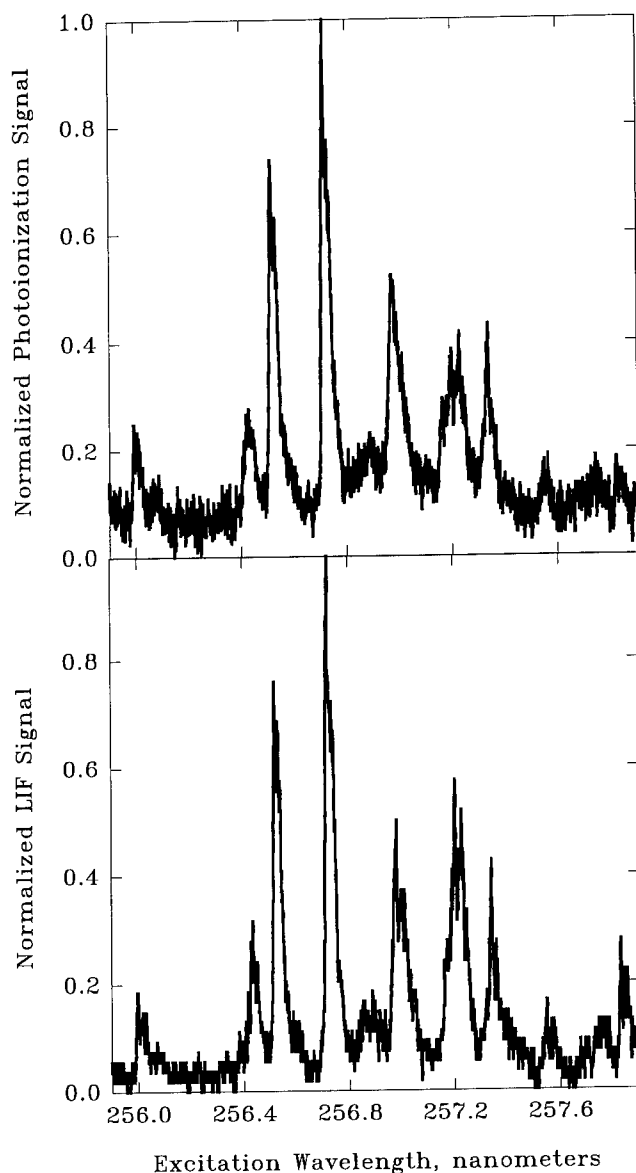


Figure 2. Comparison of LIF and Photoionization Spectra of Jet-Cooled Toluene

The apparatus described is being used to perform original surveys of spectra of a variety of organic compounds, such as toluene shown above, as well as species such as trichloroethylene, DIMP, DMMP, and the xylenes. In particular we have compared jet-cooled spectra resulting from excitation of substituted benzene derivatives, as these compounds have similar spectral features which can overlap

each other in certain spectral regions, thereby making their differentiation difficult in high pressure, room temperature spectra.

Beyond using the molecular beam fluorometer for spectral surveying, we are also studying issues associated with the relative sensitivity of each of the detection techniques. By examining the signal to noise ratio of current data, we can extrapolate the detection sensitivity for the system at 10 ppb for optimal conditions and compounds.

This work is supported by the United States Department of Energy under Contract DE-AC04-94AL85000.

## Chemical Species from Tritium-Breeding Compacts by Raman Spectroscopy

David J Taylor, Los Alamos Natl Lab, MS C348, Los Alamos NM 87545, 505-667-5309

Fred J Steinkruger, Los Alamos Natl Lab, MS C348, Los Alamos NM 87545, 505-667-0435

David E Christiansen, Los Alamos Natl Lab, MS C348, Los Alamos NM 87545, 505-667-6094

Donald J Gettemy, Los Alamos Natl Lab, MS C348, Los Alamos NM 87545, 505-667-0436

The retention of tritium in reactor breeding compacts has been studied in these experiments at conditions simulating nuclear reactor accidents, and the experimental results have been used to determine New Production Reactor safety envelopes. The tritium-breeding compacts tested contain thousands of spherical particles within a carbonaceous matrix; each particle is fabricated as a kernel of lithium aluminate, enriched in  $^6\text{Li}$  for breeding tritium by  $(n,\alpha)$  reaction, surrounded by consecutive shells of porous carbon, pyrolytic carbon, silicon carbide, and pyrolytic carbon to retain the tritium during breeding. The experiments demonstrated that in an accident with a sudden reactor temperature jump to  $1300^\circ\text{C}$ , more than 99% of the tritium would be retained within the compact for over 50 hours, which is ample time to bring such an accident under control. In these experiments, chemical species released from the compacts were measured by laser-Raman spectroscopy to enable design of chemical safety systems. Chemical species that were observed at intermediate temperatures, including  $\text{H}_2\text{O}$ ,  $\text{H}_2$ ,  $\text{CO}$ , and hydrocarbons, resulted from compact exposure to air, whereas species released at high temperatures, including HT and  $\text{CO}$ , originated within the particles. The Raman data identified the dominant tritiated species to be HT, at concentrations commensurate with measurements of total tritium using ion chambers and scintillation counter. These tests attained Raman detectability as low as 6.4 parts-per-million (ppm) for HT.

To simulate Modular High-Temperature Gas-Cooled Reactor (MHTGR) operating and accident conditions, each compact was heated in an induction furnace within a flow of  $^4\text{He}$  gas, which is the coolant in the MHTGR. These compacts, fabricated by General Atomics Inc, had previously been irradiated by neutrons in the Advanced Test Reactor at Idaho National Engineering Laboratory to varying degrees of  $^6\text{Li}$  burnup and hence corresponding quantities of tritium. In these experiments a temperature hold at  $900^\circ\text{C}$ , which simulates the upper limit of normal operating conditions of the MHTGR, was followed by a rapid temperature ramp at  $>250^\circ\text{C}/\text{min}$  to the test temperature of 1500, 1400, or  $1300^\circ\text{C}$ , which represents the reactor accident condition. While such a rapid temperature jump is not typical of a reactor accident, it represents a worst-case and permits direct measurements of diffusion coefficients. In these experiments the  $^4\text{He}$  sweep gas entrained the gas that was generated by the heated compact and transported it through the Raman cell and ion chambers to an oxidation/collection system, where tritium oxide was sorbed in ethylene glycol. The progress of tritium release was monitored by comparison of ion-chamber currents to periodic assays of tritium in the ethylene glycol scrubbers via liquid scintillation. The Raman cell was installed close to the furnace (0.3 m past the compact). Each of its four silica windows, sealed to the cell by indium-alloy O-rings, was purged by helium to prevent deposition of pyrolysis products. Two windows transmitted the vertically propagating 488-nm argon-laser beam, while side windows permitted the 1:1 imaging of Raman emission by a 60-mm Micro-Nikkor lens onto the entrance slit of an ISA HR250 spectrometer equipped with a  $600\text{-mm}^{-1}$  grating and a Photometrics CH250 camera incorporating a backside-illuminated Tektronix TK512 CCD. This combination provides simultaneous vibrational Raman



detection from 1494 to 4210  $\text{cm}^{-1}$ , covering all molecules of interest. Concentrations were determined by comparison to the simultaneously detected Raman signal from  $\text{H}_2$ , which was premixed at 1% with the He sweep gas in some tests and injected between furnace and Raman cell in the remaining tests, in order to saturate hydrogen adsorption sites in the lines and ion chambers that might trap the released tritium. Raman spectroscopy offers on-line measurements of all molecular species in the full furnace flow in real time (exposure times from 2 to 60 sec) with unambiguous identification of tritiated species in the presence of  $^4\text{He}$  sweep gas (unachievable by mass spectrometry).

The signals observed by Raman spectroscopy during the first 8 hours of Safety-Test-3 (ST3), which was the highest burnup compact tested, are shown in Fig. 1, as the compact was heated to the 900°C hold temperature. The relatively steady  $\text{H}_2$  signals represent the injected  $\text{H}_2$ , while episodes of higher  $\text{H}_2$  signals that coincide with peaks of other species represent  $\text{H}_2$  evolved from the compact. The trend labeled 'Base' in Fig. 1 shows the CCD signal at a non-Raman-resonant pixel and rises above the steady level set by window scattering during episodes of particulate releases from the compact. Based upon trends from other compacts similar to Fig. 1, the archetypal heatup sequence of these compacts initially produces evolution of molecules absorbed by the compact matrix from the air ( $\text{H}_2\text{O}$ ,  $\text{N}_2$ ,  $\text{O}_2$ ), which decline in evolution rate at higher compact temperatures while new species ( $\text{CH}_4$  and other hydrocarbons, later CO and  $\text{H}_2$ , as reduction of water in the carbon matrix is favored above 674°C) begin evolving. This entire sequence is attributed to absorption from air by the matrix, as indicated by its absence during the second ramp to test temperature in one of these tests after excluding air between the first and second ramps, coupled with its complete restoration during the third ramp after reexposure to air between the second and third ramps. An overview of ST3 is shown in Fig. 2, which shows trends of selected Raman species and ion-chamber signals during the heatup sequence and the rapid temperature ramp to 1500°C at Hr 22.7. The ion-chamber spikes following Hr 22.7 above the gradual tritium diffusion were caused by the popping of individual particles, whose internal pressures of tritium are several hundred bars at 1500°C; many correlated spikes were also observed in the Raman baseline. The sustained generation of CO was produced by carbothermic reduction of the oxide kernels in the popped particles. By fitting the Raman trends from Hr 23.0 to Hr 47.7 to a sequence of lines, a trend matching that of the ion-chamber was discerned for HT with a peak concentration of 34 ppm, compared to a concentration derived from the ion-chamber signals of 31 ppm, while alternative tritiated species showed no correlation.

Similar Raman trends observed in additional compact tests yielded interesting comparisons. Low-burnup compacts showed no particle popping, as evidenced by absence of spikes in ion-chamber and Raman-baseline signals and absence of sustained CO generation. Tritium diffusion times increased substantially at lower temperatures, exceeding 50 hrs at 1300°C, following an Arrhenius dependence with an activation energy of 4.18 eV. Tests of larger compacts using  $\text{H}_2$  premixed in the sweep gas established HT as the primary tritiated species and  $\text{T}_2$  as the secondary in high-temperature equilibrium with HT and  $\text{H}_2$ ; alternative tritiated species were not detected and thus were below 0.5% of peak HT levels. The dominance of HT in ST3 with no  $\text{H}_2$  in the sweep gas was somewhat surprising. In one test with moderate particle popping (ST7), sustained generation of  $\text{C}_2\text{H}_2$  commenced coincidentally with a particle pop after 50 hours at the test temperature of 1400°C. In several episodes of  $\text{H}_2$  evolution from compacts, the rotational structure of the Raman Q-branch was peaked at  $J=2$ , which can not be fit by equilibrium at any temperature, but indicates that the evolved  $\text{H}_2$  was pure para-hydrogen.

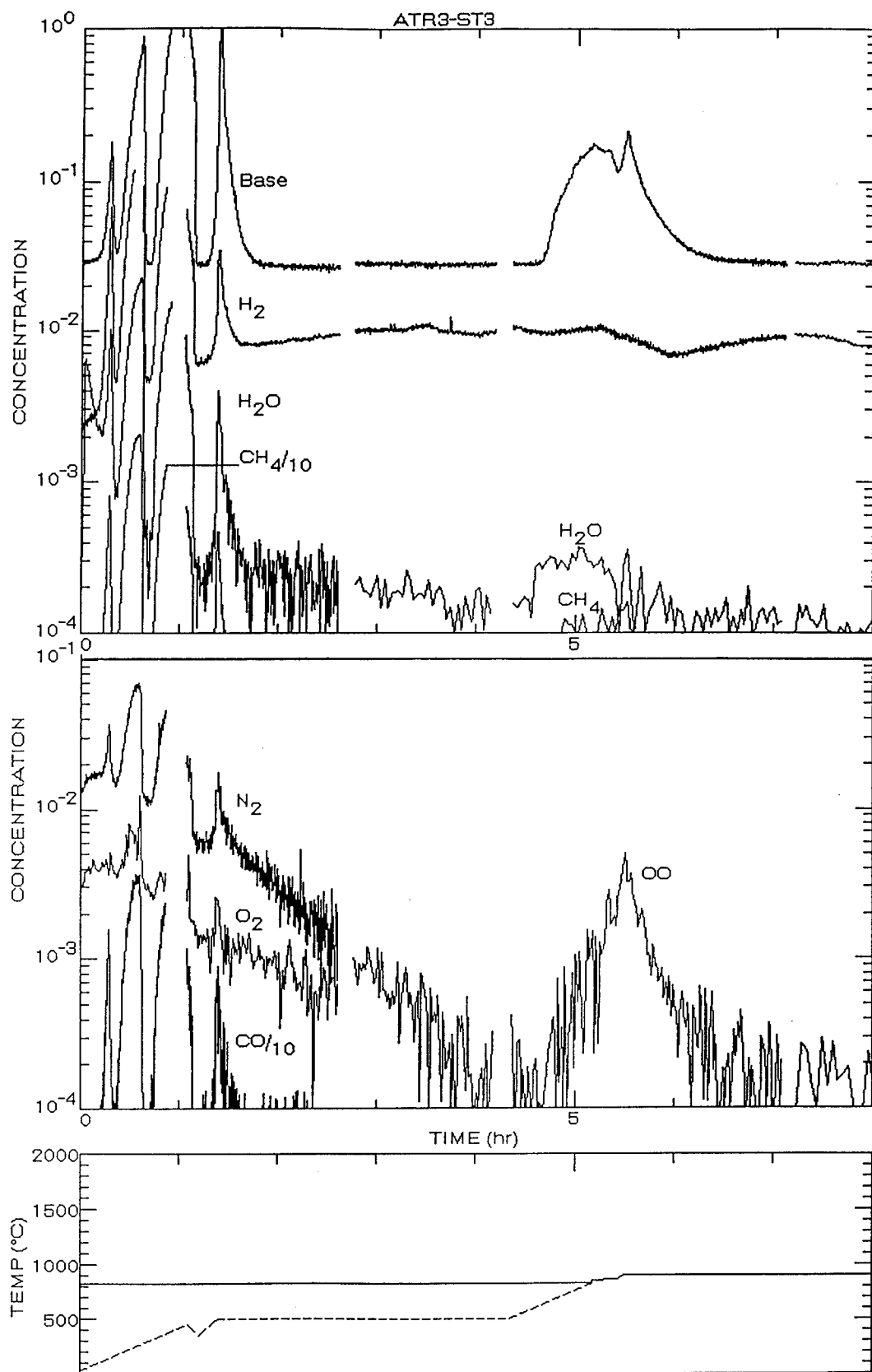


Fig. 1: Trends of Raman species during ST3 Hours 0-8.

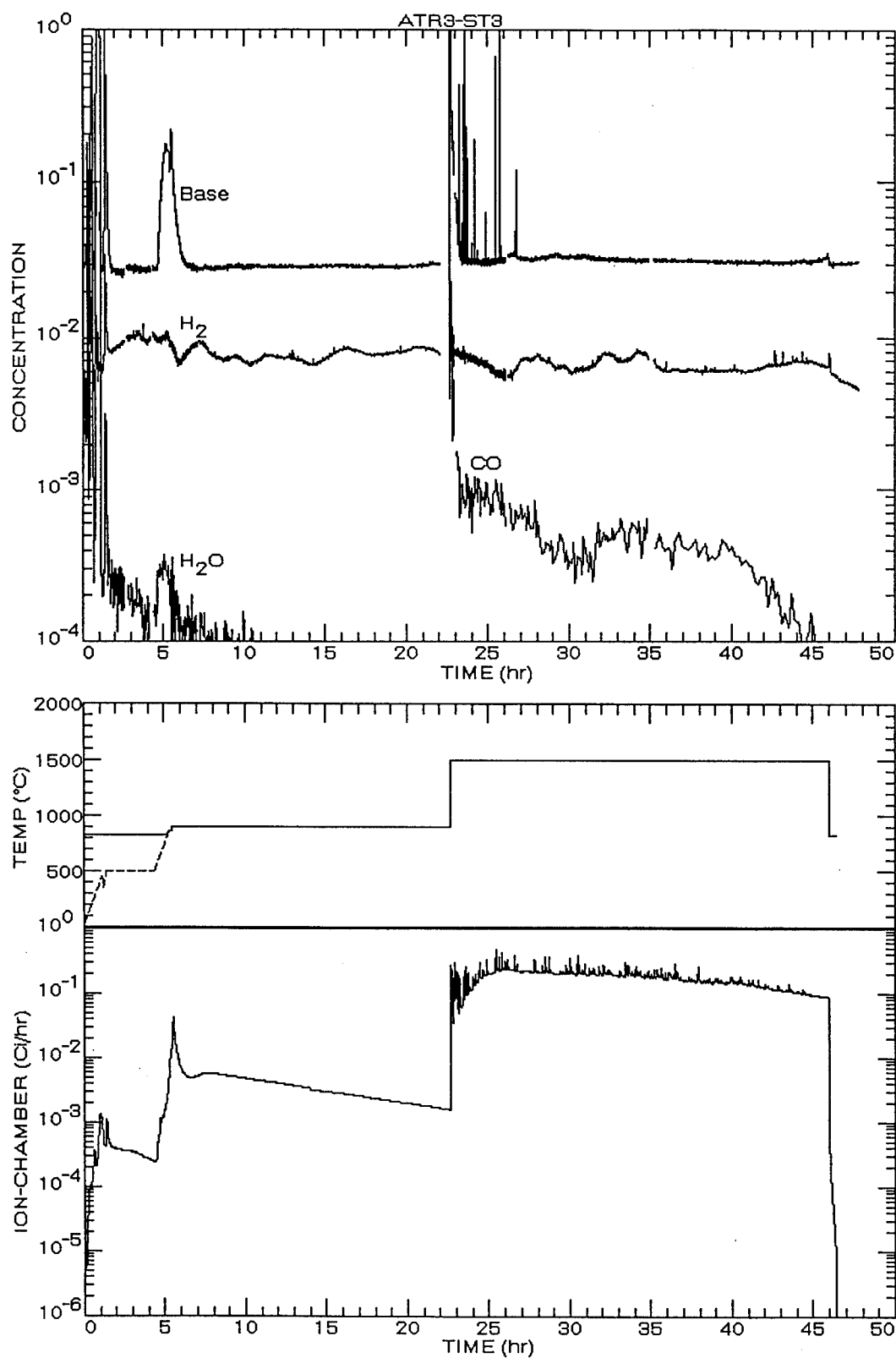


Fig. 2: Trends of selected Raman species during ST3.

## Absorption Spectra of Propylene at Carbon Dioxide (CO<sub>2</sub>) Laser Wavelengths

Mohammad A. Rob and Larry H. Mack, Jr.

University of Houston - Clear Lake

2700 Bay Area Blvd., Houston, Texas 77058

Phone: (713) 283-3780

### Introduction

Laser remote sensing techniques for detecting trace level atmospheric pollutants have made rapid advances in the past several years.<sup>1,2</sup> Molecular CO<sub>2</sub> lasers play an important role in atmospheric pollution monitoring, because its emission spectrum in the 9 - 11  $\mu\text{m}$  range falls within the largest atmospheric window and which overlap with the absorption spectra of a large number of molecules of environmental concern.<sup>2</sup> The primary pollutants that are emitted to the atmosphere by natural and anthropogenic processes are, hydrocarbons (HC), carbon oxides (CO, CO<sub>2</sub>), nitric oxides (NO, NO<sub>2</sub>), ammonia (NH<sub>3</sub>), sulfur dioxide (SO<sub>2</sub>), and etc.<sup>3</sup> The primary pollutants also go through complex chemical reactions among themselves or with the natural atmospheric constituents, to form a variety of secondary pollutants.<sup>2,3</sup> An understanding of the atmospheric chemical processes requires fast detection of primary and secondary pollutants while they reside in the atmosphere. Laser remote sensing techniques are suitable for the detection of these pollutants.

Hydrocarbons form a significant fraction of total air pollution. Among them, methane, ethylene, and propylene are abundant, specially around petrochemical companies and in automobile exhausts.<sup>3</sup> These hydrocarbons play a significant role in atmospheric chemistry. It is hypothesized that propylene (C<sub>3</sub>H<sub>6</sub>) can initiate chemical reactions with ozone and OH-radical to form several free radicals which can undergo further reactions with O<sub>2</sub>, NO, NO<sub>2</sub>, and SO<sub>2</sub> to promote the formation of photochemical smog.<sup>3</sup> Studies show that propylene works as a catalyst for NO<sub>x</sub>-O<sub>3</sub> cycle, in which case NO and NO<sub>2</sub> are converted to O<sub>3</sub> in the presence of sunlight and natural oxygen.

In the past, ethylene has been used extensively for remote sensing studies using CO<sub>2</sub> lasers. Its absorption coefficients at CO<sub>2</sub> laser wavelengths are known in case of cw, waveguide, and pulsed CO<sub>2</sub> lasers.<sup>4-6</sup> To the best of our knowledge, such studies of propylene have not been performed. Infrared spectrum of propylene shows two strong absorption bands around 3.3 and 10.6  $\mu\text{m}$  wavelength region.<sup>7</sup> The 10.6  $\mu\text{m}$  band can be studied using CO<sub>2</sub> laser. Early work on propylene was concentrated on the development of variable attenuators for CO<sub>2</sub> laser radiation. Roberts et al.<sup>8</sup> reported absorption measurement of propylene at 10.6  $\mu\text{m}$  CO<sub>2</sub> laser wavelength. Mayer et al.<sup>2</sup> mentioned overlapping of propylene absorption spectra with the 9P, 10R, and 10P branch CO<sub>2</sub> laser lines. We made systematic studies of absorption coefficients of pure propylene using about fifty lines of the above three branches of a cw CO<sub>2</sub> laser. The results will be useful for an understanding of the spectroscopy of propylene and for laser remote sensing of propylene using CO<sub>2</sub> lasers.

### Experimental

The experimental arrangement is similar to that described in reference 9. Basically, the laser beam from a commercial cw CO<sub>2</sub> laser is passed through an absorption cell (1-inch diameter and 90-cm long gold-coated copper tube) containing propylene gas. The transmitted laser power is measured using a sensitive power meter (Melles Griot model 13

PEM 001). A similar power meter is used to record variations of laser input power into the absorption cell. This is done by sampling a splitted beam from a beam-splitter in front of the cell. For each CO<sub>2</sub> laser line, transmission measurements are performed at various propylene pressures up to about 30 torr. Absorption coefficient  $\alpha$  is determined using Beer-Lambert's law:  $I = I_0 \exp[-\alpha pL]$ , where  $I_0$  is transmitted intensity without any gas,  $I$  is that with the gas,  $p$  is gas pressure, and  $L$  is the length of the cell. For each CO<sub>2</sub> laser line, a plot of  $(1/L)\ln(I_0/I)$  versus  $p$  is made, and the absorption coefficient is taken as the slope of the straight line portion of the curve. This method should give more accurate result than that from a single measurement.

## Results & Discussion

Study of propylene absorptions at various CO<sub>2</sub> laser lines show that although most of the lines follow a linear behavior after a certain pressure, at low pressures (below about 5 torr) they show nonlinear behaviors. Also the low pressure behavior is different for different lines. Figures 1(a) and (b) show absorption characteristics in case of 10P(36) and 10R(8) CO<sub>2</sub> laser lines. The deviation of absorptions from the linear behavior and their variations can be attributed to (i) the variation of pressure broadening of the propylene absorption lines, and (ii) the frequency offset between the propylene absorption line and the laser emission line.

Figure 2 shows measured absorption coefficients of pure propylene at various CO<sub>2</sub> laser lines in the 9P, 10R, and 10P branches. Table-I gives numerical values of these absorption coefficients. It is clear from the figure that 10R(8) line shows the highest

Table-I: Absorption Coefficients of Pure Propylene (in cm<sup>-1</sup>torr<sup>-1</sup>)  
at Various CO<sub>2</sub> Laser Lines.

Line	$\alpha \times 10^{-3}$	Line	$\alpha \times 10^{-3}$	Line	$\alpha \times 10^{-3}$
		10R(6)	1.07	10P(6)	1.24
		10R(8)	5.45	10P(8)	2.45
9P(10)	0.22	10R(10)	1.12	10P(10)	1.25
9P(12)	0.23	10R(12)	0.98	10P(12)	2.75
9P(14)	0.24	10R(14)	0.93	10P(14)	1.82
9P(16)	0.21	10R(16)	1.29	10P(16)	2.39
9P(18)	0.21	10R(18)	1.35	10P(18)	1.25
9P(20)	0.34	10R(20)	0.92	10P(20)	1.56
9P(22)	2.21	10R(22)	1.04	10P(22)	2.80
9P(24)	0.49	10R(24)	2.10	10P(24)	2.25
9P(26)	0.29	10R(26)	2.83	10P(26)	1.79
9P(28)	0.57	10R(28)	1.14	10P(28)	1.85
9P(30)	0.50	10R(30)	1.58	10P(30)	1.69
9P(32)	0.38	10R(32)	1.01	10P(32)	1.48
9P(34)	0.38	10R(34)	0.85	10P(34)	1.98
9P(36)	0.36	10R(36)	1.73	10P(36)	2.50
9P(38)	0.54	10R(38)	1.49	10P(38)	3.79

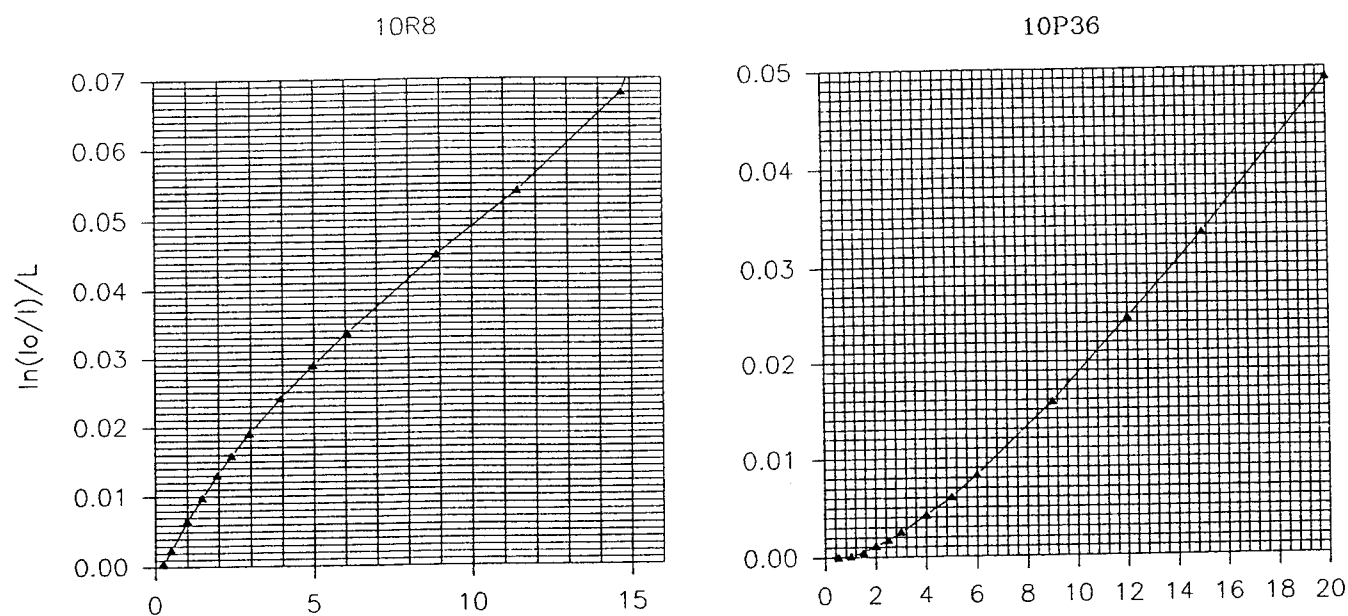


Fig.1. Absorption behavior [ $\ln(I_0/I)/L$  versus  $p$ ] of propylene at two CO<sub>2</sub> laser lines.

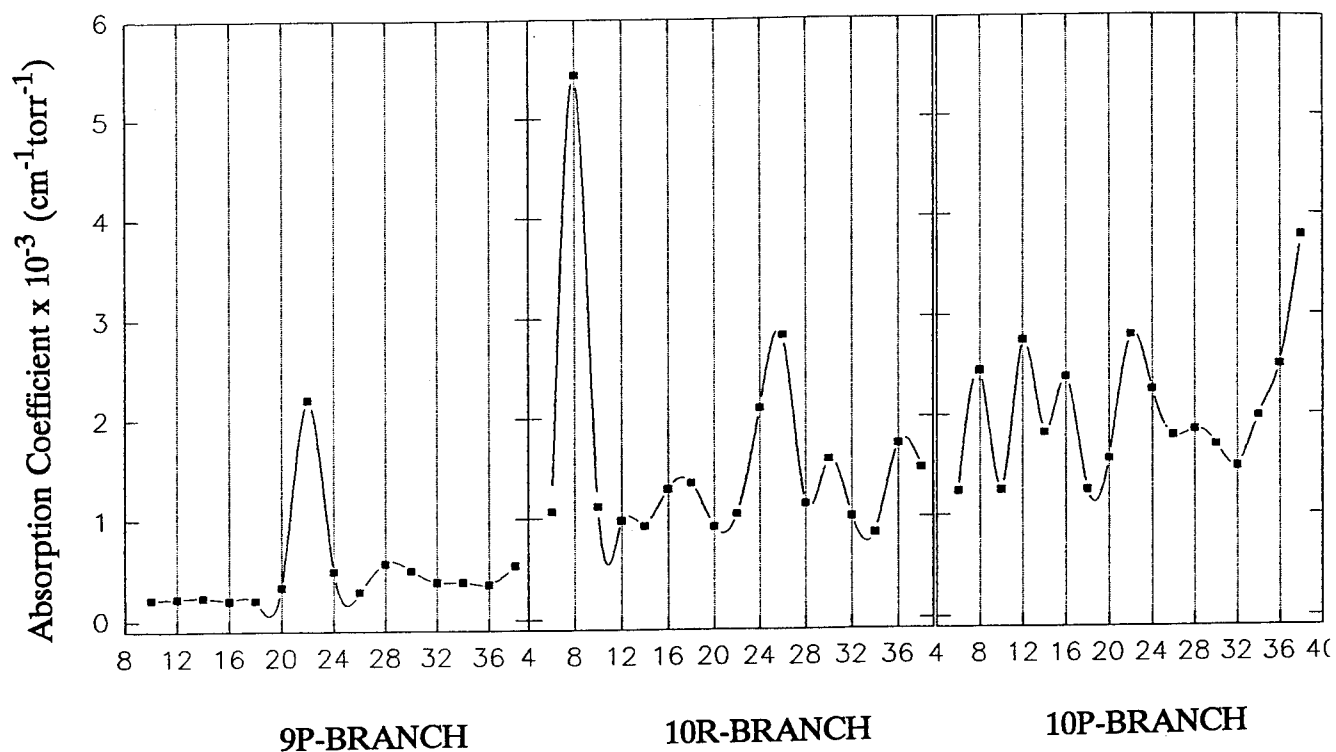


Fig.2. Absorption coefficients of propylene at various CO<sub>2</sub> laser lines.

absorption of propylene with a value of  $\alpha = 5.45 \times 10^{-3} \text{ cm}^{-1} \text{ torr}^{-1}$ . In the 9P-branch, the P(22) line has clearly a discriminatory absorption coefficient against the rest of the lines. This discrimination is very useful in designing a remote sensor for propylene detection. The 10P-branch lines on the average show higher absorptions, but there is no significant discrimination among the various lines in the same branch. Roberts et al.<sup>8</sup> reports absorption coefficient of propylene at  $10.6 \mu\text{m}$   $\text{CO}_2$  laser wavelength with a value of  $\alpha = 1.7 \times 10^{-3} \text{ cm}^{-1} \text{ torr}^{-1}$ . In our measurement, it is about  $1.55 \times 10^{-3} \text{ cm}^{-1} \text{ torr}^{-1}$  for the corresponding 10P(20) line.

## Conclusion

Absorption coefficients of pure propylene at about fifty  $\text{CO}_2$  laser lines are measured and presented. Results will be useful for laser spectroscopy of propylene and for air pollution measurement. Further study with a tunable source such as a waveguide  $\text{CO}_2$  laser can reveal frequency offsets between the propylene absorption lines and the  $\text{CO}_2$  laser emission lines.

## References

1. W.B. Grant, R.H. Kagann, and W.A. McClenny, "Optical Remote Measurement of Toxic Gases," *J. Air Waste Manage. Assoc.* **42**, 18 (1992).
2. P.L. Meyer and M.W. Sigrist, "Atmospheric Pollution Monitoring Using  $\text{CO}_2$ -Laser Photoacoustic Spectroscopy and Other Techniques," *Rev. Sci. Instrum.* **61**, 1779 (1990).
3. A.C. Stern, R.W. Boubel, D.B. Turner, and D.L. Fox, *Fundamentals of Air Pollution*, Academic press, New York (1984).
4. R.R. Patty, G.M. Russwurm, W.A. McCleanny, and D.R. Morgan, " $\text{CO}_2$  Laser Absorption Coefficients for Determining Ambient Levels of  $\text{O}_3$ ,  $\text{NH}_3$ , and  $\text{C}_2\text{H}_4$ ," *Appl. Opt.* **13**, 2850 (1974).
5. A. Olafsson, M. Hammerich, and J. Henningsen, "Photoacoustic Spectroscopy of  $\text{C}_2\text{H}_4$  with a Tunable Waveguide  $\text{CO}_2$  Laser," *Appl. Optics*, **31**, 2657 - 2668 (1992).
6. L. Giroux, M.H. Back, and R.A. back, "The Absorption of Pulsed  $\text{CO}_2$ -Laser Radiation by Ethylene at Total Pressures from 25 to 3000 Torr," *Appl. Phys.* **B49**, 307-313 (1989).
7. *The Sadtler Standard Spectra, Gases and Vapors*, Sadtler Research Laboratories, Inc., Philadelphia, PA 19104.
8. T.G. Roberts, "Compounds for Use as optical Attenuators for  $\text{CO}_2$  Laser," *Rev. Sci. Instrum.* **47**, 257-259 (1976).
9. M. A. Rob, "Atmospheric Pollution Monitoring Using  $\text{CO}_2$  Laser: Some Criteria," in *Proc. Optical Remote Sensing Applications to Environmental and Industrial Safety Problems*, SP-81, Air & Waste Management Assoc., Pittsburgh, PA (1992) pp. 415 - 421.

## UNIMOLECULAR PHOTOCHEMISTRY STUDIED BY PHOTODISSOCIATION-PHOTOIONIZATION MASS SPECTROMETRY

M.V. Johnston, P.L. Ross, S.E. Van Bramer, E.D. Leavitt, Department of Chemistry and Biochemistry, University of Delaware, Newark, DE 19716. Telephone: 302-831-8014

Photochemical reactions are commonly studied in the condensed phase or in a high pressure gas. The primary photodissociation products are inferred from distributions of stable compounds produced by secondary reactions. As these investigations are extended to molecules of increasing size and complexity, identification of the primary products becomes difficult owing to the large number of possible secondary reactions. In photodissociation-photoionization mass spectrometry (PDPI-MS), molecular photodissociation is performed at low pressure in the source region of a mass spectrometer. After a short time delay, the neutral photodissociation products are softly ionized with coherent vacuum ultraviolet radiation and mass analyzed. Unlike photochemical experiments at high pressure, PDPI permits direct observation of the entire product distribution on the microsecond timescale.

The basic experimental setup is shown in Figure 1. Photodissociation is performed with an excimer laser at either 193 nm or 248 nm. Tunable vacuum ultraviolet radiation is generated by four wave mixing of ultraviolet and/or visible radiation. Nonresonant mixing is performed in a phase matched mixture of xenon or krypton and argon. Resonant mixing is performed by tuning the laser system to a two-photon transition of either mercury or krypton. The resonant process is much more efficient, generating  $10^{11}$  to  $10^{12}$  photons per pulse.

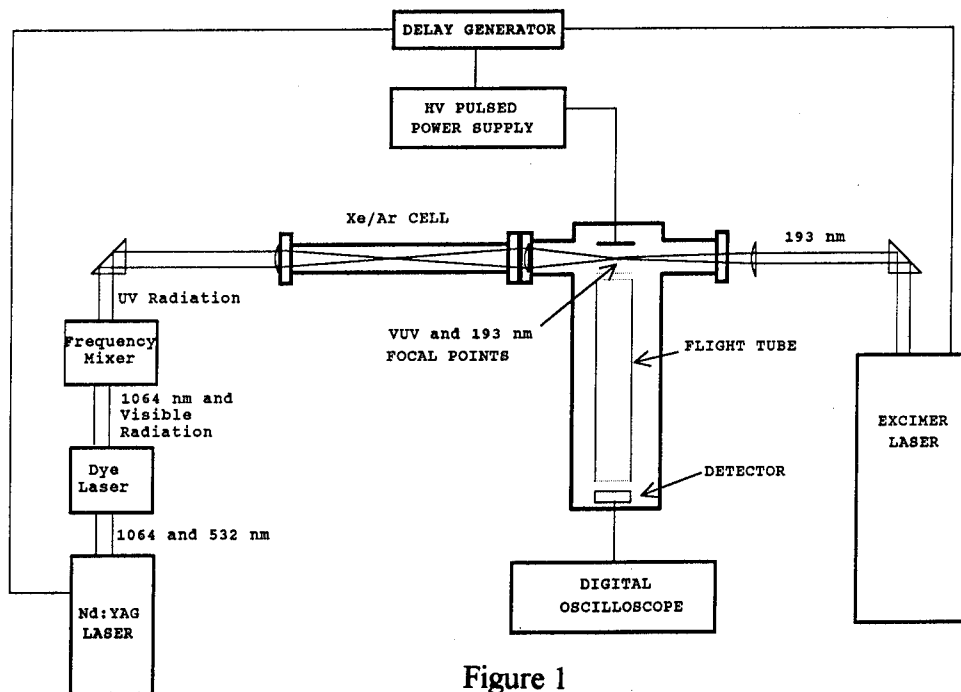
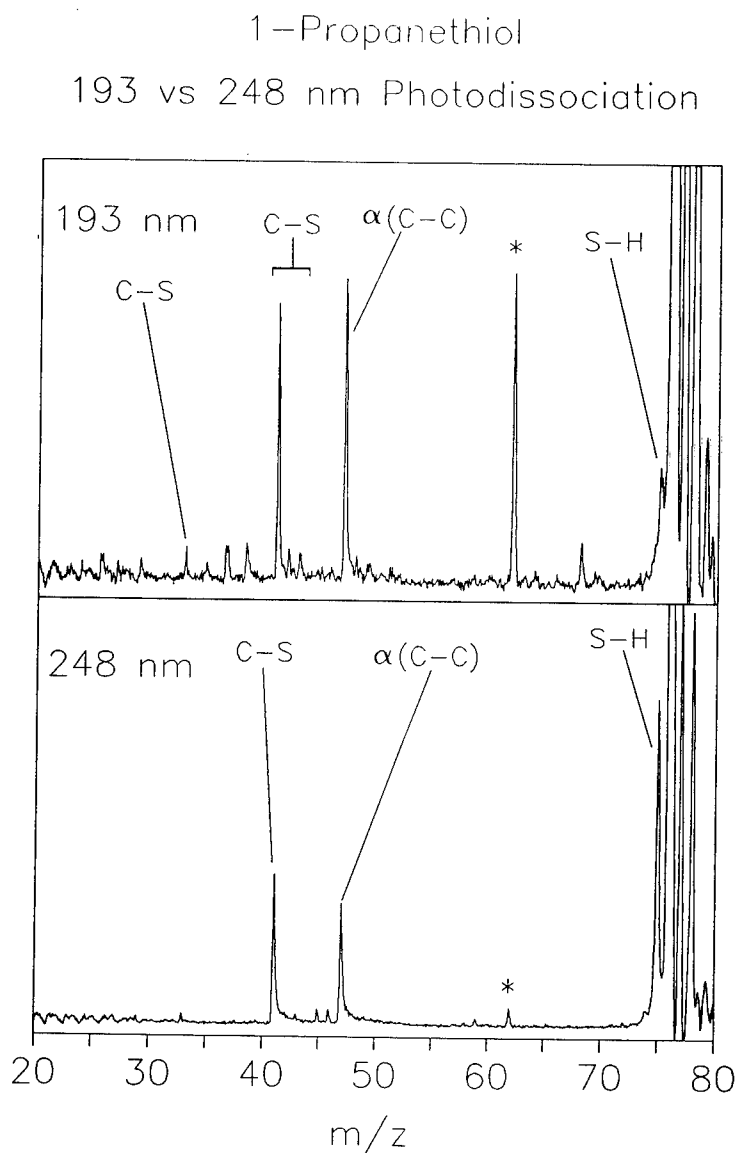


Figure 1



We have used PDPI to study the photochemistry of aliphatic molecules in the  $C_3$  to  $C_{10}$  size range.<sup>1-3</sup> An example of this work is shown in Figure 2 for propanethiol. Three major decomposition pathways are observed: C-S, C-C, and S-H bond cleavage. For other alkanethiols, the relative branching ratios for these processes are strongly dependent upon molecular structure. In addition, there is strong evidence for excited state photochemistry. Cleavage of the S-H bond (368 kJ/mole) is the highest energy process but its branching ratio is uniformly larger with 248 nm than with 193 nm. This behavior is opposite what would be expected on the basis of ground state bond energies but is consistent with the excited state electronic configurations which show a greater contribution from  $\sigma^*_{SH}$  at 248 nm than at 193 nm.



**Figure 2**

Our current work involves other aliphatic molecules of the form R-X (R = alkyl group) where the C-X bond energy is much lower than that of a typical C-C bond. In many cases, C-C bond cleavage can effectively compete with C-X bond cleavage even though the bond energy difference is greater than 100 kJ/mole. Cleavage of the C-C bond appears arise from excited state photochemistry.

#### References

1. S.E. Van Bramer and M.V. Johnston, Org. Mass Spectrom. 1992 27, 949.
2. S.E. Van Bramer and M.V. Johnston, J. Amer. Soc. Mass Spectrom. 1993 4, 65.
3. P.L. Ross and M.V. Johnston, J. Phys. Chem. 1993 97, 10725.

# Wavelength Modulation Spectroscopy of Oxygen A Band Transitions for Non-Intrusive Concentration Measurements

A. D. Jackson

A. N. Dharamsi\*

Department of Electrical and Computer Engineering  
Old Dominion University  
Norfolk VA 23529-0246  
Tel: (804) 683-4467

S. K. Chaturvedi

Department of Mechanical Engineering  
Old Dominion University  
Norfolk VA 23529

\* To whom correspondence should be addressed.

## I. INTRODUCTION

The technique of Frequency Modulation (FM) and Wavelength Modulation Spectroscopy has been used [1] very successfully recently to perform several different types of measurements, with the applications of this technique growing as advances in semiconductor technology result in the availability of reliable, tunable single-mode semiconductor diode lasers in parts of the electromagnetic spectrum which were previously inaccessible this way. We discuss measurements of absorption lines in the weak oxygen A band (the rotational lines in the  $0 \leftarrow 0$  vibrational rung of the  $b^1\Sigma_g^+ \leftarrow X^3\Sigma_g^-$  low-lying electronic transition) by using wavelength modulated absorption spectroscopy. These lines are quite weak, being electric-dipole forbidden and spin-forbidden.

Our motivation for measuring the near infrared lines of the Oxygen molecule is that such measurements allow compact semiconductor diode lasers to be used in applications where there is a need to monitor and control, in real time, the concentration of oxygen. Our interest lies in making measurements in a wind-tunnels, under different operating conditions. We have measured the absorption due to several lines in the Oxygen A band, and examined the effects of pressure on these lines. The weakness of the Oxygen A band lines notwithstanding, we have been able to make measurements of fractional Oxygen concentration changes of less than  $5 \cdot 10^{-3}$ . We discuss the results obtained, concentrating on a description of the work done on the RQ (11,12) line at  $13150.187 \text{ cm}^{-1}$  (760.445 nm).

## II MODULATION SPECTROSCOPY WITH SECOND HARMONIC DETECTION

If an incident beam of light of initial intensity  $I_0(\nu)$  traverses a distance  $L$  in a material then it is attenuated, by the Beer-Lambert Law, and for weak absorptions,  $I(\nu) = I_0(\nu)[1 - \alpha(\nu)L]$ . In a wavelength modulation spectroscopic measurement, the frequency

of the incident light is modulated,  $v(t) = \bar{v} + a \cos \omega t$ . If it is assumed that the intensity of the laser is independent of the wavelength, an approximation that is reasonable in tunable diode

laser experiments, then  $\alpha(\bar{v} + a \cos \omega t) = \sum_{n=0}^{\infty} H_n(\bar{v}) \cos n\omega t$ , where  $n$  is an integer. When the signal is measured by a Lock in Amplifier with  $n$ th harmonic detection, and the modulation index is small, one finds [1] that the processed signal will be proportional to,

$$H_n(\bar{v}) = \frac{2^{1-n}}{n!} a^n \frac{d^n \alpha(v)}{dv^n} \Big|_{v=\bar{v}}, \quad n \geq 1.$$

Detection at the modulation frequency ( $n=1$ ) gives the first derivative of the absorption coefficient with respect to frequency, while second harmonic detection yields the second derivative, etc. In this manner, the derivatives of the absorption coefficient are obtained. It is well known that such techniques yield a much larger signal to noise ratio than direct absorption measurements, and extremely weak lines have been probed in this manner.

### III. EXPERIMENTAL RESULTS AND DISCUSSION

The experimental apparatus used in this work is shown in Fig 1.

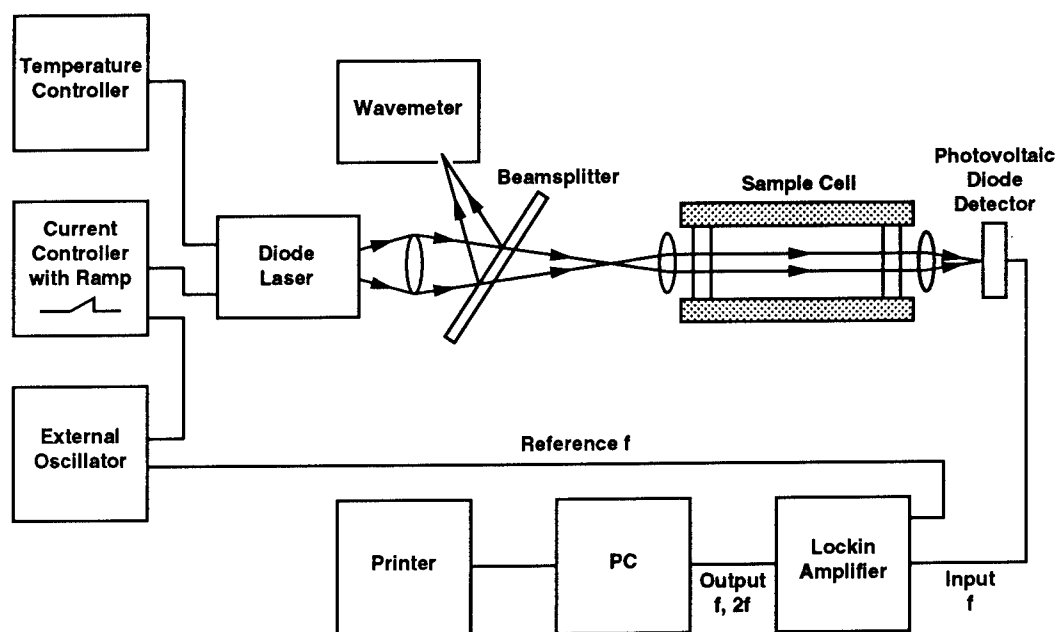


Fig. 1 Experimental Apparatus Used.

Figs. 2 and 3 show typical results obtained for the absorption lines in the oxygen A band. Detection was by a Lock-in Amplifier, both at the modulation frequency and its second harmonic. Hence, the first and second derivatives  $(\delta(\alpha)/\delta(v))$  and  $\delta^2(\alpha)/\delta(v)^2$  were obtained as shown in Figs. 2 and 3 respectively.

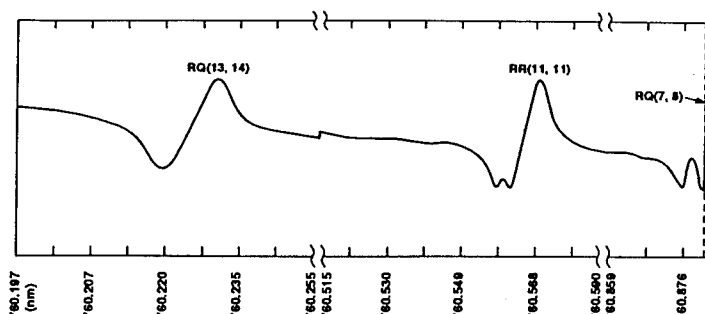


Fig. 2 Three lines in the  $O_2$  A absorption band ( $b^1\Sigma_g^+ \leftarrow X^3\Sigma_g^-$ ;  $v'' = 0, v' = 0$ ). Wavelength Modulation Spectroscopy with detection at the fundamental frequency.

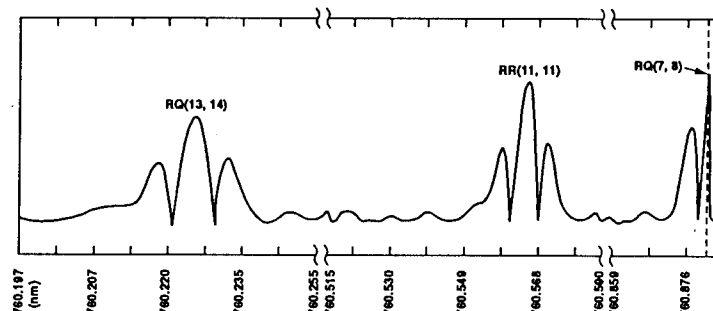


Fig. 3 Three lines in the  $O_2$  A absorption band ( $b^1\Sigma_g^+ \leftarrow X^3\Sigma_g^-$ ;  $v'' = 0, v' = 0$ ). Wavelength Modulation Spectroscopy with Second Harmonic Detection.

Figs. 4 and 5 show the theoretically expected line-shapes and their first and second derivatives, for both Lorentzian and Gaussian profiles. It is seen that these have the same shapes and features as the experimental results shown in Figs. 2 and 3. (Note that the latter have been measured in absorption, and therefore are inverted with respect to the former as expected.)

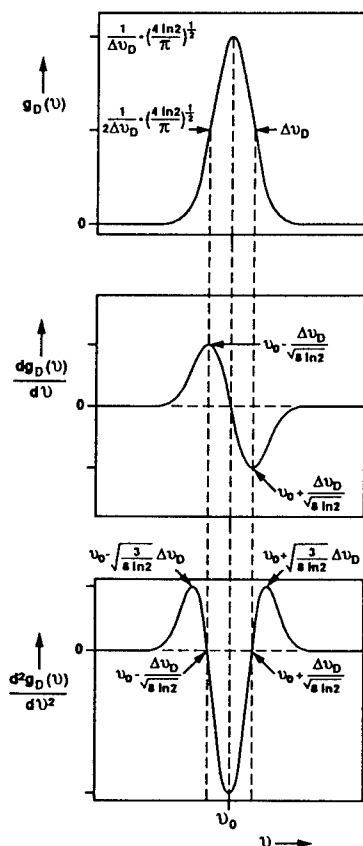


Fig. 4 Gaussian Lineshape Function and its Derivatives (Relevant in Doppler-Broadened Domain)

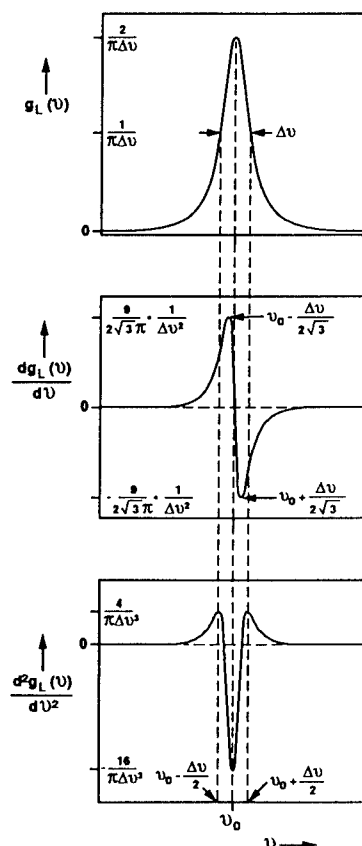


Fig. 5 Lorentzian Lineshape Function and its Derivatives (Relevant in Collision-Broadened Domain)

Absorption spectra were measured at various pressures of  $O_2$  in the sample cell, as well as in air. The results are shown in Fig. 6, which also shows the absorption signal calculated theoretically.

It is seen that the line collision-broadens as we move out from the Doppler regime, and the peak value shows a saturation and a gradual fall, as expected. The theoretical results have been computed by working out the expressions for modulation spectroscopy with harmonic detection, and introducing the Doppler and Lorentzian lineshape functions to describe the behavior in the low and (relatively) high pressure regions. We have normalized the signal to account for the transfer function (Volts per incident radiant Watts/m<sup>2</sup>) of the detector and Lock-in amplifier, but not used any adjustable parameters to obtain the fits shown. In the intermediate pressure region, the experimental results are found to match those that would be expected by using a Voigt profile for the absorption line.

The results clearly show that the method used would be suitable for monitoring the concentrations of various species in a non-intrusive manner. Temperature measurements can be made by comparing the relative intensities of adjacent rotational-vibrational lines.

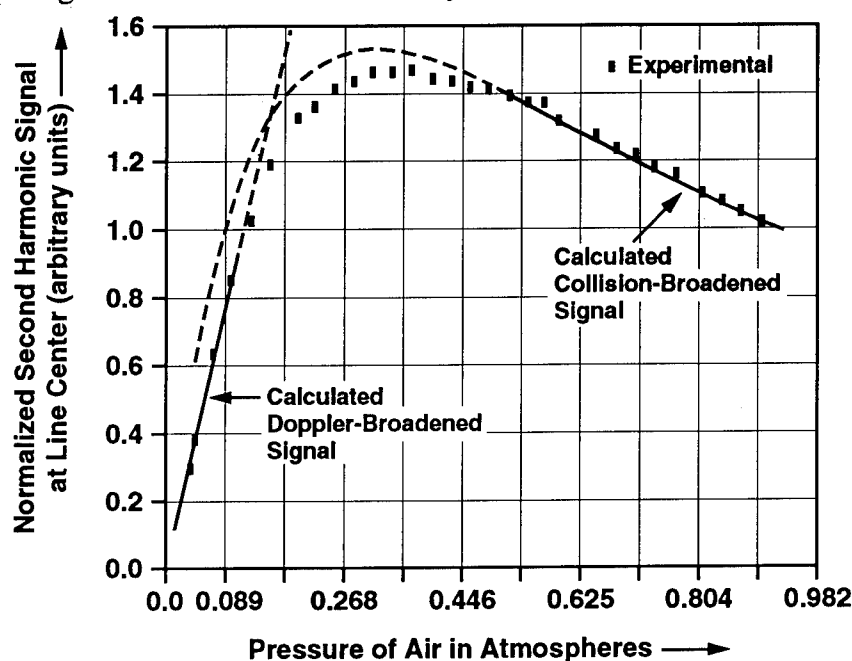


Fig. 6 Comparison between Experimental and Theoretical Results

## V. REFERENCES

- [1] J. Reid and D. Labrie, "Second-Harmonic Detection with Tunable Diode Lasers", *App. Phys. B*, **26**, 203, 1981.
- [2] P. W. Milloni and J. Eberly, *Lasers*, Wiley Interscience, N. Y., 1988.
- [3] A. N. Dharamsi, A. D. Jackson and S. K. Chaturvedi, "Non-Intrusive Measurements of Gaseous Concentrations and Temperatures", *Proceedings of International Congress on instrumentation in Aerospace Simulation Facilities*, Saint-Louis, France, Sept 1993.
- [4] A. D. Jackson, A. N. Dharamsi and S. K. Chaturvedi *Applied Spectroscopy* (to be submitted)

## Silicon Processing Chemical Diagnostics and Control Using Diode Lasers

Edward A. Whittaker, H. C. Sun, C. K. Ng  
Department of Physics and Engineering Physics  
Stevens Institute of Technology  
Hoboken, New Jersey 07030  
201-216-5707  
ewhittak@vaxc.stevens-tech.edu

B. Singh, V. Patel  
David Sarnoff Research Center  
CN5300  
Princeton, New Jersey 08543-5300

Infra-red diode laser absorption spectroscopy has long been a powerful tool for molecular spectroscopists and analytic chemists. Through recent improvements in lead salt laser fabrication lasers with modest power (up to several milliwatts), good beam quality and broad tunability (as much as 30% of center frequency) are now available. In addition, very low absorbance species detection, free of window induced interference fringes is now possible by utilizing a combination of frequency and wavelength modulation via the diode laser injection current.<sup>1</sup> This modulation approach also lends itself to a simple feedback method that may be used to lock the laser frequency to a particular molecular absorption line and thus enable real time measurements of that species' absorbance in the presence of high levels of electrical background noise often found in industrial settings.<sup>2</sup>

Using these technological developments we have implemented a lead salt diode laser spectrometer for use in silicon plasma processing chemical diagnostics and as a sensor for real time process control. In our spectrometer, the diode temperature is controlled to as low as 20K using a closed cycle refrigerator. The current is controlled using a low noise current source. Sensitive, fringe free absorption spectroscopy signals are induced by mixing the dc injection current with both 40 MHz rf and a 70 kHz triangle wave. The laser is detected by a HgCdTe photodetector and demodulated using an rf mixer and lock-in amplifiers set to consecutive harmonics of the triangle wave. The laser frequency may be locked to a resonance by using the appropriate lock-in amplifier harmonic signal fed back to the injection current. The entire spectrometer is controlled using a digital signal processor running on a personal computer.

Figure 1 shows a typical high resolution spectrum obtained using our spectrometer. The diode laser beam passed through a 36 cm column of 10 mTorr of SF<sub>6</sub> and was tuned to an absorption band at 945 cm<sup>-1</sup>. SF<sub>6</sub> is a commonly used feedgas for polysilicon etch processes. The signal is free of window induced fringes as well as baseline drift arising from amplitude modulation at the rf modulation frequency. In Fig. 2 we show the amplitude of the strongest peak of Fig. 1 as a function of SF<sub>6</sub> pressure. The signal varies linearly with increasing pressure, until in the mTorr range the absorbance is strong enough that the laser carrier becomes attenuated and

the signal rolls over. The low pressure portion of the scan is shown expanded in the inset and has a slope of  $165 \mu\text{V}/\text{mTorr}$ . We may estimate the limiting sensitivity by calibrating the modulated signal with actual absorbance measured at high pressure, and converting the observed  $67 \text{ nV}/\text{Hz}$  photocurrent fluctuation to an equivalent absorbance and doing so yields an absorbance limit of  $7.8 \times 10^{-6}$  for  $\text{SF}_6$ . This figure will be relatively higher or lower for other gases depending on the Doppler linewidth and proximity of overlapping rotational lines.

The economics of microelectronic circuit manufacture dictate a drive to ever diminishing feature size which in turn places severe constraints on critical processing steps such as polysilicon gate and oxide layer etches. Tool designers require insight on such issues as etch rate and etch selectivity. Such insights require an understanding of the chemical processes taking place in the reactor or 'tool' of sufficient predictability to be useful at the design stage and to that end, we have begun to gather chemical data on realistic etch processes using the diode laser spectrometer. Coupled with nascent modeling efforts that attempt to include neutral reaction chemistry, these efforts should soon begin to provide a more complete picture of the etching process.

Our most recent efforts have been directed towards developing an understanding of etch processes based on low pressure, high density plasma sources.<sup>3</sup> Here we present data taken from a series of measurements on the behavior of two types of fluorocarbon discharges used for silicon oxide etching. In particular, we measured the relative concentration of  $\text{CF}_2$  and  $\text{CF}_3$  radicals in pure  $\text{C}_2\text{F}_6$  and  $\text{CHF}_3$  rf discharges driven by an inductively coupled rf source. These radicals play an important role in both the etch process as well as in polymer deposition on the side-walls of the etched microelectronic feature.

The reactor used was designed and equipped for process research but in essential respects approximates industrial type etch tools. The discharge was struck by energizing both an inductively coupled coil source and a capacitively coupled electrode. In Fig. 3 we show the variation of  $\text{CF}_2$  concentration as a function of the feed gas base pressure with 500 W and 300 W of rf power applied to the inductively coupled and capacitively coupled electrodes respectively. Gas flow was maintained at 100 sccm. Figure 4 shows the corresponding scan for  $\text{CF}_3$ . The two species show dramatically different behaviors in the two types of plasmas. The differences in the behavior of these two discharges is also reflected in their etch and polymer formation properties. With appropriate modeling to support this data we expect to be able to correlate our chemical results with actual etch properties.

Each data point required only 20 ms or so for the actual measurement and such high bandwidth naturally suggests the use of our system as a real time process sensor that could be applied in a control system. One critical control issue involves etch end point detection, that is, sensing when a particular process has proceeded long enough to complete the removal of the desired layer. As layer thicknesses diminish along with lateral feature size, precise end point detection becomes increasingly important. The problem is exacerbated for etch steps where the actual etched area is only a few percent of the wafer area.



The sensitivity of diode laser absorption spectroscopy makes possible extremely sensitive end point detection. As evidence, we present in Fig. 5 the measured concentration of the silicon etch end product  $\text{SiF}_4$  as  $\text{SF}_6$  etching proceeded through a multilayer wafer structure consisting of  $5000\text{\AA}$  of polysilicon over  $5000\text{\AA}$  of oxide on a silicon wafer. The top part of the figure shows the output from a laser interferometer which monitors layer thickness. The transition occurring as the poly layer cleared is clearly marked by the reduction in the fringe rate. The lower part of the figure shows the concentration of  $\text{SiF}_4$  measured in real time with the diode laser spectrometer. A sharp drop in concentration takes place once poly etching ceases, reflecting the reduced etch rate of oxide in an  $\text{SF}_6$  etch. Based on a careful analysis of such data we estimate the ability to detect end point with a signal-to-noise ratio of at least 50 for an 8" wafer with 1% exposed area.

In summary, we have developed a sensitive diode laser absorption spectrometer which has a clearly demonstrated potential for both process diagnostics and process control. We have implemented this capability for silicon plasma processing but the technique is generic and should have wide applicability in many applications which use gas phase process steps.

### References

1. H.C. Sun and E.A. Whittaker, *Appl. Opt.* **31**, 4998 (1992).
2. H. C. Sun and E. A. Whittaker, *Opt. Eng.* **32**, 453 (1993).
3. J. Hopwood, C.R. Guarnieri, S.J. Whitehair and J.J. Cuomo, *J. Vac. Sci. Technol. A* **11**, 152 (1993).

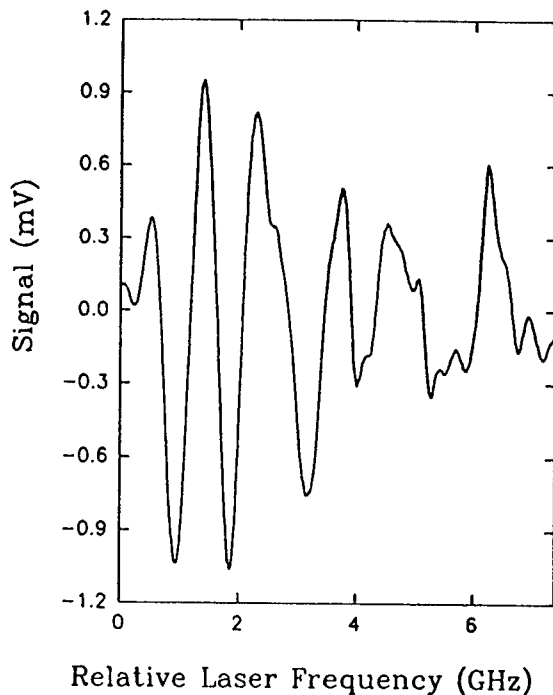


Figure 1: High resolution diode laser absorption spectrum of  $\text{SF}_6$ .

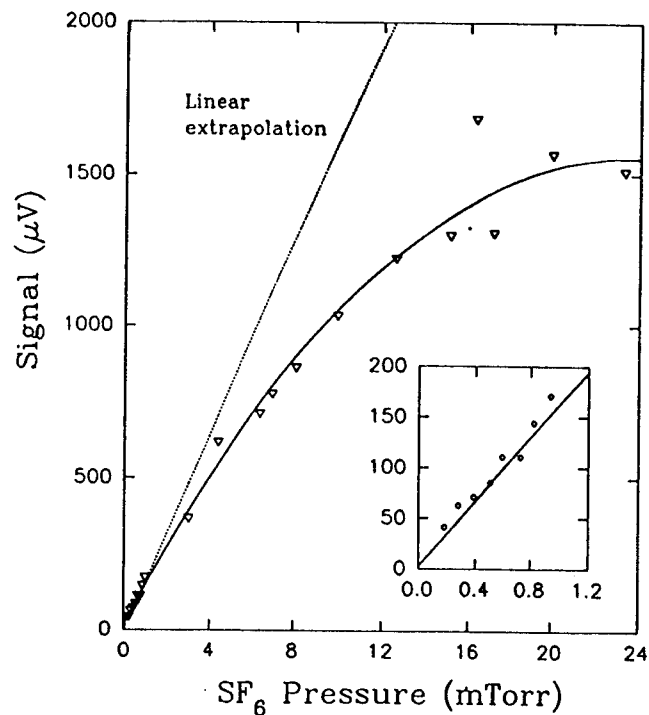


Figure 2: Modulated laser signal vs.  $\text{SF}_6$  pressure.

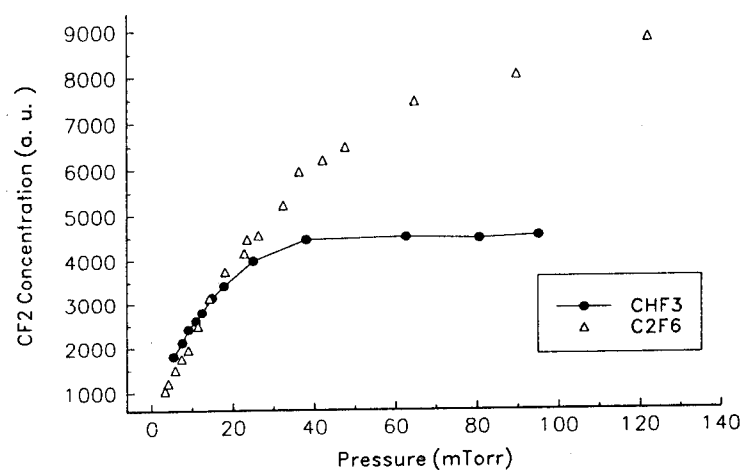


Figure 3: CF<sub>2</sub> concentration vs feed gas pressure in an inductively coupled plasma reactor.

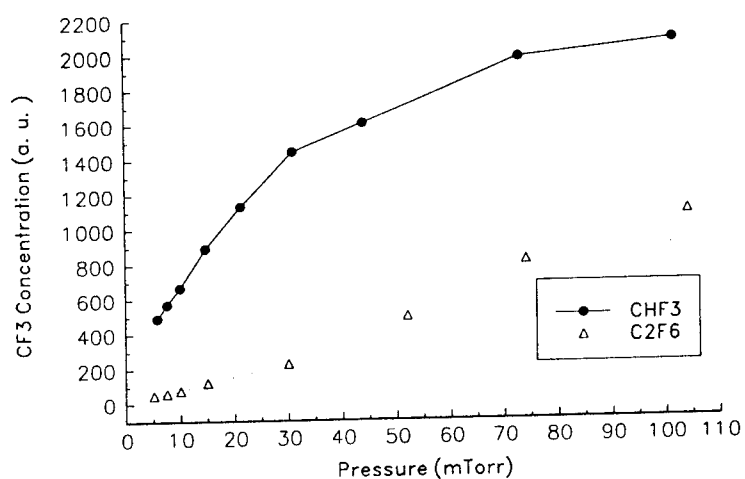


Figure 4: CF<sub>3</sub> concentration vs feed gas pressure in an inductively coupled plasma reactor.

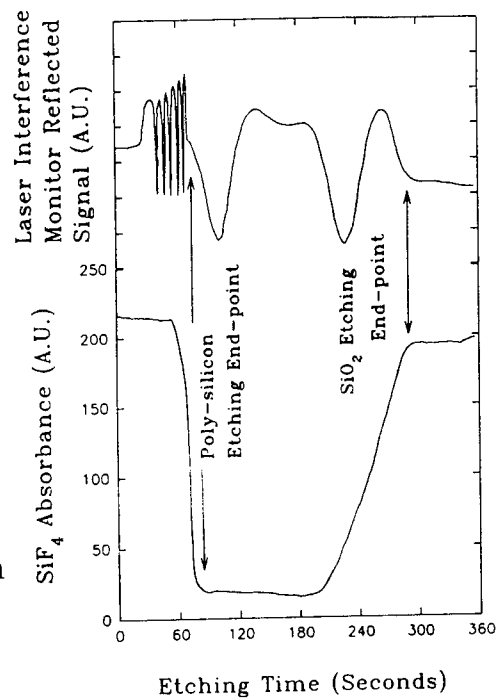


Figure 5: Etch end point detection using laser absorption by SiF<sub>4</sub>.

**Detection of Chlorine and Oxygen in a Microwave-Induced Plasma  
Using Frequency Modulation Spectroscopy**

Ring-Ling Chien  
E. L. Ginzton Research Center, Varian Associates, Inc.  
3075 Hansen Way, Palo Alto, CA 94304  
(415)424-5892

Frequency modulation spectroscopy (FMS) in the wavelength range 700-1500 nm, is becoming increasingly important as an analytical technique for two reasons. One is the rapid development of diode lasers and the other is the improvement in detector technologies. Near-infrared diode lasers are inexpensive, reliable, and readily available. Line-locked wavelength modulation with second-harmonic ( $2f$ ) detection using these diode lasers has been demonstrated to be a sensitive and accurate absorption technique.<sup>1</sup> This technique is ideal for small molecules such as H<sub>2</sub>O, HCl, CO, and CO<sub>2</sub>. By locking the wavelength to the molecular line of interest, the technique is well suited for continue and real-time monitoring applications as in gas chromatography (GC).

Although FMS is a rather sensitive detection technique, the signal intensity eventually depends on the absorption strength of molecules of interest. Absorption of molecules in the near-IR region arises from the higher harmonics of vibrational overtones and combination bands of O-H, C-H, and, N-H bonds. These transitions are much weaker than the fundamental vibrational absorption in the far-IR region. Accordingly, the S/N one obtained for these small molecules using near-IR diode lasers is several orders away from the required detection limit of a GC detector.

A possible alternative method to overcome the detection limit is to perform FMS on excited atoms generated in a helium microwave-induce plasma (MIP) coupled to a GC. Helium-MIP has been demonstrated as an efficient excitation source for non-metallic elements. Many emission lines of C, N, O, S, Cl, and Br exist in the near-IR region.<sup>2</sup> For example, oxygen atom has a strong transition at 777.19 nm, Chlorine atom has several transitions at 774.498, 776.918

nm, and 782.139 nm. The oscillator strength of these atomic lines is easily five orders larger than the absorption strength of small molecules.

We have set up an FMS-MIP system as shown in Figure 1. The atomizer was constructed from a Beenakker-type microwave cavity operated under reduced pressure about 10 torr. The discharge tube was made of alumina to avoid background absorption from the oxygen atoms sputtered from the tube. An oxygen purifier is also inserted in the pure-helium line to reduce the residual oxygen in the system. In parallel with the pure helium gas is a gas mixture with 100 ppm of oxygen or chlorine balanced with helium. By switching between the gas mixture and pure gas lines, the background absorption could be subtracted.

The FM system contains both 2nd and 3rd harmonic detection. The diode laser is modulated at 10 MHz, and the signals at 20 MHz and 30 MHz were measured. The 3rd harmonic signal is about 10 dB weaker than 2nd harmonic. In real-time gas monitoring, the frequency of the laser is set to the desired atomic transition and must be long-term stable. A feed-back control based on the 3-rd harmonic signal to lock the frequency of the diode laser will be build.

Very strong  $2f$  signal, about 5% absorption, was obtained in the 100 ppm oxygen line. Using a very conservative estimated detection limit of  $1 \times 10^{-6}$  absorption, this yields the detection limit of 20 ppb for oxygen atoms assuming the background oxygen could be eliminated.

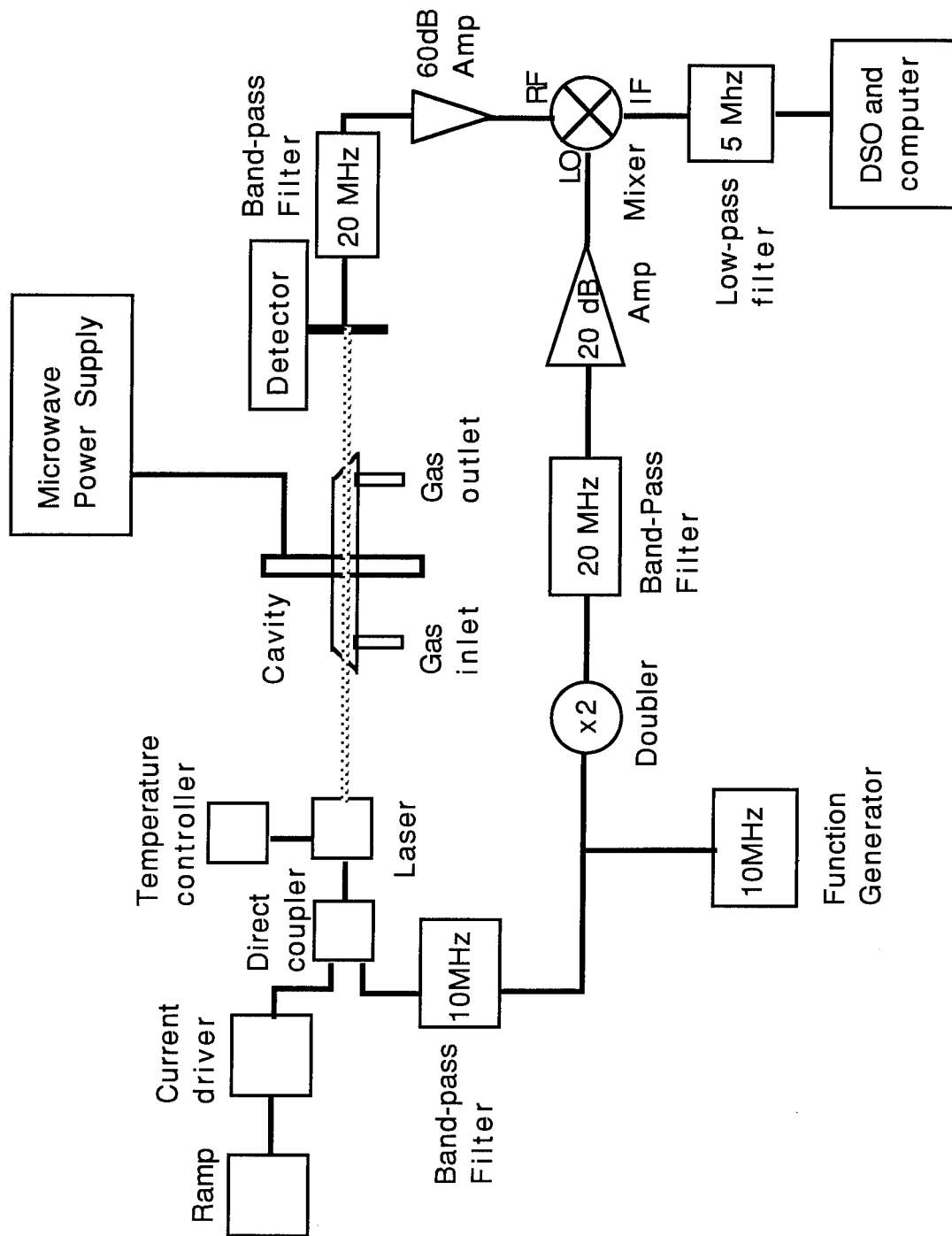
One of the major sources of noise in our FMS system is the etalon fringes created by the parallel windows on the sample cell. We have cut the tubing at the end of the cell into a small angle and replaced the windows with wedged plates to eliminate the interference fringes. The S/N is improved by more than an order of magnitude. We could easily detect less than 1 ppm chlorine atoms at 774.498 nm. As a matter of fact, there are several chlorine lines with much stronger transition at longer wavelength around 830 nm. We should be able to reach a detection limit of 100 ppb chlorine atoms using different laser diodes.

One potential problem in diode laser spectroscopy is the spectral interference due to side mode absorption. We have investigated this phenomenon in details. Although the laser we used is called "single-longitudinal-mode", in reality there are lots of side modes centered around the lasing wavelength with a spacing of about 0.3 nm between them. The ratio of light intensity between the lasing mode and side modes depends on injection currents, operating temperature and device quality. In a well-engineered laser diode, the ratio could reach more than three orders of magnitude. In the worst case, the diode possesses two dominated modes at all operating conditions. This side mode absorption creates problem if the desired weak transition is adjacent to a strong transition of other atoms. One example is the chlorine line at 776.918 nm and oxygen line at 777.193 nm. We observed two overlapped FM peaks even the spectrometer showing only a single laser line at 776.92 nm. Although one could choose other chlorine lines away from the interference, this issue needs to be addressed.

In conclusion, we have shown that sensitive detection of excited atoms could be obtained in the FMS-MIP system. However, there are many problems have to be solved before GC-FMS becomes commercially available. A major drawback is that the emission wavelength and tunability of each individual diode laser are rather unpredictable. Each diode has to be installed and calibrated for a specific molecule. Nevertheless, frequency modulation spectroscopy with diode lasers is an attractive and promising technique as an elemental selective detector for GC applications.

#### REFERENCES:

1. C. B. Carlisle and D. E. Cooper, *Appl. Phys. Lett.*, **56**, 805 (1990).  
N. Goldstein, S. Adler-Golden, J. Lee, and F. Bien, *Appl. Opt.*, **31**, 3409 (1992).  
D. S. Bomse, A. C. Stanton and J. A. Silver, *Appl. Opt.*, **31**, 718, (1992).
2. K. Tanabe, H. Haraguchi, and K. Fuwa, *Spectrochimica Acta*, **36B**, 119 (1981).  
D. E. Pivonka, A. J. J. Schleisman, W. G. Fateley, and R. C. Fry, *Appl Spectrosc.* **40**, 766 (1986)



Wednesday, March 9, 1994

## Condensed Phase Studies

**WA** 8:15am–10:15am  
Grand Room

Alan C. Eckbreth, *Presider*  
*United Technologies Research Center*

## **Optical Diagnostics of Single Liquid Droplets**

Michael Winter  
United Technologies Research Center  
411 Silver Lane  
East Hartford, CT 06108  
203-727-7805

### **Overview**

Most propulsion and energy utilization devices rely on the spraying of liquid-phase fuel or oxidizer, into an energy conversion chamber. The behavior of individual droplets in a spray combustor is a critical part of the combustion process, and currently we can only speculate about several fundamental aspects related to droplet heat-up and evaporation. A series of laser diagnostic techniques has been developed to measure heat and mass transfer associated with individual droplets characteristic of a spray. One such technique provides images of flow patterns along a meridian slice of small droplets using Laser-Induced Fluorescence (LIF), illustrating the presence of internal circulation. Extremely accurate vaporization rate measurements are being performed by using individual droplets as miniature lasers, producing Morphology-Dependant Resonances (MDR). MDR output mode-structure (primarily wavelength) contains information about the laser cavity dimensions and is related to droplet size. Another set of measurements is aimed at studying gas-phase-flow/flame front interactions in a microgravity environment using both planar laser-induced fluorescence and Particle Image Velocimetry, (PIV). By developing new ways of probing individual droplets, an understanding of the fundamental physics governing their behavior may be gained.

### **Droplet Slicing**

Measurement of internal circulation using laser-induced, oxygen-quenched fluorescence is being pursued under known initial conditions. Decane doped with naphthalene is used to form droplets from either a droplet-on-demand generator, an aerodynamic droplet generator, or levitated droplets formed from melting solids, which fall a short distance in a chamber filled with a carefully controlled shear flow of nitrogen and a variable amount of oxygen. A thin sheet of ultra-violet light from the fourth harmonic of a Nd:YAG laser illuminates single droplets. Sheet thickness has been significantly reduced by careful selection of a uniform portion of the initial laser beam waist. A Questar QM100, long working distance microscope, with uv quartz optics is used to provide high quality images even through the thick windows characteristic of high pressure test vessels. The microscope produces a highly-magnified image of the naphthalene fluorescence which is recorded digitally with an intensified two-dimensional CCD detector interfaced to a laboratory computer. Use of an off-the-shelf, low f# microscope is particularly useful for careful quantification of the imaging modulation transfer function which is used for ray tracing corrections on droplet slicing image data. Since oxygen is a strong fluorescence quencher, any liquid volume element which has been exposed to it by surface contact or diffusion will suffer a reduction in fluorescence intensity.



Convection from the surface due to internal circulation as well as diffusion cause image regions to appear dark. Figure 1 shows data from a 450  $\mu\text{m}$  droplet which has fallen a short distance into a uniform upward Oxygen flow. Sequential images from a single drop provide temporal measurements of flow parameters (i.e. rates). Oxygen-free experiments provide a baseline case for normalization.

### Vaporization

Evaporation was measured in shock tube experiments using morphology-dependent resonances (MDR's).<sup>1</sup> A microscope/video system can provide only rough measurements and typically is able to resolve droplet diameters to within approximately 10  $\mu\text{m}$ . With the MDR technique, small droplets ( $\leq 100\mu$  dia.) of fluid with dye dissolved in them are pumped to an upper electronic state by a pulsed laser. Stimulated emissions from dye molecules just inside the circumference of the droplet are constrained to the inner surface by total internal reflection, effectively producing a spherical ring dye laser. Within the spectral-gain envelope of the dye, frequency modes for which the circumference is an integral number of wavelengths are resonantly enhanced.

A change in droplet diameter can be determined by simply using the mode spacing of a MDR's to measure the droplet diameter twice over a given time period and subtracting one from the other to obtain the change in size. A more accurate method is to measure the shift directly by observing the shift in spectral location of a given mode between two spectra.

Laser energy to pump the dye was provided by the second harmonic of a double-pulsed Nd:YAG laser. Pulses were approximately 10 ns in length and provided virtually instantaneous measurements with respect to the droplet and gas flows. The laser system was modified to allow multiple pulsing at high frequencies with temporal spacing around 100  $\mu\text{s}$  to determine evaporation rates. The laser beam was focussed to illuminate a single droplet at a time and timing of the laser pulse was triggered from passage of the shock-pressure pulse. Using this system, a series of measurements could be acquired using differing delay times on successive pressure pulse runs to describe the evaporation enhancement.

Evaporation rate measurements were made on methanol and water droplets in a gas flow at atmospheric temperature and pressure in the facility shown in Fig. 2. Evaporation rates were determined by recording MDR's from droplets at several heights in the droplet stream and observing the spectral shift of a given mode caused by a change in diameter resulting from evaporation as the droplet proceeded down the stream. Evaporation rates after the passage of a pressure pulse are higher than that observed in the droplet stream in quiescent air because gas velocities are an order of magnitude higher under these simulated rocket conditions. Resolution time scales between MDR measurements are roughly an order of magnitude smaller, and the data demonstrated that this technique is capable of providing the necessary resolution.

### Microgravity Combustion

Rapid advances have recently been made in numerical simulation of droplet combustion under microgravity conditions, while experimental capabilities remain relatively primitive. Calculations can now provide detailed information on mass and energy transport, complex gas-phase chemistry,

multi-component molecular diffusion, surface evaporation and heterogeneous reaction, which provides a clearer picture of both quasi-steady as well as dynamic behavior of droplet combustion.<sup>2</sup> Experiments concerning these phenomena typically result in pictures of the burning droplets, and the data therefrom describe droplet surface regression along with flame and soot shell position. With much more precise, detailed, experimental diagnostics, significant gains can be made on the dynamics and flame structural changes which occur during droplet combustion. Since microgravity experiments become increasingly more expensive as they progress from drop towers and flights to spaceborne experiments, there is a great need to maximize the information content from these experiments. Sophisticated measurements using laser diagnostics on individual droplets and combustion phenomena are now being performed. The program involves a series of measurements in the NASA Learjet and KC-135 aircraft facilities to investigate the range of applicability of these diagnostics while generating fundamental data for ongoing NASA research programs in this area.

An apparatus for performing measurements aboard the NASA Learjet and KC-135 low gravity aircraft facilities is being used to perform fundamental measurements on droplets. An integrated diagnostic unit, capable of performing these measurements, includes a self-contained miniature nitrogen-pumped dye laser system, a two-dimensional intensified CCD and, an unintensified CCD imaging system. The system is operational and flight ready as shown in Fig. 3.

Measurements are currently directed at detection of unsteadiness in flame diameter and its affect on burning rate of relative droplet gas-phase flow. Results of flight experiments from parabolic trajectories will be presented.

## REFERENCES

1. Tzeng, H. M., Wall, K. F., Long, M. B. and Chang, R. K.: *Evaporation and Condensation Rates of Liquid Droplets Deduced from Structure Resonances in the Fluorescence Spectra*, Optics Letters, Vol. 9, pp. 273-275, July, 1984.
2. Cho, S. Y., Yetter, R. A. and Dryer, F. L.: A Computer Model for One-Dimensional Mass and Energy Transport in and Around Chemically Reacting Particles, Including Complex Gas-Phase Chemistry, Multicomponent Molecular Diffusion, Surface Evaporation and Heterogeneous Reaction, Journal of Computational Physics, 1991.

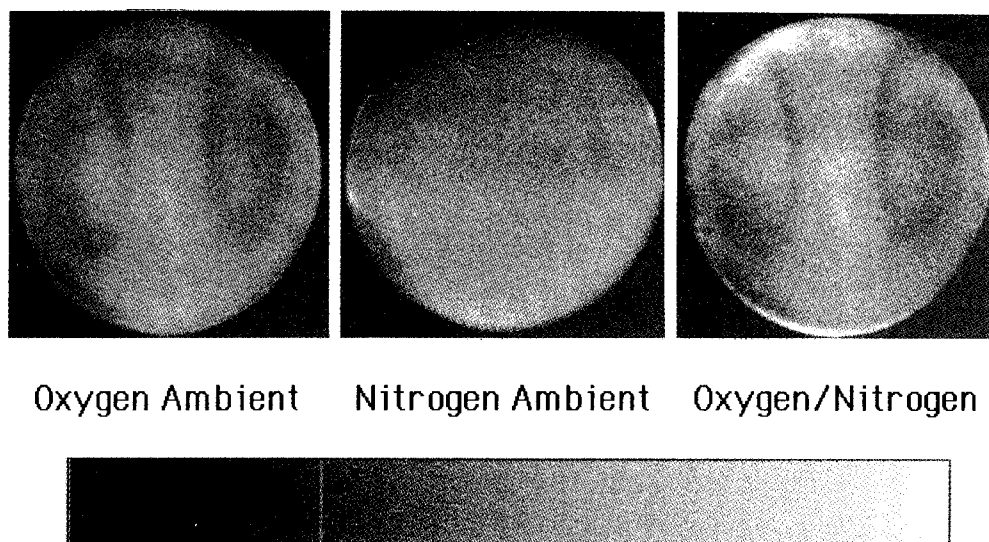


**Figure 1.** A comparison between an image of the fluorescence from a single droplet falling in a pure nitrogen environment, to that of one falling in an oxygen environment. Also shown are the result of dividing pixel by pixel the dividing each pixel in the oxygen case by the base-line nitrogen ambient data after background subtraction.

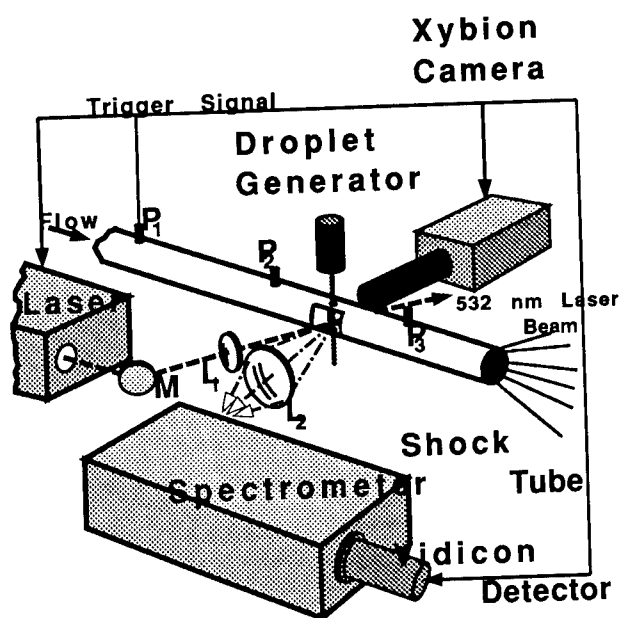


**Figure 2.** Experimental setup. The droplet stream is projected through holes in a shock tube and illuminated with the laser, timed with the passage of a shock wave. The MDR emissions are acquired with an intensified camera and dispersed in a spectrometer.

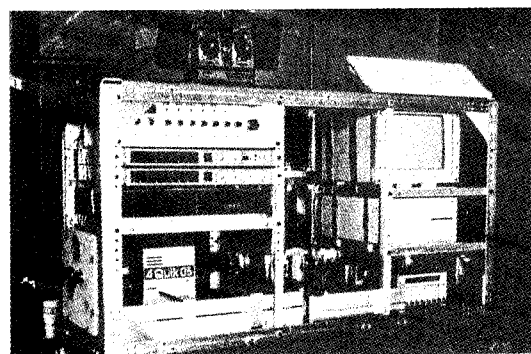


**Figure 3.** Photograph of the UTRC/NASA laser diagnostics for microgravity droplet combustion apparatus.

# Suppression of scattering resonances in inhomogeneous microdroplets

Dat Ngo

New Mexico State University Department of Physics  
Las Cruces, NM 88003

and

R.G. Pinnick

Army Research Laboratory  
White Sands Missile Range, NM 88002-5501  
Tel (505) 678-5634  
Fax (505) 678-2432

Resonance structure in elastic scattering from microdroplets was first observed more than 15 years ago by Ashkin and Dziedzic<sup>1</sup>, who measured the time evolution of scattering from slowly evaporating optically levitated silicon oil droplets. On the heels of this discovery, Chylek et al<sup>2</sup> identified the observed peaks in Ashkin's data with predicted resonances in the Mie partial wave scattering amplitudes. Resonances were characterized as either transverse electric ( $TE_n^1$ ) or transverse magnetic ( $TM_n^1$ ), having a mode number  $n$  and mode order  $l$  corresponding to the  $l$ th resonance in the  $n$ th partial wave scattering amplitude. Since these early advances, the importance of these resonances (commonly called morphology dependent resonances or MDR's) has been recognized not only in elastic scattering, but also in inelastic scattering processes<sup>3</sup>.

All of the cited experimental studies utilized homogeneous liquid droplets. However, atmospheric aerosols and cloud droplets generally contain small inclusions of insoluble material having different dielectric properties than the host liquid. Thus we pose the question: what effect do small inclusions of insoluble material have on scattering processes in both resonant and nonresonant microdroplets? In this paper we examine the effect of droplet inclusions on elastic scattering from micron-sized glycerol droplets, both on and off resonance.

In our experiment, slightly charged glycerol droplets with initial radii  $\approx 5\text{-}13\mu\text{m}$  are caught in an electrodynamic trap<sup>4</sup>. The trap is enclosed in a nearly air-tight cylindrical chamber fitted with six symmetrically-spaced windows to ensure that the trapped particle can be free of air disturbances in the room, while providing for simultaneous illumination, viewing, and detection of scattered light by trapped droplets. Droplets are illuminated with a polarized unfocused cw argon-ion laser beam with relatively low intensity ( $\approx 5\text{ W cm}^2$ ) so that insignificant heating occurs. As the droplets evaporate, scattering within a small (3.5 deg half-angle) conical solid angle, centered around 87.5 deg from the direction of forward scattering and 58 deg from the plane

containing the electric vector, is sensed through a microscope with a photomultiplier tube. The resulting signal is fed to a low pass (15 Hz) filter and digitized with a 50 Hz analog-to-digital recorder.

A portion of data for a pure glycerol droplet in the region of the  $TE_{120}^7$  resonance is shown in Fig. 1a,b. The measured resonance is slightly wider than theory, which is attributable to the finite (6 GHz) linewidth of the illuminating laser. The effect of adding monodisperse, nanometer-sized polystyrene latex particles (with nominal diameters 30, 64, and 105nm) to glycerol droplets is revealed in Fig. 1c-e. The total number of latex particles within the glycerol droplet ranges from  $2.4 \times 10^6$  for 30nm latex to  $5.2 \times 10^4$  for 105nm latex, chosen so that the droplets contain  $\approx 1$  volume percent latex. The latex inclusions cause fluctuations in the scattering signal, and the amplitude of the fluctuations increases with latex size. Fluctuations of similar magnitude, but for larger inclusions have been observed by Bronk et al<sup>5</sup>. In addition to causing fluctuations, latex also attenuates and broadens the sharpest (7th order) resonance peak. Our measurements of seeded droplets with radii  $2\mu\text{m} \leq r \leq 11\mu\text{m}$  show consistently that highest Q resonances, with modes ranging from 2nd order to 9th order, are similarly affected. Our conjecture is that scattering losses, caused by introducing latex into an otherwise homogeneous droplet, are responsible for these effects.

We are currently investigating models to explain both the observed suppression of resonances and fluctuations in scattering.

#### REFERENCES

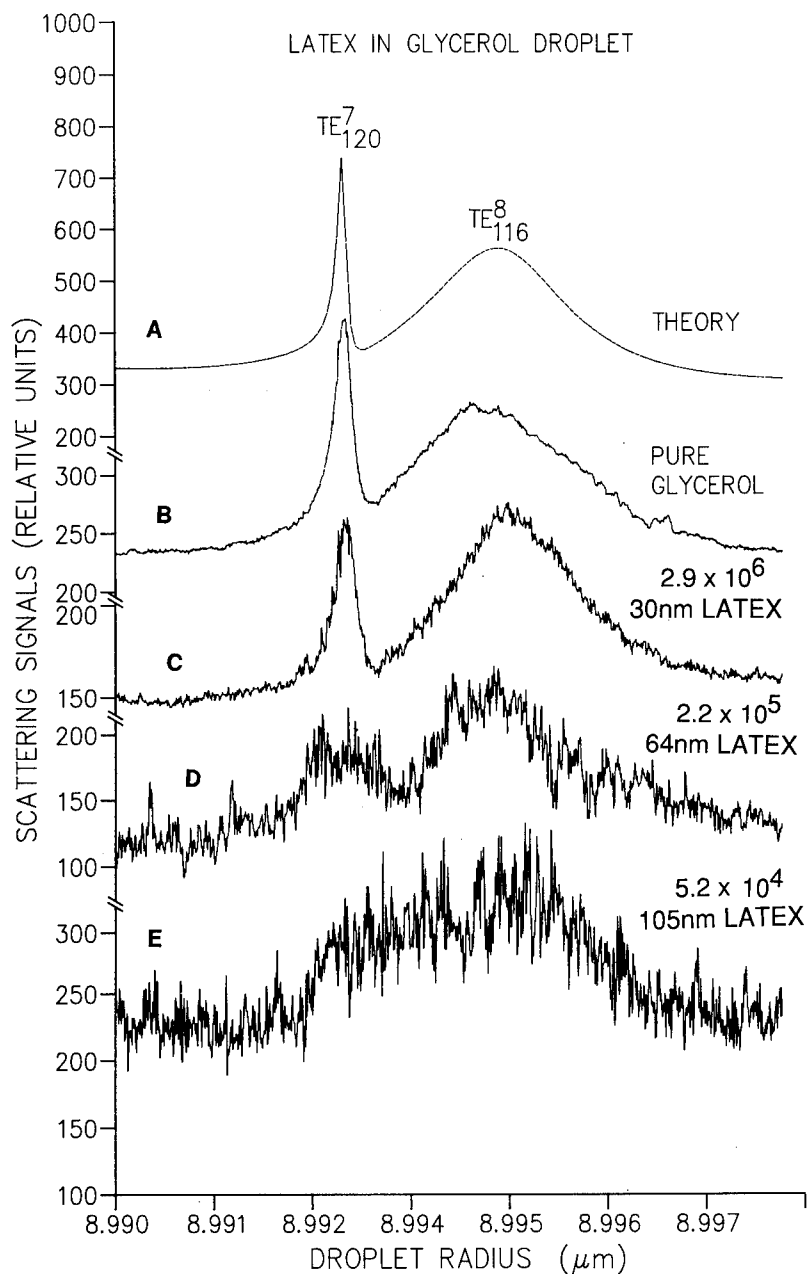
- <sup>1</sup>A. Ashkin and J.M. Dziedzic, "Observation of resonances in the radiation pressure on dielectric spheres", Phys. Rev. Lett. **38**, 1351 (1977).
- <sup>2</sup>P. Chylek, J.T. Kiehl, and M.K.W. Ko, "Optical levitation and partial wave resonances", Phys. Rev. A. **18**, 2229 (1978).
- <sup>3</sup>J. Owen, R.K. Chang, and P.W. Barber, "Morphology dependent resonances in Raman scattering, fluorescence emission, and elastic scattering from microparticles", Aerosol Sci. Technol. **1**, 293 (1982); R.E. Benner, P.W. Barber, J.F. Owen, and R.K. Chang, "Observation of structure resonances in the fluorescence spectra from microspheres", Phys. Rev. Lett. **44**, 475 (1980); J.B. Snow, S. Qian, and R.K. Chang, "Stimulated Raman scattering from individual water and ethanol droplets at morphology-dependent resonances", Opt. Lett. **10**, 37 (1985); H.-M. Tzeng, K.F. Wall, M.B. Long, and R.K. Chang, "Laser emission from individual droplets at wavelengths corresponding to morphology-dependent resonances", Opt. Lett. **9**, 499 (1984); J.-Z. Zhang and R.K. Chang, "Generation and suppression of stimulated Brillouin scattering in single liquid droplets", J. Opt. Soc. Am. B. **6**, 151 (1989).

- <sup>4</sup>S. Arnold, in Optical Effects Associated with Small Particles,

P.W. Barber and R.K. Chang, eds, (World Scientific, Singapore, 1988), Chap. 2, pp. 65-137; M. Essien, J.B. Gillespie, and R.L. Armstrong, "Observation of suppression of morphology-dependent resonances in singly levitated micrometer-sized droplets", Appl. Opt. 31, 2148-2153 (1992).

<sup>5</sup>B. Bronk, M. J. Smith, and S. Arnold, "Photon-correlation spectroscopy for small spherical inclusions in a micrometer-sized electrostatically levitated droplet", Opt. Lett. 18, 93 (1993).

Fig. 1. a) Mie scattering theory predictions for light scattered by a glycerol droplet (with refractive index  $m = 1.4746$ ) through the aperture described in the text and in the region of the  $TE_{120}^7$  resonance; b) corresponding measurements of light scattering from an evaporating glycerol droplet; c-e) same as b) except for a glycerol droplet seeded with the indicated numbers of 30nm diameter latex particles (c), 64nm particles (d), and 105nm particles (e). Seeded droplets contain  $\approx 1$  vol% latex.



## Near-field Optical Measurements at the Liquid/Air Interface

Mark Seaver and A. E. Frost  
code 5610, Naval Research Lab, Washington DC 20375. (202)767-3590

M. D. Duncan  
code 5640, Naval Research Lab, Washington DC 20375. (202)767-2507

### Introduction

Near-field optical microscopy offers the benefit of dramatically improved optical resolution [1] in exchange for working in close proximity (10-50nm) to a thin sample (<20nm). Monolayers at the liquid/air interface fulfill the thin sample criterion and are spectroscopically distinct from the supporting liquid. However, the mobility of the interface suggests that when a tapered probe approaches closely, attractive forces may cause the interface to jump up and submerge the probe at probe-sample spacings much greater than the required working distance for near-field optics. We detect the evanescent field decay above the liquid/air interfaces for glycerol, mineral oil, and water. The ability to measure these evanescent decays demonstrates that near-field approach to the liquid/air interface is possible. The measured evanescent decay lengths agree well with the predicted values. The presence of gravity waves in deep (1-2 cm) liquid samples sets a lower limit on the distance of closest approach but does not prevent near-field measurements.

### Apparatus

The apparatus consists of a mounted tapered single-mode optical fiber either directly attached to a piezo electric inchworm or held in a piezo electric tube. The inchworm's minimum approach rate is 10nm/s. Because the build up of static charge on the fiber tip will dramatically increase the tip-surface forces, we mount the fiber optic in a metal tube and ground that tube to the shaft of the inchworm. In this fashion, we expect to limit the tip-surface interaction to dispersion forces. Liquid samples consist of 10-20 ml of the pure liquid in a quartz cell, 2.0 x 4.0 cm x 4.7 cm deep, this results in a depth of 1-2 cm. The evanescent field is set up by totally internally reflecting the 632.8nm beam from a helium-neon (HeNe) laser that impinges on the sample surface from below. We also use the evanescent field above a quartz prism as calibration. The HeNe beam is chopped at about 2 kHz which enables us to use lock-in detection for evanescent field intensity measurements versus height above the sample. In all cases, the fiber tip approaches from the far field with height zero defined as the point of surface penetration in liquids or as the point of maximum signal for the prism. In liquids a >100x jump in signal makes surface penetration unmistakable. The 1-2 cm depth of liquid in the cell is sufficient to support gravity waves that resonate along the long dimension of the cell.

Shear force measurements [2] are implemented by applying an ac signal to opposite quadrants of the PZT tube. The resonance frequency depends on the length of probe extending beyond the metal sheath and varies from 5-55 kHz. The horizontal oscillation of the probe is measured with a quadrant photodiode and lock-in detection..

### Evanescent decay

Upon total internal reflection, the evanescent field penetration into the medium with a lower index of refraction is described by

$$E(z) = E_0 \exp(-z/d_p), \quad (1)$$

where  $z$  is the height above the interface and  $d_p$  is the penetration length. The penetration length depends on the wavelength ( $\lambda$ ), the angle of incidence ( $\theta$ ), and the refractive indices of the two media ( $n_1 < n_2$ ).

$$d_p = \frac{\lambda}{2\pi \sqrt{\left(\frac{n_2^2}{n_1^2} \sin^2 \theta - 1\right)}} \quad (2)$$



The evanescent field intensity,

$$I(z)=E^2(z)=E_0^2 \exp(-2z/d_p), \quad (3)$$

is what we measure experimentally and will compare with predictions of eqn. 2. For these experiments,  $n_1=1$ , the refractive index of air and  $n_2=1.46, 1.47, 1.46$ , and  $1.33$  for quartz, glycerol, mineral oil, and water respectively.

## Results

Experimentally, we measure field intensity versus time. We convert the time to height by assuming that the maximum in intensity occurs when the tip touches the prism ( $z=0$ ) or penetrates the liquid surface. We then use the specified inchworm approach speed,  $10\text{nm/s}$ , to determine the height above the surface. Fig. 1 displays the approach data for a tip approaching mineral oil. This curve shows modulations superimposed on a signal which rises as the tip approaches the interface. These modulations are caused by gravity waves resonating in the long dimension of our cell. Two facts identify wave action as the source of this modulation. First, the wave frequency as determined by observing the photomultiplier output on a scope is about  $16\text{ Hz}$ . For a gravity wave in shallow liquid, the velocity is given by  $v=(gh)^{1/2}$ , where  $g$  is the acceleration due to gravity and  $h$  is the liquid depth [3]. For a  $2\text{ cm}$  deep liquid,  $v=44.3\text{ cm/s}$  and the first three standing wave resonances along our  $4\text{ cm}$  length will occur at  $5.5, 11$ , and  $17\text{ Hz}$ . Second, the amplitude of the modulation depends on the viscosity of the liquid. This observation is consistent with the fact that the boundary layer thickness for laminar flow over a flat plate is proportional to the square root of the fluid viscosity [4]. The data in fig. 1 are for mineral oil, which is intermediate in viscosity between glycerol and water. The amplitude of the modulation in this data is roughly half the amplitude seen in water. In glycerol, wave modulation is barely observed. Because of the effect of the waves, when we compare experimental results with evanescent field predictions, we use only data from the rising baseline and ignore the modulations. This procedure best represents the decay because the exponential dependence of  $I(z)$  effectively rectifies sinusoidal variations in  $z$ .

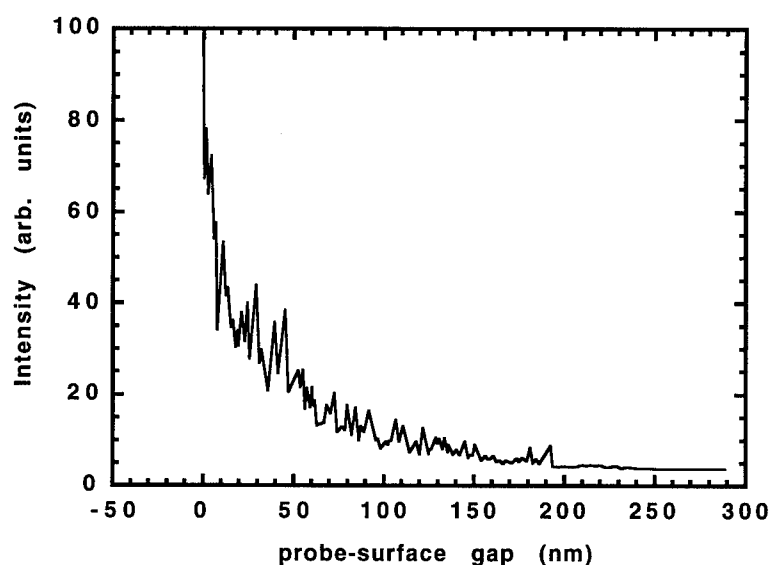


Figure 1. Evanescent field decay above mineral oil.

In fig. 2, we plot the evanescent decays observed above the liquids glycerol, mineral oil, and water. Each of these three data sets is fitted with an exponential to extract the evanescent

decay length. This procedure yields experimental decay lengths of 98, 88, and 147 nm for glycerol, mineral oil and water respectively. We calculate  $d_p$  via eqn. 2 for the three substances at 119, 121, and 158 respectively. This level of agreement may be fortuitous given the sensitivity of the calculated values of  $d_p$  to the precise angle of incidence.

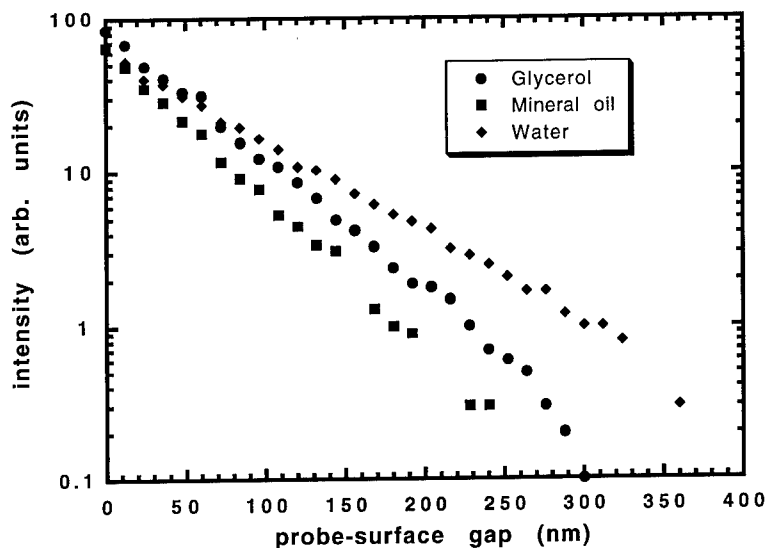


Figure 2. Evanescent signal intensity versity probe-surface gap for glycerol, mineral oil and water.

### Conclusions

We have demonstrated that near-field approach to the liquid/air interface from the air side is possible as long as dispersion forces dominate the tip-surface interaction. We have successfully approached the three liquids, glycerol, mineral oil and water, which have widely varying viscosities and different refractive indices. In all three cases the evanescent decay length agrees with the theoretical predictions. When the liquid depth is 1-2 cm, we see gravity waves modulating the evanescent decay envelope. These waves impede but do not prevent the detection of the evanescent field.

- [1] E. Betzig, J. K. Trautman, T. D. Harris, J. S. Weiner, and R. L. Kostelak, *Science*, **251** 1468, (1991)
- [2] E. Betzig, P. L. Finn, and J. S. Weiner, *Appl. Phys. Lett.* **60**, 2482 (1992).
- [3] I. G. Main, "Vibrations and Waves in Physics, 2nd ed. (Cambridge University Press, Cambridge, UK, 1984).
- [4] R. S. Brodkey and H. C. Hershey, "Transport Phenomena A Unified Approach", (McGraw Hill, New York, 1988).

## Structure and Extended Electronic States in Molecular Assemblies of Hemicyanine Amphiphiles.

Q. Song, Z. Xu, W. Lu, and P.W. Bohn, Department of Chemistry and Beckman Institute, University of Illinois at Urbana-Champaign, 600 S. Mathews St., Urbana, IL 61801

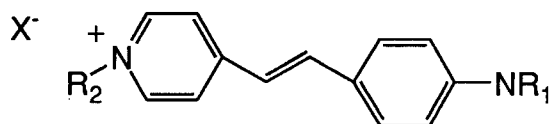
and

G.J. Blanchard, Department of Chemistry, Michigan State University, East Lansing, MI 48824

### Introduction

Hemicyanine dyes containing long alkyl chains have attracted considerable attention in recent years due to their significance as possible opto-electronic and molecular electronic materials. With large non-linear molecular polarizabilities, amphiphilic hemicyanines are readily incorporated into Langmuir-Blodgett monolayer and multilayer films, forming artificial molecular assemblies with preferred spatial and orientational order [1,2]. In contrast to centrosymmetric bulk materials, in which the individual effects are canceled, and the overall bulk second-order susceptibility vanishes [1], highly aligned structures ensure non-zero macroscopic second-order susceptibilities,  $\chi^{(2)}$ . In addition molecular assemblies of these materials have been shown to be characterized by extended electronic states in which the relationship between molecular structure and delocalization of the electronic states is a matter of current interest.

In these experiments we examine carefully the behavior of two specific hemicyanine dyes, given in Scheme 1, with respect to their linear and nonlinear spectroscopic behavior.



I:  $\text{R}_1 = \text{C}_8\text{H}_{17}$ ;  $\text{R}_2 = (\text{CH}_2)_3\text{SO}_3^-$

II:  $\text{R}_1 = \text{C}_{16}\text{H}_{33}$ ;  $\text{R}_2 = \text{CH}_3$ ;  $\text{X} = \text{Br}$

Scheme 1

## Results and Discussion

As has been shown in previous studies, LB monolayers of **I** exhibit a strong tendency toward aggregation [3,4]. This has been clearly shown by the fact that the dye self-aggregates on both water and quartz surfaces, even in the presence of a large fraction of spacer molecules, such as stearic acid. Aggregation of the dye is characterized by a blue shift of the absorption spectrum for the  $\pi$ - $\pi^*$  transition from 490 nm to 340 nm [5]. In this work, we compare the aggregation behavior of **I** and **II** and investigate the effect of aggregation on the nonlinear optical properties in the LB monolayers. A distinct difference in aggregation behavior has been observed between **I** and **II** during monolayer formation. While monolayers of **I** contain only H-aggregate species, monolayers of **II** can be prepared to contain any arbitrary aggregate structure desired. In Figures 1 and 2 we take advantage of this fact to study the SHG signal as a function of the monomer fraction in pure monolayers of dye **II**. These data are to be contrasted with typical studies in which the behavior of aggregating dyes are studied while being diluted with a non-aggregating diluent. Clearly the two wavelengths chosen for excitation, 1064 nm and 580 nm are nonresonant at  $\omega$  but resonant with the monomer-only at  $2\omega$ . Thus, the behavior observed is quite consistent with a resonance enhanced signal, i.e. the disappearance of the nonlinear susceptibility upon aggregation appears to be related to a simple shift in the electronic spectrum rather than to local-field effects or structural reorganization.

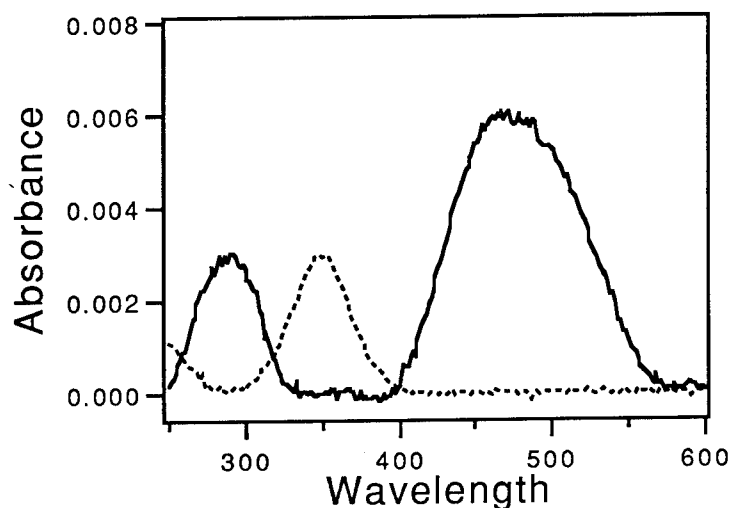


Figure 1: Absorption spectra for pure monomer (solid line) and pure aggregate (dashed line) monolayers of **II**.

The experimental results shown above illustrate the impact of molecular structure and electronic interactions (chromophore-chromophore interaction) on aggregation and on the linear

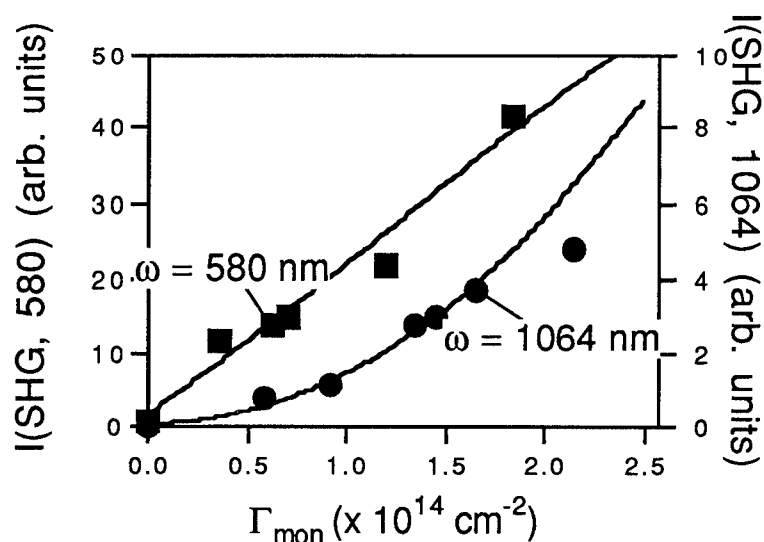


Figure 2: Plot of the SHG response as a function of the fraction of monomer in a pure monolayer of **II** on a fused silica substrate. Curves are given for excitation in which  $2\omega$  is resonant with the  $S_1$  state of the monomer ( $\lambda = 1064 \text{ nm}$ ) and in which it is resonant with the  $S_2$  state of the monomer ( $\lambda = 580 \text{ nm}$ ).

and collective nonlinear optical behavior of molecular assemblies of hemicyanine dyes. To illustrate the importance of the tail-tail interaction to the molecular packing and the impact on the optical properties for hemicyanine dyes in molecular assemblies, results from fluorescence studies of **I** in different environments have been obtained. In the monolayer sample, the fluorescence spectrum is dominated by a band centered at 530 nm, whereas in trilayer sandwich (stearic acid:**I**:stearic acid) structures, an emission band appears at 410 nm, the same position observed for the **I** in acidic solution. We propose that the emission at 410 nm arises from species, similar to those found in acidic solution, in which the tertiary amine N atoms are rotated out of the chromophore plane to form a twisted intramolecular charge transfer (TICT) state. This assignment is supported by the results from the protonation study of double chain hemicyanine dye in solution. In addition we have completed picosecond time-correlated single photon counting measurements of monolayers of **I** excited at the aggregate absorption band. The results indicate the presence of two distinct lifetime components in the monolayer, in contrast to **I** in solution which shows a clean 75 psec single-exponential decay. The aggregate is subradiant relative to the monomer and exhibits a fluorescence decay with two components: a dominant component with a 360 psec lifetime and a minor component with  $\tau = 2.4 \text{ nsec}$ . Current experiments are aimed at delineating the physical origins of the two lifetime components in the monolayer.

## Conclusions

Langmuir-Blodgett (LB) techniques have been used to construct monolayer and multilayer assemblies of a set of structurally related hemicyanines. The linear spectroscopic properties are dominated by an aggregate transition blue-shifted from the monomer in solution by  $10,000\text{ cm}^{-1}$ . The non-linear activity of hemicyanine monolayers has been investigated using surface second harmonic generation of single-sided samples in the transmission geometry. Pure dye films have been developed in which the composition of aggregate and monomer is varied, and the SHG signal tracks the monomer composition. Both linear and nonlinear results are interpreted within a model which places primacy on the *ground state* interactions in forming an extended network which facilitates the many interesting electronic phenomena exhibited by these structures.

## References

1. Meredith, G. R.; Buchalter, B.; Hanzlik, C. *J. Chem. Phys.* **1983**, 78, 1533.
2. Girling, I. R.; Kolinsky, P. V.; Cade, N. A.; Earls, J. D.; Peterson, I. R. *Opt. Comm.* **1985**, 55, 289.
3. Anderson, B. L.; Hoover, J. M.; Lindsay, G. A.; Higgins, B. G.; Stroeve, P.; Kowel, S. T. *Thin Solid Films* **1989**, 179, 413
4. Marowsky, G.; Chi, L. F.; Möbius, D.; Steinhoff, R.; Shen, Y. R.; Dorsch, D.; Rieger, B. *Chem. Phys. Lett.* **1988**, 147, 420.
5. Evans, C. E.; Bohn, P. W. *J. Am. Chem. Soc.* **1993**, 115, 3306.

## Multichannel Time-Resolved Raman Spectroscopy for Photophysical and Photochemical Studies

Julius C. Fister and Joel M. Harris  
Department of Chemistry, University of Utah  
Salt Lake City, Utah 84112  
(801) 581-7938

CCD-detected Raman spectroscopy has been used to study intermediates and nanosecond kinetics in photoinitiated reactions. Multidimensional analysis techniques are used to isolate spectra of individual transient species from those of ground state initiators, photoproducts, reactants and solvent (Fig 1). These methods address several challenges facing Raman analysis of chemical reactions. Overlap in spectra of complex mixtures complicates band assignment and intensity analysis. Raman bands of transient species created in photoinitiated reactions may be difficult to separate from other bands. Multidimensional analysis allows bands to be resolved from spectra in which background subtraction is not feasible. Furthermore, kinetic and spectral information may be simultaneously extracted from the data.

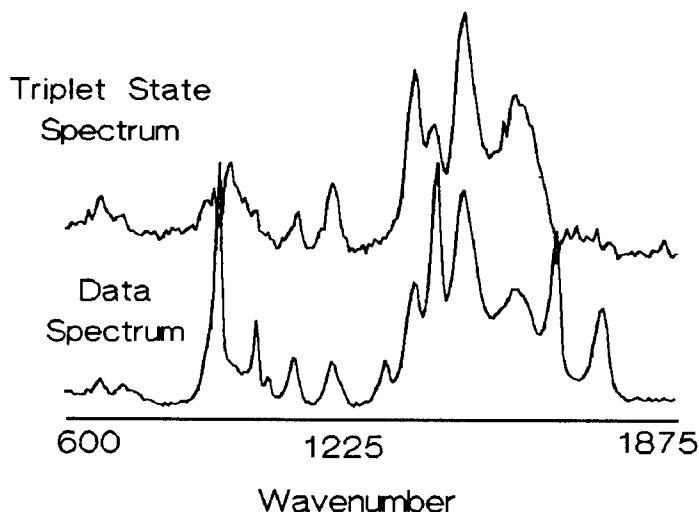


**Figure 1:** Acetophenone Triplet State Spectrum and Spectrum from Laser Intensity Data Set.

Acquisition and analysis proceeds as follows. A Nd:YAG-pumped Raman shifter produces nanosecond ultraviolet pulses in the near UV which both initiate and probe sample photophysics and photochemistry. A spectrum is obtained by integrating the signals from several thousand pulses. Laser power and/or quencher concentration are varied to obtain a matrix, **D**, of spectral data. The Raman intensities of individual components will vary as functions of these parameters according to the fixed time kinetics occurring during each laser pulse. The strength of this approach lies in extracting information from spectral variation along the complex spectral axis by

modeling response to changes along measurement dimensions having fewer degrees of freedom. Within  $\mathbf{D}$ , the wavenumber of the measurement varies as index  $i$ , and laser power (for example) varies according to index  $j$ . The observed Raman intensity at any wavenumber and power,  $d_{ij}$ , will be the sum of the contributions from the  $n$  unknown sample components:

$$d_{ij} = \sum_{k=1}^n u_{ik} c_{kj} \quad (1)$$

where  $u_{ik}$  contains the Raman intensity at the  $i$ th wavenumber of the  $k$ th component and  $c_{kj}$  is the relative contribution to the total observed Raman spectrum of the  $k$ th component at the  $j$ th power. This relationship may be expressed as the matrix product

$$\mathbf{D} = \mathbf{U} \mathbf{C} \quad (2)$$

where  $\mathbf{U}$  contains the Raman spectra of the  $n$  unknown components in its columns and  $\mathbf{C}$  contains the power dependent response curves for these components in its rows. The least squares unknown spectral matrix  $\hat{\mathbf{U}}$  is found by multiplying the data matrix by the pseudoinverse of  $\mathbf{C}$ :

$$\hat{\mathbf{U}} = \mathbf{D} \mathbf{C}^T (\mathbf{C} \mathbf{C}^T)^{-1} \quad (3)$$

Bands of any group of components whose scattering responses are linearly related will appear as one vector in  $\hat{\mathbf{U}}$ .

Generation of the response matrix  $\mathbf{C}$  begins by considering the formation and decay kinetics of each species. Triplet state acetophenone is populated during the laser pulse at a rate proportional to the instantaneous intensity:

$$\frac{d[T_1]}{dt} = \phi \sigma_1 I(t) [S_0] \quad (4)$$

where  $\sigma_1$  is the ground state absorption cross section,  $\phi$  is the triplet quantum yield (assumed to be unity for acetophenone) and  $S_0$  is the ground state concentration. Because the average time between excitation events ( $1/\text{pump rate}$ ) is small compared to the laser pulse duration, the ground state concentration remains essentially constant during the laser pulse. Integrating equation 4 yields the instantaneous triplet population at any time  $t$  during the laser pulse:

$$[T_1]_t = \phi \sigma_1 [S_0] \int_0^t I(t) dt \quad (5)$$

For a laser pulse with a gaussian temporal profile the time dependent triplet population may be described as an error function. The rate of Raman scattering from each species is given by the product of the population and laser intensity curves. Consequently, the integrated triplet state intensity is proportional to:



$$\text{Triplet Intensity} \propto \sigma_R \sigma_1 [S_0] \int_0^t I(t) \left( \int_0^t I(t) dt \right) dt \quad (6)$$

where  $\sigma_R$  is the scattering cross section. Because the time-dependent concentration of triplets is proportional to the laser intensity, the triplet state exhibits a quadratic scattering intensity dependence on laser power. In the absence of stimulated scattering, ground state and solvent band intensities vary linearly with power.

For example, Figure 1 shows the Raman spectrum of triplet acetophenone isolated from bands of ground state species in acetonitrile solution via a laser intensity dependence study. Using isotopic substitution, the distribution of electronic excitation may be determined by comparing shifts in vibrational frequencies between the ground and excited states.<sup>1</sup> Coupled with *ab initio* calculations, a powerful description of excited state geometry may be developed<sup>2</sup>.

Studies of photoinitiated chemistry require the ability to separate the spectra of the initially excited triplet states from spectra of both excited state photoproducts and ground state species. Complete separation requires that a single spectral data set be acquired as a function of both laser power and quencher concentration. The nonlinear time dependence of photoproduct formation during the laser pulse allow its spectrum to be differentiated from that of the ground state reactant. The bimolecular quenching constant,  $k_q$ , for the reaction between initiator and reactant becomes a parameter in the regression procedure increasing the informing power of the analysis. This has been performed both for energy transfer and free radical hydrogen abstraction reactions resulting in the first isolation of the biacetyl triplet state and benzophenone ketyl radical spectra.

Future work will expand the time scale of observable kinetics from nanoseconds to microseconds<sup>3</sup> by employing variable delay pump probe instrumentation. Application of analysis techniques similar to those outlined above should further increase the utility of Raman spectroscopy as a photochemical probe.

---

<sup>1</sup> Takahashi, H.; Hiura, H.; Ebihara, K. *J. Phys. Chem.* **1992**, 96, 9120

<sup>2</sup> Tahara, T.; Hamaguchi, H.; Tasumi, M. *J. Phys. Chem.* **1990**, 94, 170-178

<sup>3</sup> Beck, S. M.; Brus, L. E. *J. Am. Chem. Soc.* **1982**, 104, 1104



Wednesday, March 9, 1994

## Diode-Laser Based Measurements

**WB** 10:30am-12:10pm  
Grand Room

Ulrich E. Meier, *Presider*  
*DLR EN-CV, Germany*

## Application Of Diode Lasers To Atmospheric Diagnostics

Joel A. Silver, D. Christian Hovde, David S. Bomse, Daniel B. Oh,  
Daniel J. Kane and Alan C. Stanton  
Southwest Sciences, Inc.  
1570 Pacheco Street, Suite E-11  
Santa Fe, NM 87501  
Tel. (505) 984-1322

### INTRODUCTION

Diode lasers provide reliable, inexpensive and compact sources of light readily usable for the detection of virtually any small molecule in the gas phase. In particular, near-infrared and visible diodes exhibit properties especially attractive to real-world measurement applications: operation at room temperature, fiber optic compatibility and minimal power requirements. These lasers can be used in rugged instruments designed for long-term, unattended operation. In this paper, a diverse range of applications in atmospheric sensing is discussed.

### EXPERIMENTAL METHODS

Most applications of diode laser sensors have been based on cw absorption methods using some form of wavelength (frequency) modulation.<sup>1,2</sup> These techniques involve modulation of the laser injection current (which appears as an output frequency modulation) at some frequency  $f$  (or pair of closely spaced frequencies) with homodyne detection at some harmonic of  $f$  (or at the beat frequency in the case of two-tone modulation). Detection is performed at frequencies high enough such that the excess  $(1/f)$  noise of the laser is unimportant relative to detector noise (laser shot-noise and thermal noise). Under these conditions of quantum-limited detection, fractional absorbances of  $10^{-7}$  or better can be achieved in the laboratory. In the field, using fiber optics and with the requirements for long-term, unattended operation, absorption sensitivities on the order of  $10^{-5}$  have been demonstrated. Limitations are primarily due to fiber-induced noise and unwanted etalon effects, although non-ideal response of the laser through residual amplitude modulation and induced harmonic frequency response is also of concern.

Given a measured absorbance  $\alpha$ , the gas concentration  $n$  is determined from the definition of absorbance  $\alpha = \sigma(\nu) n l$ , where  $\sigma(\nu)$  is the absorption cross section lineshape and  $l$  the path length. For a typical near-infrared detection system, sensitivities range from about 10 ppb-m to a 10,000 ppm-m. These levels are poorer than observed with lead-salt diode lasers because near-infrared lasers probe combination or overtone bands, for which the absorption cross sections are smaller than for the mid-infrared fundamentals. Although lead-salt mid-infrared lasers have been successfully used in a variety of atmospheric measurements (especially airborne and balloon-borne sensing applications), they require cryogenic coolants, require more attention, and are not suited to harsh environments or to situations where ambient backgrounds of the gas would overwhelm the measured signal of interest (since they cannot at present readily use fiber optics). For these reasons, we believe near-infrared or visible diodes are especially promising in a number of applications.

Measurements of the gaseous sample can be performed in one of two ways. Multiple path absorption cells (using either White<sup>3</sup> or Herriott<sup>4</sup> mirror configurations) provide a compact system with a long optical path length for optimum sensitivity. These cells can be open or closed to the atmosphere. Alternatively,

one can use long open-path configurations, optionally using a retroreflector, to perform measurements across large areas. The choice of optical path design depends on the application.

The electronics required to operate the laser and perform the detection are simple and can be condensed onto one or two circuit boards. The laser can be repetitively scanned across the desired absorption feature if lineshapes are of interest, or the laser can be line-locked<sup>5,6</sup> to line center for concentration measurements. Data analysis requirements are well within the capabilities of portable PCs and a number of groups, including ours, are now studying the use of real-time DSP (digital signal processing) techniques to process the raw signals with the possibility of greatly enhanced sensitivity.

## DISCUSSION

In this Section we present a few examples of how diode lasers are being used in atmospheric sensing applications. While certainly not an exhaustive survey, this provides a flavor of the kinds of measurements which are currently possible using diode lasers.

### Airborne Hygrometers

Over the past two years, we developed an airborne hygrometer using a closed multipass cell operating at fixed pressure.<sup>7</sup> It flew for six months aboard a KC-135, running totally unattended. This device measured water vapor absorbances at  $7412\text{ cm}^{-1}$ , providing a sensitivity of 8 ppm volume mixing ratio (S/N=1). For the atmospheric conditions during most flights, this sensitivity corresponds to an approximate frost point of  $-68^{\circ}\text{C}$ . We are currently investigating the use of a custom-fabricated laser at  $7181\text{ cm}^{-1}$  where the absorption cross section is 350 times stronger. This should improve the detection limit to 23 ppb-V, corresponding to a frost point below  $-100^{\circ}\text{C}$ !

### Perimeter Monitors

Diode laser sensors can be used in hazardous environments to monitor toxic gases. For example, a perimeter monitor in a refinery or chemical plant can alert personnel to leaks. The use of fiber optics simplifies the design of intrinsically safe instruments. Low laser power guarantees eye-safe operation for open path monitoring. We are now testing perimeter monitors for hydrogen fluoride and hydrogen sulfide using near-infrared diode lasers.

### Stack Emission Monitors

The recent upgrading of EPA emission monitoring regulations, coupled with increasingly stringent emission requirements, has triggered a host of new applications for gas sensing. One example is the thermal deNO<sub>x</sub> process which uses ammonia injected into the stack exhaust stream of a power plant to reduce NO<sub>x</sub> emissions. In addition to monitoring the NO<sub>x</sub>, the amount of NH<sub>3</sub> released must also be measured to control and optimize the process stream. PSI Environmental Instruments Corporation is now beta-testing a diode laser based sensor to monitor NH<sub>3</sub>.

### Trace Gas Sensors

To improve our understanding of atmospheric chemistry, ever increasing sensitivities for measurement of both stable and radical species are required. Diode laser absorption using high frequency modulation methods can be used in this regard. In addition to the large body of research on mid-infrared sensing of many neutral species, near-infrared lasers may be useful in detecting oxy-hydrides, whose near-infrared line strengths are often comparable to those in the mid-infrared. Such species include H<sub>2</sub>O, H<sub>2</sub>O<sub>2</sub> and HO<sub>2</sub>.

### Fluxmeters

A great deal of research in recent years has focused on the sources and sinks of greenhouse gases, methane in particular. We have developed an instrument which uses an open path Herriott cell in conjunction with a sonic anemometer to measure methane fluxes by eddy correlation methods.<sup>8</sup> In collaboration with personnel at the NOAA Atmospheric Turbulence and Diffusion Division, this device was tested at a landfill in Oak Ridge, TN and measured fluxes averaging  $6,500 \text{ mg CH}_4 \text{ m}^{-2} \text{ day}^{-1}$ .

### Other Applications

In addition to atmospheric applications, diode lasers are being used in a number of other fields. In combustion, they are used for species concentration, temperature and velocity measurements in flames, wind tunnels and hypersonic engines.<sup>9-11</sup> One novel use is the measurement of major combustion species in microgravity drop tower experiments, where fiber optics are required to access a free-falling flame.<sup>12</sup> Another use is that of gas purity measurement for semiconductor manufacturing and processing. Impurities such as  $\text{H}_2\text{O}$  in feed gases must be kept at or below ppb levels, yet no satisfactory on-line diagnostic methods exist to measure their concentrations well enough. Current studies using diode lasers may be able to solve this problem.

## **FUTURE DIRECTIONS**

During the past five years, a wide variety of atmospheric and other applications for diode laser diagnostics have been demonstrated. High frequency modulation techniques permit achievement of sensitivities sufficient for these needs using near-infrared or visible diode lasers. The greatest constraint on the evolution of this field of research has been the lack of suitable lasers. Until recently, only a very few specific wavelengths (driven by commercial applications such as optical communications, CD players, and bar-code readers) were available, and these lasers may exhibit operating characteristics which are not desirable in a spectroscopic-based device. Currently about half a dozen companies, including one source in Russia, will fabricate customized lasers which are more suitable for diagnostic applications.

Current research indicates that newly designed mid-infrared lasers will soon be available. These devices operate near room temperature in pulsed mode and could make optimal use of advances in mid-infrared optical fiber technology. Adaptation of high frequency modulation methods to pulsed operation will permit the enhanced concentration sensitivity now possible with lead-salt lasers, but without any of the drawbacks. On the other end of the spectrum, visible wavelength diode lasers will permit us to access strong electronic transitions. In addition, frequency mixing schemes to generate new wavelengths is a very promising avenue of investigation. The tremendous sensitivities achievable with high frequency modulation methods do not require much laser power; in fact, for many applications a few tens of microwatts is sufficient. Thus sum or difference frequency methods using diode pumps may broaden the range of available wavelengths.

As the detection methods evolve, improved signal-to-noise levels can be expected. Digital signal processing approaches can filter and demodulate the photocurrent from the detector in real time better than analog circuitry. High speed, high resolution A/D-converters in conjunction with DSP techniques promise more reliable and rapid in-line process control or monitoring using diode lasers.

## **REFERENCES**

1. J. Silver, Appl. Opt. **31**, 707 (1992).
2. D.E. Cooper and R.E. Warren, Appl. Opt. **26**, 3726 (1987).
3. J.U. White, J. Opt. Soc. Am. **32**, 285 (1942).
4. D.R. Herriott, H. Kogelnik and R. Kompfner, Appl. Opt. **3**, 523 (1964).

5. D.S. Bomse, Appl. Opt. **30**, 3933 (1991).
6. N. Goldstein, S. Adler-Golden, J. Lee and F. Bien, Appl. Opt. **31**, 3409 (1992).
7. J.A. Silver and D.C. Hovde, Rev. Sci. Instrum. (submitted for publication, 1993).
8. D.C. Hovde, T.P. Meyers, A.C. Stanton and D.R. Matt, J. Atmos. Chem. (submitted for publication, 1993).
9. D.B. Oh and A.C. Stanton, manuscript in preparation.
10. L.C. Philippe and R.K. Hanson, Appl. Opt. **32**, 6090 (1993).
11. M.P. Arroyo and R.K. Hanson, Appl. Opt., **32**, 6104 (1993).
12. J.A. Silver, D.J. Kane and P.S. Greenberg, manuscript in preparation.

**A New Field Tunable Diode Laser Absorption Spectrometer  
For Highly Sensitive Measurements of  
Atmospheric Gases**

Alan Fried, Scott Sewell, Bruce Henry

The National Center for Atmospheric Research  
Atmospheric Chemistry Division  
PO Box 3000  
Boulder, Colorado 80307  
303 497 1475

and

James R. Drummond  
The Department of Physics  
University of Toronto  
Toronto, Ontario, Canada

The technique of tunable diode laser absorption spectroscopy (TDLAS) has been employed in a number of field investigations for studying the chemistry of both the lower atmosphere (the troposphere) as well as the middle atmosphere (the stratosphere) over the past several years.<sup>1</sup> This technique offers many advantages in such studies including: high sensitivity, high selectivity, high precision, fast response, and versatility. The present paper describes a new field TDLAS system, which has been developed at the National Center for Atmospheric Research (NCAR), for furthering our understanding of tropospheric chemistry using this spectroscopic technique. Several novel features have been incorporated in the present system such as a new commercially-available astigmatic Herriott cell and digital signal processing electronics to further improve system performance and versatility. These aspects will be discussed in the present paper along with recent measurements of formaldehyde employing this system at a remote sampling site in Colorado.



In measurements of trace atmospheric constituents, tunable diode laser systems most frequently employ multipass absorption cells to achieve low detection limits. White cells<sup>2</sup> and/or Herriott cells<sup>3</sup> are most frequently used for this purpose. To achieve pathlengths greater than 100 meters, the volume of such cells are often in excess of 10 liters and sometimes as high as 28 liters. However, it is desirable in many circumstances to achieve such long optical pathlengths in much smaller sampling volumes. Such a combination allows the gas volume to be exchanged on time scales of a second or less and this in turn opens up many advantages. For example, background spectra can be acquired frequently for effective subtraction of baseline structure to improve detection limits. Sampling with low volume cells is particularly useful for studying reactive gases like HCl and HNO<sub>3</sub> which are notorious for sticking to, and outgassing from, cell surfaces. Furthermore, small volume high pathlength cells are very useful for flux studies, aircraft measurements, and measurements of ice core samples where the analyte volume is often very limited.

The system described in the present study is designed around such a sampling cell, a novel 3 liter volume 100 meter pathlength astigmatic Herriott cell from Aerodyne Research Incorporated. In the present paper, we briefly describe the optical properties of such a cell, the fore optics necessary for coupling the radiation into and out of such a cell, and the system performance. In addition, we will also discuss the use of digital signal processing electronics to replace conventional lock-in amplifiers for signal demodulation. In this approach, the sample and reference signals are digitized and demodulation is achieved by digital multiplication. This eliminates drifts in the reference amplitude, phase, and frequency which can be prevalent in analog lock-ins.

The new TDLAS system has recently been employed in the first of a number of field studies to measure background concentrations of formaldehyde (HCHO). This gas is an important intermediate in the photochemical oxidation of hydrocarbons initiated by OH. In addition to a general lack of agreement among various techniques measuring HCHO in clean background air, present measurements are generally lower than those predicted by photochemical models. This implies an incomplete understanding of the chemistry involved (i.e., extra loss mechanisms for HCHO not in present models), incorrect OH measurements, incorrect HCHO measurements and/or standards, or all of the above. Our recent HCHO measurements will be presented.

### References

1. H.I. Schiff, editor, SPIE Proceedings, **1433**, " Measurement of Atmospheric Gases", January 21 - 23, 1991, Los Angeles, CA, 374 pages.
2. J.U. White, " Long Optical Paths of Large Aperture ", J. Opt. Soc. Amer., **32**, 285 - 288, 1942.
3. D.R. Herriott, H. Kogelnik, and R. Kompfner, " Off-axis Paths in Spherical Mirror Interferometers ", Appl. Opt., **3**, 523 - 526, 1964.

## **Laser Spectroscopy for Practical Isotope Ratio Measurements**

Robert W. Shaw, C. M. Barshick, J. P. Young, and J. M. Ramsey

Analytical Chemistry Division  
Oak Ridge National Laboratory  
P. O. Box 2008, MS 6142  
Oak Ridge, TN 37831-6142  
(615/574-4920)

### **INTRODUCTION**

Isotope ratio measurements are typically accomplished by methods that are seldom amenable to field use. An example is thermal ionization mass spectrometry (TIMS)<sup>1</sup> where solid samples are dissolved, a filament loaded with the resulting solution, the filament mounted in a source chamber, the mass spectrometer pumped to low pressure, the filament heated to produce analyte ions, and finally the ions separated according to mass in either space or time for counting. There is a need for field mass spectrometric measurements, particularly in the environmental remediation arena, where near real time results can save time and reduce costs. Miniaturized ion traps that can be deployed for field measurement of organics have been reported.<sup>2</sup> There currently are no isotope ratio methods in field use.

We have explored the concept of glow discharge sampling combined with high resolution optogalvanic spectroscopy for the quantitation of individual isotopes of analyte atoms. This scheme has been considered by others, as well.<sup>3,4</sup> Within a glow discharge, bombardment of the cathode by energetic discharge ions sputters material into the vapor both as ions and neutrals. The former can be mass analyzed directly for isotope ratio determinations.<sup>5</sup> The latter can be ionized by resonant excitation followed by collisional ionization, in a process commonly known as the optogalvanic effect.<sup>6</sup> The change in the discharge voltage brought about by disruption of the ionization equilibrium as the optical source, usually a tunable laser, is scanned over the spectrum of an analyte is a sensitive indicator of absorption.

For success in the field, a method must require a minimum of sample preparation, and should at the same time, be amenable to a variety of sample types. Glow discharge sputtering meets those requirements. Obviously for an isotopically-selective technique, the laser and the sample must exhibit spectral linewidths sufficiently narrow that excitation of the desired isotopes one at a time is possible. One exciting candidate for this application that also is well-suited for portable instrumentation is the semiconductor diode laser. For off-the-shelf GaAlAs diode lasers, the output spectral linewidth is typically 25 MHz. We have previously demonstrated the utility of diode lasers for isotopically-selective resonance ionization mass spectrometry.<sup>7</sup> The spectral linewidths for atoms in electrical discharges at about 1 to 10 Torr is dominated by Doppler broadening, resulting in approximately 1 GHz fwhm features. Atomic transitions with isotopic shifts exceeding this value can be used for isotopically-selective excitation, and conventional mass spectrometers will not be required.

## RESULTS

We have examined different hollow cathode lamps (HCLs), both commercial and locally-fabricated, to determine our ability to quantitate isotopic abundances. The commercial lamp used was a uranium hollow cathode lamp (Model 3QQAY/U, Cathodeon, Ltd.) with a cylindrical cathode that is open at both ends. The cathode was fabricated from depleted uranium with a  $^{235}\text{U}$  content of 0.3%. The locally-fabricated lamp was assembled using a four-way stainless steel cross, with two opposing ports fitted with window flanges and the remaining ports adapted for a gas inlet, vacuum pumping, and electrical feedthroughs. The flowing discharge gas was argon, and the cell pressure was maintained at 1-10 Torr. Cylindrical samples were fabricated by forming metal powders or metal oxide powders (mixed with silver powder for conductivity) using a mechanical press, similar to those used for preparation of KBr pellets for infrared spectroscopy. Discharge currents were 15 mA and up to 50 mA for the commercial and local lamps, respectively. Signal detection was accomplished by monitoring the a.c. component of the cathode voltage using a lock-in amplifier.

A CW titanium:sapphire (Ti:S) ring laser was used for exploratory spectroscopy. While diode lasers are convenient to use once an operating wavelength has been established, they suffer from limited tuning and mode-hopping problems that hamper the acquisition of survey spectra. The Ti:S linewidth was approximately 2 MHz, and output powers of up to 1.5 watts were available.

We examined the uranium line at 778.42 nm using the commercial HCL. This transition corresponds to excitation from the odd parity metastable uranium level at  $620\text{ cm}^{-1}$  ( $f^3d_{5/2}^2\ ^5K_5$ ) to the  $f^3s^2p\ ^5K_5$  level at  $13463\text{ cm}^{-1}$ .<sup>8</sup> The observed linewidth was 650 MHz fwhm for an excitation power of approximately 100 mW. The reported isotope shift for this particular transition is +3 GHz (i.e.,  $^{235}\text{U}$  at longer wavelength).<sup>9</sup> Due to hyperfine splitting, the  $^{235}\text{U}$  signal is expected to comprise approximately ten lines, spanning 6 to 10 GHz.<sup>3,10</sup> The sensitivity was purposely increased to drive the line center off-scale, so as to emphasize the line wings. A spectral feature at the frequency corresponding to the center-of-gravity isotope shift for  $^{235}\text{U}$  was observed in the low energy line wing. Similar spectra that exhibit the same weak feature have been recorded using the demountable HCL and pressed cathodes formed from uranium oxide and silver powder. Results from oxide samples are significant in that most or all of the uranium sputtered from such materials could have been molecular (e.g.,  $\text{UO}$  or  $\text{UO}_2$ ) and would have been transparent to a laser tuned to a uranium atomic line. For real-world samples, the uranium content is expected to be in some oxide form.

Spectra have also been recorded for sample cylinders fabricated from dysprosium and dysprosium oxide. Natural dysprosium comprises five isotopes of significant abundance:  $m/z$  160 (2.3%), 161 (18.9%), 162 (25.5%), 163 (25.0%), and 164 (28.2%). The 0.0 to  $13496\text{ cm}^{-1}$ , 740.8 nm dysprosium optogalvanic line ( $4f^{10}6s^2\ ^5I_8$  to  $4f^95d6s^2\ ^5K_9^\circ$ ) was examined for a  $\text{Dy}_2\text{O}_3/\text{Ag}$  sample. A multiplet was observed that exhibited components at 0.0 (weak), 1.5 (strong) and 2.7 GHz (strong). These shifts are consistent with known isotope shifts for other ground state transitions<sup>11</sup> for the three even mass isotopes, and the line intensities approximate the isotopic

abundances. Lines due to the odd mass isotopes would be split into approximately ten hyperfine components, each carrying a portion of the overall line strength; thus, they would be expected to be weak. At our current spectral resolution they disappear into the signature due to the even mass lines.

## CONCLUSIONS

Preliminary spectra have been recorded for uranium and dysprosium to test the feasibility of a practical isotope ratio measurement instrument that may find use in field settings. Isotopic signatures have been observed in both cases using a demountable hollow cathode discharge cell. Insulating metal oxide samples do not seem to be a problem, if they are mixed with a conducting host. Sputtering of tenacious oxygen getters (e.g., uranium) yield a sufficient number of neutral atoms for measurement. At this level of spectral resolution and for low abundance isotopes, the most difficult challenge will be extracting the signal corresponding to the minor isotope from the wing of the signal due to the major isotope; multiple photon excitations yielding sub-Doppler resolution should be possible however, if necessary. Quantitation, accuracy, and precision studies are presently underway using both the Ti:S and diode lasers.

## ACKNOWLEDGEMENT

Research sponsored by the U. S. Department of Energy, Office of Research and Development within the Office of Intelligence and National Security, under project number ST587. ORNL is managed by Martin Marietta Energy Systems, Inc. for DOE under Contract DE-AC05-84OR21400.

## REFERENCES

1. "Isotope dilution mass spectrometry", K. G. Heumann; in Inorganic Mass Spectrometry; F. Adams, R. Gijbels, and R. Van Grieken. eds., John Wiley & Sons, New York, 1988; p 301-376.
2. M. B. Wise, C. V. Thompson, M. V. Buchanan, R. Merriweather, and M. R. Guerin; Spectroscopy **8**, 14 (1993).
3. R. A. Keller, R. Engleman, Jr., and E. F. Zalewski; J. Opt. Soc. Amer. **69**, 738 (1979).
4. R. J. Lipert, S. C. Lee, and M. C. Edelson; Appl. Spectrosc. **46**, 1307 (1992).
5. D. C. Duckworth, C. M. Barshick, D. A. Bostick, and D. H. Smith; Appl. Spectrosc. **47**, 243 (1993).
6. D. S. King, P. K. Schenck, K. C. Smyth, and J. C. Travis; Appl. Optics **16**, 2617 (1977).

7. R. W. Shaw, J. P. Young, D. H. Smith, A. S. Bonanno, and J. M. Dale; Physical Review A **41**, 2566 (1990).
8. J. Blaise and L. J. Radziemski, Jr.; J. Opt. Soc. Amer. **66**, 644 (1976).
9. R. Engleman and B. A. Palmer; J. Opt. Soc. Amer. **70**, 308 (1980).
10. Y. Demers, J. M. Gagne, C. Dreze, and P. Pianarosa; J. Opt. Soc. B **3**, 1678 (1986).
11. G. J. Zaal, W. Hogervorst, E. R. Eliel, K. A. H. van Leeuwen, and J. Blok; J. Phys. B: Atom. Molec. Phys. **13**, 2185 (1980).

## **Wavelength Modulation Atomic Absorption Spectrometry With Semiconductor Diode Lasers**

K. Niemax<sup>1,2</sup>, C. Schnürer-Patschan<sup>2</sup>, A. Zybin<sup>3</sup>, H. Groll<sup>2</sup> and Y. Kuritsyn<sup>3</sup>

<sup>1</sup>Institute of Physics, University of Hohenheim, Garbenstr. 30, D-70599 Stuttgart, Germany, Phone: +49-711-459-2150

<sup>2</sup>Institute for Spectrochemistry and Applied Spectroscopy, Bunsen-Kirchhoff-Str. 11, D-44139 Dortmund, Germany, Phone: +49-231-1392-177

<sup>3</sup>Institute of Spectroscopy, Russian Academy of Sciences, Troitzk 142092, Russia, Phone: +7-095-334-0227

Commercial semiconductor laser diodes of the AlGaAs and AlGaInP types are small, long-lived devices with excellent spectroscopic properties [1]. They are easy to operate and have low power consumption. These are the requirements for the arrangement of many independently operating laser diodes in compact instruments for simultaneous multielement analysis [2]. The main drawback of atomic diode laser spectroscopy is the limited wavelength range of commercially available laser diodes (625-950 nm). It will be extended to shorter wavelengths in the short and medium run. However, if low radiation powers can be used in experiment, it can be overcome by second harmonic generation (SHG) in non-linear crystals. Depending on the fundamental power of the laser diodes and on the efficiency of the crystal used, extracavity SHG-powers in the nW and  $\mu$ W can be generated easily in the range 315-500 nm. Such powers are sufficiently high for laser atomic absorption spectroscopy (LAAS). A list including more than 50 elements which can be measured by LAAS with fundamental and SHG radiation is given in a recent review paper [3].

The rapid wavelength tunability of diode lasers is not only important for background correction in LAAS but also for the reduction of noise by wavelength modulation techniques (WM). The application of WM-LAAS with fundamental and SHG radiation in graphite tube atomizers, analytical flames and low-pressure plasmas will be reported. First results of WM-LAAS in graphite atomizers and low-pressure plasmas have been published recently (see [4] and [5], respectively). Depending on the laser power, the measurable absorbance in WM-LAAS is of the order of  $10^{-4}$  -  $10^{-6}$ . In conventional hollow-cathode AAS the absorption of 0.1-1 % determines the detection limit of elements. Therefore, significant reductions of element detection limits in graphite atomizers and flames have been found in comparison with conventional AAS. While graphite tube atomizers and flames were used for the measurements of metals, non-metal elements, such as halogene elements or oxygen, were measured by WM-LAAS in low-pressure plasmas probing the population of long-lived, metastable states.

#### References:

- [1] J. Franzke, A. Schnell and K. Niemax, *Spectrochim. Acta Rev.* **15** (1993) in press.
- [2] H. Groll and K. Niemax, *Spectrochim. Acta* **48B** (1993) 633.
- [3] K. Niemax, C. Schnürer-Patschan and H. Groll, *Spectrochim. Acta Rev.* **15** (1993) in press.
- [4] C. Schnürer-Patschan, A. Zybin, H. Groll and K. Niemax, *J. Anal. Atom. Spectrom.* **8** (1993) in press.
- [5] A. Zybin, C. Schnürer-Patschan and K. Niemax, *Spectrochim. Acta* **49B** (1994) in press.



Wednesday, March 9, 1994

## Diode-Laser Technology and Lidar

**WC** 7:00pm–9:00pm  
Grand Room

Colin Seaton, *Presider*  
*Coherent Laser Group*

## **Advances in Tunable Semiconductor Diode Lasers**

David G. Mehuys  
SDL, Inc.  
80 Rose Orchard Way  
San Jose, CA 95134-1356

Semiconductor diode lasers are capable of generating tunable radiation with any of narrow-linewidth, high-power, or short-pulse output. Fundamental concepts, laser characteristics, and applications will be discussed.

## Raman Lidar Profiling of Atmospheric Water Vapor

J. E. M. Goldsmith and Scott E. Bisson  
Sandia National Laboratories  
Livermore, California 94551-0969  
510-294-2432 (JEMG)

Detailed measurements of the distribution of water vapor in the atmosphere are needed for a variety of scientific inquiries, including global climate change and related issues in radiative processes (water vapor is the major greenhouse gas in the atmosphere), and studies of a variety of atmospheric processes such as cloud formation and atmospheric circulation. The Raman lidar is a leading candidate for an instrument capable of the detailed, time- and space-resolved measurements required by these and other studies.

Raman lidar operates by sending out a laser pulse and recording the atmospherically backscattered return signal as a function of time to provide range information. The return signal consists of an elastically scattered part which is useful for profiling cloud heights, aerosols, and the planetary boundary layer, and inelastically scattered parts that provide chemically specific profiles such as water vapor. The inelastic scattering utilized here is the result of the rotational-vibrational Raman effect that shifts the incident wavelength by a frequency characteristic of the molecule ( $3652\text{ cm}^{-1}$  for water vapor and  $2331\text{ cm}^{-1}$  for molecular nitrogen). Simultaneous measurement and subsequent ratioing of the water vapor and nitrogen Raman signals provides a quantitative measurement of the water vapor mixing ratio (grams of water vapor per kilogram of dry air).<sup>1,2</sup> The capabilities of Raman lidar systems have steadily improved by taking advantage of technological advances, in laser systems in particular.<sup>3-5</sup>

While Raman lidar is used currently to perform meteorologically important, sustained, reliable nighttime profiling of water vapor, daytime measurements present added challenges because of the difficulties inherent in detecting Raman signals against solar backgrounds. In our studies<sup>6</sup> of two approaches for obtaining enhanced daytime operation, namely solar-blind operation and narrowband, narrow-field-of-view operation, computer models indicated that comparable daytime performance can be anticipated using the two approaches. Because the latter approach does not degrade the nighttime performance of the lidar system, we have chosen to base our system design on a narrowband, narrow-field-of-view channel. In order to provide both improved short-range measurements and extended dynamic range, the system also incorporates a channel with a wider field of view, and hence its description as a dual-field-of-view system.

The Sandia lidar system is housed in two mobile semitrailers, one trailer serving as a mobile laboratory and the other as a support vehicle providing a data acquisition/analysis area. The lidar uses an injection-seeded excimer laser to provide a beam with reduced divergence and spectral bandwidth, operated at 308 nm during both nighttime and daytime. Enhanced dynamic range, for daytime operation in particular, is provided by using photon counting in the narrow field-of-view channel, and analog to digital conversion in the wide field-of-view channel. The characteristics of the systems are summarized in Table 1.

Table 1. Lidar characteristics

Subsystem	Characteristic	Sandia Raman Lidar
Transmitter	Laser	XeCl Excimer
	Wavelength	308 nm (XeCl)
	Energy/pulse	90 mJ
	Repetition rate	200 Hz
	Bandwidth	3 pm
	Divergence	0.4 mr
Receiver	Configuration	Dall-Kirkham
	Diameter	0.76 m
	f number	4.5
	Channel bandpass	0.4 nm
	Filter transmission	30-35%
	Field of view	Dual, adjustable (typically 0.4 mr, 4 mr)
	Ranges	2 (narrow, wide fov)
	Channels	3
	Species	Rayleigh/aerosol (308 nm) Water vapor (347 nm) Nitrogen (332 nm)
Electronics	Short range	Analog to Digital Conv.
	Long range	Photon counting
	Range resolution	75 m (0.5 $\mu$ sec)

An example of the nighttime performance of this system is presented in Fig. 1. The logarithmic scaling of the horizontal axis was chosen to enable a reasonable display of the statistical uncertainty of the lidar measurement as represented by the error bars. The uncertainty is calculated assuming a Poisson distribution in the photon counts measured by the lidar system. The overall level of agreement between the lidar and radiosonde profiles is fairly typical, and is influenced by the fact that balloon-borne packages follow local winds as they ascend, and thus the laser beam and the radiosonde do not necessarily sample the same portion of the atmosphere.

To date, significant daytime measurements with this system have been limited to ranges of 3-4 km,<sup>7</sup> limited primarily by the relatively large divergence of the excimer laser system. We are currently adding a beam-expanding telescope to the lidar transmitter to reduce the divergence of the laser beam to enhance the daytime capabilities of the system, and also incorporating a separate excimer laser to act as an amplifier to approximately double the available laser energy to enhance both daytime and nighttime operation. Measurements performed using the enhanced Raman lidar system will be presented at the meeting.

This work was supported by the U. S. Department of Energy Atmospheric Radiation Measurement (ARM) Program.

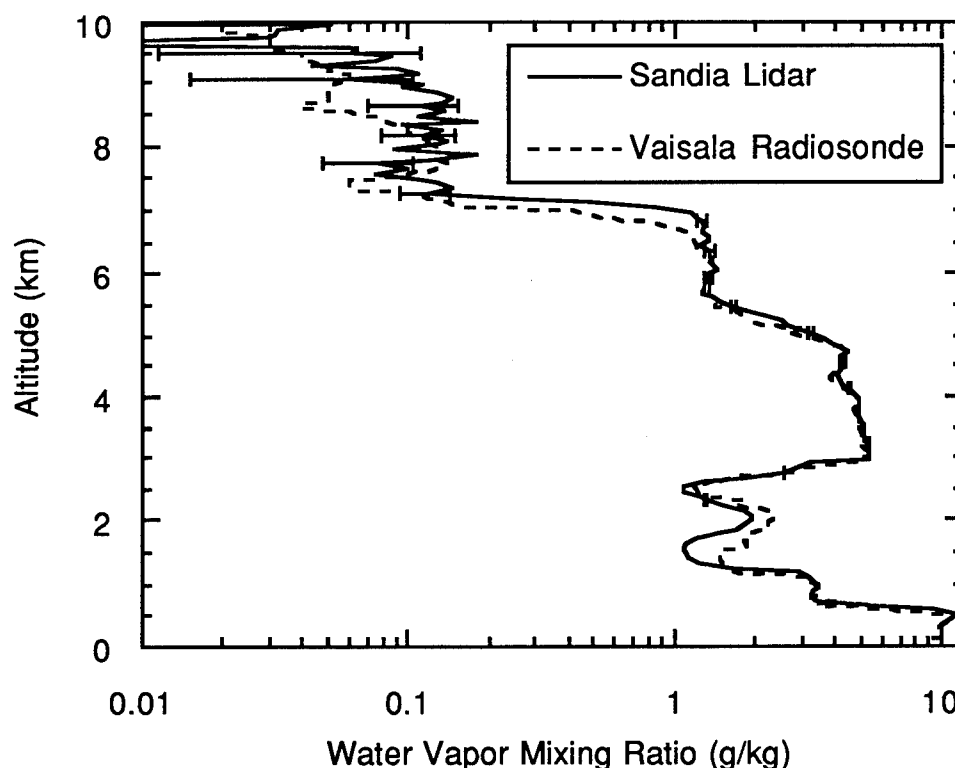


Figure 1. Vertical profiles of atmospheric water vapor measured in Livermore, California at 11:05 pm (local time) on August 4, 1993. The lidar profile represents a ten-minute average started at the time that the radiosonde was launched. The error bars represent statistical uncertainties for the lidar measurement.

#### References

1. S. H. Melfi, J. D. Lawrence, Jr., and M. P. McCormick, "Observation of Raman scattering by water vapor in the atmosphere.," *Appl. Phys. Lett.* **15**, 295-297 (1969).
2. J. Cooney, "Remote measurements of atmospheric water vapor profiles using the Raman component of laser backscatter," *J. Appl. Meteor.* **9**, 182-184 (1970).
3. S. H. Melfi and D. N. Whiteman, "Observation of lower-atmospheric moisture structure and its evolution using a Raman lidar," *Bull. Amer. Meteor. Soc.* **66**, 1288-1292 (1985).
4. S. H. Melfi, D. Whiteman, and R. Ferrare, "Observation of atmospheric fronts using Raman lidar moisture measurements," *J. Appl. Meteor.* **28**, 789-806 (1989).
5. A. Ansmann, M. Reibesell, U. Wandinger, E. Voss, W. Lahmann, and W. Michaelis, "Combined Raman elastic-backscatter lidar for vertical profiling of moisture, aerosol extinction, backscatter, and lidar ratio," *Appl. Phys. B* **55**, 18-28 (1992).
6. J. E. M. Goldsmith and Richard A. Ferrare, "Performance Modeling of Daytime Raman Lidar Systems for Profiling Atmospheric Water Vapor," *16<sup>th</sup> International Laser Radar Conference* (NASA Conference Publication 3158, Part 2, 1992), pp. 667-670.
7. Scott E. Bisson and J. E. M. Goldsmith, "Daytime Tropospheric Water Vapor Profile Measurements with a Raman Lidar," in *Optical Remote Sensing of the Atmosphere Technical Digest, 1993* (Optical Society of America, Washington, D.C., 1993), Vol. 5, pp. 19-22.

## Differential Absorption Lidar Measurements of Tropospheric Ozone

Andrew O. Langford, NOAA Aeronomy Laboratory, R/E/AL6, 325 S. Broadway, Boulder, CO 80303. (303) 497-3115.

Michael H. Proffitt, CIRES, NOAA Aeronomy Laboratory, R/E/AL6, 325 S. Broadway, Boulder, CO 80303, and University of Colorado, Boulder, CO 80309. (303) 497-3435.

Ozone is one of the most important trace species in the atmosphere and the focus of several important environmental issues. Most ozone resides in the stratosphere where it plays a critical role in protecting the biosphere from harmful solar ultraviolet radiation. A variety of observations indicate that ozone in this region is decreasing due to heterogeneous processes involving anthropogenic chlorine. In contrast, ozone is increasing at the surface due to photochemical reactions between man-made nitrogen oxides and hydrocarbons. This elevated ozone adversely affects human health and vegetation and can be transported across regional and international boundaries. Finally, ozone is the only radiatively important trace gas that absorbs both incoming ultraviolet radiation and outgoing infrared radiation. The net effect of atmospheric ozone changes on the surface radiation budget will depend on where the vertical profile changes, particularly in the upper troposphere and lower stratosphere.

Our current knowledge of tropospheric ozone comes primarily from balloon-borne ozonesondes and aircraft measurements. These instruments are invaluable for studying long term trends and specific events, but are impractical for routine observations of the vertical profile on timescales of minutes to hours. This information can, in principle, be provided by Differential Absorption Lidar (DIAL), a powerful remote sensing technique widely used to probe the spatial and temporal distribution of gaseous atmospheric constituents. Several groups are using ground or aircraft based UV DIAL to determine concentrations of ozone in the boundary layer, free troposphere, and stratosphere. While the basic principles are independent of the altitude regime, the choice of laser wavelengths and other operational characteristics must be tailored to the intended altitude range.

DIAL uses two coincident laser beams tuned to wavelengths that are absorbed to different degrees by the molecule of interest. The backscattered radiation is collected by a telescope, spectrally resolved,

and imaged onto a photomultiplier tube or other detector coupled with photon counting or fast digitization techniques. Two wavelengths are required since the laser beam is also attenuated through Rayleigh scattering by  $N_2$  and  $O_2$ , Mie scattering by particles, and possibly absorption by  $SO_2$  or other species. Ideally, the wavelengths are selected to provide a large differential absorption cross-section for the target molecule with negligible differences in the cross-sections for absorption and scattering by other atmospheric constituents. Most ozone DIAL systems operate in the Hartley band between 200 and 310 nm (UV measurements are generally preferred over IR since a strong Rayleigh backscatter return is desirable for DIAL). These systems are usually based on frequency doubled YAG-pumped dye lasers or excimer lasers coupled with one or more Raman shifters. The latter approach has the advantage of requiring only one laser (desirable for an aircraft or field package), but limits the available wavelengths.

In this paper we will focus on the NOAA Aeronomy Laboratory's Differential Absorption Lidar (DIAL) system located at Fritz Peak Observatory in the Colorado Mountains. This system is now capable of profiling ozone from 4 to 14 km above sea level in a one-minute time interval day or night. The Fritz Peak DIAL system uses two frequency doubled YAG-pumped dye lasers for maximum versatility. This makes it possible to reduce the wavelength separation to only 3 nm (288-291 nm) or as far as statistical limitations will allow. These wavelengths are long enough to allow measurements to  $\geq 14$  km, but short enough to permit a large reduction in the sky background. The large dynamic range ( $\geq 10^6$ ) in the return signal is accommodated through the use of two parallel detection channels that cover different altitude ranges, signal-induced bias corrections to the photomultiplier signals, and large scale dithering techniques to reduce digitizer nonlinearities.





Wednesday, March 9, 1994

## Poster Session 2

**WD** 8:50pm–10:30pm  
Teton Room

A Dual Fabry-Perot Optical Fiber Sensor<sup>①</sup>

Qi Wang

Huazhong University of Science and Technology  
 Department of Physics  
 Wuhan, Hubei, 430074, China

1. INTRODUCTION

Interferometric fiber—optic sensors, while capable of high resolution, have in general been accompanied by a limited unambiguous operating range. They also have had limited applicability for measurement temperature, strain and displacement. Owing to the problem of initiating the system, i. e. the interferometer switch off, all the information about the measured phase will be lost and new initial conditions must be determined when system is turn on again<sup>(1)</sup>. A. S. Gerges had presented a system which is a Michelson interferometer with two equal length arms. A digital feedback servo is used to track the zero optical path difference<sup>(2)</sup>. However, the optical fiber in Gerges's system are inherently distributed sensors. This can be a disadvantage when point measurement are required. G. Beheim had presented another system in which a Fabry-Perot cavity is used as a sensing cavity<sup>(3)</sup>, a Michelson interferometer is used to measure the spacing of the sensing cavity. Let us call it FPM system. The central peak of the interferometric fringe in FPM system is nearly as higher as other peaks. This makes the system very difficult to lock in the central peak. Also, the central peak's half-width of the FPM system is comparatively larger than that of dual F-P system (DFP). This limits the resolution of FPM system. G. Beheim has also presented a dual F-P cavities system. But its electronics can not make sure that the system is locked in the central peak of the transmitted optical signal<sup>(4)</sup>.

In this paper, a dual F-P system in which an equal optical gap of the two cavities are kept by electrical feedback servo is built. The system includes a control electronics to search central interferometric peak when electrical power switch on. The system is capable of measuring the state of remotely set F-P cavity which can be connected to the receiver via multimode optical fibers. The essence of the technique is that a short coherence length source (white light source) is used in the system. When the system locked in the central peak of the transmitted optical power, we can measure the remotely located sensing cavity's spacing by measuring the reference cavity's spacing which is in the benign environment.

2. ANALYSIS OF DUAL F-P CAVITIES INTERFEROMETER (DFP)  
AND F-P MICHELSON INTERFEROMETER (FPM) .

Firstly, we consider the salient feature of an interferometer which consists of a series arrangement of two F-P cavities (DFP) (see Fig. 1 (A)). Spectrally broad band light is first transmitted through a sensing cavity (with a mirror separation of  $L_s$ ) and then transmitted through a reference cavity (with a mirror separation of  $L_r$ ). For this analysis, all four mirrors are assumed to be identical with a reflectivity of  $R$  and a transmissivity of  $1-R$ . Both  $L_s$  and  $L_r$  are much greater than  $L_0/2$ , where  $L_0$  is the source's coherence length, therefore, in general, the output of the dual F-P cavities interferom-

① The project supported by National Natural Science Foundation of China

eter will independent of either  $L_s$  or  $L_r$ . An exception occurs in the case of interest here, where  $L_s \approx L_r$ . In this case the interferometer's output varies with  $e$ , where  $e = L_s - L_r$ . From Ref. 6, if the source has spectral intensity distribution  $i(k)$ , then for  $L_s \approx L_r$ , the interferometer output intensity  $I(e)$  is given by<sup>(4)</sup>

$$I(e) = A \int \frac{i(k)}{1 + B \sin^2(ke)} dk \quad (1)$$

$$A = \frac{(1-R)(1+R^2)}{(1+R)^3} \quad (2)$$

$$B = \frac{4R^2}{(1-R^2)^2} \quad (3)$$

Secondly, in the FPM system, A broadband light is first reflected from a Fabry-Perot interferometer and transmitted through a Michelson interferometer (see Fig. 1 (B)). The source has spectral intensity distribution  $i(k)$ , where  $k$  is the wave number. the output of the FPM system  $I'(e)$  is given by G. Beheim<sup>(3)</sup>.

$$I'(e) = A_0 - A_1 V(L_s - L_r) \cos(2K_0(L_s - L_r) - \varphi), \quad (4)$$

where,

$$A_0 = \frac{1}{4} \frac{R}{1+R} \quad A_1 = \frac{1}{8} R \frac{1-R}{1+R} \quad (5)$$

$$V(L_s - L_r) = \text{EXP}(-(\sigma(L_s - L_r))^2) \quad (6)$$

$L_s$ ,  $L_r$  are optical length of the F-P cavity and path difference of Michelson cavity respectively,  $R$  is the reflectivity of the F-P cavity's mirrors,  $k_0$  is the average wave number of the source's spectrum.  $d$  is the half band width of FPM system;

$$d = \frac{\lambda_0}{2} \quad (7)$$

Form Eq. 1, we obtain the half-width of central peak in the DFP system<sup>(4)</sup>:

$$d' = \frac{1-R^2}{\pi R} \frac{\lambda_0}{2} \quad (8)$$

From Eq. 8, we know that the half-width of central peak in the DFP system varies with reflectance  $R$ , while FPM system's half-width of the central peak is always  $\lambda_0/2$  regardless the amount of mirrors reflectivity. Here,  $\lambda_0$  is the central wave length of the light source. If we choose a high reflectance  $R$  in DFP system, then  $\frac{(1-R^2)}{\pi R} \ll 1$ , and  $d' \ll d$ , we can obtain a comparatively narrow half-width of the central peak. So DFP system is possible to get a high resolution.

### 3. EXPERIMENTAL PROCEDURE AND RESULTS

The experimental setup is shown in Fig. 3. A 30W white lamp is as the source. The step index fiber is used, which has the core diameter 50- $\mu\text{m}$ . GRIN lenses were used at every fiber end in order to collimate the optical output and to provide high coupling efficiently between fiber ends. The gap of the cavity is about 15 $\mu\text{m}$ . One mirror of the sensing cavity is mounted on a PZT translator which is used to simulate a slowly varying sensor signal. The fiber used to collect the optical output from the sensing cavity is similar to that which was used to guide the optical power into the sensing cavity. The output of the collecting fiber is guided into the reference cavity (F-PR), and then is detected by a photodetector. One of the mirrors of the reference cavity is driven by a 2 $\mu\text{m}$  range PZT tube. The other mirror can be moved by a

mechanical micrometer. The spacing of the reference cavity is adjusted to about 15 $\mu$ m by the micrometer. All mirrors used in either sensing cavity or reference cavity are coated with aluminum. The reflectance of the mirrors is about 0.9. A servoloop is used to control the spacing of the reference cavity. It causes the spacing of the reference cavity to lock in the spacing of the sensing cavity while scanning the spacing of the reference cavity. To prevent servoloop control in one of the subsidiary peaks (Fig. 2) a secondary loop associated with them. Whenever the transmitted optical power exceeds a preset threshold value, say 2/3 of the central transmitted optical power peak (2/3 of the central peak value is higher than the subsidiary peak value in my experiment), the secondary loop sets the initial condition required to allow the primary loop to gain control. The reference cavity's mirror which is mounted on a PZT tube to provide both high frequency modulation of the reference cavity's spacing and tuning of its average value. This PZT translator has a displacement range of 2 $\mu$ m. The reference cavity's spacing is modulated with a constant amplitude at 1KHz. The amplitude of the electrical signal is about 5V. The output of the photodetector is amplified and synchronously demodulated at 1KHz in a lock-in amplifier. The output of the lock-in amplifier varies as a function of the spacing difference between the reference cavity and the sensing cavity as shown in Fig. 4. For a small differences in cavity length, the output signal is<sup>(4)</sup>:

$$E = -K f(R, K_0) \frac{e}{(1 + B(k_0)^2)^2} \quad (9)$$

where

$$K = CAe k_0^2 \quad (10)$$

$$f(R) = 2AB = \frac{8R^2(1 + R^2)}{(1 - R)(1 + R)^5} \quad (11)$$

The constant K is dependent on the incident optical power C, the magnitude of the spacing modulation applied to the reference cavity  $\Delta e$ , and the average wave number of the broadband source  $k_0$ .  $f(R)$  is dependent on the mirror reflectance R.  $e$  is the difference between the reference cavity spacing and the sensing cavity spacing. The curve that the Eq. 9 given is very similar to what have been shown in Fig. 4, which is obtained by the experiment. When  $e \ll \frac{\lambda_0}{2\pi\sqrt{B}}$  (in the case of here when  $e < 20\text{nm}$ ), we can obtain:

$$E = -kf(R)e. \quad (12)$$

The output signal E is used as an error signal for the servo control circuit. The servo control adjusts the reference cavity's spacing to become equal to the sensing cavity's spacing when the spacing difference  $L_s - L_r$  are dropped in range between  $-20\text{nm}$  and  $20\text{nm}$  (see Fig. 4). Once the primary loop controls the reference cavity's spacing on the sensing cavity's spacing, the ramp signal generator is disconnected from the loop by the switch. At this time, the DC output of the HV amplifier is a measurement value of reference cavity's spacing, i. e., the same as the sensing cavity's spacing. The spacing of the reference cavity can be measured by some other method, for example, as described in Ref. 7.

The sensitivity of the PZT translator which is used to drive the sensing cavity is equal to the one used in reference cavity. Once the reference cavity's spacing be locked in one of the sensing cavity's spacing, the measurement of the reference cavity's spacing will give the sensing cavity's spacing. This measurement is performed by measuring the output voltage of the amplifier. When the driving voltage of PZT translator in the sensing cavity is changed, the servoloop will slave the reference cavity's spacing to follow the change of the sensing cavity's spacing. The Variation of HV amplifier output voltage is a function of variation of the driving voltage of the sensing cavity. Fig. 5 shows the variation of HV amplifier output against the variation of the driving voltage of the sensing cavity when the primary loop locks in the central peak of the transmitted optical power.

#### 4. DISCUSSION AND CONCLUSION

The model proposed in this paper to realize remote optical fiber sensing involves a white light source and multimode fibers. This means that we can couple much higher optical energy into sensing system. Also, the sensitivity of the sensing cavity is very high. The half-width of the central peak can reach the order of 0.01 $\mu$ m. If the sensing F-P interferometer is replaced by a piece of plane parallel transparent plate, with surfaces of high reflectivity coating, the system can be

designed to measure the spacing change between two parallel surfaces, which may be caused by temperature change, strain, humidity, etc, and, because the sensor is passive, they can be used in high-temperature areas or other electrically hostile environment. This instrument also has the advantage of providing high immunity to the effects of wavelength-dependent variations in the fiber-link's transmissivity. Immunity to the effects of temperature-induced variations in the optical source's spectrum is another important advantage of this instrument.

There are some different methods to measure the spacing of reference cavity. One of the methods is the use of a capacitor sensor in which the measurement accuracy can reach the order of  $0.01\mu\text{m}^{(7)}$ . The accuracy of the method used in this paper depends largely on the linearity of the PZT element.

## 5. REFERENCES

1. D. A. Jackson, and J. D. C. Jones, "Fiber Optic Sensor". *Opt. Acta*, Vol, 33, 1469—1503 (1986) .
2. A. S. Gerges "Interferometric Fiber-optic Sensor Using a Short-coherence-length Source" *Electron. Lett.* Vol. 21. 1110—1111 (1987) .
3. G. Beheim "Remote Displacement Measurement Using a Passive Interferometer With a Fiber-Optic Link " *Appl. Opt.* , Vol. 24, pp 2335—2340, (1985) .
4. Q. Wang "An Optical Fiber Multiplexing System Using Fabry-Perot Cavities " *Rev. Sci. Instrum* Vol. 64, No. 1, P82—86 (1993) .
5. G. Beheim, K. Fritsch, and R. N. Poorman, "Fiber-linked Interferometric Pressure Sensor", *Rev. Sci. Instrum.* Vol. 58, P1655—1659 (1987) .
6. M. Born and E. Wolf. *Principles of Optics*, 6th ed. (Pergamon, New York, 1980), Chap. 7. p. 360.
7. K. Fritsch, *Rev. Sci. Instrum.* Vol. 58, 861 (1987) .

Fig. 1 (A) The Dual Fabry-Perot cavities arrangement.

Fig. 1 (B) The Fabry-Perot cavity and Michelson interferometer arrangement.

Fig. 2. Transmittance of the two F-P cavities as a function of their spacing difference. The spacing of both cavities are about  $15\mu\text{m}$ . All mirror reflectances are about 0.9.

Fig. 3. The experimental setup of the remote sensing system using dual Fabry-Perot cavities.

Fig. 4. The demodulated signal as a function of the spacing difference between the reference cavity and the sensing cavity.

Fig. 5. Variation of the HV amplifier output of the servoloop vs variation of the driving voltage of the sensing cavity.

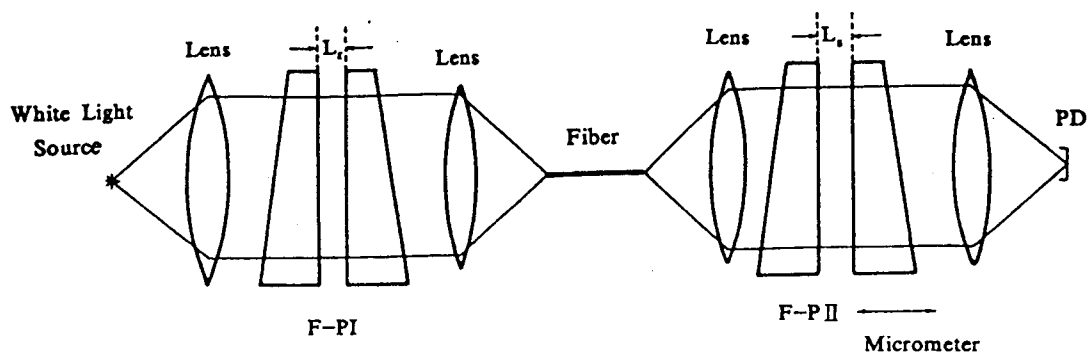


Fig. 1 (A) The Dual Fabry-Perot cavities arrangement.

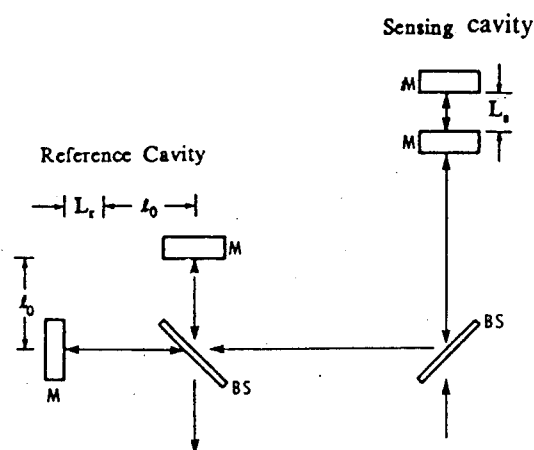
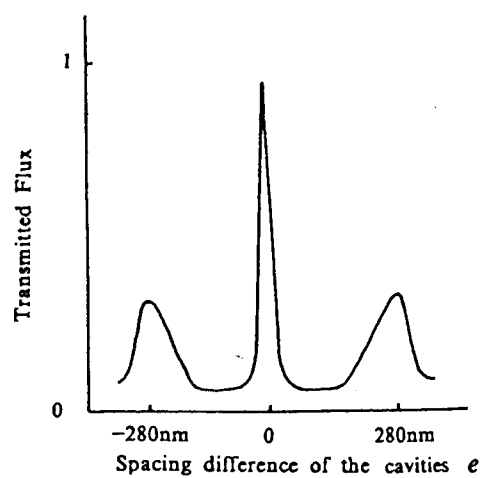


Fig. 1 (B) The Fabry-Perot cavity and Michelson interferometer arrangement.

Fig. 2. Transmittance of the two F-P cavities as a function of their spacing difference. The spacing of both cavities are about  $15\mu\text{m}$ . All mirror reflectances are about 0.9.

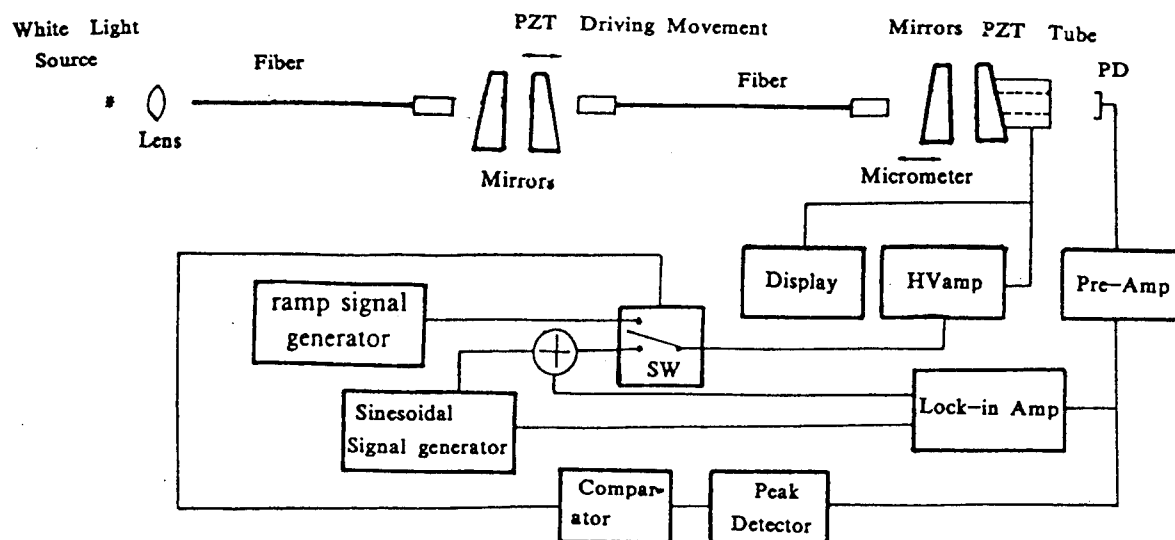


Fig. 3. The experimental setup of the remote sensing system using dual Fabry-Perot cavities.

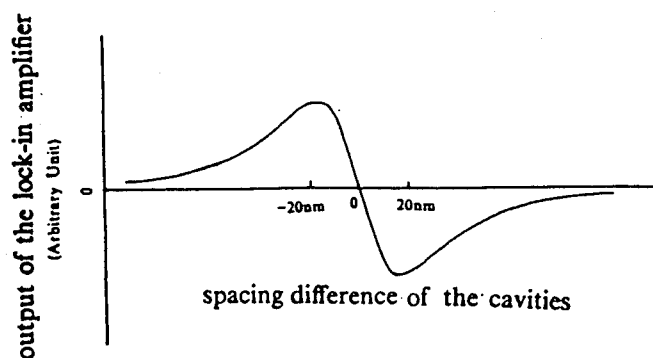


Fig. 4. The demodulated signal as a function of the spacing difference between the reference cavity and the sensing cavity.

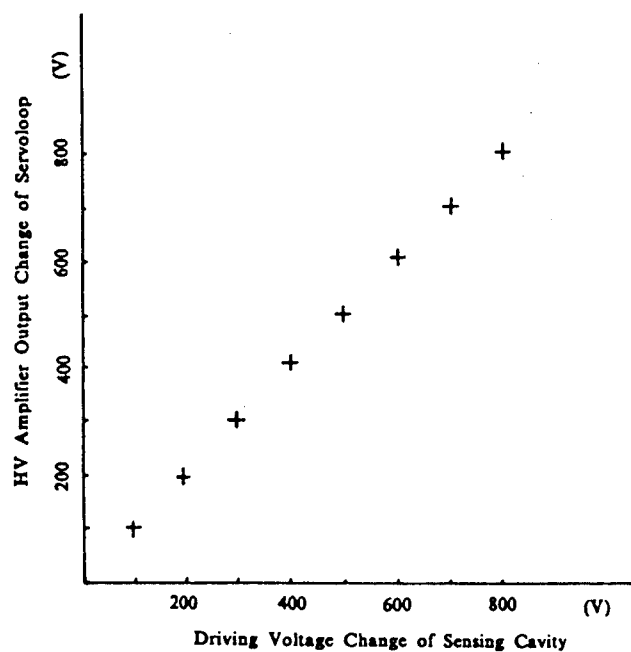


Fig. 5. Variation of the HV amplifier output of the servoloop vs variation of the driving voltage of the sensing cavity.

Fiber-Optic Sensor based on Porous Polymer doped by Dye:  
Detecting Ammonia in Liquid Media.

D.B.Bondarenko, S.M.Dolotov, M.F.Koldunov, E.P.Ponomarenko  
N.M.Sitnikov, A.V.Startsev, T.V.Tulaikova.

Fiber-optic sensors have many attractive features i.e.

- (1) They are not subject to electrical interference.
- (2) They can be used in the active and explosive media.
- (3) Unlike electro-chemical sensors, they have not any reference electrodes.

Besides a fiber-optic sensor may be designed reliable and inexpensive and miniaturized. Therefore the development of fiber-optic sensors is currently an active area of research (See, for example, in Ref.[1-5]).

There are several different types of fiber-optic sensors. Herein a chemical sensor inserted in fiber line is described. It is able to detect ammonia in gases and liquids, is very sensitive and reversible. It should be emphasized that in contrast to other sensors detecting hereafter detects ammonia it is possible to modify the chemical composition of the sensor for detecting other toxic gases or metal ions.

The sensors are made of porous polymer fiber activated by bromocresol purple dye. They are 1 mm in diameter and 0.5-5 cm in length and are inserted in a fiber line by plastic plugs. The monomer composition used to manufacture the porous polymer includes methylmetacrilat and triethyln glykoldimethakrilat. These materials were chosen owing to the fact that co-polymer made of them has a good optical and mechanical properties and is hydrophobic. The octane used as inert solvent is added to monomer mixture to form the porous structure. There are several dyes that may be used to detect ammonia. We used the bromocresol purple because of its spectral characteristics: its absorption increases at  $\lambda=632$  nm when acted upon by ammonia. This fact allows a to be



used.

The composition was polymerized in glass capillary and then the porous fiber sample was taken out of it. The sample was washed with acetone to remove the inert solvent and dye unbonded with polymer structure. The characteristics of sensor were stable and reproducible as a result of this treatment.

The fiber has a good optical quality. This is due to a small pore dimension with respect to operation wavelength. The study of the sensor sample by electron microscope gives a dimension of pores of about 0.05-0.1  $\mu\text{m}$ , hence the pores are much smaller as compared to the wavelength of He-Ne laser light.

The principle of the chemical sensor operation is based on the variation of light absorption (or transmission) in a fiber line when dye-ammonia complexes originated as a result of chemical reaction



where K is dye, A is ammonia, KA is their complex and  $\beta$  is an equilibrium constant. For the sensor to be reversible the chemical reaction must be reversible as well. In this case the complex concentration may be written as follows

$$[KA] = \frac{\beta[A]}{1+\beta[A]} C \quad (2)$$

where C is the sum of free and combined dye molecules, [K] and [A] and [KA] are concentrations of dye and ammonia and dye-ammonia complex, respectively.

The absorption (or transmission) level of a sensor in fiber line may be found from Lambert-Beer's law

$$I = I_0 \exp(-\alpha - [KA]\epsilon L) \quad (3)$$

where  $\alpha$  is absorption of a porous polymer fiber without dye, L is sensor length,  $\epsilon$  is molecular extinction of dye-ammonia complex, I and  $I_0$  are transmitted and incident light intensities.

The Eq. 3 shows that it is more convenient to deal with optical density since its value is directly related to ammonia concentration

$$D = \ln \left[ \frac{I_0}{I} \exp(\alpha) \right] = \frac{\beta[A]}{1 + \beta[A]} \times C \epsilon L \quad (4)$$

The  $\exp(\alpha)$  associated with initial absorption may be omitted by procedure of calibration.

In accordance with (4), the  $\beta^{-1}$  defines the range of ammonia concentration that can be measured and if  $[A] \ll \beta^{-1}$  then  $D$  is proportional to  $[A]$ .

The sensor inserted in an optical fiber line was placed in a chamber at designed concentration of ammonia or in a vessel containing ammonium solution in distillate water. The radiation of He-Ne laser was introduced into a fiber and after propagation through the fiber it was received by photo detector. The signal of photo detector was measured by a digital voltmeter or fed in logarithmic amplifier to measure directly the level of the optical density defined by relationship (4).

Application of hydrophobic co-polymer yields one important property of the sensor. It can operate in liquids and humid media because water does not penetrate into polymer pores. It is easy to check. This experimentally: the transmission of the fiber line does not change when the sensor has been dipped in water. So the absorption level of light in a sensor does not depend on humidity. In addition the sensor does not exhibit variation of absorption if water pH changes. It has been established experimentally that the absorption level does not change when either alkali or acid are added to water.

Response curves of the sensor placed in ammonia solution in distillate water at 22°C are depicted in Fig.1. The transmission level is normalized to its maximum value which takes place when the ammonia concentration is equal to zero. The transmission decreasing is observed during 5-10 minutes, then quasi-equilibrium state is achieved and the transmission becomes constant. The level of equilibrium transmission for different sensor samples different by about 15% or less. The temporal dependence of the sensor transmission for different samples was reproducible as well. So in accordance with experimental data represented in Fig.1 the sensor is reversible with recovery time of about 30-40 minutes. It should be noted that the recovery

process may be repeated many times without any change of the sensor characteristics.

The recovery time may be decreased to 10-30 second, if a sensor is placed in hot water at the temperature of 90-100°C. This means that the velocity of kinetic processes grows with the temperature increase. The response curves for a sensor in ammonia solution at different temperatures are depicted in Fig.2. In accordance with Fig.2, temperature increase by 20°C leads to a two-fold increase of the kinetic processes.

At last in Fig.3 the transmission of a sensor versus ammonia concentration in equilibrium state is depicted. This result is in a good agreement with relationship (4) and hence the sensor operation obeys the theory outlined above.

In accordance with Fig.1, the transmission of a sensor decreases by 1/e in 1-2 minutes. The sensitivity, S, i.e. transmission variation with respect to variation of gas concentration in equilibrium state is  $10^{-2}$  litre per milligram. Supposing dye-ammonia complexes are formed on a pore surface and using the small ammonia concentration approach one may write

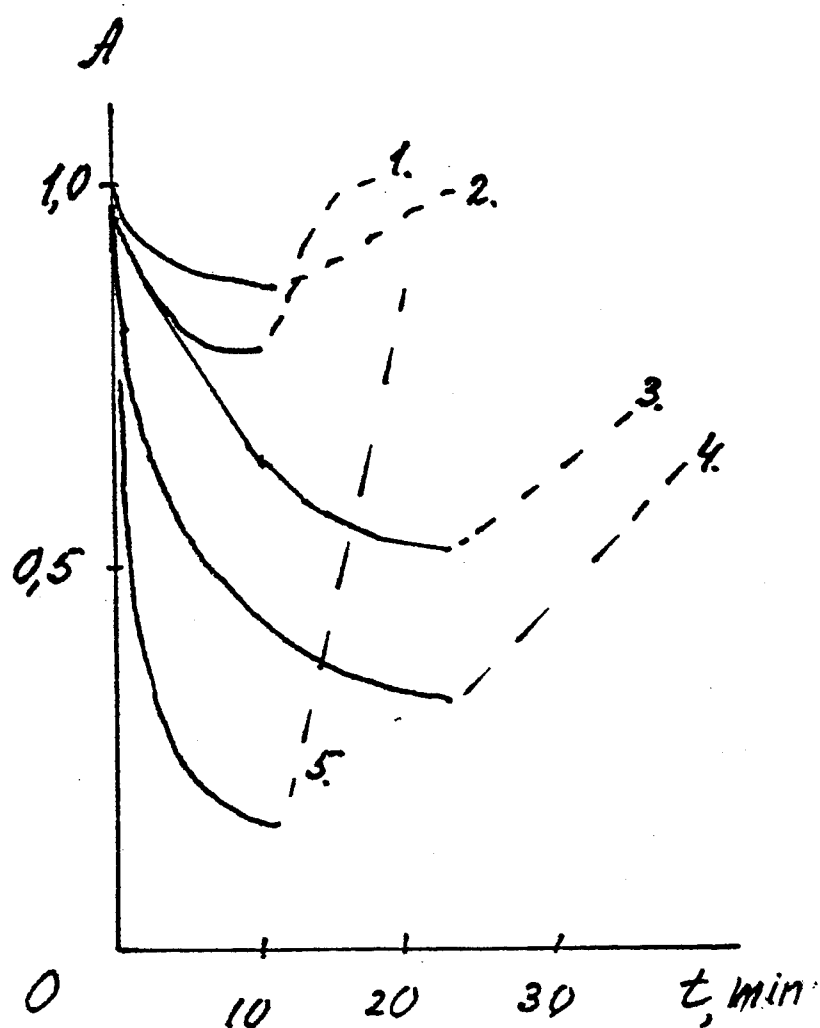
$$S = \beta L \mu / R \quad (5)$$

where  $\mu$  is porosity i.e. pores volume divided by whole volume of sample and R is pore size. Thus the sensor sensitivity increases when its length and its porosity are increased. The lowest ammonia concentration measured herein was 0,004% with a 5 cm long sensor. In this case transmission decreased by 5%.

In summary, the chemical sensor described in this paper is reliable and inexpensive and miniaturized. It has a good sensitivity and its operating time is rather small. The sensitivity of a sensor may be increased with its porosity increasing. The sensor is reversible and may be used both in gases and liquids. pH of medium has no effect on its operation.

### References

1. M.R.Shahriari,Q.Zhou,G.H.Sigel. Optics Letters, 1988 Vol.13, No 5, p. 407-409.
2. Q.Zhou, D.Kritz, L.Bonnell, G.H.Sigel. Applied Optics, 1989, Vol.28, No. 11, p. 2022-2027.
3. J.F.Guliani, H.Wohltjen, N.L.Jarvis. Optics Letters, 1983, Vol. 8, No 1, p. 54-56.
4. W.Rudolf Seitz. Analytical Chemistry, 1984,Vol. 56, No 1, p. 16-34(A)
5. L.L.Blyler, R.A.Liberman, L.G.Cohen, J.A.Ferrara, J.B.Macchesney. Polimer engineering and science, 1989, Vol. 29, No 17, p. 1215-1218.



1.  $C = 40 \text{ mg/l}$
2.  $C = 50 \text{ mg/l}$
3.  $C = 100 \text{ mg/l}$
4.  $C = 150 \text{ mg/l}$
5.  $C = 200 \text{ mg/l}$

Fig. 1. Intensity of the light transmittion (  $A$  ) normalized at its maximum value versus time (  $t$  ) at different concentration (  $C$  ).

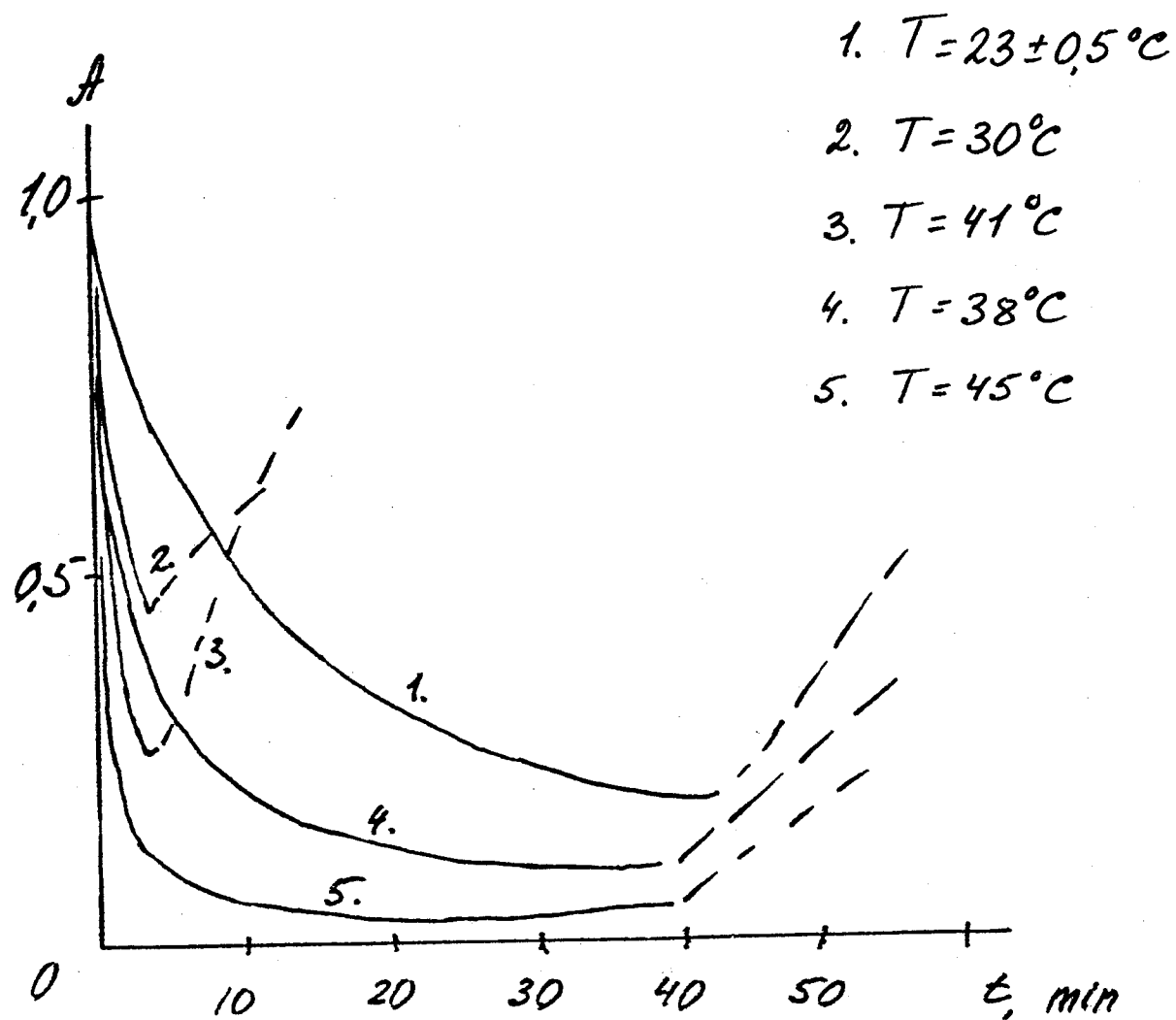


Fig. 2. Time respons sensors curves versus in ammonia solution at different temperature (  $T$  ).

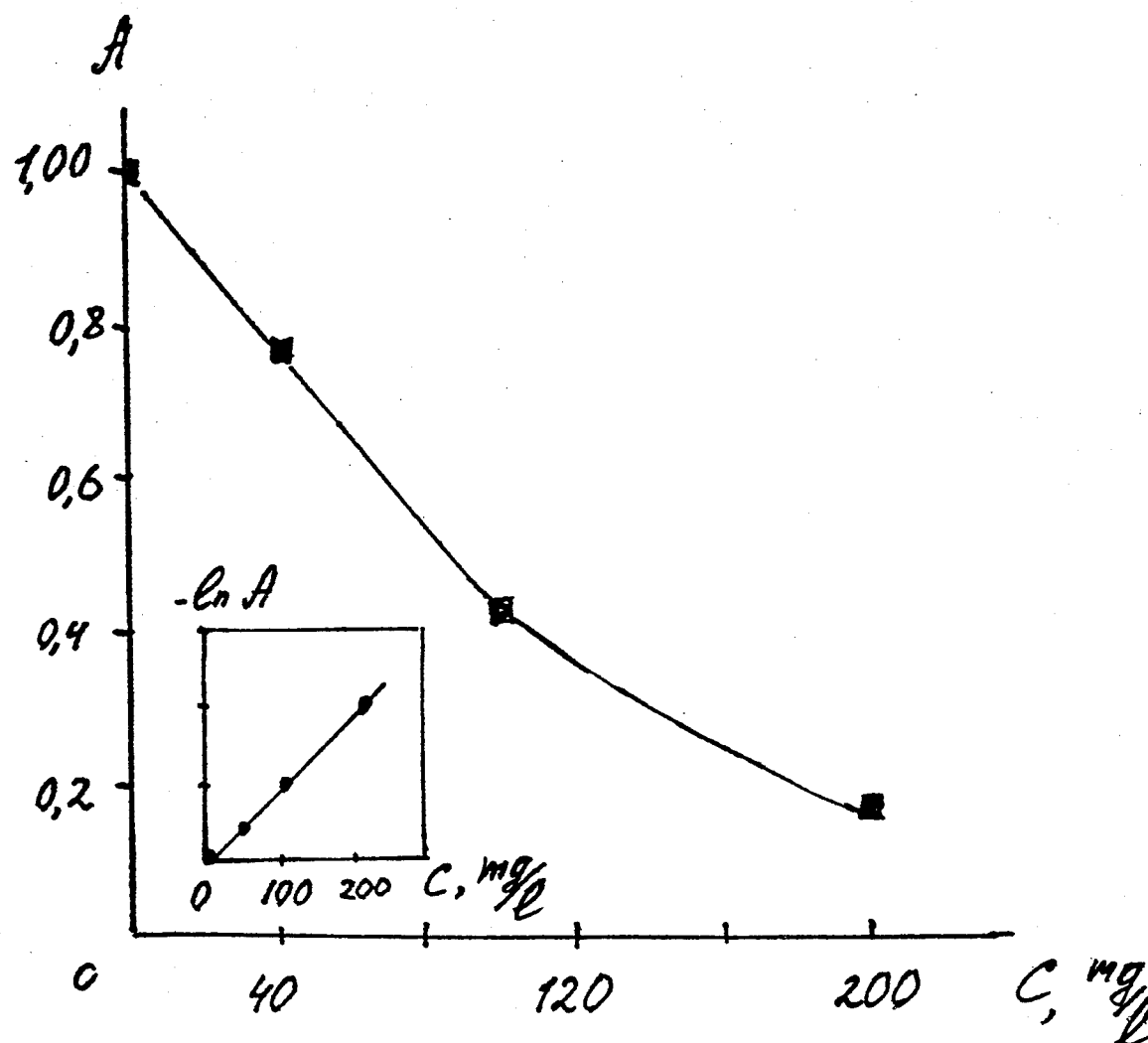


Fig. 3. Light intensity in sensor element depend on ammonia concentration.

# IR Heterodyne Receiver For High Resolution Measurements of Molecular Species in the Stratosphere

P.K. Cheo and Y. Zhou

University of Connecticut, U-157, Storrs, CT 06269, (203)-486-4816

Remote sensing of trace molecules by measuring solar absorption spectra in the mid-IR region has been proved to be one of the useful methods to explore the earth's atmosphere. To fully resolve the Doppler broadened line profiles in the stratosphere, a resolving power of  $> 10^5$  is required and only available technique is laser heterodyne spectroscopy[1].

The optical heterodyne detection using CO<sub>2</sub> lasers was developed for very high resolution spectroscopy[2]. The allowed spectral range limited by the photomixer bandwidth was less than 1500 MHz for each laser line. By using a tunable diode laser(TDL) as local oscillator, the TDL heterodyne spectrometer(HS) can provide broad spectral range with high resolution. When the TDL is current tuned, absorption spectrum can be measured with a single bandpass filter and a relatively narrowband photomixer. The measurements of solar absorption of ozone lines and other trace gases[3][4][5] using TDLHS have been reported by many researchers worldwide. However, the disadvantage of TDLHS lies in the following. First, due to limited useful single mode output power from TDL, it is difficult to reach quantum noise limited operation in the photomixer. Second, it is difficult to maintain sufficient wavelength stability due to temperature and current fluctuations, the accuracy of the measurements of some 'minor' gases which require very long integration time (minutes to hours) is limited, and also the frequency calibration of TDL is cumbersome and the accuracy of the spectral position is difficult to maintain. The last but not the least, the beam quality, excess noise, the linewidth and mode purity in a frequency scan for a TDL are usually much worse than a well designed and stabilized CO<sub>2</sub> laser. All these will degrade the performance of heterodyne detection in terms of its sensitivity and spectral resolution.

A tunable CO<sub>2</sub> sideband laser generated by a phase modulator[6] has been developed at University of Connecticut. The capability of this laser source has been demonstrated to yield accurate and reliable data on absorption line profiles, line strengths, linewidth and frequency shifts of NH<sub>3</sub> molecules[7]. A new heterodyne spectrometer using the tunable sideband laser as a local oscillator has been constructed at UConn. It has all the advantage of a CO<sub>2</sub> Laser with more than 10 mw oscillator power, good beam quality, narrow linewidth and stable single mode. It also provides very accurate frequency and wide tunability ( $\pm 10$  GHz) for each of CO<sub>2</sub> laser lines in 9 - 12  $\mu$ m.

The accuracy of remote sensing of atmospheric gases using laser heterodyne spectrometer is dependent on the sensitivity and resolution of the spectrometer, the accuracy of the spectra line parameters and the efficiency and reliability of data inversion algorithm. The accurate line parameters can be retrieved by least-square fitting Voigt profile with recorded data from direct absorption measurements using tunable CO<sub>2</sub> sideband laser source[7]. Using a gas handling system with proper temperature control, spectral line parameters of O<sub>3</sub>, HNO<sub>3</sub> and some other molecular gases will be measured. The data will be used to process the remote sensing data of solar absorption spectra from the heterodyne measurements and to retrieve vertical distribution profiles and number densities of those molecules in the stratosphere.

Fig.1 shows the configuration of tunable sideband laser heterodyne spectrometer. It consists of four sub-systems: local oscillator, solar tracker and thermal source (used for calibration), IR photomixer, post-electronics and data acquisition.

The local oscillator is a tunable sideband laser source. Precise frequency tuning in the 9 - 12  $\mu$ m region is obtained by phase modulation of a family of isotopic CO<sub>2</sub> lasers using frequency



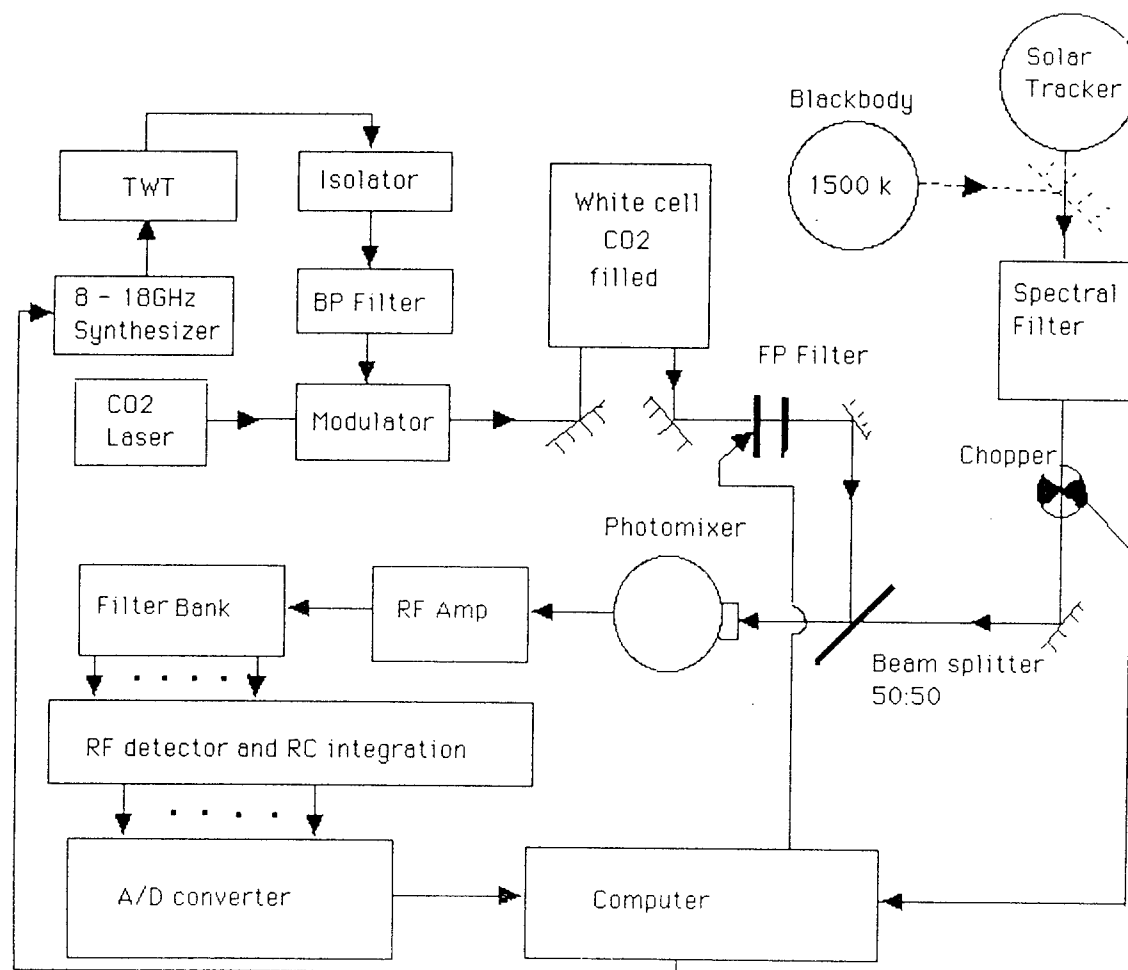


Fig.1 IR Heterodyne Receiver Using a Tunable CO<sub>2</sub> Sideband Laser As the Local Oscillator.

synthesized microwave fields. For each laser line the modulator generates upper and lower sideband with about 1% of total laser power at the frequency off-set by 8-18 GHz from the carrier using an input microwave power of 20 w. The carrier is eliminated by the absorption through a CO<sub>2</sub> filled white cell. To achieve a good phase match with the signal beam, a pure single mode with a Gaussian wavefront can be recovered by the collimation optics after the white cell using a small pinhole at the focal point as a spatial filter. A Fabry-Perot interferometer selects upper or lower sideband and rejects the other and residual carrier. The microwave frequency, the central frequency of the FP bandpass filter and the data acquisition are synchronously controlled by the computer. The microwave drive source consists a synthesized sweeper (8 to 18 GHz, -5 to 20 dBm) and a TWT amplifier. The local oscillator excess noise mostly comes from microwave drive source which will be transferred to the CO<sub>2</sub> sideband by phase modulation. At the output of the photomixer, the excess noise will auto-heterodyne by itself. The beats lie in the frequency range up to tens of MHz. We have studied this problem by performing a series of measurements with several microwave signal sources and TWT amplifiers. The results show that the dominate noise is

the phase noise of TWT amplifier. This problem is being solved by rebuilding the present ITT made TWT to reduce the phase noise. Alternatively, a low noise TWT can be constructed using two stage amplifier. The first stage uses a solid state amplifier to provide an output of one watt and the second stage uses a low gain TWT to raise the power to 10 watts. With this system the noise figure can be reduced by about 13 dB. Further improvement can be made by employing a microwave isolator and a bandpass filter between TWT and modulator. The isolator can suppress the reflected microwave power and the bandpass filter can reduce high order harmonics.

The solar tracker is a clock-drive equatorial telescope mount and a 3 inch flat mirror aligned in a proper position to get a stationary solar beam for the measurements of  $O_3$  and  $NHO_3$ . For the measurements of some 'minor' molecules, a fully automatic tracker is needed to keep long term tracking accuracy. A 1500 K Blackbody source is used as a reference and also as a calibration source. Another component for thermal signal path is a bandpass filter to block the solar flux with frequency outside the detection region.

Photon mixing and data acquisition includes beamsplitter, photomixer, pre-amplifier, RF electronics (amplification, filter banks, RF detectors) and data acquisition (lock in amplifier or a integration unit, D/A converter, computer interface, control software). The receiver bandwidth is dependent on detection sensitivity with respect to the integration time for each of filter channels. The present system has two filter channels with 1- 5MHz and 2 - 10MHz working in the scan mode(frequency scan). A small scale filter bank has also been designed which can cover about 100 MHz with a minimum bandwidth of 5 MHz. The signal to noise ratio can be enhanced by a factor of square root of N in the scan mode if N is the number of filters with equally spaced bandwidth. In the case of some 'minor' molecules measurement, very long integration time is needed, therefore the scan mode is not suitable. In this case the filter bank minimum frequency coverage is the width to cover the entire spectral line.

One of the major challenge in the measurements of stratospheric trace species is the interpretation of the raw spectra data. Commonly used method is the standard radiative transfer inversion. The vertical distribution profile and number density of  $O_3$  and  $HNO_3$  can be derived from raw spectra data[1]. A knowledge of the partial pressure distributions will greatly enhance this data inversion processing. The critical parameters will be determined from direct absorption measurements using a temperature and pressure controlled gas cell. Because of our unique high frequency accuracy of the local oscillator, it is possible to determine the local dynamic feature such as wind velocity from the total line shift of raw spectra.

### References

- [1] M.Abbas, V.Kunde, M.Mumma, T.Kostiuk and D.Buhl, "Stratospheric Sounding by Infrared Heterodyne Spectroscopy", J. of Geophys. Res., Vol. 84, NO. A6, 1979
- [2] T. Kostiuk and M. Mumma, "Remote sensing by IR Heterodyne Spectroscopy", Appl. Opt. 2, 2644, 1983
- [3] C.T. McElroy, A.Goldman, P.F.Fogal and D.G.Murcray, Heterodyne Spectrophotometry of Ozone in the 9.6 -  $\mu m$  Band Using a Tunable Diode Laser", J. of Geophys. Res., Vol. 95,NO.D5, 1990
- [4] H.Fukunishi, S.Okano, M.Taguchi and T.Ohnuma, "Laser Heterdyne Spectrometer Using a Liquid Nitrogen Cooled Tunable Diode Laser For Remote Measurements of Atmospheric  $O_3$  and  $N_2O$ ", App. Opt., Vol.29, No.18, 1990
- [5] Hoell,J.M., C.N. Harward and W. Lo, "High Resolution Atmospheric Spectroscopy Using a Diode Laser Heterodyne Spectrometer", Opt.Eng. 22, 21, 1982
- [6] P. K. Cheo, "Frequency Synthesized and Continuously Tunable IR Laser Source in 9 - 11  $\mu m$ ", IEEE J. Quant. Electron. OE-20 700 (1984)
- [7] P. K. Cheo, Z. Chu, L. Chen and Y. Zhou"Applications of A Tunable  $CO_2$  Sideband Laser For High - Resolution Spectroscopic Measurements of Atmospheric Gases", Appl. Opt. 32 836 (1993)

## **Population and Thermal Grating Contributions to Degenerate Four-Wave Mixing Line Shapes**

Paul M. Danehy  
High Temperature Gasdynamics Laboratory  
Stanford University  
Stanford, CA 94305-3032, USA  
Tel. (415) 723-1823

Ernest J. Friedman-Hill and Roger L. Farrow  
Combustion Research Facility  
Sandia National Laboratories  
Livermore, CA 94551-0969, USA  
Tel. (510) 294-3259 (RLF)

Degenerate four-wave mixing (DFWM) is a laser-induced grating technique that shows increasing potential as a diagnostic probe for reactive environments. Traditionally, the development of DFWM as a diagnostic for gaseous systems has focused on using the population-grating (PG) mechanism to measure concentration and temperature. Recently, several authors have observed a thermal-grating (TG) mechanism in gases. This mechanism is similar to that observed for many years in liquids and solids.<sup>1</sup> The gas-phase thermal-grating mechanism deserves further study since it can complicate population-grating measurements, or can itself be useful for making quantitative measurements.

The TG mechanism differs from the familiar PG mechanism in several ways. As in the PG mechanism, a spatially modulated pattern of light generated by two interfering laser beams results in spatially modulated absorption of energy by the medium. In the PG mechanism, this perturbation results in a spatially modulated absorption/dispersion grating that diffracts a third incident laser beam to generate DFWM signal. For the case of the TG mechanism, additional processes are required. Collisional quenching can convert the absorbed energy to heat, resulting in a spatially modulated heat addition to the gas. This heat input, and its accompanying density change, form a grating in the real part of the refractive index of the gas. The DFWM signal generated by diffraction from this grating completes the thermal grating process.

Theoretical descriptions of DFWM line shapes for the PG mechanism are developed in Abrams et al.<sup>2</sup> We also utilize nearly degenerate four-wave mixing (NDFWM) line shapes based on Nilsen and Yariv.<sup>3</sup> These perturbative treatments include the effects of molecular motion but exclude the effects of saturation. For thermal gratings, the line shapes are most easily described by simple grating theory.<sup>1</sup> The two interfering beams, usually called the forward-pump and probe beams, are absorbed by some resonant species. In the presence of a quenching collisions, the

resulting heat addition induces an index modulation. Given this index modulation, one can calculate the scattering efficiency for an incident beam. For the case of DFWM in the thermal grating regime, this incident beam, known as the backward pump, diffracts with an efficiency proportional to  $\sigma(\nu)^2$ , where  $\sigma(\nu)$  is the frequency-dependent absorption cross-section.

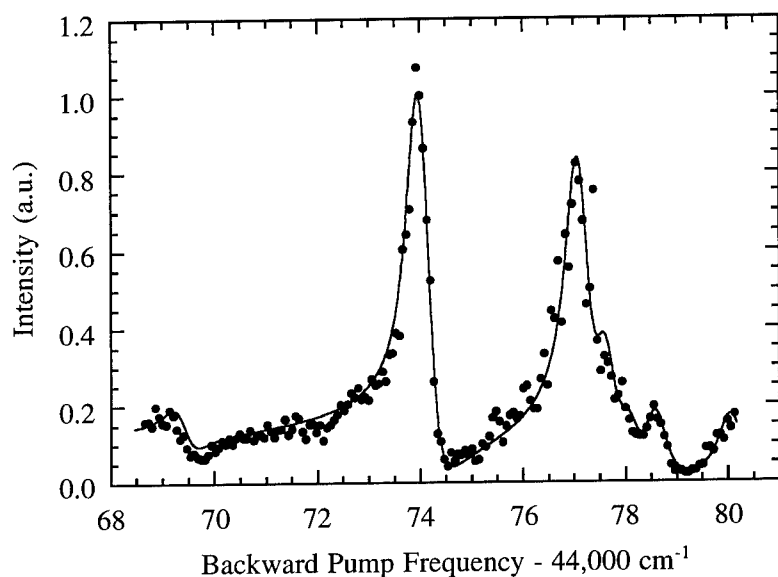


**Fig. 1**

Nearly-degenerate four-wave mixing spectrum near the  $O_{12}(2)$  line of NO. The  $O_{12}(2)$  is the strongest line in the spectrum; at  $44,074\text{ cm}^{-1}$ . These measurements were performed in 300 Torr  $\text{N}_2$  by scanning the backward-pump frequency while holding the forward-pump and probe frequencies fixed to line-center of the  $O_{12}(2)$  line.

The setup used in this experiment is similar to that described in Ref. 4. To perform DFWM scans, we used the single-mode output from a pulse-amplified ring-dye laser which was doubled and mixed to obtain a linewidth of  $\sim 0.004\text{ cm}^{-1}$  at 226 nm. This linewidth was sufficient to resolve the features observed at these experimental conditions ( $\sim 0.25\text{ cm}^{-1}$  FWHM pressure width,  $0.1\text{ cm}^{-1}$  Doppler width). To obtain NDFWM spectra, we substituted a second independently tunable laser for the backward-pump beam. This beam originated from a pulsed-dye laser which was doubled and mixed, resulting in a linewidth of  $\sim 0.16\text{ cm}^{-1}$ . We performed measurements on small concentrations ( $\sim 65\text{ mTorr}$ ) of NO using  $\text{N}_2$  and  $\text{CO}_2$  as buffer gases due to their vastly different quench rates (the quench rate by  $\text{CO}_2$  is approximately  $10^4$  times larger than by  $\text{N}_2$ ). We probed transitions in the  $O_{12}$  and  $P_2+P_{12}$  branches in the  $A^2\Sigma^+(\nu'=0) \leftarrow X^2\Pi(\nu''=0)$  band of NO.

Shown in Fig. 1 are NDFWM measurements obtained by exciting the line-center frequency of the  $O_{12}(2)$  transition with the forward pump and probe, while scanning the frequency of the backward pump. The central resonance results from the expected PG scattering from the  $O_{12}(2)$  line. This peak is strongly heterodyned with a non-resonant contribution from thermal gratings, resulting in a strong asymmetry. The TG contribution does not depend on the frequency of the backward pump since scattering is occurring from gas density modulations instead of molecular resonances as in the PG mechanism.

We also observe strong signals when the backward pump is tuned to resonance with lines in the  $P_2+P_{12}$  bandhead. Rotational energy transfer (RET) is likely the mechanism populating these states, forming an RET-induced grating. To model this severely non-equilibrium molecular distribution, we adjusted the populations of the different rotational levels for best fit during the data analysis. Furthermore, the contributions from the non-resonant thermal grating and from a baseline offset were varied. The linewidth (assumed equal for all lines) was adjusted in the fit as a first-order approximation for the effects of saturation. The main source of noise in the data is a jitter in the delay between the two lasers. Best-fit parameters indicate that thermal grating intensity is  $\sim 7\%$  as large as the population grating intensity for these conditions.

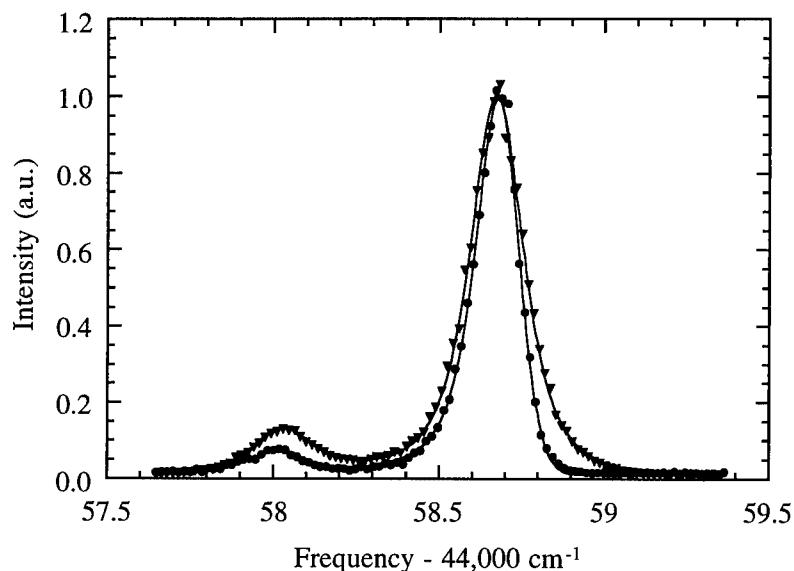


**Fig. 2**

Experimental (symbols) and theoretical (curves) DFWM frequency scans of the  $O_{12}(16)$  (left) and  $O_{12}(6)$  (right) lines of NO. The results obtained in 297 Torr of  $\text{CO}_2$  (triangles) correspond to conditions dominated by thermal gratings, while measurements obtained in 300 Torr  $\text{N}_2$  (circles) are dominated by population gratings.

This estimate of the relative contributions of the two mechanisms was used to calculate the DFWM line shapes for the  $O_{12}(6)$  and  $O_{12}(16)$  lines of NO in nitrogen, shown in Fig. 2. The fit to the  $\text{N}_2$  data includes a 5.4% thermal grating contribution on the  $O_{12}(6)$  line (estimated by multiplying the TG contribution measured on the  $O_{12}(2)$  transition by the ratio of the absorption cross sections squared). We used the Voigt profile to calculate this  $\sigma(\nu)^2$  thermal grating contribution. The majority of the intensity in this fit was calculated from the population-grating moving-absorber model, using the four-photon linestrengths as described in Ref. 5. The TG contribution was calculated using one-photon linestrengths. Furthermore, we corrected for measured laser beam absorption and allowed a small (2%) non-resonant contribution to the signal from long range resonances. To analyze these DFWM spectra, we varied only the transition frequencies and a baseline offset for best fit.

As mentioned above,  $\text{CO}_2$  has a much larger quench rate than  $\text{N}_2$ . Thus, when the  $\text{N}_2$  buffer is replaced by  $\text{CO}_2$ , more of the absorbed energy is added to the gas as heat. This results in

a much larger contribution to the signal from thermal gratings. Using DFWM measurements performed on the  $O_{12}(2)$  line in a static cell for a number of pressures of  $CO_2$ ,<sup>6</sup> we estimated that the ratio of TG to PG signal at 297 Torr of  $CO_2$  was  $\sim 15$ . Again, scaling this ratio to the  $O_{12}(6)$  line and using the corresponding contributions from the TG and PG mechanisms as described above, we modeled the DFWM spectrum recorded in  $CO_2$ . The observed spectrum and fit, shown in Fig. 2, illustrate two of the fundamental differences between the two grating mechanisms. First, the  $N_2$  spectrum, which is dominated by population gratings, shows a more severe linestrength dependence, as evidenced by the smaller relative size of the  $O_{12}(16)$  peak. This is in agreement with theory based on two-level absorbers: in the weak saturation limit, thermal gratings scale as  $\sigma^2$  while population gratings scale as  $\sigma^4$ .<sup>1,2</sup> Second, the line shapes dominated by the TG mechanism are broader than those dominated by the PG mechanism. The difference in these widths is directly related to Doppler broadening. The TG line shape (calculated directly from the Voigt profile) is Doppler-broadened, while the PG line shape (in the phase-conjugate geometry) is Doppler-free.

The theoretical models and experimental data are in excellent agreement, lending credibility to our understanding of the thermal grating mechanism. Residual imperfections in the fits are likely due to the effects of saturation which have not been addressed here.

This work was supported by the U.S. Department of Energy, Office of Basic Energy Sciences, Division of Chemical Sciences and the Office of Industrial Technologies, Division of Advanced Industrial Concepts. Partial funding for PMD was provided by the Air Force Office of Scientific Research, Aerospace Sciences Directorate.

- (1) H. J. Eichler, P. Günter and D. W. Pohl, *Laser-Induced Dynamic Gratings* (Springer-Verlag, New York, 1986).
- (2) R. L. Abrams, J. F. Lam, R. C. Lind, D. G. Steel and P. F. Liao, in *Optical Phase Conjugation*; R. A. Fischer, Ed.; (Academic Press, San Diego, 1983), pp. 211-284.
- (3) J. Nilsen and A. Yariv, Opt. Comm. **39**, 199-204 (1981).
- (4) R. L. Farrow and D. J. Rakestraw, Science **257**, 1894-1900 (1992).
- (5) E. J. Friedman-Hill, L. A. Rahn and R. L. Farrow, J. Chem. Phys. (submitted).
- (6) See paper by R. L. Farrow, P. H. Paul, E. J. Friedman-Hill, and P. M. Danehy, "Degenerate Four-Wave Mixing for Quantitative Diagnostic Measurements", in this digest.

## Laser Diagnostics by Electrostrictive Gratings in the Gas Phase

A. Stampanoni-Panariello, W. Hubschmid, B. Hemmerling

Paul Scherrer Institute

CH-5232 Villigen PSI, Switzerland

Phone: +4156992476 FAX: +4156982327 E-Mail: HEMMERLI@CAGEIRA5A

### Introduction

Over the past two decades laser induced gratings (LIGs) have been widely used to study various properties of optical media. Refractive index changes are induced by optical fields through resonant and nonresonant mechanisms, respectively. Depending on the physical mechanism which is responsible for the formation of LIGs, this technique is suited for studying different processes in the solid, liquid, and gas phase. Resonant LIGs have been used for the detection of excited state absorption in the gas phase [1] and for the measurement of ultrafast phenomena [2]. Furthermore, LIGs have been applied for the measurement of flame temperature [3] and for the study of fast combustion processes [4]. Recently, two-color laser-induced gratings have been proposed as a new spectroscopic method for detecting rovibronic transitions of excited molecules in the gas phase [5,6] and for the detection of atomic hydrogen in low pressure  $H_2/O_2$  flames [7].

Besides resonant processes, molecular orientation (Kerr effect), redistribution, third order nonresonant polarizability, and electrostriction are nonresonant mechanisms which lead to a change of the refractive index in the material under investigation. Mostly, a signal arising from such processes is treated as a unwanted contribution because it may obscure the resonant signal. In the following we like to show that nonresonant techniques may prove to be valuable tools for diagnostic purposes especially in cases when the transition is not within the wavelength range accessible by lasers.

In a usual arrangement, two laser beams intersect at an angle  $\theta$  in the medium and create an intensity interference pattern. A grating like modulation of the density is generated by electrostriction giving rise to two counterpropagating sound waves (phonons) whose wavelength and orientation match the interference pattern geometry. This spatially periodic standing wave acts like a time-dependent volume grating [8,9]. A probe beam is Bragg-diffracted off of this grating into the signal beam. Because of the long decay time of acoustic waves, the LIG can be described as an integrated intensity grating.

We used this novel LIG technique to measure the dissipation of acoustic waves and their velocity in the gas phase. The results were compared with theoretical calculations including the effect of stochastic optical fields. Furthermore, we demonstrate the generation of high-quality two-dimensional images by this technique.

## Experimental

The experimental configuration used to obtain and study LIG is schematically shown in Fig.1. Two frequency doubled Nd:YAG lasers (Continuum NY81-20) with a pulse duration of about 8 ns FWHM and a beam diameter of about 6 mm are used. The output of laser 1 is split by a 50% beamsplitter (BS1) into two excitation beams which set up the grating. In order to achieve equal path lengths for this two beams, one of the excitation beams first passes through a delay line formed by three prisms. This beam is directed by a second 50% beamsplitter (BS2) into a gas cell where it crosses the second excitation beam at an angle  $\theta$ . The gas cell is about 70 cm long and can be filled with different gases up to a pressure of 5 bar. The output of laser 2 provides a probe beam which is counter-propagating to one of the excitation beams. Furthermore, the probe beam is perpendicularly polarized to the excitation beams. The polarizer P1 protects laser 1 against damage by the light of laser 2. In the same

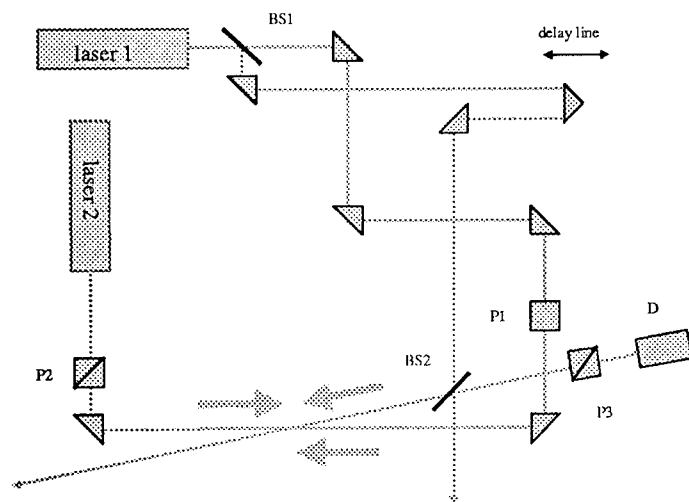


**Fig.1:** Experimental setup. BS1:beamsplitter (R=30%), BS2:beamsplitter (R=50%), P1,P2,P3 polarizer.

connected to a photomultiplier tube (PMT) coupled to a boxcar averager.

The flashlamps of laser 2 were externally triggered by the fire command of laser 1 in a master/slave configuration. A time delay between the laser pulses is achieved electronically by means of a digital delay generator (Stanford Research Systems DG535). The trigger output of laser 1 is connected to the delay generator which triggers the Q-switch of laser 2 after a chosen delay time. The variation of the delay time and the data acquisition was under control of a PC.

way acts polarizer P2 as a protection of laser 2. The probe beam is diffracted off the grating into a signal beam. Satisfying the Bragg condition, the signal beam is counter-propagating to the second excitation beam. In a previous work we found that the signal beam is also phase conjugated to the excitation beam [10]. Part of the signal beam passes through the beamsplitter BS2. Stray light, especially from the beamsplitter BS2, is efficiently suppressed by a polarizer P3 in the path of the signal beam. Spatial filtering is achieved by focusing the signal beam into a 200  $\mu\text{m}$ -diameter optical fiber (15 m long) which is



## Results and Discussion

The grating formation can be treated in the continuum approximation as the grating spacing is large compared to the mean free path at the chosen gas pressure. Furthermore, the typical time between two collisions of a molecule is small compared to the other time scales, i.e. pulse duration of the laser and attenuation constant of the density wave. With the assumption of Gaussian statistics for the laser exciting the grating the effect of stochastic optical fields is included in the calculation.

The two excitation pulses are crossed inside the gas cell where they generate an acoustic standing wave which acts like a volume grating. Assuming plane waves with a Gaussian intensity profile the interference of the excitation beams results in a sinusoidal intensity distribution. Phase matching occurs for a pure sinusoidal volume grating only for the  $m=\pm 1$  diffraction orders.

The optical path length of the two excitation beams was aligned to be equal. The temporal delay between the two lasers was adjusted in such a way that the three beams meet each other at the same time in the overlapping volume. When the difference in optical path length between the two excitation beams varies, the signal intensity changes drastically showing the

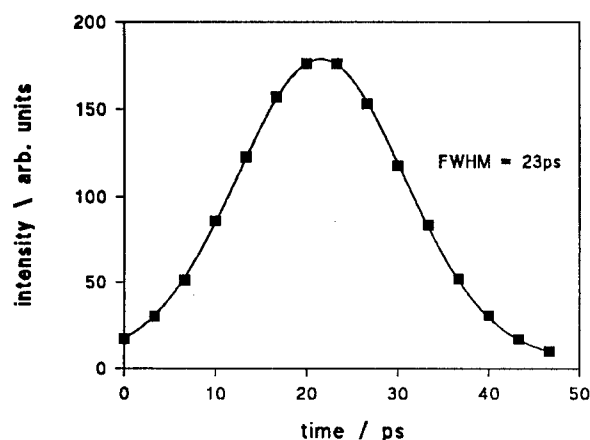
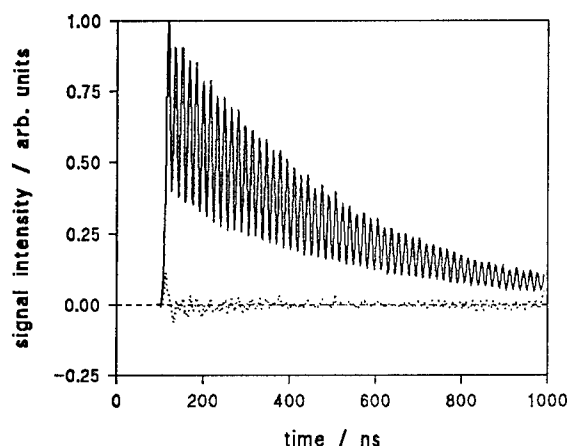


Fig.2: Signal intensity versus time delay between the two excitation beams (squares = measured values; solid line = Gauss fit). The time scale has an arbitrary offset.

effect of the coherence length of the laser on the grating reflectivity (see Fig. 2). The displayed data were recorded in ambient air. They can be fit well by a Gaussian line form with a FWHM of 23 ps corresponding to a bandwidth of the laser of  $0.93 \text{ cm}^{-1}$ .

The dependence of the signal intensity was investigated in air over the intensity range of  $15 \text{ MW/cm}^2$  to  $90 \text{ MW/cm}^2$ . A double logarithmic plot of signal intensity versus laser intensity displays a linear relationship with a slope of  $3.2 \pm 0.1$ . There is no evidence of saturation even at the highest laser intensities used.

Furthermore, the dependence of the signal intensity upon pressure was measured in air at room temperature. A quadratic relationship is found over the pressure range of 80 mbar to 5 bar (slope  $2.089 \pm 0.005$ ). The measured cubic dependence of the signal intensity and its quadratic variation with the pressure agree with the theoretical calculations for a LIG based on electrostriction.



**Fig.3:** Signal intensity versus time delay between the excitation beams and the probe beam. The time scale has an arbitrary offset.

dissipation of the sound wave is measured to be  $(7086 \pm 32) \cdot 10^{-9} \text{ m}^2/\text{s}$  corresponding to a decay time of  $\tau = 395 \text{ ns}$ . With the assumption that the velocity of sound is in principle well known this method could be used to measure the temperature.

The crossing angle between the excitation beams,  $\theta = 2.9^\circ$ , corresponds to a wavelength of the sound wave of  $10.5 \mu\text{m}$ . The amplitude of the grating oscillates periodically twice during each acoustic cycle. In Fig. 3. the intensity of the diffracted beam is displayed versus the time delay between the excitation beams and the probe beam. The measurement was made in argon at 5 bar with the time delay varied in steps of 2 ns. The oscillations of the amplitude of the standing acoustic wave are very well visible. The dots represent the difference between the measured and calculated values. From the best fit one gets for the velocity of sound a value of  $v = (324.34 \pm 0.07) \text{ m/s}$  which agrees well with the literature value of  $321 \text{ m/s}$  [11]. The

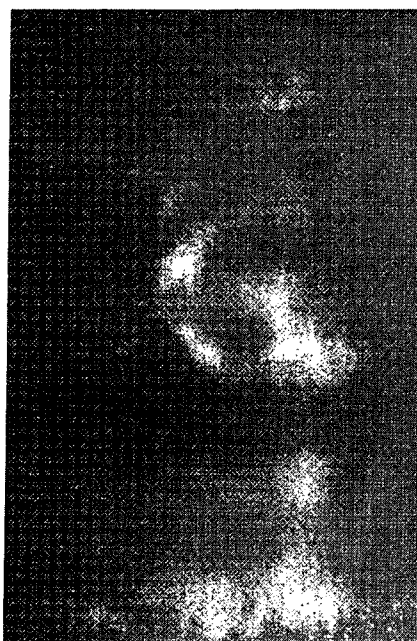


**Fig.4:** Single shot image of a helium jet in air. The diameter of the nozzle was about  $0.1 \text{ mm}$ .

The experimental setup was slightly modified in order to demonstrate the imaging capabilities of the LIG technique. One of the excitation beams and the counter-propagating probe beam are formed into a light sheet of about  $500 \mu\text{m}$  thickness and  $6 \text{ mm}$  height. The signal beam counter-propagating the second excitation beam carries information on the overlapping area of the laser sheet and the circular excitation beam. The signals obtained from different gases differ strongly. Helium, for example, produces a signal which is about 7500 times smaller than that produced in ambient air. Figure 4 displays a single shot image showing a helium jet in air. The areas of low partial air pressure and therefore high helium concentration are displayed bright and the atmospheric air region is dark.

In conclusion, electrostrictive LIGs have been used to measure the dissipation of sound waves and their velocity in the gas phase. Furthermore, this novel technique has shown to have a potential for remote monitoring of gas mixing processes without the need of any tracer material.

## References

- [1] C.C Hayden, D.W. Chandler, M.A. Butine, M.W. Kimmel, M.J. Jaska: Sandia Technical Review (1992)
- [2] R. Trebino, C.E. Barker, A.E. Siegman: IEEE J. Quantum Electron. **22**, 1413 (1986)
- [3] T.R. Brewer, J.T. Fourkas, M.D. Fayer: Chem. Phys. Lett. **203**, 344 (1993)
- [4] J.T. Fourkas, T.R. Brewer, H. Kim, M.D. Fayer: Opt. Lett. **16**, 177 (1991)
- [5] M.A. Butine, D.W. Chandler, C.C. Hayden: J. Chem. Phys. **97**, 707 (1992)
- [6] M.D. Wheeler, I.R. Lambert, M.N.R. Ashfold: Chem. Phys. Lett. **211**, 381 (1993)
- [7] J.A. Gray, J.E.M. Goldsmith, R. Trebino: Opt. Lett. **18**, 444 (1993)
- [8] K.A. Nelson, R.J.D. Miller, D.R. Lutz, M.D. Fayer: J. Appl. Phys. **53**, 1144 (1981)
- [9] K.A. Nelson, D.R. Lutz, M.D. Fayer, L. Madison: Phys. Rev. B **24**, 3261, (1981)
- [10] B. Hemmerling, A. Stampanoni-Panariello: Appl. Phys. in press
- [11] Encyclopedie des Gaz, L'Air Liquide, Elsevier Scientific Publishing Company, Amsterdam (1976)

## Measuring CO Concentration and Temperature in a CH<sub>4</sub>/air Premixed Flame with Broadband Coherent Anti-Stokes Raman Spectroscopy

J.W. HAHN and S.N. PARK

*Korea Research Institute of Standards and Science,  
P.O.Box 3, Taedok Science Town, Taejeon, 305-606, Korea  
Phone:(42)868-5221, Fax:(2)231-6813*

K.T. KANG and S.H. CHUNG,

*Department of Mechanical Engineering, Seoul National University,  
Seoul 151-742, Korea*

Coherent anti-Stokes Raman spectroscopy (CARS) has been widely used as a diagnostic tool for probing the temperature and species concentration of gas phase samples. CARS concentration measurements are typically performed either from the integration<sup>1,2</sup> or from the shape of a CARS spectrum.<sup>3, 4</sup> If the resonant signal of CARS is much bigger than the nonresonant background, integration of the CARS spectrum depends linearly on the squares of the concentration of the species. In practice, this method can be used to measure the concentration of major species. When the fraction of a species goes down to the order of a few percentage, the nonresonant background becomes comparable to the resonant signal of CARS and interferes with the resonant signal. In such a case, the portion of the nonresonant background included in the integration of the CARS spectrum leads to a large error in the concentration measurement. The interference of the nonresonant background and the real term of the resonant signal of CARS form modulation dips on the spectrum that are sensitive to the concentration. Recently Hahn et al.<sup>5</sup> proposed a new technique for measuring the minor species concentration from the modulation dip of nonresonant background of broadband CARS spectrum.

In the present work we measured the steady profiles of temperature and CO concentration in a CH<sub>4</sub>/air premixed flame of a counterflow burner with the broadband CARS and the results were compared with the numerical calculations.

The detailed description of the CARS spectrometer used in the experiment was given previously<sup>6, 7</sup> and a brief description will be made here. A frequency-doubled Nd:YAG laser (Quantel YG660) produced the 532 nm light, giving ~150 mJ pulse energy, 7~8 ns pulse duration, and 10 Hz repetition rate. Most of the energy of the frequency doubled Nd:YAG laser(>90 %) was used in pumping a dye laser for Stokes beam. To reduce the mode noise in broadband CARS spectra, the amplified spontaneous emission(ASE) from a home-made dye laser was used as the Stokes beam. The bandwidth(FWHM) of ASE was ~100 cm<sup>-1</sup>. We adjusted the center

wavelength of ASE by changing the concentration of the rhodamine 640 dye to  $3.2 \times 10^{-5}$  M in a base solution of  $7.2 \times 10^{-5}$  M kiton red 620 to produce ASE with a center wavelength near 600.6 nm for CO CARS experiment. The pulse energy of ASE was  $\sim 8$  mJ.

To avoid the cross coherence effect<sup>8, 9</sup> between the two pump beams, we selected a  $\sim 5$  cm path delay. The pump and the Stokes beams were horizontally polarized and we recorded the CARS signal with the same polarization. BOXCARS phase matching was employed for the experiment and the beams were collimated with an achromatic lens ( $f=25$  cm). The waists of the pump and the Stokes beams in the collimating lens were  $\sim 2$  mm, and the distance between axes of the two pump beams was  $5 \sim 6$  mm. The CARS signal was passed through a monochromator (Jovin-Yvon U1000) equipped with a 1200 groove/mm grating and then detected by an optical multichannel analyzer (OMA, Princeton Instrument, EIRY1024).

We used a counterflow burner setup to analyzing the structure of the  $\text{CH}_4/\text{air}$  premixed flame. Due to the inherent simplicity of the flow field, the counterflow burners have been frequently adopted in the experimental and the theoretical studies of the structure of stretched flames.<sup>10</sup> In this study, two axisymmetric premixture jets were impinging on each other, then two steady planar flames could be stabilized. Because of this nature, one dimensional measurement in the axial direction ensures to reveal the flame structure.

To have the uniform velocities at the nozzle exits, we used wind tunnel types of divergent-convergent nozzles with the contraction ratio of 320:1. The nozzle diameters and the separation distance between the two counterflow nozzles were 7.0 mm. Each combustible premixture flow was shielded by a nitrogen flow issuing through the slit between the main premixture nozzle and the concentric nozzle surrounding it to prevent the effect of ambient air as an oxidizer. To reduce overheating, we placed a water jacket around each nozzle exit. The  $\text{CH}_4/\text{air}$  premixture was supplied to the upper and the lower burners with the same concentration, and the flow velocity at both exit nozzles was 0.8 m/s. The volume fraction of the fuel was 7.0 %. The CARS measurements were performed along the axis of the flame by vertically translating the counterflow burner.

The calculation of temperature was performed with the CARSFIT code (Sandia National Laboratory, PC version 05-06-92). The CO concentration was determined from the ratio( $R$ ) of the modulation dip to the nonresonant background of the broadband CARS spectrum. In the previous work<sup>5</sup>, it has been showed that the ratio can be described in the following functional form of

$$R = a(\gamma + b\gamma^2)\exp(cT) \quad (1)$$

where  $T$  is temperature and the concentration ratio in %. The coefficients  $a$ ,  $b$ , and  $c$  were system parameters determined by the slit function of the detection system, laser line broadening, etc. In present experiment  $a$ ,  $b$ , and  $c$  were determined to be 1.03,

$-0.108$  and  $-8.8 \times 10^{-4}$ , respectively. The CO concentration was obtained by the following procedure. First, we measured the broadband CARS spectrum of CO, and subtracted the baseline due to the dark signal or the background noise. Second, we normalized this spectrum with the broadband CARS spectrum of the nonresonant signal of Ar. From this, we derived the ratio from magnitudes of the signal and the modulation dip in the normalized spectrum. Finally, we calculated the CO concentration from Eq.(1) using the temperature determined from the  $N_2$  CARS spectrum.

To compare these experimental results, the structure of the flame was analyzed numerically. In the boundary layer formulation of the counterflow, the conservation equations for mass, momentum, energy, and chemical species were solved.<sup>11</sup> The reaction mechanism consisted of 174 elementary steps (including reverse reactions) and the species accounted here were 33 reaction elements.<sup>12</sup> The numerical scheme included the Newton-Raphson method, the Euler time integration and the adoptive grid method to cover the steepness problem in the temperature and concentration profiles coupled with the reaction rates.

We measured the temperature profile in the flame from CARS spectra of  $N_2$  prior to the CO concentration measurements and the result is shown in Fig. 1. The temperature profile in the figure is the results of the best fit of  $N_2$  CARS spectra. The solid line in the figure is the results from the numerical calculation and the two results agree well in both the magnitudes and their gradients. The measured profile of the CO concentration in the flame is shown in Fig.2. Also, the numerical calculation is shown as a solid line. The agreement between these two results are satisfactory.

In summary we have studied experimentally and numerically the structure of the  $CH_4$ /air premixed flame of a counterflow system. The profiles of temperature and CO concentration were obtained and the comparison between the experimental and the numerical results showed satisfactory agreement.

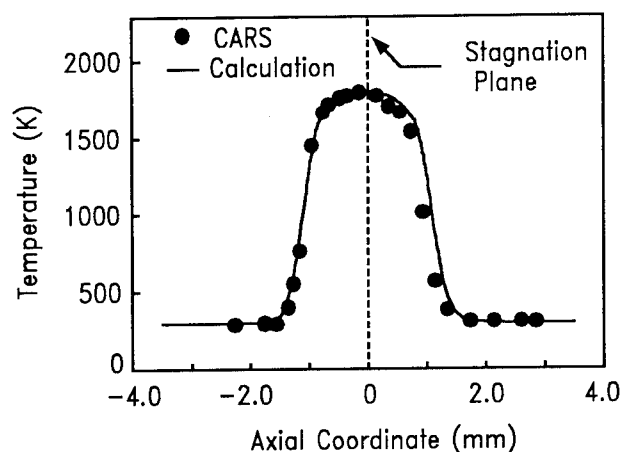


Fig.1. Temperature profile measured along the axis of the  $CH_4$ /air premixed flame in the counterflow burner.

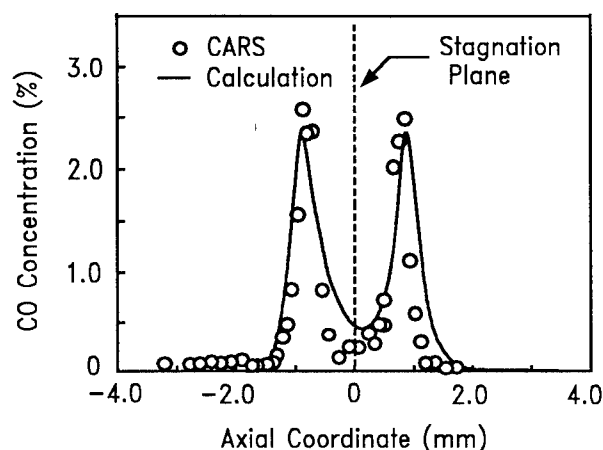


Fig.2. CO concentration profile measured along the axis of the  $\text{CH}_4/\text{air}$  premixed flame in the counterflow burner.

## References

1. R. E. Regnier and J. P. E. Taran, *Appl. Phys. Lett.* **23**, 240(1973).
2. W. M. Tolles, J. W. Nibler, J. R. McDonald and A. B. Harvey, *Appl. Spectro.* **31**, 253(1977).
3. R. J. Hall and A. C. Eckbreth, "CARS Application to Combustion Diagnostics," in *Laser Applications*, J. F. Ready and R. K. Erf, Eds. (Academic Press, Orlando, 1984), Vol. 5, p. 213.
4. R. L. Farrow, R. P. Lucht, G. L. Clark and R. E. Palmer, *Appl. Opt.* **24**, 2241(1985).
5. J. W. Hahn, et al., *Appl. Spectro.* **47**, 710(1993).
6. J. W. Hahn, S. N. Park, E. S. Lee and C. Rhee, *Korean J. Appl. Phys.* **4**, 314(1991).
7. S. N. Park, J. W. Hahn and C. Rhee, *Korean J. Appl. Phys.* **5**, 9(1992).
8. H. Kataoka, S. Maeda and C. Hiroso, *Appl. Spectro.* **36**, 565(1982).
9. L. A. Rahn, R. L. Farrow and R. P. Lucht, *Opt. Lett.* **9**, 223(1984).
10. S. H. Chung, J. S. Kim, and C. K. Law, *Twenty-first Symposium on Combustion*, p. 1845, The Combustion Institute, 1986.
11. M.D. Smooke, J. Crump, K. Seshadri, and V. Giovangigli, *Twenty-third Symposium on Combustion*, pp. 463-470, The Combustion Institute, 1990.
12. N. Peters and B. Rogg, *Reduced Kinetic Mechanism for Applications in Combustion System*, (Springer-Verlag, Berlin-Heidelberg, 1993), pp. 8-12.

# Species Identification and Conversion Measurements in a Carbon Tetrachloride Radio Frequency Plasma Using Coherent Raman Techniques

R. Rodriguez, and F.V. Wells

Idaho State University, Chemistry Dept., Pocatello, ID 83209 (208) 236-2613

Radio frequency plasmas are used in the electronics industry in various phases of microcircuitry processing. Deposition and etching are two key areas where these types of plasmas are used. In recent past, carbon tetrachloride,  $\text{CCl}_4$ , has been used in the etching of metals such as aluminum.<sup>1</sup> However, one of the problems associated with using this gas as an etchant is the formation of a glow polymer which coats the walls of the chamber and can interfere with the etching.<sup>2</sup>

The identity of the glow polymer is not exactly known, but it appears to be a polychloroethylene-acetylene mixture. Partial pressure mass spectral studies indicate that the predominate stable products of the decomposition of  $\text{CCl}_4$  in the plasma are  $\text{Cl}_2$  and the polymer.<sup>3</sup> This can be seen in Figures 1a and 1b which show the difference in the mass spectra with just  $\text{CCl}_4$  flowing in the reactor and with the plasma ignited.

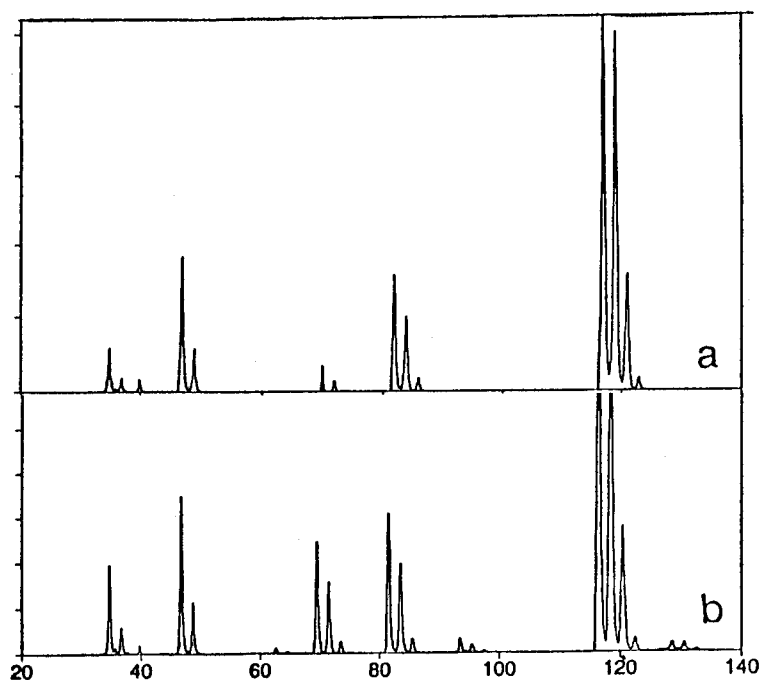


**Figure 1. Mass Spectral Data of  $\text{CCl}_4$  in the Plasma Reactor**  
 a) Mass spectrum with no plasma    b) Mass spectrum with plasma  
 Note the primary difference is in the peaks near 70 amu which correspond to  $\text{Cl}_2$ , and the smaller peaks near 97 amu which correspond to dimerization.

The use of coherent Raman techniques in probing the plasma gives more direct evidence of the species present in the plasma. The overlap of multiple laser beams defines the probing volume which is on the order of a cubic millimeter. Various regions of the plasma can be explored



using this technique rather than sampling just one region of the chamber which is the case with partial pressure mass spectrometry.

The experimental arrangement consists of a 6.6 L aluminum parallel plate cylindrical reactor. The diameter of the reactor is 0.23 m and the water cooled electrodes are circular with a 0.11 m diameter. There are four window ports on the reactor to provide for laser beam access. The flow of  $\text{CCl}_4$  and the overall constant pressure in the chamber were maintained by electronic mass flow controllers. A box coherent Stokes Raman scattering, CSRS, arrangement was used to provide maximum spatial resolution. A doubled Nd:YAG laser beam split into two beams, and a 355 nm pumped dye laser beam were focused into the plasma chamber. The CSRS signal was detected after filtering and dispersion through a single grating monochromator. Profiling of the reactor volume was accomplished by raising or lowering the reaction chamber and by translating it toward or away from the laser source.

Calibration curves for concentration measurements were generated by flowing  $\text{CCl}_4$  and  $\text{Cl}_2$  into the chamber in the absence of a plasma. The 459 band of  $\text{CCl}_4$  and the  $554\text{ cm}^{-1}$  of  $\text{Cl}_2$  were used in the calibration and the subsequent concentration and conversion measurements. In addition the bandwidth of the profile allowed for determination of the vibrational temperature since hot bands contribute even at room temperature.

Studies to date have focused on the effect of flow rate and radio frequency power on the conversion of  $\text{CCl}_4$ . Typical results from a profiling study of  $\text{CCl}_4$  signal strength carried out along an axis at a height corresponding to the center of the plasma are given in Figure 2. The profile extended from the center of the electrode along a line to a place near the window on the reactor. Note that the edge of the platen occurs at about 50 mm.

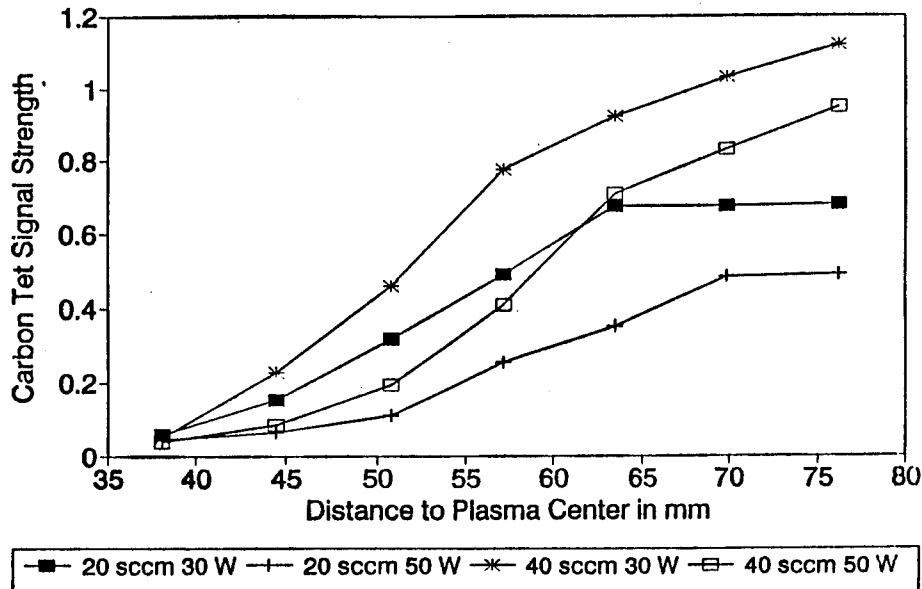


Figure 2. CSRS Signal at  $459\text{ cm}^{-1}$  as a Function of Distance from the Plasma Center. The different curves indicate the relative importance of power and flow rate on the conversion of  $\text{CCl}_4$  to products.

From these studies it is apparent that conversion of the  $\text{CCl}_4$  varies as a function of distance from the center of the plasma, actually outside the region between the two parallel plates. Within the parallel plate region apparently nearly 100% conversion is taking place. This differs from other plasma studies on  $\text{GeH}_4$  and  $\text{SiH}_4$  using CARS where the conversion was a maximum of 60% in the case of  $\text{GeH}_4$ .<sup>4</sup> Like  $\text{CCl}_4$ ,  $\text{GeH}_4$  also polymerizes in plasma environments to give long chain polygermane chains. The difference however could be that the maximum power/area in the other study was less than half the power in these studies.

Figure 2 shows how the conversion varies with flow rate and power. At 20 sccm the conversion at all points (except within the plates) is larger than the conversion at higher flow rates both for the 30 and 50 watt cases. In addition the 50 W of radio power caused more conversion at all points outside the platen chamber as compared to the 30 W case for both flow rates. Thus the minimal conversion (highest carbon tetrachloride signal) occurred for the case of lowest power and highest flow rate. The most conversion occurred for the case of highest power and lowest flow rate. It is interesting that near the edge of the plates higher power seemed to cause more conversion, but further away a lower flow rate dominated in the conversion. This is indicative that much of the carbon tetrachloride flow is bypassing the region between the parallel plates. Bypassing would be enhanced at higher flow rates and would show up as decreased conversion near the walls of the reactor whereas the region between the platens could be largely unaffected by higher flow rate.

#### References

1. D.L. Flamm, and G.K. Kerb, in Plasma Etching, (Auciello and Flamm eds.), Academic Press, (1989).
2. D.W. Hess, Plasma Chem. Plasma Proc., 2, 141 (1982).
3. F.V. Wells, Unpublished Results
4. J.W. Perry, P.Y.H. Shing, and C. E. Allevato, Appl. Phys. Lett., 52, 2022 (1988).

## **Laser Light-Scattering Interferometry for Real-Time Diagnostic Studies of Aerosols Produced by a New High-Efficiency Nebulizer**

Akbar Montaser and Huiying Liu

Department of Chemistry, George Washington University, Washington, DC 20052  
Telephone: 202-994-6480

### **1. INTRODUCTION**

Laser light-scattering interferometry or the Phase/Doppler technique has been used in a wide variety of particle-sizing applications, including diagnostic studies of combustion processes, nozzle sprays, and droplets in the atmosphere [1-5]. In this technique, radiation from a laser is split into two or four beams, the beams are focused and crossed over a very small measurement volume. As the droplets or particles pass through the intersection of the laser beams, scattering occurs and temporal and spatial frequencies of the droplets or particles are recorded to obtain droplet velocities, diameter, and concentration. The principle behind this measurement technique is similar to that for the laser Doppler velocimetry, except that scattered light is detected at large angle using two or more photodetectors. If a two-beam system (1D or one-component system) is used, particle size (0.5 to 10,000  $\mu\text{m}$ ) and particle velocities can be simultaneously measured in one direction on a microsecond time scale (down to 0.8  $\mu\text{s}$ ). With the two-component system (2D system), these parameters are assessed in two directions. In short, a Phase/Doppler instrument allows measurements of temporal and spatial information for a particle field. In contrast, the droplet size measured with laser Fraunhofer diffraction [6,7] represents a line-of-sight integral measurement, and droplet velocity information cannot be obtained.

For plasma spectrochemical analysis, the test solution usually is converted into an aerosol by a variety of sample introduction devices [8]. The combination of pneumatic nebulizer and spray chamber, typically used in inductively coupled plasma (ICP) spectrometries, offers the advantages of simplicity and low cost, yet it suffers from two drawbacks: low analyte transport efficiency (usually 1-2%), and relatively large sample consumption (1-2 mL/min). These barriers limit the detection power of ICP spectrometries and preclude chemical analysis when sample size is restricted. The low transport efficiency of the pneumatic nebulization system is partly associated with the removal of large droplets from the aerosol by the spray chamber prior to introduction into a plasma. This separation is essential because the presence of large droplets in the plasma results in incomplete processes related to vaporization, atomization, excitation, and ionization. Clearly, there exists a definite need in the ICP community for a simple, low-cost nebulizer that can efficiently produce aerosol at solution uptake rate of less than 100  $\mu\text{L}/\text{min}$ .

Recently, a new high-efficiency nebulizer (HEN) was introduced into the marketplace (J. E. Meinhard Associates, Inc. Santa Ana, CA) for ICP spectrometries. Compared to the conventional pneumatic nebulizer, HEN is unique because it operates at very low sample uptake rate (down to 10  $\mu\text{L}/\text{min}$ ) at a back pressure of up to 170 psi. Our studies were conducted to gain a better understanding of aerosol formation and transport in HEN, thus contributing to the improvement of performance indices of analytical atomic and mass spectrometries. Both the primary and tertiary aerosols from a HEN were studied using light-scattering interferometers having two or four crossed laser beams. With the four-beam system, particle velocity can be measured in two dimensions ( $U_x$  and  $U_y$ ), thus providing useful information on the trajectory of the particles. As far as we know, this is the first application of a four-beam system for the diagnostic study of aerosol produced by nebulizers used in atomic spectrometry.

### **2. EXPERIMENTAL**

Two Phase/Doppler instruments were used for particle-size and particle-velocity measurements (DANTEC Measurement Technology, Mahwah, NJ). The two-beam particle dynamics analyzer (1D PDA) was equipped with a HeNe laser and a fiber PDA detector unit that included three photomultiplier tubes (PMT). The 2D PDA instrument included a 300-mW air-cooled argon-ion laser, a fiber PDA detector unit with three PMTs, and a velocity extension unit that incorporated one PMT.

Either pure water or solutions containing  $\text{HNO}_3$ ,  $\text{H}_2\text{SO}_4$ , or  $\text{NaCl}$  were nebulized by the HEN. The primary aerosol was probed spatially and temporally as a function of injector gas flow rate, sample uptake rate, and the distance from the nebulizer tip. Tertiary aerosol was inspected as it exited from a Scott-type spray chamber through a 12-mm long tube having an inside diameter of 7 mm. The solution uptake rate and injector gas flow rate for the HEN were varied from 0.011 to 1.17 mL/min and from 0.40 to 0.96 L/min, Ar, respectively. For all measurements with the HEN, a back pressure of 170 psi was maintained. For comparison, tertiary aerosol of pure water, produced by another pneumatic nebulizer (Type TR-70, J. E. Meinhard Associates, Inc.), was probed at a back pressure of 70 psi. This nebulizer was operated at solution uptake rates of up to 1.6 mL/min.

### 3. RESULTS AND DISCUSSION

#### 3.1 Effect of experimental parameters on Sauter mean diameter and span

Particle size is the most important parameter for characterizing an aerosol field. For pneumatically-generated aerosol, the Sauter mean diameter (the volume-to-surface-area ratio for the entire particle field or  $D_{3,2}$ ) is the most appropriate term to describe the droplet diameter [1-8]. The width of the droplet-size distribution is expressed by the span [4-7]. For a nearly monodisperse aerosol, the parameter span  $[(D_{90}-D_{10})/D_{50}]$  is close to zero. In this expression,  $D_{10}$ ,  $D_{50}$ , and  $D_{90}$  refer, respectively, to droplet diameters below which 10, 50, and 90% of the cumulative aerosol volume are found.

The effects of sample uptake rate on  $D_{3,2}$  and span are shown in Figures 1 and 2, respectively, for tertiary aerosol of pure water from a HEN and a TR-70 pneumatic nebulizer. Three main points may be noted at two sets of injector gas flow rates. First,  $D_{3,2}$  decreases with increasing injector gas flow rate for both nebulizers. This behavior is expected, and is similar to our previous observation [4] for a TR-50-A1 pneumatic nebulizer (J. E. Meinhard Associates, Inc.). Second, both the  $D_{3,2}$  and span for the HEN seem to increase with solution uptake rate up to 220  $\mu\text{L}/\text{min}$ , but remain constant thereafter. Third, at the same operating conditions, the HEN provides aerosols with  $D_{3,2}$ -values substantially smaller (approximately 2  $\mu\text{m}$ ) than those for the TR-70 nebulizer. Because of its smaller  $D_{3,2}$ -value and span, especially at low solution uptake rate, one should expect improved analytical performance in ICP spectrometries, particularly in relation to the reduction of matrix effects.

#### 3.2 Effect of experimental parameters on aerosol concentration and volume flux

The influence of uptake rate on the concentration (number density) of the tertiary aerosol of water is shown on Figure 3 for the HEN and the TR-70 nebulizer operated at nearly the same injector gas flow rate ( $\sim 1.00$  L/min). Note that the concentration of aerosol from the HEN at each sample uptake rate is larger than that of the TR-70 nebulizer. A more important parameter, from an analytical point of view, is the volume flux of aerosol in the plasma, i.e., the total volume of the particles (depends heavily on the volume mean diameter) passing a cross-sectional area in a given direction per unit time [4,5]. The effect of sample uptake rate on the volume flux is illustrated in Figure 4. The experimental conditions are similar to those for Figure 3. At solution uptake rate less than 220  $\mu\text{L}/\text{min}$ , volume flux of aerosol from the HEN is larger than that for the TR-70 nebulizer while an opposite trend is found at higher uptake rates. According to Sharp [9,10], droplets with diameter less than 8  $\mu\text{m}$  contribute most significantly to the signal-to-noise ratio. The accumulated volume (not shown in the Figures) due to droplets having a diameter less than 8  $\mu\text{m}$  is 90% for the HEN compared to 55% for the TR-70 nebulizer. Thus, even though volume flux is larger at high solution uptake rates for the TR-70 nebulizer, the signal-to-noise ratio cannot be improved significantly due to the presence of the larger droplets.

#### 3.3 Effect of experimental parameters on droplets velocity

Knowledge of droplet velocity is important for plasma spectrometry because of two main reasons. First, at very high velocities, droplets may not stay in the plasma long enough to undergo adequate vaporization, atomization, excitation, and ionization. Second, droplets having different diameters and velocities produce emission at different locations in the plasma, thus leading to signal fluctuation. Correlation plots for droplet diameter-velocity are presented in Figure 5 for primary and tertiary aerosol from the HEN at a sample uptake rate of 0.085 mL/min.

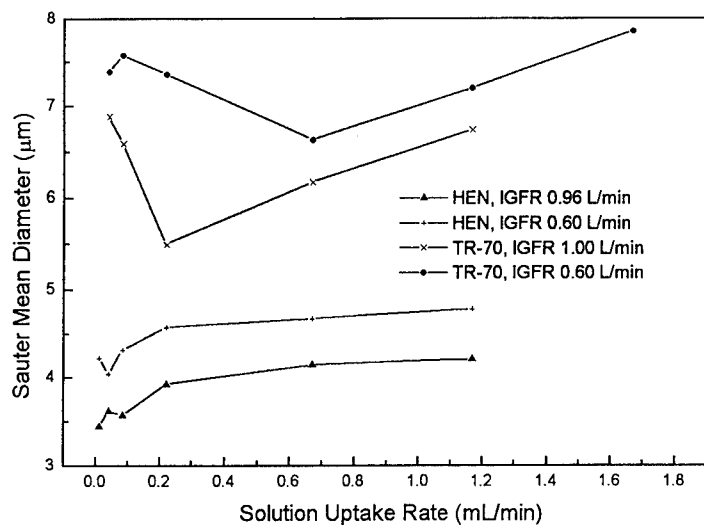


Fig. 1. Effect of solution uptake rate on Sauter mean diameter of tertiary water aerosol produced by HEN and TR-70. IGFR: injector gas flow rate

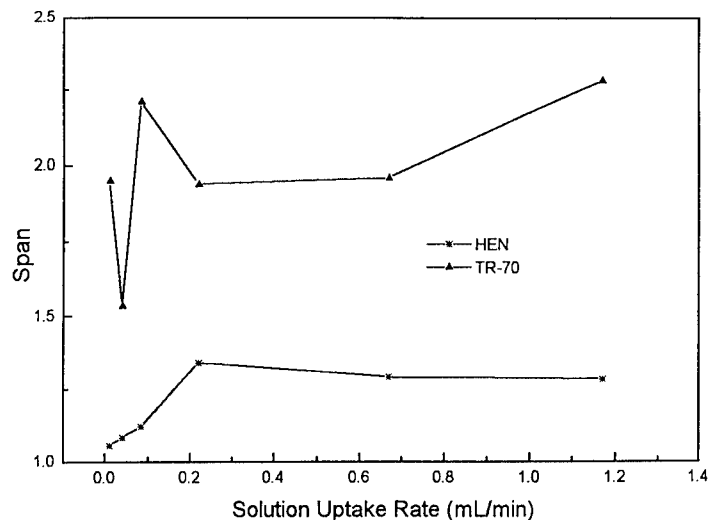


Fig. 2. Effects of solution uptake rate on span of tertiary water aerosol produced by HEN and TR-70 at injector gas flow rate 0.96 and 1.00 L/min, respectively.

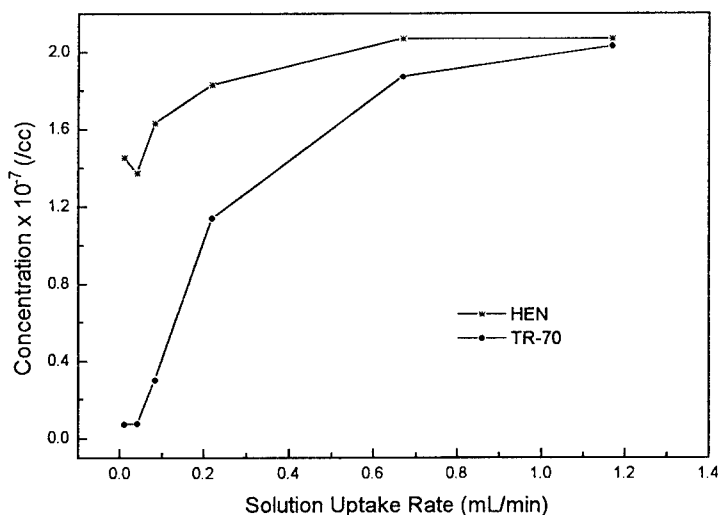


Fig. 3. Effect of solution uptake rate on the concentration of the tertiary water aerosol produced by HEN and TR-70 at injector gas flow rate 0.96 and 1.00 L/min, respectively.

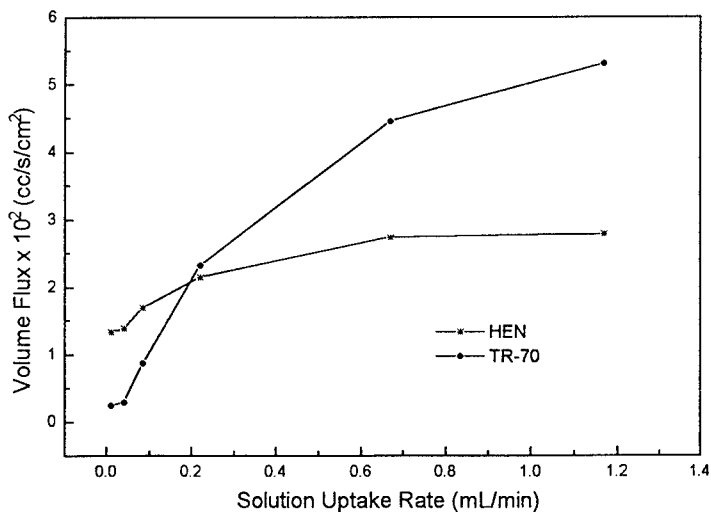


Fig. 4. Effect of solution uptake rate on the volume flux of tertiary water aerosol generated by HEN and TR-70 at injector gas flow rate 0.96 L/min and 1.00 L/min, respectively.

A wide velocity distribution is observed for the primary aerosol, both for the  $U_y$  and  $U_x$  components (Figure 5A and 5B, respectively). The axial velocity for most primary droplets is approximately 20 m/s. Note that most tertiary droplets (Figure 5C) travel at nearly the same velocity, much slower than the primary droplets.

The results summarized above have addressed some of our findings for primary and tertiary aerosol. During this poster presentation additional data are presented for nebulization of three solutions at different concentrations. Also, time-resolved analysis of droplet-size and velocity for both primary and tertiary will be presented.

#### 4. CONCLUSIONS

Laser-light scattering interferometry is a valuable tool for characterizing new nebulizers developed for atomic and mass spectrometry. This preliminary study on a new high-efficiency nebulizer reveals that this device produces very fine aerosol with Sauter mean diameter much smaller than that of the conventional pneumatic nebulizers. This characteristic is clearly evident at solution uptake rate less than 200  $\mu\text{L}/\text{min}$ . While a wide velocity distribution is observed for the primary aerosol, this distribution is relatively narrow for the tertiary aerosol. It is thus important to monitor the fate of droplets in the plasma in order to examine the effects of the nebulizer performances on the detection power, precision, and accuracy of analytical measurements in ICP spectrometries.

#### REFERENCES

1. W. D. Bachalo, J. Laser Applications, 33, July 1989.
2. W. D. Bachalo, W.D., Appl. Opt, 19, 363 (1980).
3. W. D. Bachalo, M. J. Houser, J. Opt. Eng. 23, 583 (1984).
4. R. H. Clifford, I. Ishii, A. Montaser, and G. A. Meyer, Anal. Chem. 62, 390 (1990).
5. R. H. Clifford, P. Sohal, H. Liu, and A. Montaser, Spectrochim. Acta. 47B, 1107 (1992).
6. A. Canals, J. Wagner, R. F. Browner, V. Hernandis, Spectrochim. Acta, 43B, 132 (1988).
7. M. A. Tarr, G. Zhu, and R. F. Browner, Appl. Spectrosc. 45, 1424 (1991).
8. A. Gustavsson "Liquid Sample Introduction into Plasmas" in Inductively Coupled Plasma in Analytical Atomic Spectrometry, A. Montaser, and D. W. Golightly, Eds., 2nd Ed. VCH, New York, 1992.
9. B. L. Sharp, J. Anal. At. Spectrom. 3, 613 (1988).
10. B. L. Sharp, J. Anal. At. Spectrom. 3, 939 (1988).

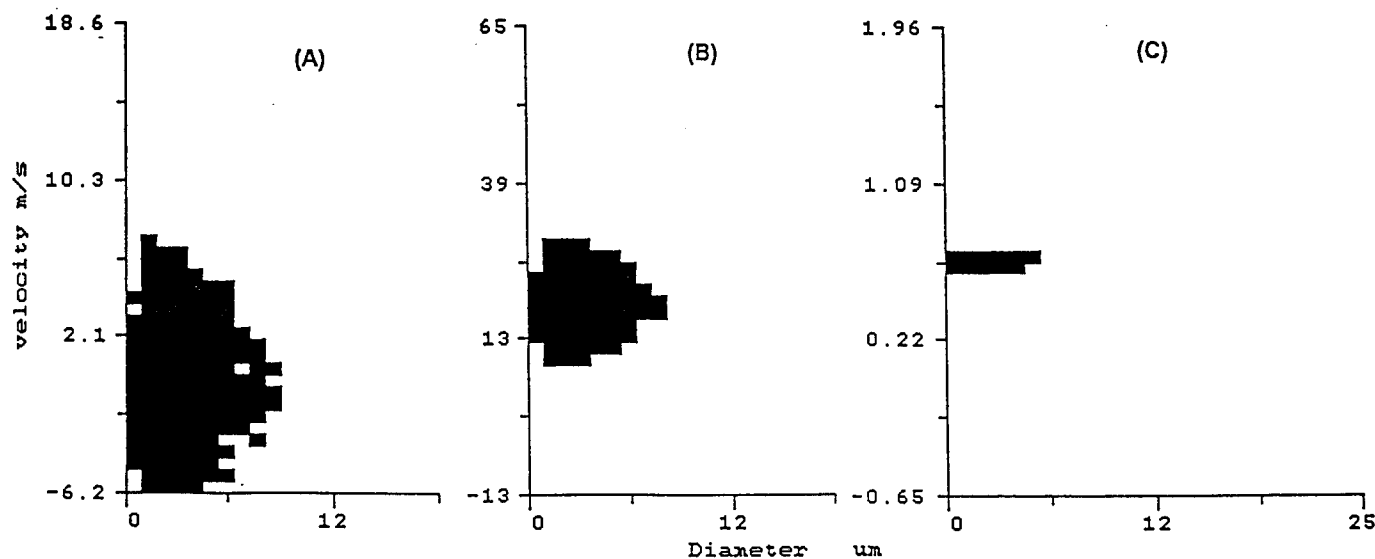


Fig. 5. Velocity-diameter correlation plots for aerosols generated by HEN at injector gas flow rate of 0.96 L/min and solution uptake rate of 0.085 mL/min. (A) and (B): Velocity ( $U_y$ )-diameter and velocity ( $U_x$ )-diameter correlation plots of primary aerosol at the center of the spray located 3.5 cm from nebulizer tip, respectively. (C): Velocity ( $U_x$ )-diameter correlation plot of tertiary aerosol.

(A) (B) (C)

# Trapping of Laser Desorbed Ions in an Ion Trap Mass Spectrometer Using a Gated RF Field

G. C. Eiden, A. W. Garrett, M. E. Cisper, N. S. Nogar, and P. H. Hemberger

Chemical Sciences and Technology Division; Los Alamos National Laboratory

Los Alamos, New Mexico, USA; 505-665-4896.

We report a new method for trapping laser desorbed ions in a quadrupole ion trap mass spectrometer (ITMS). This method, gated RF trapping, improves the trapping efficiency by over two orders of magnitude over previous methods. If the RF trapping field is applied before the laser fires, there will be a large potential barrier for injection of ions into the trap.<sup>1</sup> In general, ions either have insufficient energy to penetrate the entrance barrier, or they penetrate the entrance barrier and pass through the trap because the entrance and exit barrier heights are the same. Collisions reduce the kinetic energy of desorbed ions and increase the probability of trapping. Gated RF trapping takes advantage of the risetime of the RF in the ITMS: the laser is fired early in the rise of the RF and ions are presented with a small potential barrier to entry into the trap, but by the time the ions cross the trap the barrier has risen substantially, hindering their escape. Ions are more efficiently trapped than by buffer gas collisions alone and good sensitivity is obtained at very low buffer gas pressures ( $10^{-5}$  Torr) allowing high mass resolution operation. This simple picture is complicated by factors such as Debye shielding, plume reactions, and buffer gas collisions. In this paper, we describe the effects of laser-to-RF phase and delay, and buffer gas pressure and composition.<sup>2,3</sup>

The apparatus is based on a Finnigan-MAT ITMS and a Questek XeCl excimer laser.<sup>4</sup> Trimethylphenyl ammonium iodide (TPA-I) was desorbed from a direct insertion probe guided through a hole in the ring electrode. The laser pulse (308 nm;  $3\text{--}9 \times 10^5$  W/cm<sup>2</sup>) is fired during the rising edge of the trapping RF potential (Fig. 1). Mass spectra were acquired with either the ITMS software or by digitizing the ion signal directly. Spectra were recorded while varying laser-to-RF delay in steps of either 10  $\mu$ sec or 50 nsec (coarse and fine steps corresponding to variations of delay and phase, respectively). Signal vs delay and phase have been measured for variation of  $V_{\text{max}}$  (the steady state RF amplitude; Fig. 1), buffer gas pressure and composition, ring electrode DC potential, and ion mass. The data have also been plotted against barrier height by converting delay to RF potential and then to barrier height using the pseudopotential model.<sup>1</sup> The digitized data allow greater insight into the laser desorption of TPA-I by resolving modest isobaric interferences. For example, we observe a doublet peak at 254 Da which we assign to  $\text{I}_2^+$  (253.81 Da) and a hydrocarbon derived from TPA-I (observed  $m/z$  254.13). The predicted splitting is  $0.29 \pm 0.01$  Da and the observed splitting is  $0.32 \pm 0.02$  Da. The resolution and mass accuracy are thus sufficient to determine the presence of molecular iodine in the observed cation spectrum.

The pseudopotential model approximately describes the motion of trapped ions, but in our experiment, the boundary conditions used in the derivation of the pseudopotential model do not apply. However, the model provides a framework for discussing the signal vs delay and barrier height data. Based on our computer simulations of laser desorption using the Ion Trap SIMulation (ITSIM) programs by Julian, *et al.*,<sup>5</sup> trapping occurs (or not) in the first pass of an ion through the trap; simulation and experiment are in qualitative agreement. The signal vs delay behavior can be explained by the potential barrier model as follows. When the laser is fired, the RF amplitude is low (early delay and/or small  $V_{\text{max}}$ ) and ions can penetrate the entrance barrier. As ions cross the trap, the RF increases enough that the ions are reflected and

trapped. Thus, the rising signal at short delay in Figure 4 corresponds to a potential barrier that is sufficiently large to trap the ions when they reach the far side of the trap. The falling signal at later delay times corresponds to a potential barrier that is too large to allow ions to penetrate the trap; they are reflected at the entrance. Similarly, the falling edge is associated with reflection of ions at the entrance to the trap. The signal reaches a maximum at an intermediate time when these two effects are balanced. The signal vs delay also depends on phase, Debye shielding, buffer gas pressure and composition, and ring electrode DC potential.

Figure 2 shows the cation mass spectrum observed for simultaneous laser desorption/ionization and electron impact ionization (EI). Peaks at  $m/z$  121 and 197 are 10 times as intense as the  $271^+$  peak. EI alone shows only masses due to residual air and hydrocarbon species. A series of peaks spaced by 74-76 Da, beginning at  $121^+$ , is observed in both the LD only and LD/EI mass spectra. This series of peaks is due to sequential addition of phenylene with the  $121^+$  ion in the desorption plume. The peaks marked with \* in Fig. 2 appear in only the LD/EI spectrum and indicate the nature of the neutral species in the laser plume. Most of these peaks consist of iodo-hydrocarbons and metallic species from the probe tip material. Specifically, we observe  $I^+$ ,  $HI^+$ ,  $CH_3I^+$ , and  $C_6H_5I^+$ .

Figure 3a shows the phase dependence of the  $197^+$  signal. The curves have been normalized to facilitate comparison of their shapes and the phase shift. For the delay range shown, there is a  $90^\circ$  shift in  $\phi_{\max}$ , the phase angle at maximum signal. Similar data for other masses are plotted in Figure 3b as  $\phi_{\max}$  vs delay.  $\phi_{\max}$  is  $230^\circ$ - $340^\circ$  for cations and  $0^\circ$ - $90^\circ$  for anions. On the time scale of the RF period ( $\mu\text{sec}$ ), ions can move significant distances (1-3 mm) at the velocities typical of laser desorption. Ions launched at favorable phase angles can penetrate the interior of the trap rapidly. Ions launched at less favorable phase angles remain near the electrodes longer. Depending on phase, ions are initially either accelerated or decelerated thereby affecting how far into the trap the ion moves in the first cycle of the RF after the laser fires. This will affect how strong a field the ion sees in subsequent cycles of the RF. This picture is consistent with deep modulation of the ion signal with phase at long delay (and less modulation at short delay) because long delays correspond to ions attempting to penetrate large potential barriers at the trap entrance.

Buffer gas collisions reduce the kinetic energy of the ions which should shift the signal vs delay curves to shorter delay (lower barrier height). The shift to shorter delay should occur for either an increase in the buffer gas pressure or mass. This is the opposite of what is experimentally observed (Figure 4). Collisions also have the effect of broadening the initial, narrow angular distribution of trajectories characteristic of laser desorption,<sup>6</sup> which also affects trapping efficiency. High buffer gas pressure also damps ion motion and ions tend to occupy a smaller volume near the center of the trap; this leads to better sensitivity and mass resolution.<sup>7</sup> Figure 4 shows the effect of He pressure on the signal vs delay. Two aspects of pressure effects are considered, absolute signal levels and the shape of the signal vs delay curves. The signal increases by a factor of  $\sim 8$  for an increase in pressure from  $7 \times 10^{-7}$  Torr to  $5 \times 10^{-4}$  Torr. The data in Figure 4 have been normalized for comparison of their shapes, but in all cases, the signal is higher at higher pressure and at any delay time. The signal vs delay curves for the  $121^+$  signal are similar over the range of pressures in Fig. 4. The  $197^+$ ,  $271^+$ ,  $347^+$ , etc., curves show a more pronounced pressure dependence, especially for the falling edges. The pressure behavior of the  $271^+$  signal may be due to different velocity distributions and trajectories for the  $121^+$  ions versus higher mass reaction products. Low mass ( $\leq 136$ ) ions formed by dissociation of the parent and high mass ( $> 136$ ) ions formed by reaction of the parent or its fragments will have different trajectories. At higher pressure the  $271^+$  ions are formed more efficiently by



collisional stabilization of the reaction complex, but the  $271^+$  ions are also formed earlier in the plume expansion as pressure is increased. This may have the effect of producing  $271^+$  ions with higher kinetic energies, leading to the observed shift in the higher pressure curves to longer delay.

The anion and cation signal vs delay are compared in Figure 5. The anion curve is broadened relative to the cation curve. We invoke different explanations for the broadening on the rising and falling edges. We begin by considering differences in Debye shielding<sup>8</sup> for anions and cations. Most of the electrons produced by the laser pulse are immediately ejected from the trap by the RF field present when the laser fires (RF  $\sim 100$  V/cm); some remain due to the shielding effects of the cations. This leaves a nominally charge neutral plume: the cation charge balanced by anions and electrons. Unshielded electrons are *unable* to penetrate the barrier since the barrier height scales as  $1/\text{mass}$ . As the plume moves into the trapping volume, electron trajectories become unstable (the stability limit for an electron in the ITMS is 0.007 Volts) and the electrons are stripped from the plume. Also, the plume expands as it moves away from the probe, further reducing the shielding of both cations and anions. The rapid loss of electrons, a cation to anion ratio of 20-100:1,<sup>4</sup> and plume expansion leads to much lower Debye shielding of the cations compared to the anions. We therefore predict that at the entrance to the trap the more highly shielded anions require a larger RF potential for effective trapping to occur, that is, the anion signal vs delay curves are shifted towards longer delay time (larger barrier), in agreement with the experiment. The rising edges of the signal vs delay curves correspond to ion loss (or trapping) at the far side of the trap; Debye shielding is expected to be unimportant here because of plume expansion and ejection of the electrons. However, the disparate shielding for cations and anions that occurs early in the plume expansion results in different desorption velocities and in different behavior at the far side of the trap. Specifically, anions will have lower kinetic energies than cations and should be trapped at a lower RF amplitude (shorter delay), as observed. Lower velocities also allow more time for the RF amplitude to increase as the ions cross the trap. It is therefore not surprising that the anion signal rises as much as 40  $\mu\text{sec}$  *earlier* than the rise in the RF potential.

Figure 6 shows signal vs delay data for four masses plotted against barrier height. If laser desorption processes result in similar velocities for all ions, then the kinetic energy of the ions would be proportional to their mass and, based on the trapping model above, the signal vs barrier height curves should not overlap. On the other hand, if the kinetic energies of all ions are similar, then the curves should overlap. As Figure 6 shows, the situation for LD/ITMS of TPA-I is more complicated. The data taken at a phase angle of  $180^\circ$  exhibit falling edges whose position is proportional to mass, suggesting ions desorbed with similar velocities. The data taken at other phase angles show curves which are better overlapped than the data at  $180^\circ$ , but the overlap is not perfect.

1. F. G. Major and H. G. Dehmelt, *Phys. Rev.*, **170**, 91 (1968).
2. G. C. Eiden, A. W. Garrett, M. E. Cisner, N. S. Nogar and P. H. Hemberger, *Int. J. Mass Spectrom. Ion Processes*, manuscript in preparation, (1993).
3. G. C. Eiden, M. E. Cisner, M. L. Alexander, P. H. Hemberger and N. S. Nogar, *J. Am. Soc. Mass Spectrom.*, **4**, 706-709 (1993).
4. M. L. Alexander, P. H. Hemberger, M. E. Cisner and N. S. Nogar, *Anal. Chem.*, **65**, 1609-1614 (1993).
5. R. K. Julian Jr., H.-P. Reiser and R. G. Cooks, *Int. J. Mass Spectrom. Ion Processes*, in press (1993).
6. H. M. Urbassek and D. Sibold, *Phys. Rev. Lett.*, **70**, 1886-9 (1993).
7. G. C. Stafford Jr., P. E. Kelley, J. E. P. Syka, W. E. Reynolds and J. F. J. Todd, *Int. J. Mass Spectrom. Ion Processes*, **60**, 85-98 (1984).
8. S. C. Beu, C. L. Hendrickson, V. H. Vartanian and D. A. J. Laude, *Int. J. Mass Spectr Ion Proc.*, **113**, 59-79 (1992).

FIGURE 1

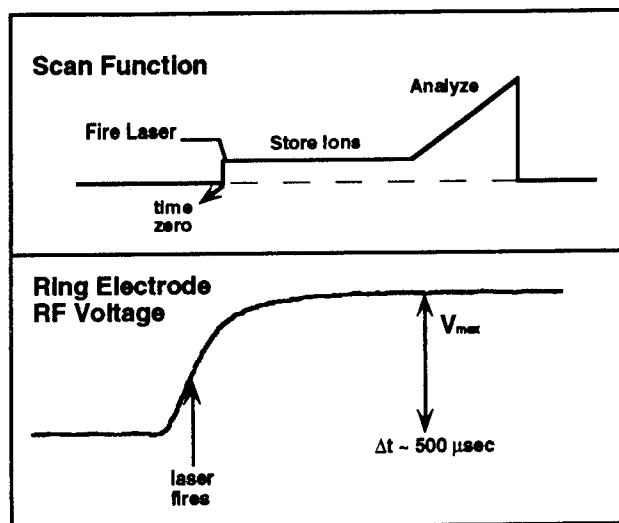


FIGURE 2

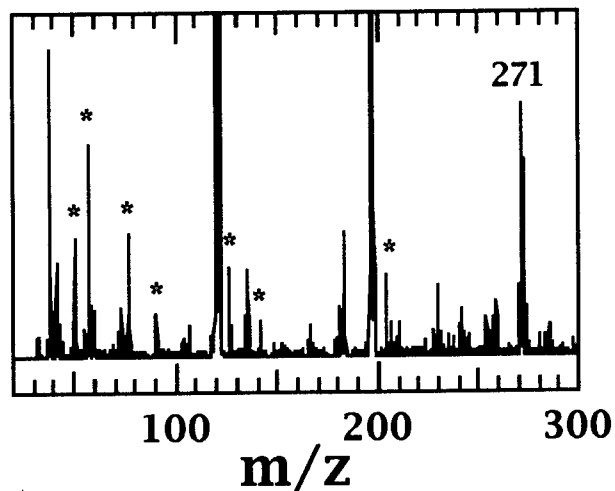


FIGURE 3

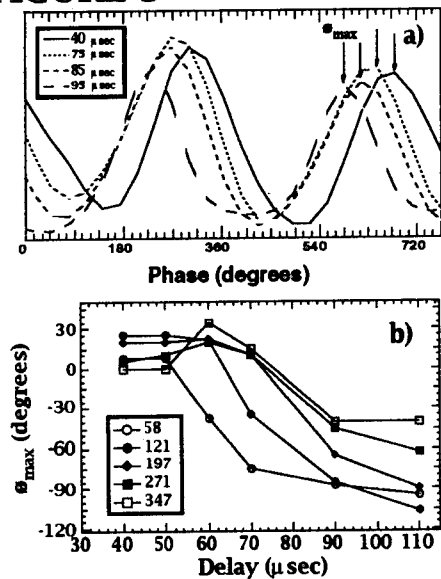


FIGURE 4

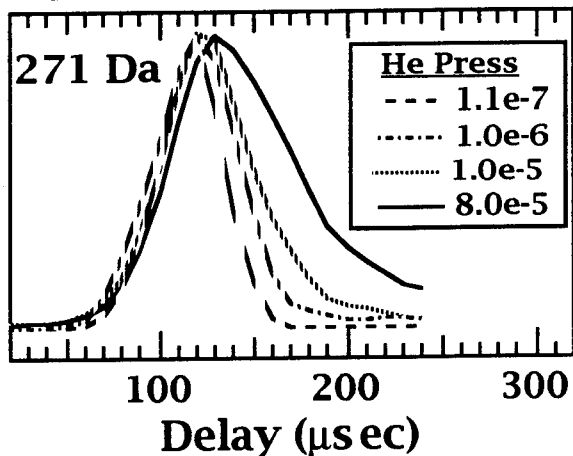


FIGURE 5

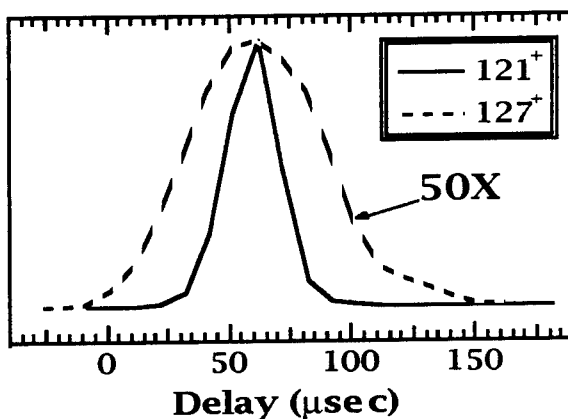
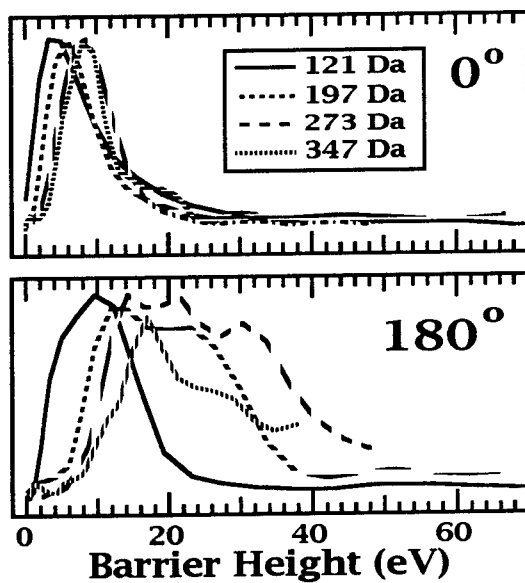


FIGURE 6



## **Potential Application of Three Laser-Based Bacteria Detection Techniques to The Meat Processing Plants - A Review**

Nee-Yin Chou

CW Optics, Inc., 117 Quantico Loop, Yorktown, VA 23693-2611, (804) 867-7893

Yud-Ren Chen

Instrumentation and Sensing Lab, USDA, ARS, BARC, Bldg. 303, BARC-EAST  
10300 Baltimore Avenue, Beltsville, MD 20705-2350, (301) 504-8450

### **INTRODUCTION**

This review was prompted by the concerns of the recent serious incidence of bacterial contamination, especially in raw or partially cooked meat. There are 4 million cases of food poisoning reported annually, most of them are caused by bacteria. Recent GAO testimony on food safety stated that the meat inspection system has changed little since it was first instituted in 1906 and is not capable of addressing today's concerns about microbial contamination (1).

Our initial investigation was centered on the rapid optical techniques for the detection of *Salmonella* on meat carcass. The techniques also can be applied to other bacterial species. The detection of bacteria in food using conventional culture and serological identification methods is often lengthy and requires costly handling and storage of food during testing. Laser-based optical detection techniques have been used to detect and identify microorganisms in simple backgrounds in the laboratory environment. The potential uses of the laser techniques for detecting bacterial contamination in meat at meat processing plants were investigated.

### **OPTICAL DETECTION METHODS**

Rapid bacteria detection methods by optical means have been centered around three major techniques, UV fluorescence, differential light scattering, and resonance Raman scattering.

#### **(1) UV Fluorescence**

When illuminated with UV radiation, the aromatic protein amino acids (tryptophan, phenylalanine, and tyrosine) in the cell walls absorb the radiation and reradiate the energy as fluorescence. The UV-excited fluorescence measurements range from the fluorescence intensity decay of different species of bacteria (2) to the time or frequency-domain measurements (3). Fluorescence detection also can be accomplished by using evanescent optical fiber sensors (4).

## **(2) Differential Light Scattering**

Distinguishable and reproducible light scattering patterns from different species of bacteria and spores in liquid suspension or airborne were investigated twenty-five years ago (5). These patterns are comprised of the angle dependence of the scattered irradiance for incident light polarized either perpendicular or parallel to the scattering plane. The elastic scattering properties can be fully described by the Mueller matrix.

One technique for measuring the Mueller matrix elements was reported by Bronk, *et al.*, (6) to determine the parameters of simple, homogeneous, spherical cell models (e.g., cell size, wall thickness, refractive index, and cytoplasm) with great precision because of the strong dependence of the features of the pattern on these parameters. However, large departures from sphericity in the cellular shapes could result in light scattering patterns that differ very much from those of spherically symmetric particles that systematic interpretation might be difficult.

## **(3) Raman and Resonance Raman Scattering**

Raman spectroscopy is a powerful tool for studying biomolecular vibrations compared with infrared studies, because of the omnipresence of water in biological cells. For example, conformational changes of chromophoric groups attached to biomolecules can be monitored by changes in the Raman spectrum. However, Raman scattering is a weak spectroscopic effect. The intensities of vibrations associated with the chromophoric portion of the biomolecule can be enhanced by a factor of  $10^6$  when the excitation and absorption frequencies are matched, as in resonance Raman. Detection of biomolecules using UV resonance Raman has been systematically studied (7, 8). Different Gram-type organisms can be distinguished with this technique (8).

## **OPTICAL BACKGROUND CONSIDERATION**

Since the initial objective was to investigate potential optical methods for bacterial detection on chicken carcasses, background signals from the skin were considered. The skin is a turbid medium where scattering is large compared with absorption. Much effort has been made in the study of light propagation in tissue due to the wide use of lasers for surgical and therapeutic applications (9). There have been some experimental studies on the transmission and reflection of UV radiation through excised human skin (10) and the fluorescence detection of endogenous protoporphyrin in human skin (11). There has been, however, little work on UV radiation optics on the skin. This is perhaps not surprising in view of the complex structure of the organ, which includes such derivatives as hair follicles, sweat glands, and sebaceous glands. Based on a numerical solution of the equation governing radiation transport in matter, Diffey (12) calculated the transmission and reflection values in human skin and derived the scattering and absorption coefficients.

## SIGNAL LEVEL ESTIMATION

The minimum detectable concentration of any bacteria species is dependent on the signal-to-noise ratio. Signal levels expected for a measurement of Bacteria-A on a chicken carcass that contains Bacteria-A and other bacteria are examined. Scattered light arising from nine sources must be considered. The origins of the scattered light include: reflected laser light from the chicken carcass, reflected laser light from the Bacteria-A, reflected laser light from the other bacteria, fluorescence of the chicken carcass, fluorescence of the Bacteria-A, fluorescence of the other bacteria, resonance Raman scattering from the chicken carcass, resonance Raman scattering from the Bacteria-A, resonance Raman scattering from the other bacteria.

A signal is detectable if the signal-to-noise ratio (SNR) is greater than 1. The SNR was estimated to be

$$SNR = \frac{K_1 N_S N_I N_P}{[K_2 N_S N_I N_P + K_3 N_P + K_4]^{1/2}} \quad (1)$$

where  $N_S$  is the number of Bacteria-A that are illuminated by the laser,  $N_I$  is the number of indicator molecules contained in each Bacteria-A, and  $N_P$  is the number of pulses in a series of measurements. The numerator represents the signal current, where  $K_1$  is a function of the detector quantum efficiency  $\eta$ , gain  $G$ , wavelength  $\lambda$ , the transmittance of optical filter or filter-spectrometer combination, and the scattering or fluorescence cross section  $\sigma$ .  $K_2$  is the product of  $K_1$  and  $2eB$ , where  $e$  is electronic charge and  $B$  is the detector bandwidth.  $K_3$  is a function of  $\eta$ ,  $G$ ,  $\lambda$ ,  $e$ ,  $B$ , and the Raleigh line.  $K_4$  is a function of the dark current.

The  $K$ s can be calculated for resonance Raman, fluorescence or differential light scattering signals. We calculated the  $K$ s for the resonance Raman based on the following assumptions: a uniform distribution of bacteria, a typical Nd:YAG laser operating at 266 nm with a 30 Hz pulse rate and a 10 mJ pulse energy, a Raman shift of 1350  $\text{cm}^{-1}$  from the 266 nm line (8), an approximated resonance Raman cross section of  $10^{-25} \text{ cm}^2 \text{ sr}^{-1}$  per molecule (13), a system throughput of  $10^{-1}$  at the desired wavelength and  $10^{-8}$  at the Raleigh line, a collection solid angle of  $4 \times 10^{-3} \text{ sr}$ , a reflection coefficient of  $10^{-1}$  for the chicken carcass and the bacteria (12), a detector dark current of  $10^{-10}$  amps, a gain of  $10^6$ , a quantum efficiency of 0.25, and a detector bandwidth of  $10^8 \text{ Hz}$ . Using  $N_P$  equal to 100 pulses and solving for the product of  $N_S$  and  $N_I$  yields

$$N_S N_I = 7.6 \times 10^{11} \quad (2)$$

for a SNR of 1.

The large product is due to the high optical background caused by the Rayleigh line. This intense background is not present in the resonance Raman measurements from bacteria suspended in solution. It is possible to reduce the background and increase the signal by using an appropriate laser wavelength to approach the resonance condition. Because resonance Raman scattering does not involve a virtual intermediate state, the scattering time

is slow ( $10^{-12}$  to  $10^{-5}$  seconds). If the scattering time associated with the indicator molecules is long (approximately  $10^{-8}$  seconds), it is possible to use a picosecond laser and appropriate gating circuitry to reduce the background.

## APPLICATION TO MEAT PROCESSING PLANTS

Because resonance Raman and laser fluorescence techniques can provide real-time detection of bacteria, they have potential application in the meat processing industry. Further work on signal enhancement and background reduction need to be investigated.

## REFERENCES

1. J. W. Harman, Government Accounting Office Report, GAO/T-RCED-93-10 (1993).
2. B. V. Bronk and L. Reinisch, *Variability of Steady-State Bacterial Fluorescence with Respect to Growth Conditions*, Appl. Spectrosc. **47** 436 (1993).
3. J. R. Lakowicz, *Principles of Frequency-Domain Fluorescence Spectroscopy and Applications to Protein Fluorescence*, Cell Structure and Function by Microspectrofluorometry, Academic Press (1989).
4. R. A. Ogert, L. C. Shriver-Lake, and F. S. Ligler, *Toxin Detection Using a Fiber Optic-Based Biosensor*, SPIE Proceedings **1885** 11 (1993).
5. P. J. Wyatt, *Differential Light Scattering: a Physical Method for Identifying Living Bacterial Cells*, Appl. Opt. **7** 1879 (1968).
6. B. V. Bronk, W. P. Van de Merwe, and M. Stanley, *In Vivo Measure of Average Bacterial Cell Size From a Polarized Light Scattering Function*, Cytometry **13** 155 (1992).
7. N. Cho and S. A. Asher, *UV Resonance Raman Studies of DNA-Pyrene Interactions: Optical Decoupling Raman Spectroscopy Selectively Examines Minor Groove Bound Pyrene*, J. Am. Chem. Soc. **115** 6349 (1993).
8. W. H. Nelson, R. Manoharan, and J. F. Sperry, *UV Resonance Raman Studies of Bacteria*, Appl. Spectrosc. Rev. **27** 67 (1992).
9. S. J. Madsen, B.C. Wilson, M.S. Patterson, Y.D. Park, S.L. Jacques, and Y. Hefetz, *Experimental Tests of a Simple Diffusion Model for the Estimation of Scattering and Absorption Coefficients of Turbid Media from Time-Resolved Diffuse Reflectance Measurements*, Appl. Opt. **31** 3509 (1992).
10. R. Marchesini, A. Bertoni, S. Andreola, E. Melloni, and A.E. Sichirollo, *Extinction and Absorption Coefficients and Scattering Phase Functions of Human Tissues in Vitro*, Appl. Opt. **28** 2318 (1989).
11. K. Konig, A. Ruck, and H. Schneckenburger, *Fluorescence Detection and Photodynamic Activity of Endogenous Protoporphyrin in Human Skin*, Opt. Eng. **31** 1470 (1992).
12. B. L. Diffey, *A Mathematical Model for Ultraviolet Optics in Skin*, Phys. Med. Biol. **28** 647 (1983).
13. S. D. Christensen, *Raman Cross Section of Chemical Agents and Simulants*, Appl. Spectrosc. **42** 318 (1988).

# Fluorescence Lifetime Measurements in a Flow Cytometer by Amplitude Demodulation Using Digital Data Acquisition Technique.

C.Deka, J.A. Steinkamp; Group LS-1, MS M888, Los Alamos National Laboratory, Los Alamos, NM 87545, Telephone 505-665-1939, FAX 505-665-3024

and

Larry A. Sklar; Cytometry, School of Medicine, University of New Mexico, Albuquerque, NM 87131, Telephone 505-277-7249.

**INTRODUCTION:** In this paper we demonstrate, for the first time, fluorescence lifetime measurements by amplitude demodulation from fluorescence signals with time dependent amplitudes in a flow cytometer using digital data acquisition techniques. The lifetime measurements in the flow cytometer have been compared to standard fluorescent lifetime measurements in bulk suspensions. The present technique provides a method for analyzing chemical and biological species based upon their individual excited state lifetime. We also discuss the factors influencing the accuracy of the measurements by this method and the possible solutions to those problems.

The adaptation of the phase-sensitive fluorescence lifetime measurement technology<sup>[1]</sup> to flow cytometry<sup>[2,3]</sup> over the last few years has generated much interest in the biochemical and biological research community. In all the work reported until now on the phase-sensitive flow cytometer technology, the measurement of fluorescence lifetimes has been based upon the capability to measure only the phase shift of the modulated fluorescence signal of a fluorescent particle or cell relative to the modulated excitation signal<sup>[2,3,4]</sup>. However, it is well known from the principles of frequency-domain fluorescence spectroscopy that the amplitude demodulation index of a fluorescence signal contains valuable information relating to the fluorescence dynamics of a system under investigation. It can serve as an effective and necessary parameter, complimentary to the measured phase shift, to provide a quick evidence of any heterogeneity of the fluorescence decay or the presence of excited state reactions<sup>[5]</sup> in the system in a single measurement performed at a single frequency. Also, when measured over many frequencies, the information contained in the amplitude demodulation of the fluorescence signal can be used to extract intrinsic fluorescence lifetimes as effectively as the information on the phase shift<sup>[6]</sup>.

In contrast to conventional cuvette based frequency-domain lifetime spectroscopy, the modulated fluorescence signals in flow cytometer have a time dependent amplitude which makes the measurements rather complicated. Pinsky *et. al.*<sup>[4]</sup> have used a phase sensitive signal limiter which converted the fluorescence signal with a time dependent amplitude to one with a constant amplitude and measured the phase shift of the resulting constant amplitude signal. However, in that method the information on the amplitude demodulation is permanently lost. In this paper we demonstrate, for the first time, direct fluorescence lifetime measurements in a flow cytometer based upon the information contained in the amplitude demodulation of a fluorescence signal without altering or modifying the original signal.

**THEORY:** In a flow cytometer fluorescent cell/particles flow across a focused cw laser beam which is sinusoidally modulated in intensity. If the spatial mode of the laser is TEM<sub>00</sub> with a gaussian cross sectional intensity profile then a fluorescent particle traveling across the laser beam experiences an excitation signal of the form:

$$\mathcal{E}(t) = \mathcal{E}_0 [1 + m_{ex} \sin(\omega t)] e^{-b(t-t_0)^2} \quad (1)$$

where  $m_{ex}$  is the modulation depth,  $\omega = 2\pi f$  ( $f$  is the modulation frequency) and  $\mathcal{E}_0$ ,  $b$  and  $t_0$  are the parameters of the gaussian envelope profile of the excitation signal.

The solution of the rate equation for the general case of a multi-exponential system due an excitation given by equation (1) is of the form

$$N(t) = F_o \left( \sum_i \alpha_i \tau_i \right) \left\{ [1 + m_{ex} M_{eff} \sin(\omega t - \phi_{eff})] e^{-b(t-t_o)^2} + \sum_i f_i e^{-t/\tau_i} \int_0^t 2b(t-t_o) e^{t/\tau_i} [1 + m_{ex} \cos(\phi_i) \sin(\omega t - \phi_i)] e^{-b(t-t_o)^2} dt \right\}. \quad (2)$$

$M_{eff}$  in equation (2) has the same meaning as the effective modulation index of the fluorescence signal in the constant amplitude phase sensitive theory.  $f_i$  is the fractional contribution,  $\tau_i$  is the fluorescence lifetime and  $\alpha_i$  is the pre-exponential factor of the impulse response corresponding to the  $i$ th component of the decay.  $F_o$  is a constant which depends on the power density of the excitation beam and the absorption cross-section of the molecules being excited. Fluorescence intensity is proportional to  $N(t)$ .

The integral in the second summation in equation (2) can not be integrated in a closed analytical form. Computer simulation has shown that its contribution to the total fluorescence signal is usually of the order of  $\pm 0.1\%$ . At  $t_o$ , the time when the fluorescent particle goes through the center of the gaussian laser beam, the value of the correction term actually goes to zero. Thus, in the neighborhood of  $t_o$  the equation (2) become identical with the approximate form presented by Steinkamp *et. al.*[2] and the amplitude demodulation index  $M_{eff}$  can be written as:

$$M_{eff} = m_{ex}^{-1} \left[ \frac{I_{\max}(t_{\max})/G(t_{\max}) - I_{\min}(t_{\min})/G(t_{\min})}{I_{\max}(t_{\max})/G(t_{\max}) + I_{\min}(t_{\min})/G(t_{\min})} \right] \quad (3)$$

where  $G(t) = e^{-b(t-t_o)^2}$ , and  $t_{\max}$  and  $t_{\min}$  are the times at which the modulated oscillating fluorescence signal goes through the maxima and minima intensities respectively. An apparent amplitude modulation lifetime  $\tau_m$  may be calculated using the relation[6]

$$\tau_m = \omega^{-1} [(1/M_{eff}^2) - 1]^{1/2}. \quad (4)$$

For practical purpose equation (3) can be further simplified if the modulation frequency is sufficiently high and the period of the sinusoidal oscillation is much smaller in comparison to the width of the envelope of the fluorescence signal. We have conducted extensive computer simulated analysis to investigate this aspect but due to limitations on the length of the present article the details of the simulation work are not discussed here. The underlying assumption leading to the simplification of equation (3) is that for sufficiently high modulation frequencies the portion of the gaussian envelope between any two consecutive maxima of the oscillating fluorescence signal may be considered linear (Figure-1). Then equation (3) can be rewritten as

$$M_{eff} = m_{ex}^{-1} \left[ \frac{1 - 2 I_{\min}(j) / (I_{\max}(j+1) + I_{\max}(j))}{1 + 2 I_{\min}(j) / (I_{\max}(j+1) + I_{\max}(j))} \right] \quad (5)$$

where  $I_{\max}(j)$  and  $I_{\min}(j)$  are the magnitudes of the  $j$ th peak (maximum) and trough (minimum) of the oscillating fluorescence signal respectively (Figure-1). The advantage of using equation (5) is that it is not necessary to keep track of the fluorescence signal as a function of time nor is there any strict requirement to know the parameters  $b$  and  $t_o$  exactly.

**EXPERIMENT:** The phase sensitive fluorescence lifetime flow cytometer has been described in detail elsewhere[2,3]. A cw laser beam at 488 nm from an water cooled Ar-ion laser (Spectra Physics Model 2025) is sinusoidally modulated at 20 MHz by passing it through a Conoptics Model 350 electro-optic modulator (EOM). The beam is then passed through a wedged-plate beam splitter. The reflected part of the beam is collected by a PMT and the signal from this PMT is used to measure the modulation depth of the excitation beam,  $m_{ex}$ . The transmitted beam is focused by a pair of crossed cylindrical lenses at the center of the flow channel. A hydrodynamically focused stream of fluorescent particles pass across the focused region of this intensity modulated laser beam. The fluorescence from the particles are detected by a PMT / pre-amplifier (Comlinear CLC 401) combination at 90° to the direction of the excitation laser beam. The fluorescence signal is digitized in a fast digital sampling oscilloscope (LeCroy 7200A) and acquired by an IBM compatible 486 PC (ZEOS 486) equipped with a National Instruments IEEE 488 data acquisition



board. The trigger level and the time base of the oscilloscope is adjusted such that only about ten periods around the maximum of the modulated fluorescence signal are acquired. At the end of the acquisition all the waveforms are analyzed by softwares developed to calculate automatically the amplitude modulation lifetime  $\tau_m$  for all the acquired events and to obtain the frequency distribution (histogram) of the lifetime data. For comparison we also generated the histogram as a function of the maximum fluorescence intensity for each event. In this experiment we have used two different types of fluorescent micro spheres from Coulter Corporation, namely, Immuno Check 5927 and DNA Check 5949. Figure-2b shows the histogram of events as a function of amplitude modulation lifetime of Immuno Check 5927 micro spheres at 20 MHz. The corresponding histogram as a function of maximum fluorescence intensity is shown in Figure-2a. Each bin of the lifetime histogram has a width of 200 ps. Figure-2c and -2d shows the histograms of maximum fluorescence intensity and  $\tau_m$  for the DNA Check 5949 micro spheres. We summarize the results of the flow cytometric experiment and compare them with data obtained on a cuvette based multi-harmonic frequency domain fluorescence lifetime machine(SLM 48000).

TABLE-1

Comparison of amplitude modulation lifetimes  $\tau_m$  of different fluorescent microspheres measured at modulation frequency 20 MHz in flow (Frequency Domain Phase Sensitive Flow Cytometer) and in bulk liquid suspension (SLM 48000).

	FLOW CYTOMETER				SLM 48000
	mean $\tau_m$	mode $\tau_m$	cv* for $\tau_m$	cv for $E_{max}$	mean $\tau_m$
Immuno Check 5927	7.09 ns	7.1 ns	2.3%	5.9%	6.8 ns
DNA Check 5949	6.91 ns	6.9 ns	2.4%	2.5%	6.8 ns

\* cv (coefficient of variation) is defined as the standard deviation divided by the mean.

**DISCUSSION:** We have demonstrated that the amplitude modulation lifetime can be measured with sufficient accuracy for modulated fluorescence signals with time dependent amplitudes in flow cytometers. In the process of this present experiment we also observed the following: (1) the amplitude modulation lifetime measured and calculated using an equation of the form given by Eq. (5) is fairly accurate at high modulation frequencies, (2) the accuracy of the amplitude demodulation lifetime measurements are more sensitive to instrumental characteristics, such as the linear dynamic range and the frequency response characteristics of the detectors used as the laser monitor (the reference signal) and the fluorescence detector (FL1) compared to phase shift measurements<sup>[2-3]</sup>. Further modifications on the detector electronics to increase the linear dynamic range as well as the useable frequency range are currently in progress.

**ACKNOWLEDGEMENT:** This work was performed at the Los Alamos National Laboratory, Los Alamos, NM, under the joint sponsorship of the United States Department of Energy, the Los Alamos National Flow Cytometry Resource (NFCR) and the National Institutes of Health (Grant Nos. P41-RR01315 and R01-RR07855). The frequency domain lifetime measurements on the bulk suspensions were conducted at the Cytometry laboratory, University of New Mexico (UNM). The authors would like to acknowledge fruitful discussions with Dr. James H. Jett and Robb Habbersett of NFCR and thank Greg Jones of UNM for his cooperation in the use of the SLM 48000 fluorescence lifetime machine.

#### REFERENCE:

1. Lakowicz, J. R. and Cherek, H., J. Biochem. Biophys. Methods, **5** (1981) 19-35.
2. Steinkamp, J. A. and Crissman, H. A., Cytometry **14** (1993) 210-216.
3. Steinkamp, J. A., Yoshida, T. and Martin, J. C., Rev. Sci. Instrum (1993), in press.
4. Pinsky, B. G., Ladasky, J. J., Lakowicz, J. R., Berndt, K. and Hoffman, R. A., Cytometry, **14** (1993):123-135.
5. Lakowicz, J. R. and Balter, A., Biophys. Chem. **16** (1982) 99-115.
6. Lacowicz, J. R., Principles of Fluorescence Spectroscopy, Plenum Press, New York and London.

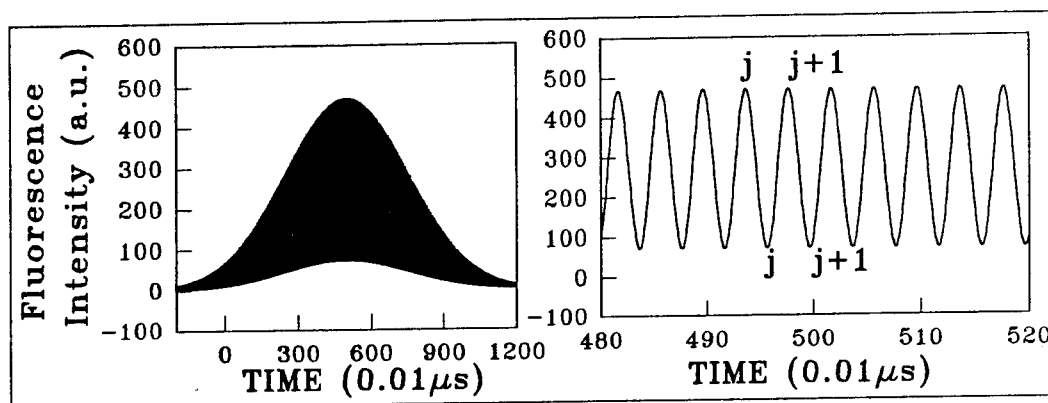


**Figure 1.** Simulated fluorescence signal at modulation frequency of 25 MHz. The graph on the right hand side is the portion of the same signal in a 400 ns time interval around  $t_0$ .

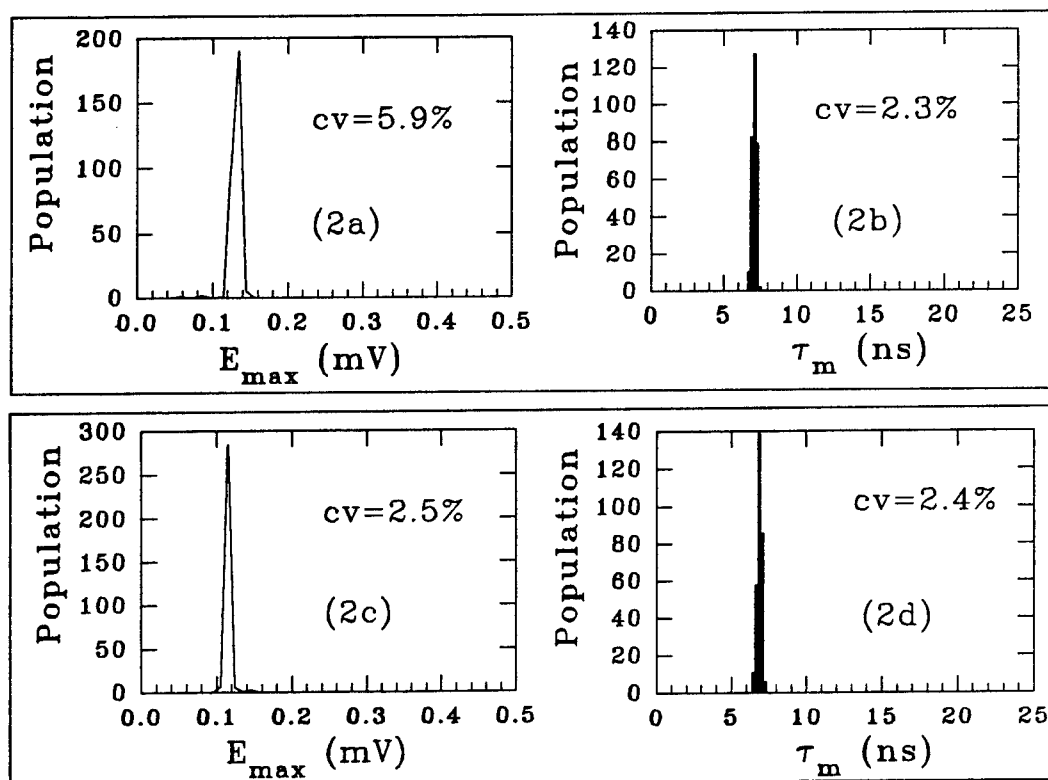


**Figure 2.** Histograms of maximum fluorescence intensity ( $E_{\max}$ ) and amplitude modulation lifetime  $\tau_m$  for Immuno Check microspheres #5927 (2a & 2b) and DNA Check microspheres #5949 (2c & 2d).

Thursday, March 10, 1994

## Aerosol Studies

**ThA** 8:15am–10:15am  
Grand Room

Kay Niemax, *Presider*  
*Institute für Spektrochemie und Angewandte, Germany*

# Chemical Analysis of Single Aerosol Particles Using Laser Ionization

*D. M. Murphy*  
*NOAA Aeronomy Laboratory*  
*325 Broadway*  
*Boulder CO 80303*

Aerosol particles are known to be extremely important for both radiative climate forcing and atmospheric chemistry. A basic requirement for understanding aerosol effects is knowledge of the composition of particles. Both heterogeneous chemistry and cloud condensation properties depends on the composition. Aerosol composition also provides essential information on the sources of particles.

We have developed a portable instrument to make in situ measurements of the composition of individual, sized particles with diameters between 0.3 and 10  $\mu\text{m}$ . Particles enter the instrument through a differentially pumped nozzle. They then pass through a continuous laser beam. The scattered light signal provides both size information and the trigger for a miniature excimer laser. Ions produced when the excimer laser beam strikes the particles are analyzed in a time of flight mass spectrometer to provide a complete mass spectrum for each aerosol particle (Figure 1). Analysis of volatile species is feasible because the measurement takes place less than 400  $\mu\text{s}$  after a particle enters the instrument and because the particles never touch any surfaces.

The use of an excimer laser for the ionizing pulse is dictated by the requirement that the laser fire before the particle moves a significant distance from where it is sensed. That requirement, about 1  $\mu\text{s}$ , excludes most pulsed lasers. We use an MPB PSX-100 excimer laser that puts out about 4 mJ per pulse at 248 nm. A custom time of flight mass spectrometer was designed to provide the necessary resolution and dynamic range to deal with the ion signals from a laser ionization process. The system has a signal to noise of over 1000 for single particles. Either positive or negative ions can be examined.

Tests have been conducted both on known aerosols generated in our laboratory and on ambient aerosol particles. The positive and negative ion spectra provide complementary information on the composition of aerosol particles (Figure 2). Ambient spectra have shown that individual aerosol particles vary dramatically in composition (Figure 3).

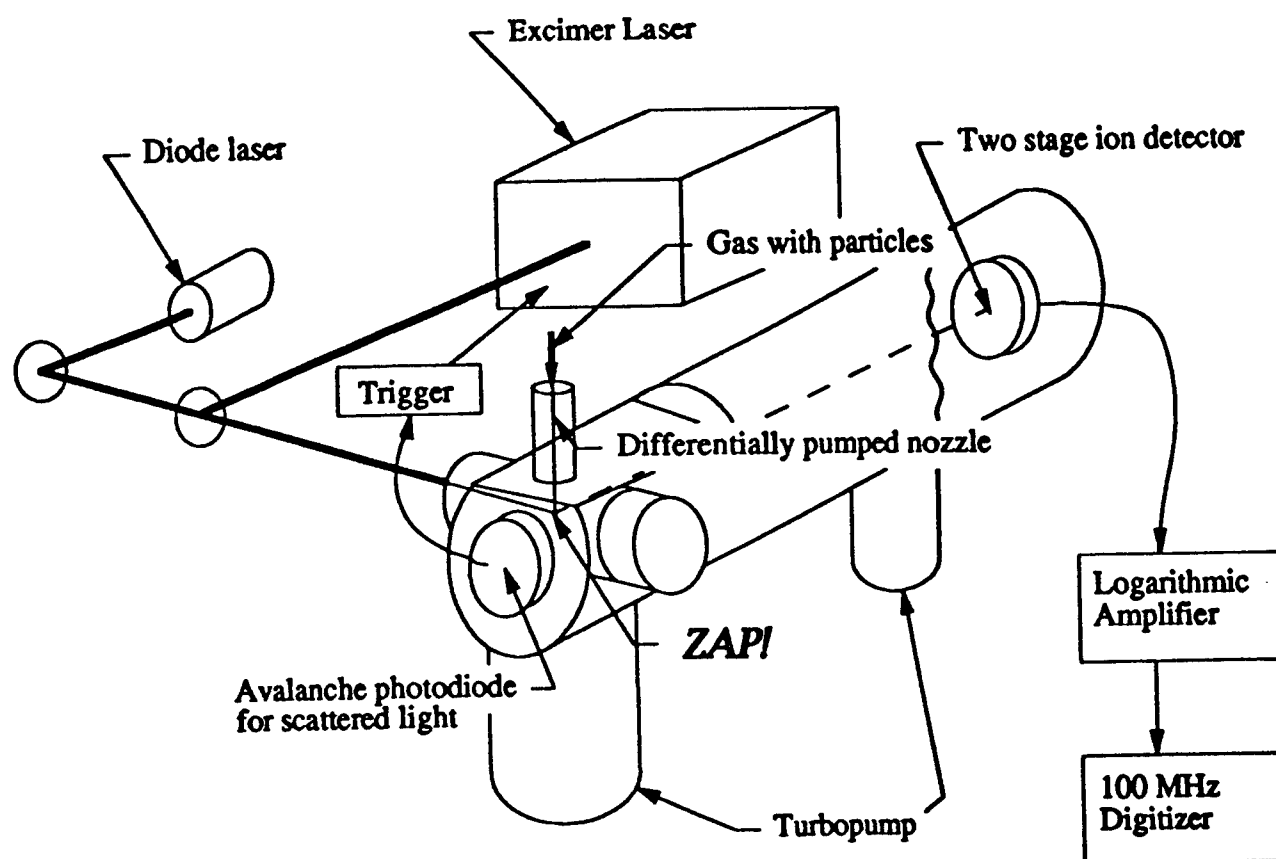


Figure 1. Diagram of the mass spectrometer system to analyze single aerosol particles.

## Ammonium Sulfate 0.3 $\mu\text{m}$ diameter

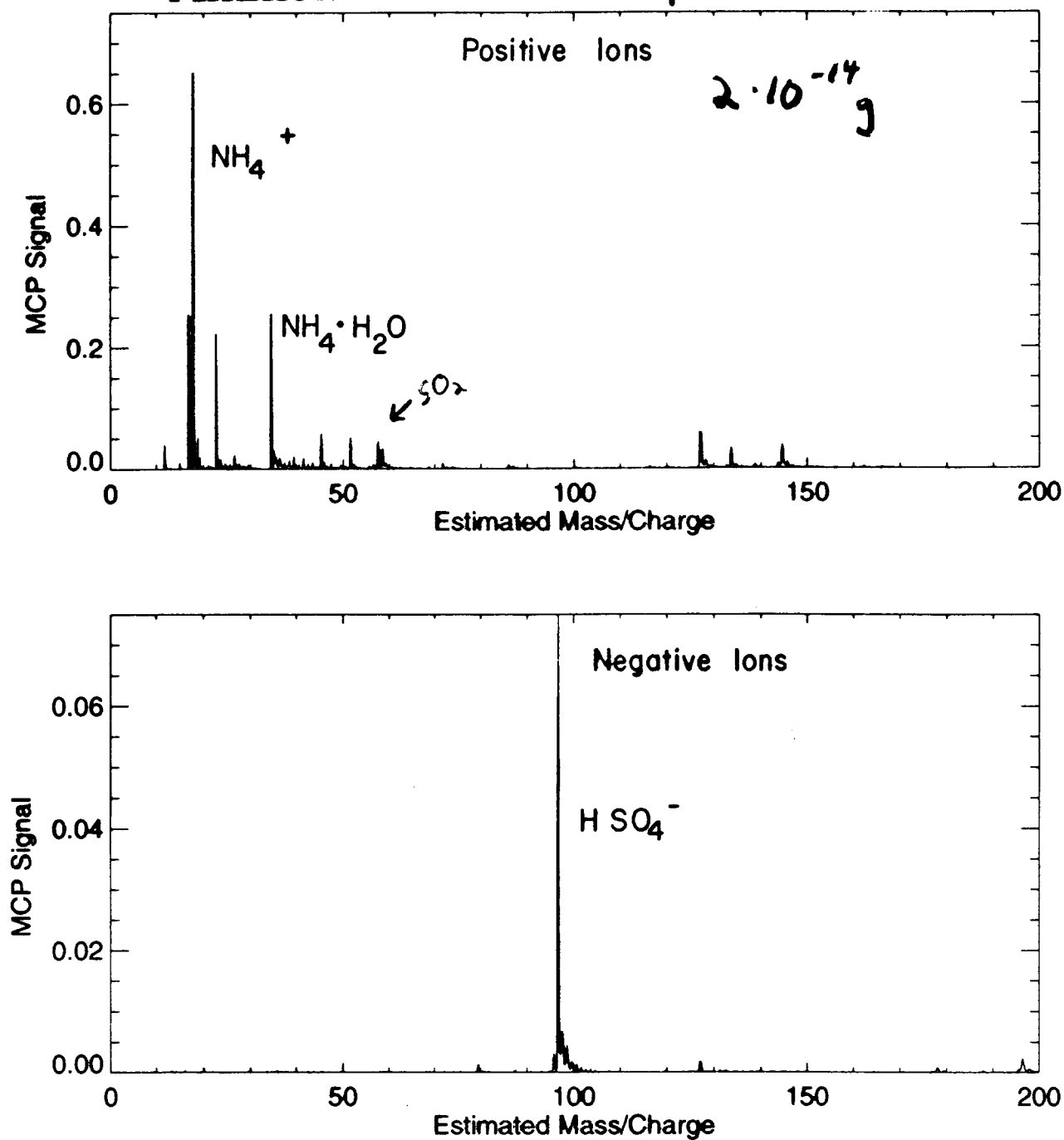


Figure 2. Positive and negative ion spectra of ammonium sulfate aerosol particles generated in the laboratory.

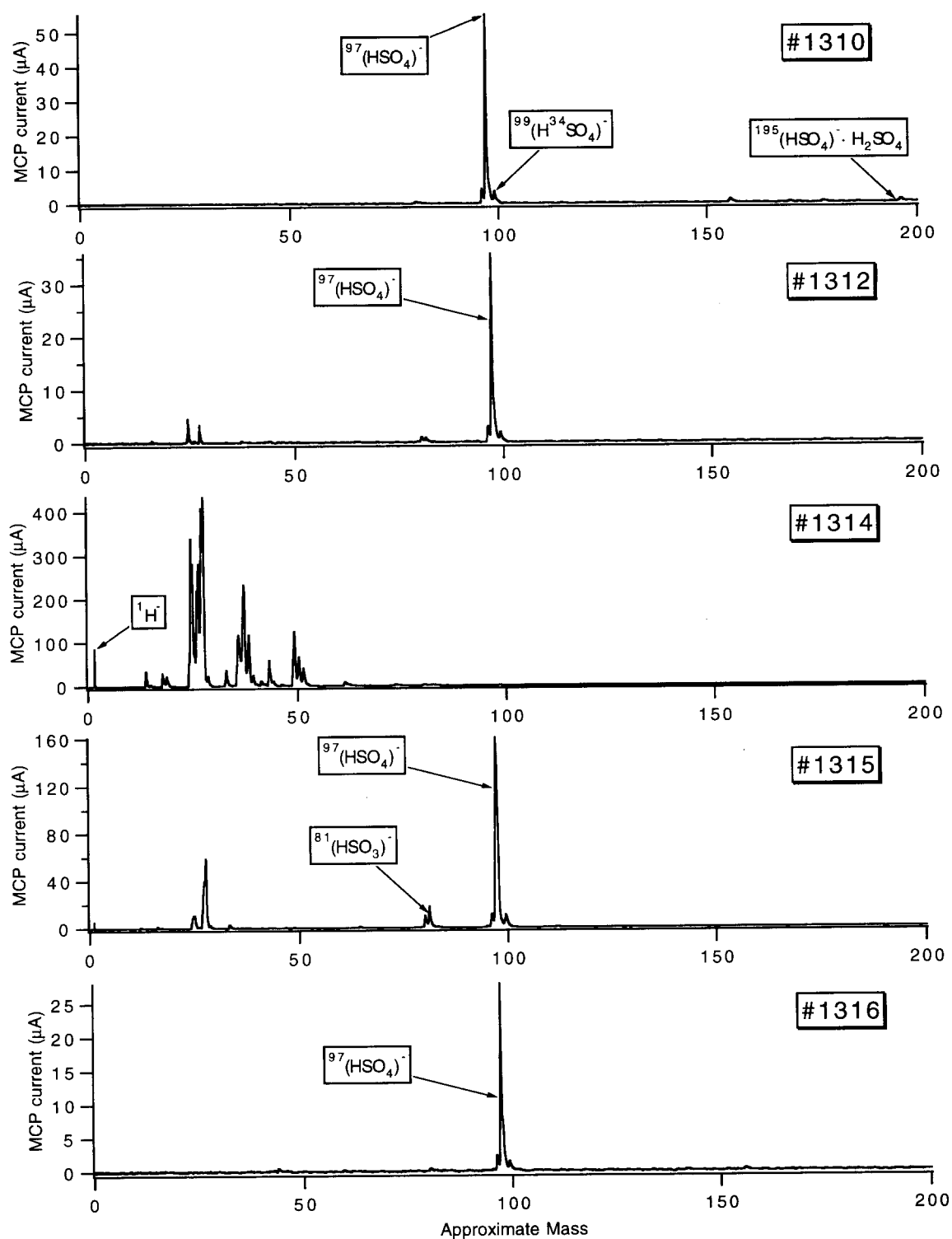


Fig. 3 Spectra of 7 successive negative ion spectra taken September 26, 1993. Numbers 1311 and 1313 were either false triggers or the excimer laser missed the particle.

**ON-LINE ANALYSIS OF SINGLE MICROPARTICLES BY  
RAPID SINGLE-PARTICLE MASS SPECTROMETRY**

M. V. Johnston, P.G. Carson, K.R. Neubauer, B.A. Mansoori, Department of Chemistry and Biochemistry, and A.S. Wexler, Department of Mechanical Engineering, University of Delaware, Newark, DE 19716

Numerous methods have been developed to analyze particulate matter in ambient aerosols. Typically, particle composition is measured by removing the particles from the gas by filtration or impaction and transporting the sample to a laboratory where "off-line" analysis is performed with either bulk or single particle analytical techniques. There are several difficulties with these methods. First, the sample is collected over an extended period of time, so short term temporal variations in the composition cannot be resolved. Second, compounds may condense on or evaporate from the impactor surface or filter over the course of sampling, altering their composition. Third, the turnaround time between sampling and analysis is slow. For these reasons, off-line analysis based upon filtration or impaction cannot be easily adapted to real-time sampling and analysis and they may not give analytical results that are representative of the true composition. These problems can be overcome with on-line methods of analysis.

Currently, there are three promising technologies for on-line analysis of ambient aerosols: laser induced breakdown spectroscopy or LIBS,<sup>1</sup> inductively coupled plasma atomic emission spectroscopy or ICP-AES,<sup>2</sup> and rapid single-particle mass spectrometry or RSMS.<sup>3,4</sup> Another method, particle analysis by mass spectrometry or PAMS,<sup>5</sup> has been extensively studied but it is applicable to only a limited range of materials. LIBS has the advantage that the analysis is performed in-situ, so sampling artifacts are eliminated. However, LIBS is an atomic emission based technique and therefore gives only elemental composition. It cannot be used to speciate inorganic materials, to determine isotopic distributions, or to detect organic compounds. ICP-AES is also an atomic emission technique and is subject to the same limitations as LIBS. Furthermore, ICP-AES requires isokinetic sampling of the aerosol, so sampling artifacts are possible. RSMS, on the other hand, can be used to determine elemental composition, to determine isotopic distributions, to speciate inorganic materials, and to detect organic molecules. Therefore, a wide variety of aerosols can be analyzed. RSMS has the limitation that isokinetic sampling of the aerosol particles into a vacuum is required. However, this problem can be minimized through proper instrumental design and operation.

Figure 1 shows the configuration of our instrument. Aerosols are generated with either a vibrating orifice aerosol generator (liquids) or a powder dispenser (solids; particulate matter on filter media). The aerosol flows through a mixing chamber where reaction may occur with the



surrounding gas. The flow from the mixing chamber is sampled both by an aerodynamic particle sizer and the laser mass spectrometer. The aerosol is sampled by separating the particles from the ambient gas with a two-stage momentum separator. Particles enter the source region of the mass spectrometer and scatter radiation from a continuous helium-neon laser beam. The transit time between the inlet and source region is approximately 0.5 ms, so loss of volatile components is minimized. The current optical system allows particles 0.5  $\mu\text{m}$  diameter and above to be detected by light scattering. The scattered radiation from each particle triggers an excimer laser (193 or 248 nm) which ablates the particle in-flight and a time-of-flight mass spectrum is recorded. Hundreds of particles can be analyzed per minute, with each particle giving a unique mass spectrum that can be related to composition.

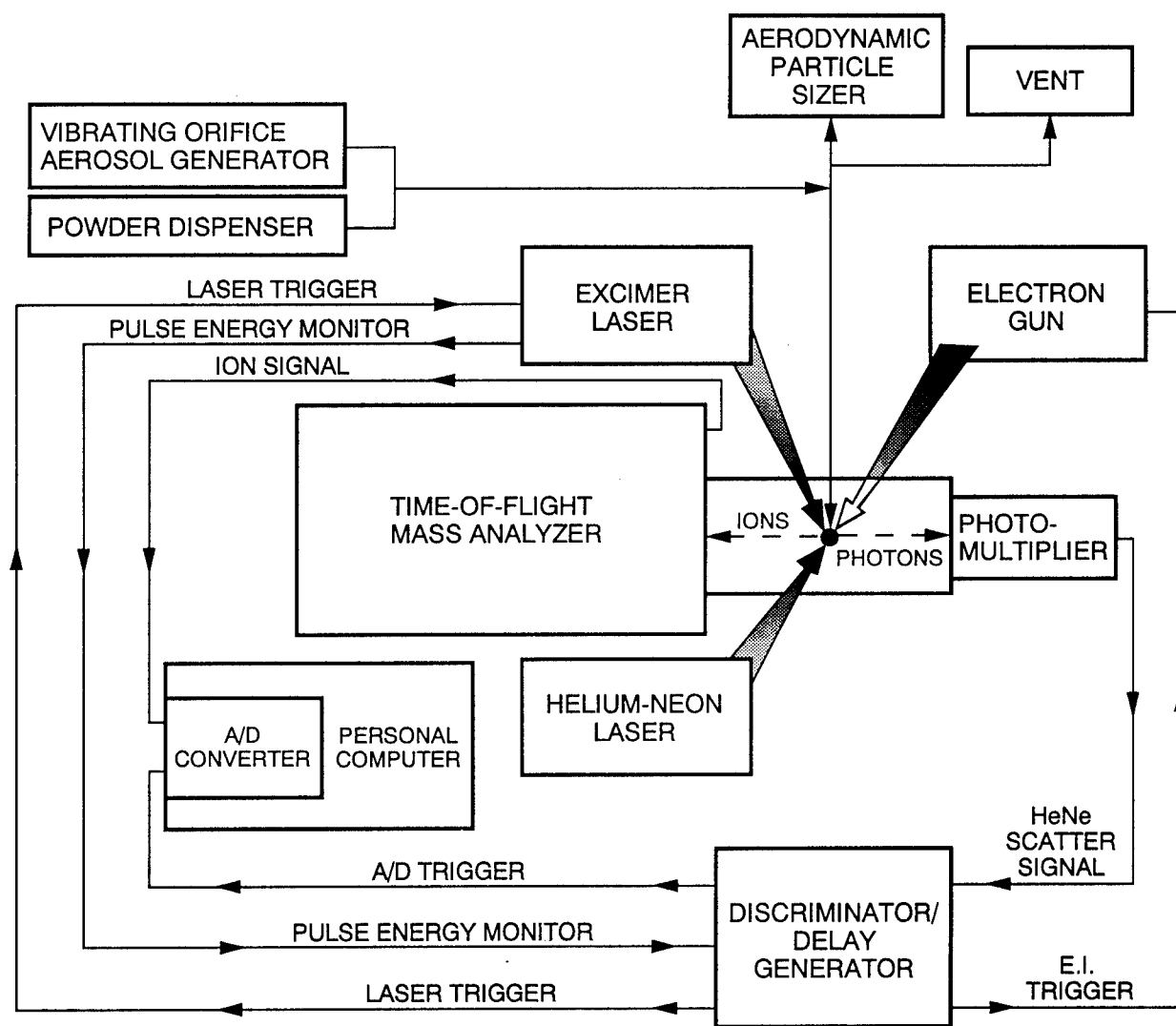


Figure 1

Figure 2 shows the positive and negative ion spectra of 3.5  $\mu\text{m}$  diameter NaCl particles. (These spectra were obtained from different particles.) Better than unit mass resolution is achieved across the entire mass range.

Our current work involves laboratory-generated aerosols that simulate field measurements. The mass spectra suggest that this method is capable of detecting trace metal and organic markers, assessing the oxidation states of chromium compounds, and discerning particle composition heterogeneities.

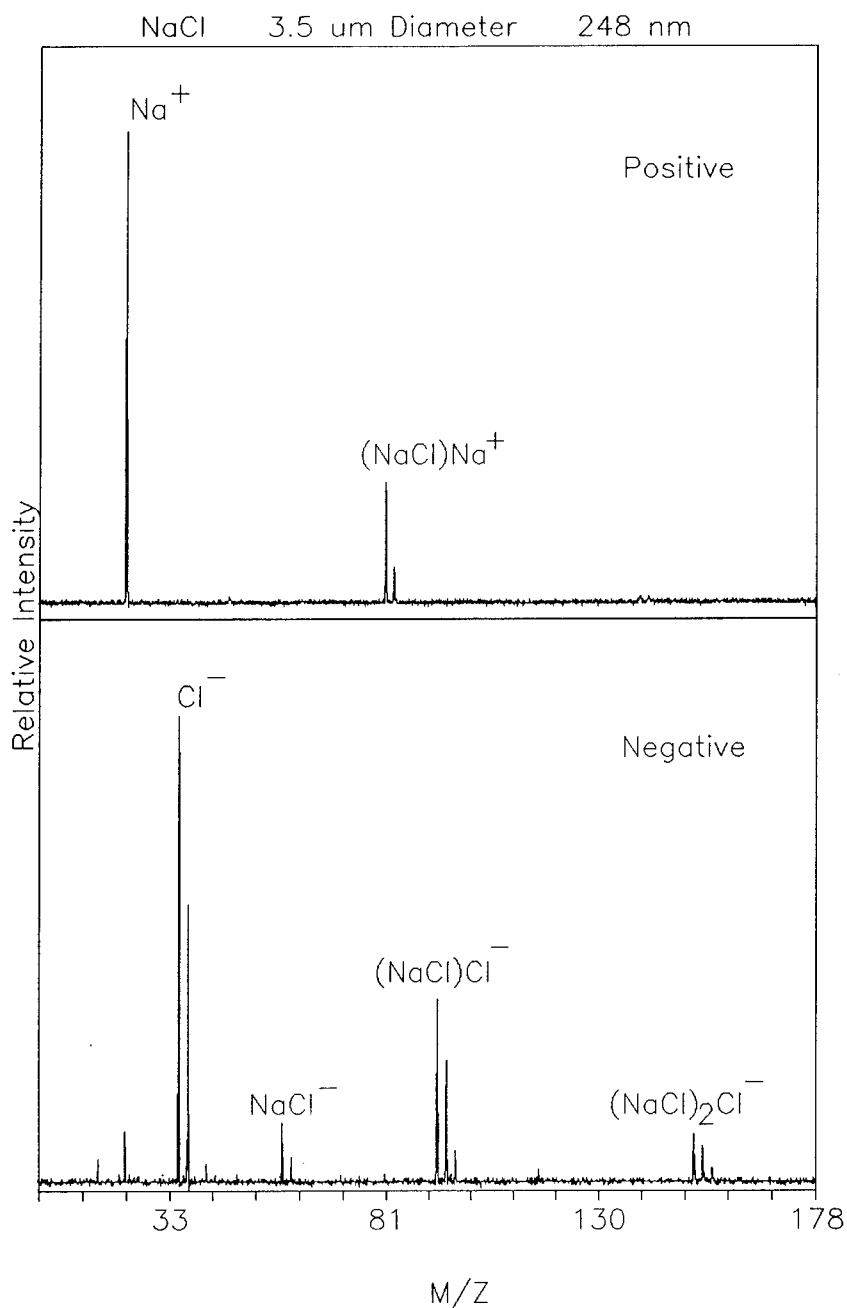


Figure 2

### References

1. L.J. Radziemski, T.R. Loree, D.A. Cremers, and N.M. Hoffman, *Anal. Chem.* 1983 55, 1246.
2. U.K. Bochert and W. Dannecker, *J. Aerosol. Sci.* 1989 20, 1525.
3. M.P. Sinha, *Rev. Sci. Instrum.* 1984 55, 886.
4. P.J. McKeown, M.V. Johnston, and D.M. Murphy, *Anal. Chem.* 1991 63, 2069.
5. J.J. Stoffels and J. Allen in Physical and Chemical Characterization of Individual Airborne Particles, ed. K.R. Spurny, Ellis Horwood Limited, Chichester, West Sussex, England, 1986, Chapter 20.

## **Mass Spectrometry of Individual Microparticles in an Ion Trap**

J. M. Ramsey, J. M. Dale, M. Yang, and W. B. Whitten  
Chemical and Analytical Sciences Division  
Oak Ridge National Laboratory  
Oak Ridge, TN 37831-6142  
(615) 574-5662

The characterization of individual microparticles has become more important recently with the increasing need for meteorological, environmental, medical, and intelligence data (1). Early attempts at on-line analysis used a heated filament to evaporate a portion of the particulate sample. Ionization in some cases occurred on contact, in other experiments, a supplemental electron beam was employed. Off-line measurements on individual particles have been made by laser microprobe analysis, SIMS, and by optical measurements (1). There have been several recent reports of on-line single particle measurements with pulsed laser desorption and ionization with time-of-flight mass spectrometry (2-4).

Several techniques have been developed at our laboratory for off-line laser sampling and mass analysis of individual microparticles within an ion trap mass spectrometer (5-7). The particles in these measurements are either shaken from a hopper within the vacuum chamber (5,6) or are individually levitated electrostatically within the trap electrodes prior to sampling (7). We are currently developing the technology necessary to introduce individual particles at atmospheric pressure into the ion trap without disrupting the vacuum in the mass spectrometer, and to ensure the interaction of the pulsed laser beam and rapidly moving particle within the ion collection region.

The experiments that we have done on single particle mass spectrometry used an ion trap mass spectrometer for the analysis. The ion trap mass spectrometer is a three-dimensional electric quadrupole formed from a ring electrode and two hyperbolic end caps. Ions of a broad or narrow mass to charge ratio can be stored electrostatically within the electrodes. In the simplest mode of operation, ions of different masses are ejected sequentially from the trap into a detector by ramping the rf voltage on the ring electrode. The detector is usually a Channeltron electron multiplier mounted outside one of the end cap electrodes. Unit mass resolution from 10 to 600 amu can be achieved in this way. For molecular species, it is possible to selectively trap ions of a single mass to charge ratio, collisionally dissociate them, and subsequently mass analyze the resulting fragment ions. This additional information, which cannot be obtained with time-of-flight instruments, helps to eliminate isobaric interferences. The high storage and detection efficiency of the ion trap permits this process to be repeated several times if needed (8). The ion trap configuration has several additional features that make it ideal for the present application. The sampling and ionization occur in the center of the trap so it is easy to collect and store a large fraction of the ions produced. Furthermore, the ion trap operates most efficiently with a modest pressure (0.1 Pa) of buffer gas (9) so the interface with an atmospheric pressure particle source is not so demanding.

We have made several modifications to the commercial ion trap configuration for particle laser ablation mass spectrometry. Several small holes have been drilled in the ring electrode to allow passage of laser beams for particle sensing and ablation. Also, provision had to be made to admit particles into the trap electrodes. For intensive chemical characterization of a single particle, the particle can be charged and electrostatically levitated at the center of the trap. Under these conditions, Raman and fluorescence spectroscopy can be performed. Subsequently, laser ablation mass spectrometry can be done by changing the operating conditions of the trap.

If a large number of particles are to be mass analyzed one-by-one, they can be shaken from a solenoid-driven hopper. When the particles pass through the center of the trap, they are intercepted by an ablation laser pulse and the resulting ions stored and mass analyzed by conventional ion trap methods. A unique feature of ion trap mass spectrometry is that tandem MS can be performed with high efficiency. This is especially valuable on real samples that usually are a mixture of numerous substances. Ions of a single mass, usually the parent ion, are first isolated, then collisionally dissociated. The mass spectrum of the fragments can be determined with no background due to the other components of the sample. In this way, a substance can be positively identified with high detection sensitivity. We have been easily able to detect pg quantities of tetraphenyl phosphonium bromide and related compounds on the surface of SiC particles in this way.

Single charged microparticles can be suspended in the trap by applying a common mode audio frequency voltage and a differential dc bias to the end caps. The ion trap rf voltage is applied to the ring electrode but doesn't affect the motion of the microparticle. The capture is performed at atmospheric pressure. When the chamber has been pumped to the desired operating pressure, the particle can be released by grounding the end caps. Ions produced by laser ablation/desorption are then stored and analyzed as before. Both organic and inorganic particles have been analyzed in this way.

Many of the applications we envision would benefit substantially from real-time sampling. We are undertaking some modifications to adapt the existing mass spectrometer for real-time analysis of individual airborne microparticles. The microparticles and a small amount of surrounding air are admitted to an antechamber of the vacuum system through a small capillary. Most of the air is removed by differential pumping of this antechamber while the particles pass through the orifice of a conical skimmer into the main chamber. The pressure in this chamber is kept at 0.1 Pa for optimum operation of the ion trap mass spectrometer. The particle trajectory passes through the center of the ion trap electrodes where their presence is detected by light scattered from a CW laser beam. This signal is used to trigger the pulsed laser for the ablation/desorption. Our progress with this system will be described.

This research was supported by the U.S. Department of Energy, Office of Arms Control and by the Strategic Environmental Research and Development Program. Oak Ridge National Laboratory is managed by Martin Marietta Energy Systems, Inc. under contract DE-AC05-84OR21400 with the U.S. Department of Energy.

## REFERENCES

1. K. R. Spurny, in *Physical and Chemical Characterization of Individual Airborne Particles*, K. R. Spurny, Ed., Horwood Ltd., Chichester, 1986, p 6.
2. M. P. Sinha, *Rev. Sci. Instrum.* **55**, 886 (1984).
3. P. J. McKeown, M. V. Johnston, and D. M. Murphy, *Anal. Chem.* **63**, 2073 (1991).
4. W. D. Reents, Jr., A. Swanson, S. Downey, A. N. Mjjsce, A. J. Muller, B. Emerson, D. J. Siconolsi, and J. D. Sinclair, *Proc. 41st ASMS Conference on Mass Spectroscopy and Allied Topics*, San Francisco 1993, p 640.
5. J. M. Dale, W. B. Whitten, and J. M. Ramsey, *Proceedings of the 39th ASMS Conference on Mass Spectrometry and Allied Topics*, Nashville, May 19-24, 1991, p 536.

6. J. M. Dale, M. Yang, W. B. Whitten, and J. M. Ramsey, Proceedings of the 40th ASMS Conference on Mass Spectrometry and Allied Topics, Washington DC, May 31-June 5, 1992, in press.
7. W. B. Whitten, J. M. Dale, and J. M. Ramsey, Proc. First Int. Symp. on Explosive Detection Technology, Atlantic City, Nov. 13-15, 1991, in press.
8. J. N. Louris, J. S. Brodbelt-Lustig, R. G. Cooks, G. L. Glish, G. J. Van Berkel, and S. A. McLuckey, Int. J. Mass Spectrom. Ion Proc. 96, 117 (1990).
9. G. C. Stafford, Jr., P. E. Kelley, J. E. P. Syka, W. E. Reynolds, and J. F. J. Todd, Int. J. Mass Spectrom. Ion Proc. 60, 85 (1984).

## Raman Spectroscopy Measurements of Single Reacting Aerosol Microparticles

Scot D. Rassat and E. James Davis  
 Department of Chemical Engineering, BF-10  
 University of Washington  
 Seattle, WA 98195  
 Telephone: (206) 543-2250

The chemical reaction between sorbent particles and sulfur dioxide ( $\text{SO}_2$ ) is used to remove  $\text{SO}_2$  from stack gases. The addition of powdered limestone to coal in the fluidized bed coal combustor generates calcium oxide ( $\text{CaO}$ ) which reacts with the  $\text{SO}_2$  to form  $\text{CaSO}_3$  at low temperatures and  $\text{CaSO}_4$  at temperatures above 700 K. The utilization of the limestone is known to be low (about 20%) because the pores of the  $\text{CaO}$  plug as the product forms. This research was conducted to examine the reaction between  $\text{CaO}$  and  $\text{SO}_2$  to elucidate the rate-controlling processes, to generate  $\text{CaO}$  particles with a more open pore structure, and to develop techniques for single particle measurements at elevated temperatures.

The work has been performed with single particles levitated in an electrodynamic balance (EDB). The EDB was coupled to a Raman spectrometer as shown in Figure 1. Additional details have been published by Rassat *et al.* (1,2). To study gas/microparticle reactions at elevated temperatures a  $\text{CO}_2$  infrared heating system was constructed. The IR beam was split, and the resulting beams were focused on the levitated particle using the IR optics shown in the figure. The EDB uses superposed ac and dc electrical fields to maintain a charged microparticle in the laser beams. An argon-ion laser was used to provide the illumination needed for spontaneous Raman emission.

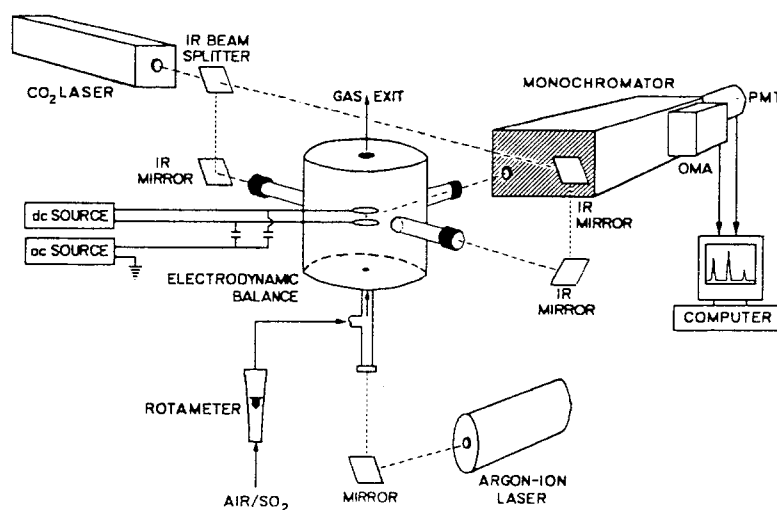


Figure 1. The apparatus used for gas/particle chemical reaction measurements.

Figure 2 shows a sequence of Raman spectra (3) for a calcium oxide microparticle reacting with  $\text{SO}_2$  gas in a humid nitrogen stream. The spectra indicate that calcium hydroxide ( $\text{Ca(OH)}_2$ ) is formed as an intermediate compound, and the  $\text{Ca(OH)}_2$  then reacts with  $\text{SO}_2$  to form calcium sulfite-hemihydrate ( $\text{CaSO}_3 \cdot 0.5\text{H}_2\text{O}$ ) product. The spectra indicate the development of the sulfite and hydration water functional groups of  $\text{CaSO}_3 \cdot 0.5\text{H}_2\text{O}$  at Stokes shifts of 1000 and 3379  $\text{cm}^{-1}$ , respectively, and the hydroxyl group of  $\text{Ca(OH)}_2$  at 3619  $\text{cm}^{-1}$ . At long reaction times ( $>180$

min.) the spectroscopic data show hydroxide and sulfite peak heights approach a limiting value, suggesting that the reaction shuts down prior to complete consumption of the available hydroxide.

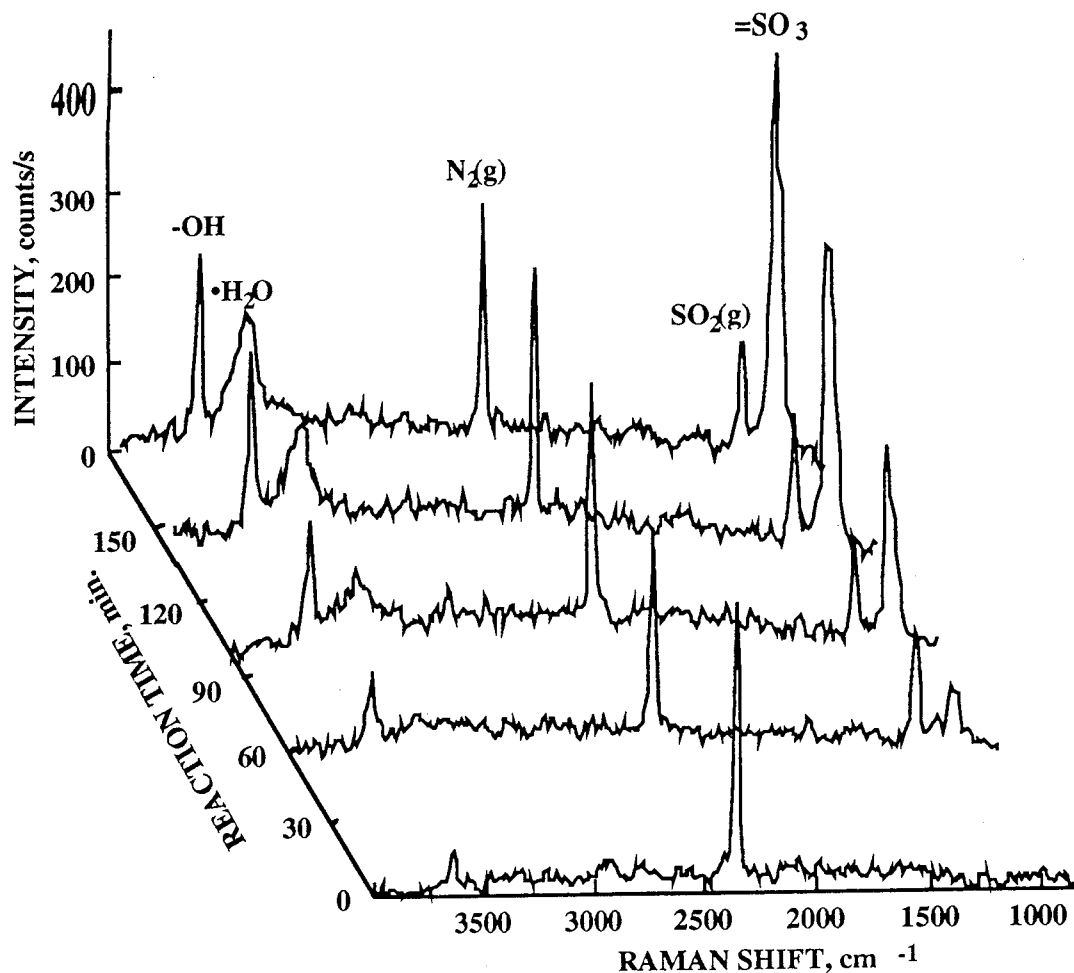


Figure 2. Time series of Raman spectra for the reaction of a CaO microparticle with water vapor and SO<sub>2</sub> in a N<sub>2</sub> carrier gas.

As demonstrated in Figure 2, the room temperature reaction is too slow to be technologically important. At higher temperatures reaction rates increase, but the CaO utilization efficiency decreases due to the fact that the change in reaction rate with temperature outpaces the rate of change of diffusion of the reacting gaseous species within the particle. Therefore, surface reaction is favored and the pores plug relatively quickly.

A possible means for improving CaO conversion in flue gas desulfurization operations is to develop a more porous oxide structure. We examined the *in situ* formation of CaO from levitated calcium nitrate tetrahydrate (Ca(NO<sub>3</sub>)<sub>2</sub>•4H<sub>2</sub>O) microparticles. This material has a low melting point (318 K) and is readily spherized. The oxide formed by decomposition is theoretically greater than 85% porous, assuming the lattice structure does not collapse. The decomposition of a levitated particle of Ca(NO<sub>3</sub>)<sub>2</sub>•4H<sub>2</sub>O presents two major challenges: (i) maintaining particle stability in the intense infrared laser beams used to heat the particle and (ii) measuring the microparticle temperature. Asymmetrical particles are difficult to maintain in the beams, so spherical particles are desired.



A novel Raman spectroscopic technique based on the ratio of Stokes to anti-Stokes spectral intensities from a single microparticle has been applied for its temperature measurement. The intensities of Stokes and anti-Stokes Raman vibrational lines depend on the populations of the ground and excited vibrational states, respectively. With increasing temperature the population of excited vibrational levels grows at the expense of the ground state population, and therefore, the relative ratio of the magnitudes of the Stokes and anti-Stokes Raman peaks decreases. The effect of temperature on the Stokes / anti-Stokes intensity ratio for a uniformly absorbing species is given by (4)

$$\exp\left[-\frac{hc\tilde{\nu}_k}{k_B T}\right] = \frac{I_a(\tilde{\nu}_k)}{I_s(\tilde{\nu}_k)} \left(\frac{\tilde{\nu}_o - \tilde{\nu}_k}{\tilde{\nu}_o + \tilde{\nu}_k}\right)^4, \quad [1]$$

where  $I_s[\tilde{\nu}_k]$  and  $I_a[\tilde{\nu}_k]$  are the Raman intensities of the Stokes and anti-Stokes lines, respectively,  $T$  is the absolute temperature,  $h$  is Planck's constant,  $k_B$  is Boltzmann's constant, and  $c$  is the speed of light *in vacuo*. The absolute value of the Raman shift of the  $k$ -th vibrational mode is  $\tilde{\nu}_k$ , and  $\tilde{\nu}_o$  is the frequency of the excitation source. This technique has been used for bulk systems (4,5) and for high temperature gases, but to the authors' knowledge this is the first attempt to measure single microparticle temperatures via Raman methods.

Stokes and anti-Stokes spectra were obtained for particles of  $\text{Ca}(\text{NO}_3)_2 \cdot 4\text{H}_2\text{O}$  and rutile titanium dioxide ( $\text{TiO}_2$ ). For  $\text{Ca}(\text{NO}_3)_2 \cdot 4\text{H}_2\text{O}$  the ratios of the peak heights and areas corresponding to the nitrate vibrational modes at  $744\text{ cm}^{-1}$  and  $1068\text{ cm}^{-1}$  were determined to estimate the particle temperature using Eq. [1]. The particle temperature was varied by changing the IR laser intensity, and the results are presented in Figure 3 as a function of laser power. At these moderate temperatures the particle temperature increases nearly linearly with the laser intensity.

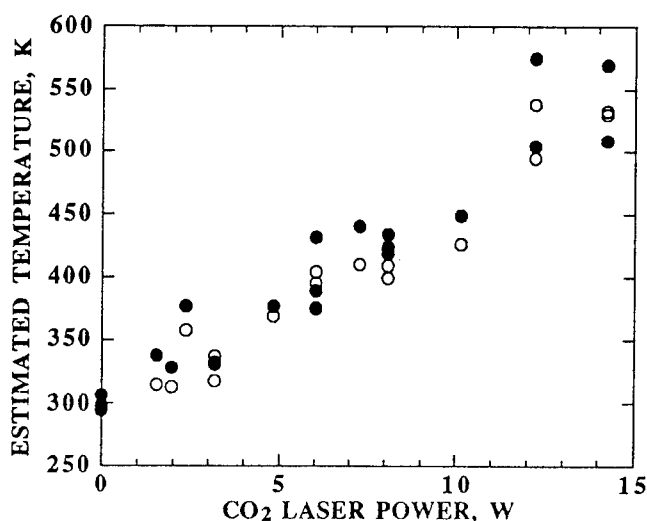


Figure 3. Stokes/anti-Stokes Raman temperature measurements of an IR-heated microparticle of  $\text{Ca}(\text{NO}_3)_2 \cdot 4\text{H}_2\text{O}$  based on peak areas (filled points) and peak heights (open points).

For the  $\text{TiO}_2$  particles we examined the point-by-point ratios of the Stokes and anti-Stokes Raman spectra in the range  $100\text{--}800\text{ cm}^{-1}$ . Figure 4 shows the results for a  $\text{TiO}_2$  microparticle held at room temperature. The point-by-point ratios scatter about 300 K, which indicates that even for the very low anti-Stokes intensities encountered at room temperature the method appears to be valid.

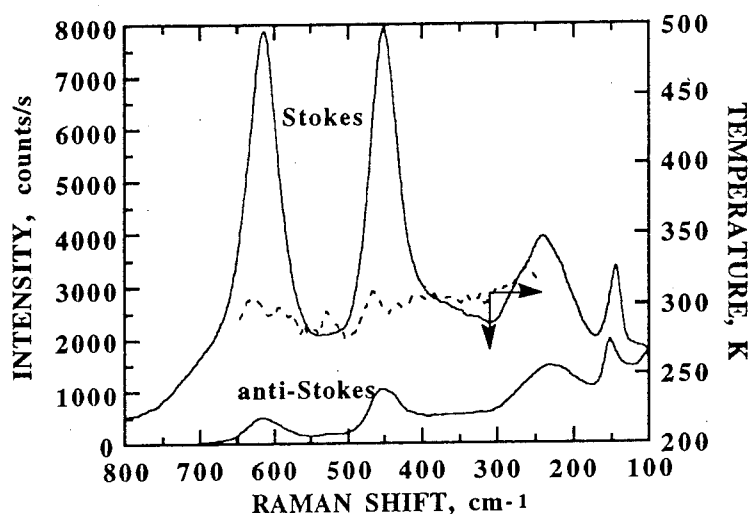


Figure 4. Point-by-point Stokes/anti-Stokes temperature estimates for a rutile  $\text{TiO}_2$  microparticle at room temperature.

These preliminary studies of microparticle/gas chemical reactions and particle heating demonstrate that laser light scattering and laser heating can be used to explore such reactions at elevated temperatures under very well-controlled conditions.

## REFERENCES

1. Rassat, S. D., T. M. Allen and E. J. Davis, Raman Spectroscopy Studies of Combustion-Related Microparticles, *Proc. SPIE* **1862**, 182-191 (1993).
2. Rassat, S. D. and E. J. Davis, Chemical Reaction of Sulfur Dioxide with a Calcium Oxide Aerosol Particle, *J. Aerosol Sci.* **23**, 165-180 (1992).
3. Davis, E. J., S. D. Rassat and W. Foss, Measurement of Aerosol/Gas Reaction Rates by Microparticle Raman Spectroscopy, *J. Aerosol Sci.*, **23** (Suppl. 1) S429-S432 (1992).
4. Malyj, M. and J. E. Griffiths, Stokes/anti-Stokes Raman Vibrational Temperatures: Reference Materials, Standard Lamps, and Spectrophotometric Calibrations, *Appl. Spectrosc.* **37**, 315-333 (1983).
5. Kip, B. J. and R. J. Meier, Determination of the Local Temperature at a Sample during Raman Experiments Using Stokes and Anti-Stokes Raman Bands, *Appl. Spectrosc.* **44**, 707-711 (1990).

## Laser Ionization of Biomolecules in Solution

Kermit K. Murray, Michelle D. Beeson and David H. Russell

*Department of Chemistry*

*Texas A&M University*

*College Station, TX 77843-3255*

*Ph. 409-845-0613, Fax 409-845-9485*

### Introduction

Many powerful laser based methods are unavailable for the analysis of molecules in solution. Techniques for the analysis of liquids are particularly important for the study of biomolecules, whose natural environment is a water solution. Mass spectrometry is a powerful analytical technique, but liquids and mass spectrometers are fundamentally incompatible. We have developed a technique for laser ionization of biomolecules in solution by applying matrix-assisted laser desorption ionization (MALDI) to liquid aerosols. In the typical MALDI experiment, the analyte biomolecule is deposited from solution onto a metal surface with a 100 to 50,000 molar excess of a suitable matrix, usually a UV absorbing organic acid.<sup>1</sup> The solvents are allowed to evaporate and the sample is inserted into the source region of a mass spectrometer. Light from a pulsed laser is absorbed by the matrix causing both ablation of the surface and ionization of the intact biomolecule. In the aerosol MALDI experiment,<sup>2,3</sup> the analyte biomolecule is dissolved in a methanol solution with an ultraviolet absorbing matrix. The aerosol is sprayed into vacuum, desolvated, and ionized by pulsed UV laser radiation. The ions are mass separated in a time-of-flight (TOF) mass spectrometer. Aerosol MALDI mass spectra have been obtained for a variety of peptides and proteins with molecular weights as large as 80,000. We have used aerosol MALDI as a liquid chromatography detection method<sup>4</sup> (LC/MS) and as a probe of aerosol and cluster chemistry.<sup>5</sup> This paper gives a general description of aerosol MALDI and discusses some recent results for peptide and protein ionization.

### Experimental

The aerosol MALDI apparatus has been described in detail previously<sup>2,3</sup> and will be only briefly outlined here. The aerosol formation and ionization regions of the apparatus are shown schematically in Figure 1. Aerosols are formed from an acidified methanol solution of the biomolecule of interest and a suitable matrix molecule. The liquid solution is loaded into a syringe pump and introduced into a pneumatic nebulizer at a flow rate of 0.5 mL/min. The aerosol passes through a heated drying tube to remove solvent before ionization; this drying step is crucial for the formation of ions from the aerosols. The aerosols are ionized by the 355 nm frequency tripled output of a pulsed Nd:YAG laser focused into the source region of a TOF mass spectrometer. The ion formation and time-of-flight regions of the apparatus are shown schematically in Figure 2 (the aerosol beam points into the page). Ions are accelerated perpendicularly to the aerosol and laser beams and mass separated in a 1.1 m flight tube.

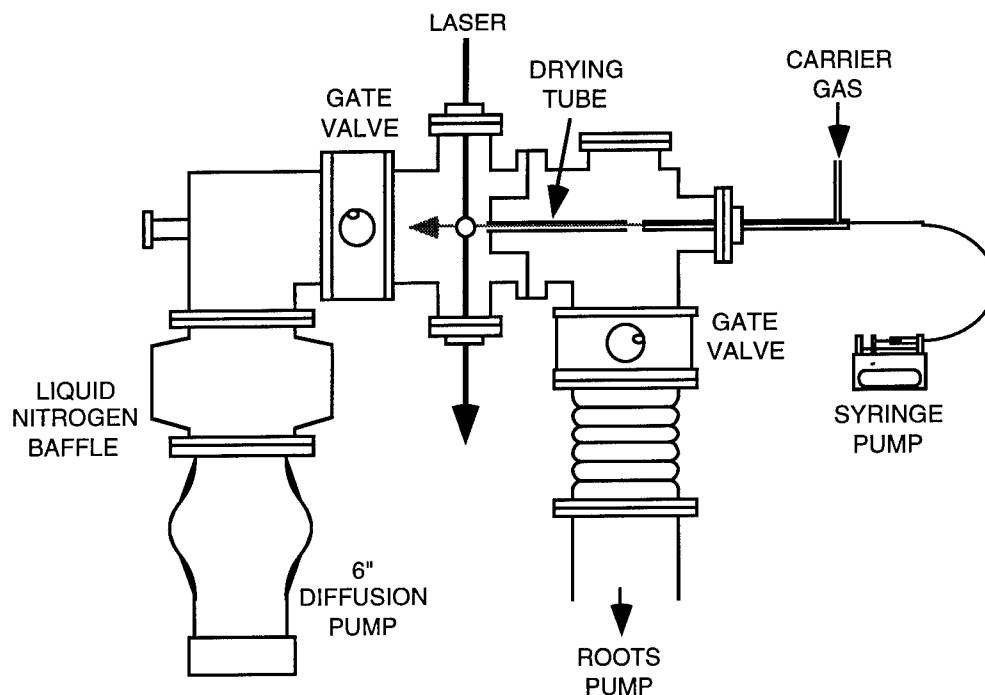


Figure 1. Aerosol MALDI apparatus: aerosol formation.

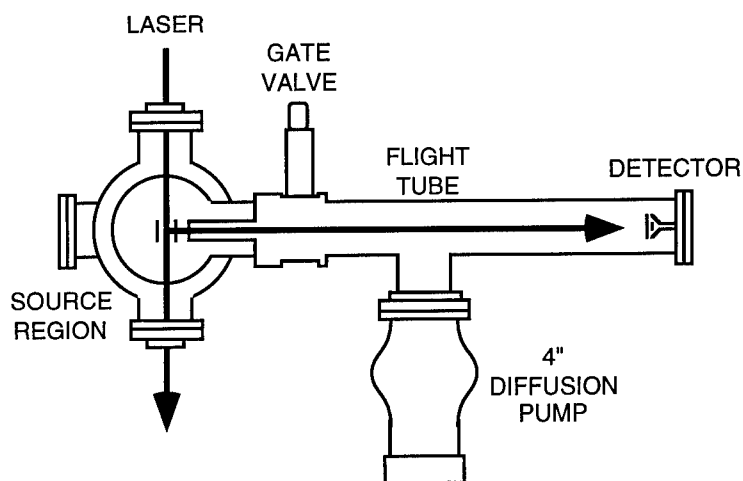


Figure 2. Aerosol MALDI apparatus: time-of-flight mass spectrometer.

## Results and Discussion

Aerosol MALDI has been used to obtain the mass spectra of several peptides and proteins using a number of different matrix molecules.<sup>2-5</sup> An example of the ionization of a small peptide is shown in Figure 3. The mass spectrum was obtained with  $\alpha$ -cyano-4-hydroxy cinnamic acid at a matrix to analyte molar ratio of 50. The aerosol solution was 200 nmol of bradykinin and

10  $\mu\text{mol}$  of matrix per mL of methanol acidified with 5 % trifluoroacetic acid. The laser pulse energy was 1.5 mJ for a fluence of 0.1 J/cm<sup>2</sup> and an irradiance of 15 MW/cm<sup>2</sup> at the laser and ion beam intersection. The ion beam acceleration voltage was 15 kV and the spectrum is the average of 1000 laser shots. The large peak near 1000 u is assigned as protonated bradykinin, labeled  $[\text{M}+\text{H}]^+$ . The smaller peaks to the right of the  $[\text{M}+\text{H}]^+$  peak are clusters of bradykinin and matrix and matrix fragments. To the left of the bradykinin  $[\text{M}+\text{H}]^+$  peak is a peak associated with doubly charged bradykinin near 500 u and below 500 u the mass spectrum is dominated by protonated methanol clusters.<sup>3</sup> The mass resolution based on the width of the bradykinin  $[\text{M}+\text{H}]^+$  peak is 125.

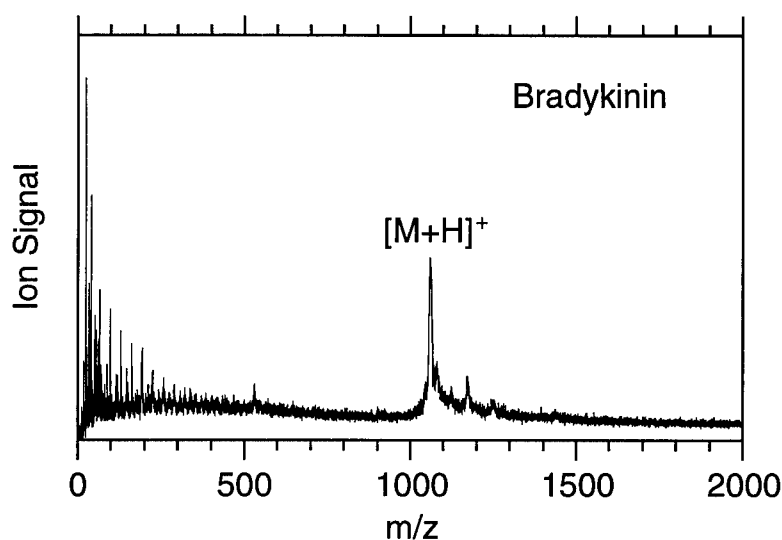


Figure 3. Aerosol MALDI mass spectrum of bradykinin ( $M_r = 1060$ ).

A mass spectrum of the protein bovine albumin is shown in Figure 4. The aerosol solution was 30 nmol of bovine albumin and 10  $\mu\text{mol}$  of  $\alpha$ -cyano-4-hydroxy-cinnamic acid per mL of methanol acidified with 5 % trifluoroacetic acid. The spectrum is the average of 1000 laser shots at 15 mJ pulse energy and an irradiance of 160 MW/cm<sup>2</sup>. The extraction voltage was 15 kV. The mass peaks corresponding to the singly, doubly, and triply charged bovine albumin are labeled  $\text{M}^+$ ,  $2\text{M}^+$ , and  $3\text{M}^+$  respectively. The resolution, based on the width of the peak labeled  $\text{M}^+$ , is 10 and consequently peaks associated with albumin clustered to matrix or solvent are not resolved.

The results presented here and other published results<sup>2-5</sup> show that aerosol MALDI has great potential as an analytical technique. We are currently refining the apparatus with particular focus on the issues of mass resolution, data acquisition rate, and detection limit. A high repetition rate laser and rapid data acquisition electronics can improve the data acquisition rate. Optimization of data acquisition rate, aerosol transport, laser-aerosol overlap, aerosol drying, and ion collection can lead to an increase in detection limit from the current nmol range to the fmol range or lower. Instrument improvements underway include ultrasonic nebulization, desolvation in the presence of a high

pressure drying gas, an improved vacuum system, and dual acceleration stage ion optics. We are also developing an interface between aerosol MALDI and a Fourier transform mass spectrometer.

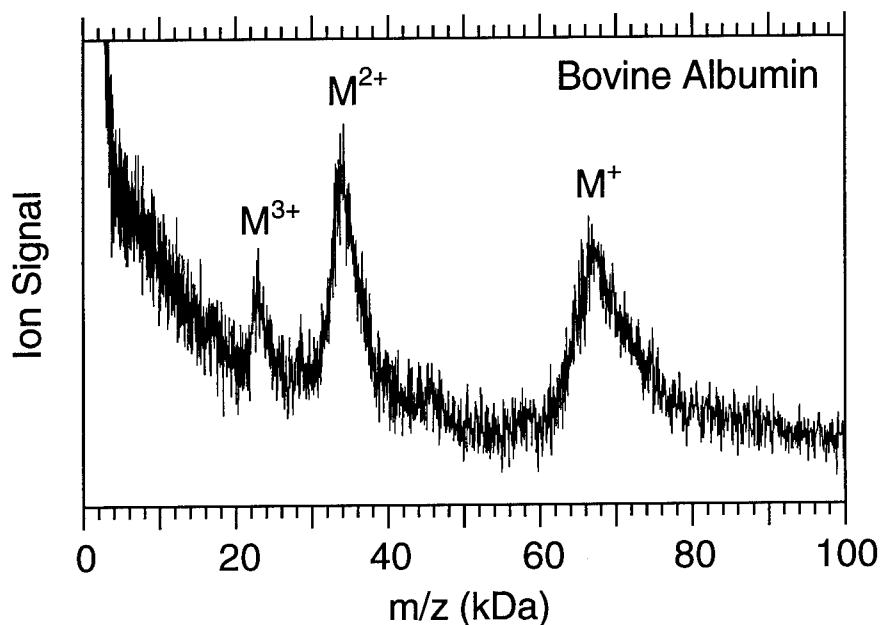


Figure 4. Aerosol MALDI mass spectrum of bovine albumin ( $M_r = 66,430$ ).

## References

1. Hillenkamp, F; Karas, M; Beavis, R. C.; Chait, B. T.; *Anal. Chem.* **1991**, 63, 1193-1202 A.
2. Murray, K. K.; Russell, D. H. *Anal. Chem.* **1993**, 65, 2534-2537.
3. Murray, K. K.; Russell, D. H., *J. Am. Soc. Mass Spectrom.* in press.
4. Murray, K. K.; Russell, D. H., *Proc. ASMS Conf. Mass Spectrom. Allied Top.*, 41st **1993**, 780a-b.
5. K. K. Murray and D. H. Russell, proceedings of the *Second International Conference on Laser Ablation*, Knoxville, TN, April 19-22, 1993, (in press).

Thursday, March 10, 1994

## Laser Desorption/Ablation and Condensed Phase Probes

**ThB** 10:30am–12:10pm  
Grand Room

Andrew Sappey, *Presider*  
*Los Alamos National Laboratory*

## **Fundamental Investigations of the Mechanism of Laser Desorption and Ionization in Matrix Assisted Laser Desorption / Ionization**

Gary R. Kinsel, Kent Gillig, Ricky Edmondson and David H. Russell

*Texas A & M University, Department of Chemistry, College Station, TX 77843*

*Phone: 409-845-0613, FAX: 409-845-9485*

### **Introduction**

The recent development of Matrix Assisted Laser Desorption / Ionization (MALDI) has sparked a revolution in the field of high molecular weight mass spectrometry.<sup>1</sup> Time-of-flight (TOF) mass spectra of proteins weighing up to 300,000 Da are now routinely produced and this achievement has fostered a variety of bioanalytical applications which were previously unapproachable using conventional mass spectrometric techniques. These successful applications have burgeoned in spite of a poor understanding of the mechanism of analyte desorption and ionization under MALDI conditions. An improved understanding of the MALDI mechanism should aid in overcoming a number of limitations of the current state-of-the-art and forms the motivation for the work described.

One of the fundamental parameters which describes the mechanism of MALDI laser desorption and ionization is the kinetic energies ( $E$ ) with which the analyte ions are emitted from the probe surface. Initial studies performed under zero accelerating electric field conditions suggested that all ions, regardless of mass, achieve a similar velocity during laser desorption.<sup>2</sup> Entrainment of the ions through collisions with the expanding plume of desorbed neutral material was suggested as a mechanism to explain this observation. This effect would necessarily lead to increasing  $E$  with increasing ion mass. In contrast, subsequent studies under high accelerating electric field conditions showed a deficit in total ion  $E$  which increased with increasing ion mass.<sup>3</sup> To address this apparent inconsistency and to expand our understanding of the underlying physical processes occurring in MALDI we have performed both detailed ion signal profile analyses and direct ion  $E$  measurements for ions produced under a variety of MALDI conditions.

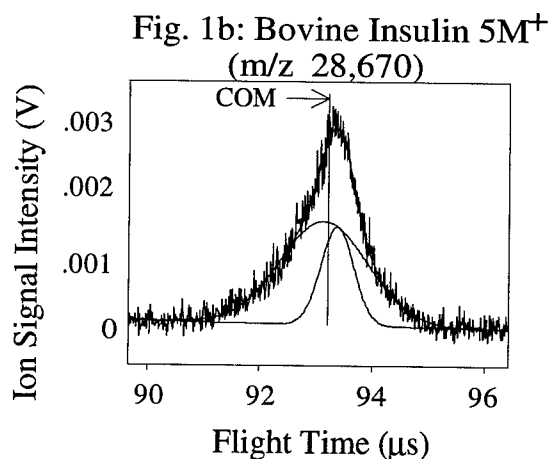
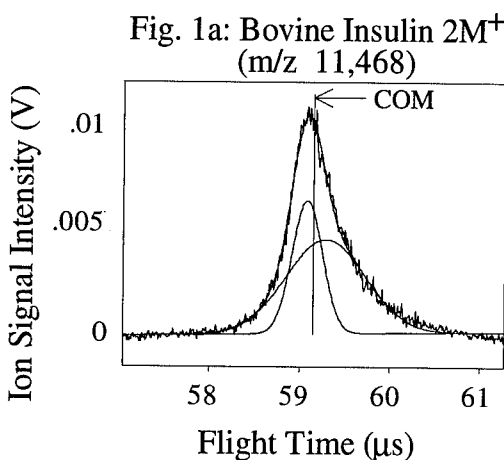
### **TOF Mass Calibration and Ion Signal Profile Analysis**

For a group of ions formed with a given energy  $E$ , the TOF calibration equation may be derived from the fundamental relationship,  $E = 1/2 mv^2$ , to give:  $t = km^{1/2}$  where  $t$  is the measured flight time for an ion of mass  $m$ , and  $k$  is an instrument defined constant. In practice, an instrument dependent offset constant,  $b$ , must be added to the calibration equation to account for the finite delay between firing of the laser for ion formation and the actual start of data collection to give:  $t = km^{1/2} + b$ .<sup>4</sup> The net result of this relationship is that a measurement of the flight times for a minimum of two known mass ions under a given set of experimental conditions allows the calibration constants  $k$  and  $b$  to be determined. With these constants a mass may be assigned to any ion signal from its measured flight time. The principle assumption in arriving at the TOF calibration equation is that  $E$  is a constant for all mass ions under a given set of experimental conditions. However, the ion  $E$  studies alluded to in the introduction suggest that this assumption is not valid for MALDI experiments, although whether a positive or negative ion  $E$  defect occurs, is not clear. Regardless, any systematic mass dependent increase or decrease of ion  $E$  should be apparent as a deviation from mass calibration linearity and a detailed analysis of the mass



calibration of a series of ions of known mass ranging over an extended mass range should reveal these deviations.

We have examined the mass calibration of bovine insulin clusters with masses ranging from 5734 Da ( $n = 1$ ) to 68,808 Da ( $n = 12$ ) formed by MALDI with  $\alpha$ -cyano-4-hydroxy-cinnamic acid matrix. Initially, flight times for the cluster ion signals were assigned based on the center of mass (COM) of the detected ion signal profiles. Linear regression of the range of known cluster ion masses and COM flight times gave the calibration constants  $k = 0.547964$  and  $b = 0.410802 \mu\text{s}$ . The  $R^2$  value of 0.999993 reveals a highly linear calibration response. However, a discrepancy is revealed by the calculated calibration constants. Data collection on the TOF instrument used to perform these studies is triggered by a fast photo diode positioned to detect a reflection of the desorbing laser pulse and should result in a data collection time offset ( $b$  value) of no more than 30 ns. Clearly this value cannot be reconciled with the calculated COM  $b$  value. A close examination of the individual detected cluster ion profiles gives insight into this problem. Figure 1a shows the bovine insulin dimer and the flight time of the COM of the ion signal profile. The asymmetric form of ion signal profile causes the center of mass of the peak to be shifted to longer flight times relative to the peak maximum. Figure 1b shows the bovine insulin pentamer and COM flight time. Here the asymmetric shape of the peak pushes the COM flight time to shorter times relative to the peak maximum. Across the entire range of cluster ion signal profiles the COM gradually shifts from the high mass side of the peak maximum to the low mass side. This response could easily explain the higher than expected calculated calibration  $b$  value and suggests that alternative methods of determining ion signal flight times need to be explored.

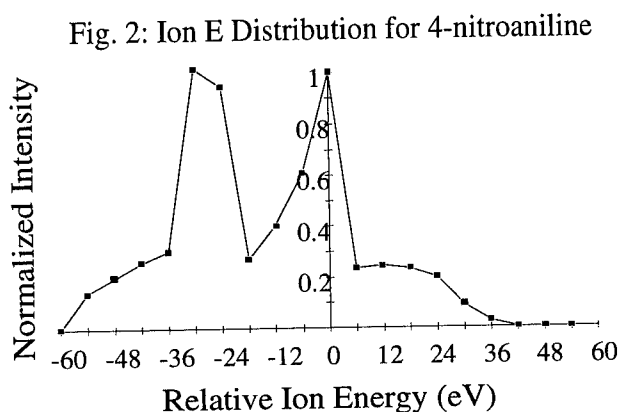


After testing a variety of single component and higher order multi-component curve fitting routines, it was found that a two component Gaussian fit of the ion signal profiles gave the best overall fit with the lowest residual. The two component fit consists of a sharp and broad component and these fits are shown in figures 1a and 1b for the bovine dimer and pentamer. A linear regression of the flight times of the sharp components of the deconvoluted ion signal profiles gives the calibration constants  $k = 0.551847$  and  $b = -0.029999 \mu\text{s}$ . This  $b$  value is completely consistent with that expected for the TOF instrumentation. Furthermore, the  $R^2$  value shows the highest linearity of all calibration regressions at 0.999999. Clearly, no mass dependent positive or negative ion  $E$  defect applies to the ions which make up the sharp component of the bovine cluster ion signals.

The flight time behavior of the broad component is more difficult to interpret. At low masses the ions making up the broad component show an apparent ion E deficit leading to longer flight times than the nominally correct cluster ion flight time (taken to be the flight time of the sharp component). At high masses the broad component shows an apparent ion E excess leading to shorter flight times than the nominally correct cluster ion flight time. One mechanism which fully explains the observed broad component flight time behavior while remaining consistent with the earlier ion E measurements, incorporates a constant ion entrainment velocity and delayed gas phase ion formation. At low mass the excess energy resulting from ion entrainment is insufficient to compensate for the acceleration energy lost due to delayed ion formation. As the mass of the ion increases the entrainment ion E gradually matches and exceeds the acceleration energy deficit leading to an overall E excess. Computational modeling supports this mechanism and indicates an ion entrainment velocity of 900 m/s and a point of ion formation 35  $\mu\text{m}$  from the probe surface.

### Ion Kinetic Energy Measurements

A direct measure of MALDI ion E's has also been performed using a hybrid electrostatic analyzer TOF mass spectrometer (E-TOF) developed in this laboratory. In these experiments the transmission energy bandpass of the E-TOF is set to 6 eV using the mechanical slits and the voltages applied to the ESA are scanned while holding the acceleration voltage constant. An example of a kinetic energy scan for the  $m/z$  139 parent ions produced from the MALDI matrix 4-nitroaniline at a source region accelerating electric field of ca. 9420 V/cm is shown in figure 2. The horizontal scale represents the ion E relative to the full accelerating voltage. It is observed that the 4-nitroaniline ion E distribution is extremely broad ranging from ca. -60 eV to +48 eV. Furthermore, a distinctive bimodal form to the ion E distribution appears with one distribution peaking at an ion E of -28 eV and the second distribution peaking at an ion E of 0 eV. This bimodal ion E distribution is consistently observed at source region accelerating electric fields of 6440 V/cm and 3360 V/cm although the position of the maxima and width of the ion E distributions change with electric field strength. These values are given in table 2. Studies of this type performed on a variety of MALDI matrices and several lower molecular weight analyte species consistently show similar bimodal ion E distributions.



Accelerating Field (V/cm)	Peak Ion E Comp. 1	Peak Ion E Comp. 2
9420	-28 eV	0 eV
6440	-22 eV	0 eV
3360	-18 eV	+ 10 eV

The mechanism proposed to explain the cluster ion signal profiles is supported by the E-TOF MALDI ion E measurements. The sharp component of the cluster ion signal profiles is consistent with the ion E distribution centered around 0 eV. These ions must arise primarily from analyte

ionization at the probe surface and feel little effect from ion entrainment or delayed ion formation. Indeed, comparisons of theoretically calculated and experimentally measured ion flight times show exact agreement for all ion signals having positive ion E's. The second component of the ion E distribution peaking at -28 eV is consistent with a group of ions undergoing delayed gas phase ionization at a distance ca. 30  $\mu\text{m}$  from the probe surface. Furthermore, comparisons of theoretically calculated and experimentally measured ion flight for those ions having energy deficits show an increasing time discrepancy with increasing energy deficit: the experimental flight times being greater than the calculated flight times. If this time discrepancy is attributed to the time required for the precursor material to move to the position of delayed ion formation, an entrainment velocity may be calculated. Using this approach an ion entrainment velocity of ca. 600 m/s is calculated. All features of the previously described mechanism are consistent with the MALDI ion E distributions measured using the E-TOF.

## Conclusion

Two mechanisms of ion formation are needed to adequately explain the mass dependent detected ion signal profiles and the measured ion E distributions produced in a MALDI experiment. One component is best described as a surface ion formation mechanism where ions are desorbed with a constant, mass independent average ion E. No collisional ion entrainment or delayed ion formation appears to act upon these ions. The second component is best described as a gas phase ion formation mechanism where neutral precursors to the observed ions achieve a constant velocity prior to delayed ion formation at some point distant from the probe surface. Increasing ion energy with increasing ion mass due to constant velocity ion entrainment combined with a constant ion energy deficit due to delayed gas phase ion formation causes the total ion E to gradually shift from an apparent ion E deficit to an apparent ion E excess. The cluster ion profile analyses and E-TOF MALDI ion E measurements may be seen as essentially identical, independent support for the proposed mechanism of laser desorption and ion formation.

- 
1. (a) F. Hillenkamp, M. Karas, R. C. Beavis and B. T. Chait, *Anal. Chem.* **63**, 1193A (1991); (b) B. T. Chait and S. B. H. Kent, *Science* **257**, 1885 (1992); (c) M. Karas, U. Bahr and U. Giessman, *Mass Spectrom. Rev.* **10**, 335 (1991).
  2. (a) R. C. Beavis and B. T. Chait, *Chem. Phys. Lett.* **181**, 479 (1991); (b) B. Spengler and R. J. Cotter, *Anal. Chem.* **62**, 793 (1990); (c) Y. Pan and R. J. Cotter, *Org. Mass Spectrom.* **27**, 3 (1992).
  3. (a) J. Zhou, W. Ens, K. G. Standing and A. Verentchikov, *Rapid Commun. Mass Spectrom.* **6**, 671 (1992).
  4. (a) R. J. Cotter, *Anal. Chem.* **64**, 1027A (1992); (b) R. B. Opsal, S. M. Colby, C. W. Wilkerson, Jr. and J. P. Reilly in *Lasers and Mass Spectrometry* ed. by D. M. Lubman, Oxford University Press, Oxford (1990).

## Time-resolved Thermometry in a Condensing Laser-ablated Copper Plasma Plume by Doppler-resolved Laser Induced Fluorescence

David K. Zerkle and Andrew D. Sappey  
 Los Alamos National Laboratory  
 Chemical and Laser Sciences Division  
 MS J565, CLS-2  
 Los Alamos, NM 87545  
 (505) 665-7101

Doppler-resolved laser-induced fluorescence (LIF) excitation scans of the Cu atom ground state are used for thermometry in laser-ablated plasma plumes. The resulting LIF line shape is analyzed by fitting Voigt profiles to determine the Doppler width of the transition which then yields directly, translational temperature. Temperature is an extremely important parameter in determining the rate and extent of condensation occurring in metal vapor plumes such as the copper plumes which we have been studying. The other seminal controlling parameter, density, has been determined using a combination of hook spectroscopy and planar laser-induced fluorescence (PLIF) as described in several preceding papers<sup>1,2</sup> and a newer, more extensive study which is to be published<sup>3</sup>. In this work, the plume is produced by excimer laser bombardment of an OFC copper target rotating in a vacuum chamber (308 nm, > 20 J/cm<sup>2</sup>, 1-5 GW/cm<sup>2</sup>). The copper plasma plume expands rapidly into a helium or argon background gas at pressures of 1 and 10 torr. Scans with 25 torr of background gas yield no useful data as a result of various broadening mechanisms which make fitting unique Voigt profiles difficult. We find that plumes expanding into argon are kinetically hotter and cool more slowly than those in helium. For example, temperatures in 1 torr of helium and delay times between the ablation and probe pulses of 0.5, 1.0 and 3.0 msec are  $1800 \pm 250$  K,  $1600 \pm 200$  K, and  $1300 \pm 150$  K, while temperatures in 1.0 torr of argon for identical delays are  $3900 \pm 700$  K,  $3000 \pm 350$  K, and  $2600 \pm 250$  K. In 10 torr of helium, the temperatures are  $300 \pm 150$  K,  $300 \pm 300$  K, and  $300 \pm 300$  K for delays of 0.2, 0.5, and 1.0 msec; whereas temperatures for the identical delay times in argon background gas at 10 torr are  $2000 \pm 350$  K,  $1600 \pm 200$  K, and  $1000 \pm 100$  K. This result helps to explain our earlier observation that the rate of disappearance of Cu atom due to condensation reactions in these plumes is faster in helium than in argon as well as the more general observation that forming clusters and particulate in argon is not as easy as in helium<sup>3,4</sup>. Physically, this likely results from the higher thermal conductivity of helium relative to argon making helium better suited at removing the excess heat from the plume.

An earlier paper describes a preliminary investigation of plume structure and condensation kinetics using planar laser-induced fluorescence (PLIF) and an initial attempt to measure kinetic temperature via rotationally (partially) resolved excitation scans of the A - X electronic system of Cu<sub>2</sub> which is present in the plume as a result of condensation reactions<sup>2</sup>. To our knowledge, that paper represents the only previous direct attempt to study the condensing plume system, although condensation is intrinsic to the formation of clusters in the "Smalley" source and to laser ablation production of fine catalytic metallic powders. Because of limitations relating to the determination of temperature using Cu<sub>2</sub> thermometry described below, this study uses the more applicable Doppler technique. This technique has been used previously by Dreyfus to determine Cu atom kinetic temperatures in laser - ablated copper plumes in vacuum<sup>5</sup>.

In earlier experiments, partially resolved LIF scans of Cu<sub>2</sub> rotational structure in the A-X band system were obtained in helium background gas for pressures as low as 5 torr<sup>6</sup>. An insufficient number density of Cu<sub>2</sub> prevented performing this experiment at lower background gas pressures. Fits to the spectra indicated that the rotational temperature of the Cu<sub>2</sub> was near 300 K even at time delays as short as 300  $\mu$ s. This was a surprising result and was attributed to the many collisions with the presumably cold background gas required to deactivate the nascent nonequilibrium rovibrational distribution of the Cu<sub>2</sub> molecule. It was assumed that the background gas was not necessarily in kinetic equilibrium with the Cu atoms, and thus the Cu<sub>2</sub> thermometry was abandoned as a Cu atom temperature diagnostic. However, combined with the Cu atom Doppler

temperatures resulting from this work, the above result is confirmed and a more coherent explanation emerges.

A complete summary of the Doppler-resolved temperatures measured appears in Table 1. The data indicate that copper plumes ablated into 1 torr of helium exhibit a temperature of approximately 1800 K at 0.5 milliseconds delay. A plot of saturation temperature vs. vapor pressure for copper is shown in Figure 1. Because the plume temperature doesn't drop below the equilibrium saturation temperature until long after the ablation pulse, condensation doesn't occur to any noticeable extent in this plume; virtually all of the decrease in Cu atom PLIF signal as a function of delay time can be accounted for by plume volumetric expansion alone. The same situation is represented for plumes expanding into argon background gas at 1 torr, with even higher temperatures and less measurable condensation.

Table 1

Pressure	Delay (ms)	Temperature (K)	
		Argon	Helium
1 torr	0.5	$3900 \pm 700$	$1800 \pm 250$
	1.0	$3000 \pm 350$	$1600 \pm 200$
	3.0	$2600 \pm 250$	$1300 \pm 150$
10 torr	0.2	$2000 \pm 350$	$300 \pm 150$
	0.5	$1600 \pm 200$	$300 \pm 300$
	1.0	$1000 \pm 100$	$300 \pm 300$

That condensation does not occur is corroborated by two additional experimental findings. First, we observe that very little  $\text{Cu}_2$  is detected using PLIF in either 1 torr of helium or argon<sup>3</sup>. Second, very little particulate is produced in these plumes until the background gas pressure is increased to 5 - 10 torr, at which point some begins to form in helium background gas. Particulate formation is not observed in argon background gas even at 100 torr. These observations would lead to the conclusion that copper plumes in helium cool much more quickly than in argon, and that even at 100 torr argon plumes are still hot enough to thwart the formation of copper dimer. This conclusion is supported by the temperature data taken in 10 torr helium and argon background gases.

Doppler LIF scans indicate that the plume temperature in 10 torr of helium has dropped to 300 K within 200 microseconds of the ablation event (see Table 1). This confirms the earlier finding that LIF scans of  $\text{Cu}_2$  rotational structure indicate that the temperature is nearly 300 K with at least 5 torr of helium. The reason condensation occurs in these plumes is that cooling occurs quickly, dropping the temperature below the equilibrium saturation temperature at 10 torr. This leads to extremely high supersaturation and condensation occurs rapidly.

In 10 torr of argon, temperatures are lower than for one torr of argon, but are still quite high, ranging from 2000 K at 200 microseconds delay to 1000 K at 1 ms delay. Therefore supersaturation is achieved within this time window and condensation does occur. However, not as much particulate is produced as with 10 torr of helium and the reason is likely as follows. We never observe very high  $\text{Cu}_2$  LIF signals with argon background gas. This is the result of two effects. First, the bandhead of the A-X (0,0) transition occurs for relatively low J levels. As a result, the bandhead feature which we excite here becomes less intense relative to the rest of the spectrum in the high temperature argon plumes. The second and dominant effect is that the equilibrium constant for the reaction  $\text{Cu} + \text{Cu} + \text{M} = \text{Cu}_2 + \text{M}$  is highly temperature sensitive with the equilibrium shifting strongly towards dissociation at increased temperature. The equilibrium constant for the formation of copper dimer is 23 orders of magnitude greater at 300 K than at 1000 K<sup>7</sup>. Since not much  $\text{Cu}_2$  is formed, the amount of particulate formed decreases.

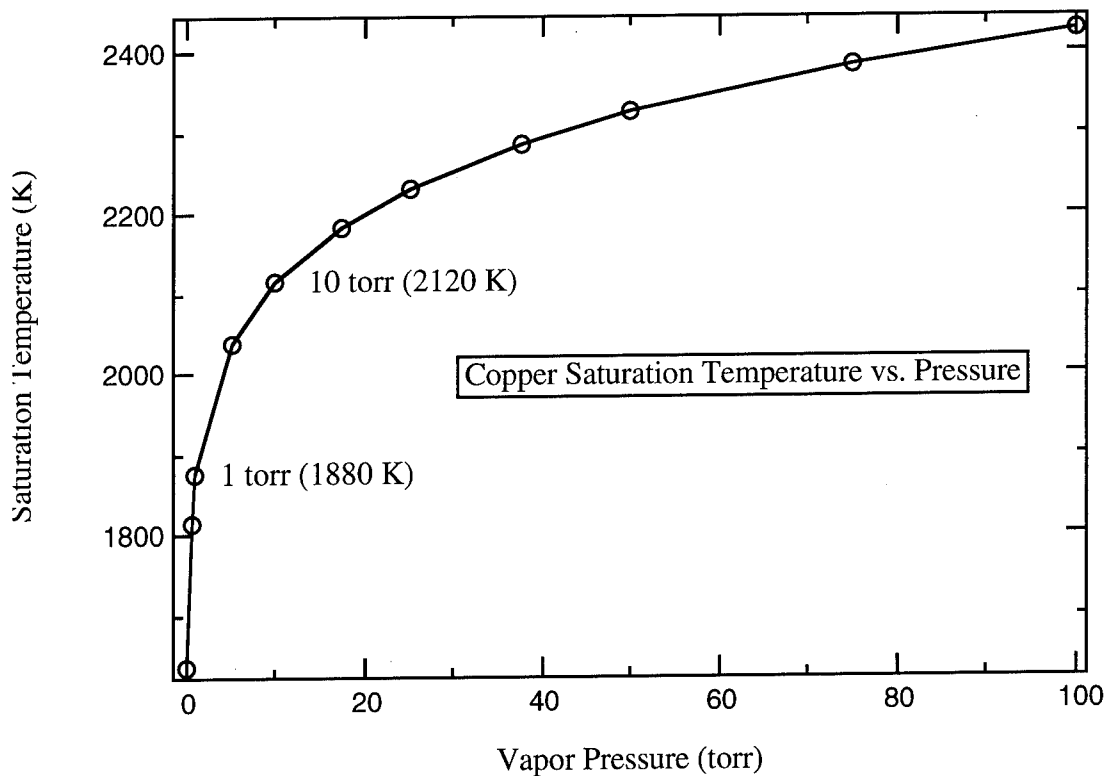


FIG. 1. Copper equilibrium saturation temperature vs. vapor pressure.

#### References

- 1 A.D. Sappey, T.K. Gamble, and D.K. Zerkle, Appl. Phys. Lett. **62**, 564 (1993).
- 2 A.D. Sappey, T.K. Gamble, J. Appl. Phys. **72**, 5095 (1992).
- 3 D.K. Zerkle, A.D. Sappey, in preparation.
- 4 A.D. Sappey, Ph.D. Thesis, University of Wisconsin at Madison, p. 283 (1988).
- 5 R.W. Dreyfus, High Temp. Sci. **27**, 503 (1990).
- 6 A.D. Sappey, T.K. Gamble, Appl Phys B **53**, 353 (1991).
- 7 J.L. Lyman, Los Alamos National Laboratory, CLS-4, personal communication (1993).

## RESONANT LASER ABLATION: THRESHOLD BEHAVIOR AND SEMIQUANTITATIVE ASPECTS

J. E. Anderson, G. C. Eiden and N. S. Nogar  
(505) 665-7279

Chemical Sciences and Technology, MS J565  
Los Alamos National Laboratory  
Los Alamos, New Mexico 87545

### Introduction

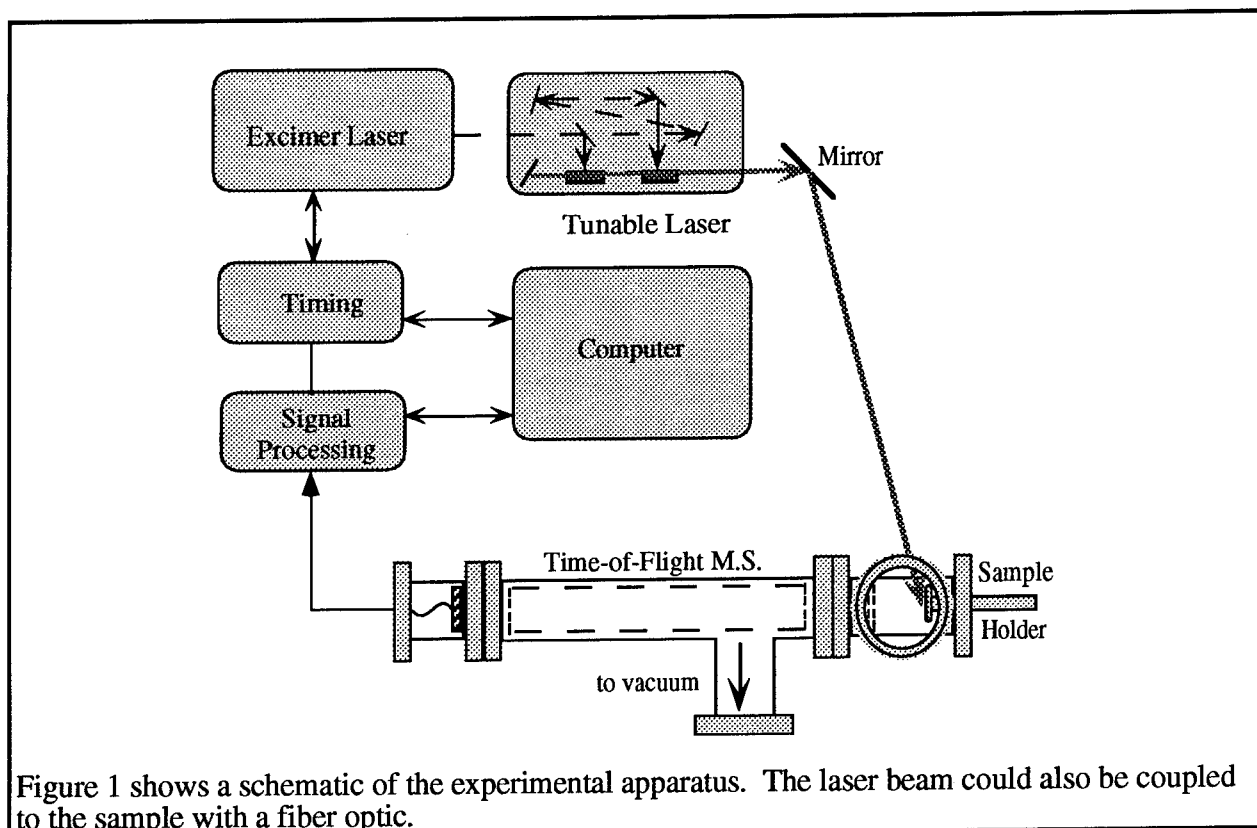
Ever since the first report of laser action, it has been recognized that laser ablation (evaporation/volatilization) may provide a useful sampling mechanism for chemical analysis. In particular, laser ablation is rapidly gaining popularity as a method of sample introduction for mass spectrometry. Since its original description, numerous research papers and review articles have appeared on various aspects of laser mass spectrometry.<sup>1, 2</sup> While most laser ablation/mass spectrometry has been performed with fixed frequency lasers operating at relatively high intensities/fluences ( $\geq 10^8$  W/cm<sup>2</sup>,  $\geq 1$  J/cm<sup>2</sup>), there has been some recent interest in the use of tunable lasers to enhance the ionization yield of selected components in an analytical sample. This process has been termed resonant laser ablation (RLA).<sup>3-5</sup> Potential advantages of RLA include: 1) simplification of the mass spectrum, by enhancement of signal from the analyte of interest; 2) improvement of the absolute detection limits by improving the ionization efficiency, and 3) improvement in relative sensitivity by reduction of spurious signal in the detection channel of interest (due to bleed through from adjacent mass channels or from isobaric interferences).

We report here on aspects of RLA behavior for a number of metals and semiconductors. Low levels of detection and semiquantitative analysis are demonstrated. Near-threshold behavior and laser power dependence are discussed.

### Experimental

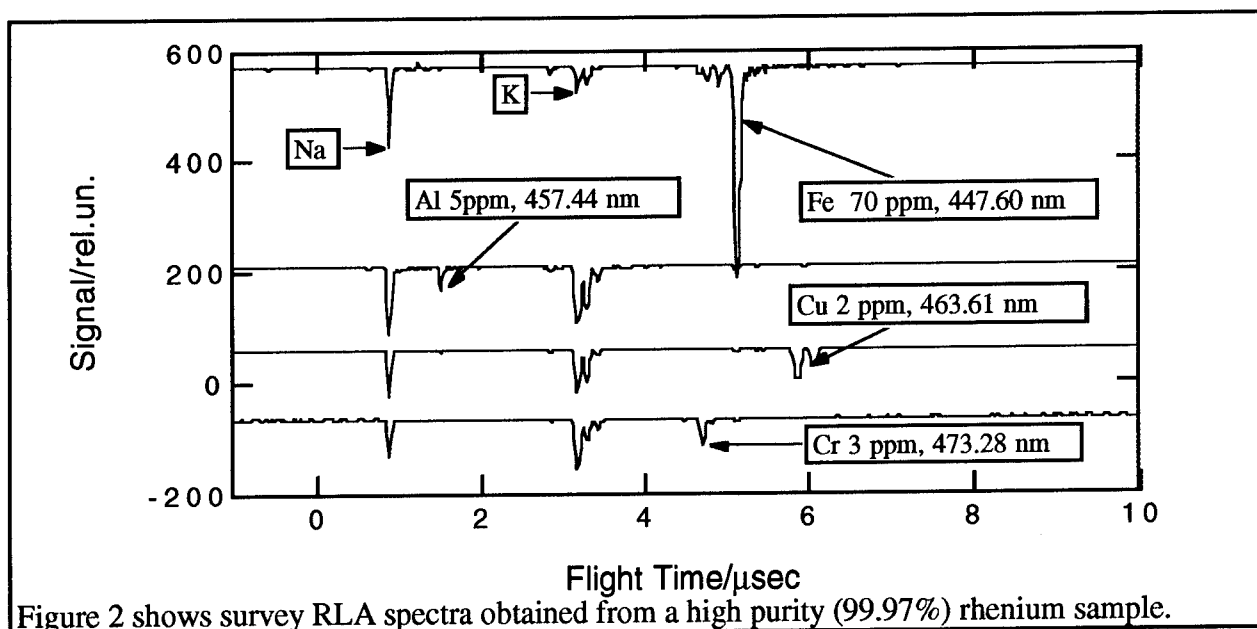
Figure 1 depicts a schematic of the experimental apparatus. Typical pulse energies lie in the range 1-100  $\mu$ J, focused to a spot approximately circular, with a beam diameter ( $1/e^2$ )  $\leq 250$   $\mu$ m. Since the angle of incidence is  $\approx 11^\circ$ , this projects to a beam area  $\approx 2.5 \times 10^{-3}$  cm<sup>2</sup>. For nominal 15 nsec pulses, this corresponds to an intensity  $2.5 \times 10^5 \leq I \leq 2.5 \times 10^6$  W/cm<sup>2</sup>. Mass analysis was by a linear time-of-flight mass spectrometer, pumped to a vacuum better than  $1 \times 10^{-7}$  Torr, with unit mass resolution up to 200 Da. Operating potentials were varied throughout these experiments, leading to a variety of observed flight times.

Samples were typically polished metal or semiconductor surfaces. The metals typically had trace impurities ranging in concentration from 1 ppb to 50 ppm. In some instances, analytical solutions or slurries were pipetted onto the surface.



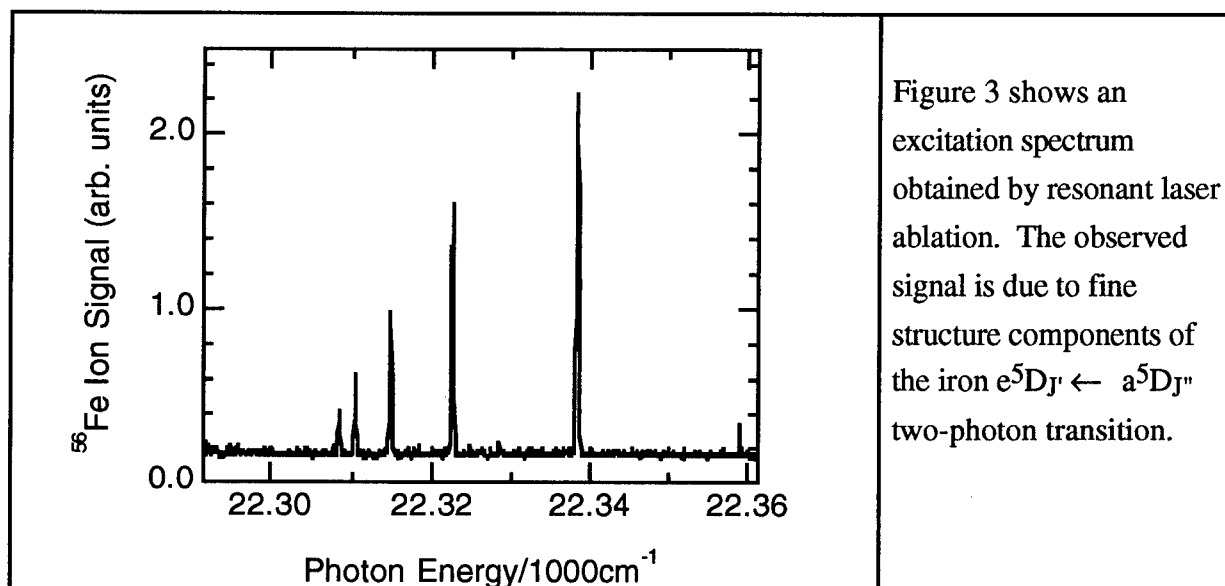
### Results and Discussion.

Figure 2 depicts survey spectra obtained from a polished rhenium sample. In virtually all instances, the spectra exhibited signals due to Na, K and, in some cases, Ca. These are presumably observed due to the combination of low ionization potential and high volatility.





In some instances (copper targets, for instance) signal due to off-resonance ionization of the bulk material was also observed. All the (optically) resonant signals reported in this work are due to "2+1" (photons to resonance + photons to ionize) ionization processes. As can be seen from Figure 2, the signal size scales monotonically with concentration. Trace components, manufacturers stated concentration, and the wavelength used for the resonant ablation process are indicated. The absolute accuracy could be improved by scaling the observed signal to that of sodium, or in some cases, to the bulk material. Currently, however, absolute concentrations can only be determined to  $\approx 5X$ . Improvements are expected with experience.



Spectroscopic information can also be obtained, even on relatively low concentration species, as shown in Figure 3. This spectrum was generated from a sample containing iron ( $\approx 70$  ppm) in rhenium (99.97%).

An initial driving for this work was the determination of small amounts of technetium in mixed nuclear waste. Figure 4 shows results for a nickel target containing Tc at  $\approx 1$  part in  $10^{15}$ . Iron appears because it is present in substantial concentration in the nickel. This spectrum exhibits more than normal evidence of nonresonant ionization (in part due to the very low concentration of analyte). Iron and nickel are major components of the target, while cadmium is observed because of an accidental near-resonance with the Tc transition used in this work.

Significant evidence was obtained during this work to indicate that the evaporation step is non-thermal. For the conditions used in our work, the maximum temperature (obtained from a simple one-dimensional calculation with temperature-invariant thermodynamic values<sup>6</sup>) for the copper target is  $< 500$  °C. This corresponds to the evaporation of  $< 1$  copper atom per shot. This is clearly inconsistent with the signal levels we observe. Hence, the generation of gas phase species

must involve other laser-material interactions, such as direct electronic (multiphoton) excitation, with subsequent photochemical or photophysical desorption.

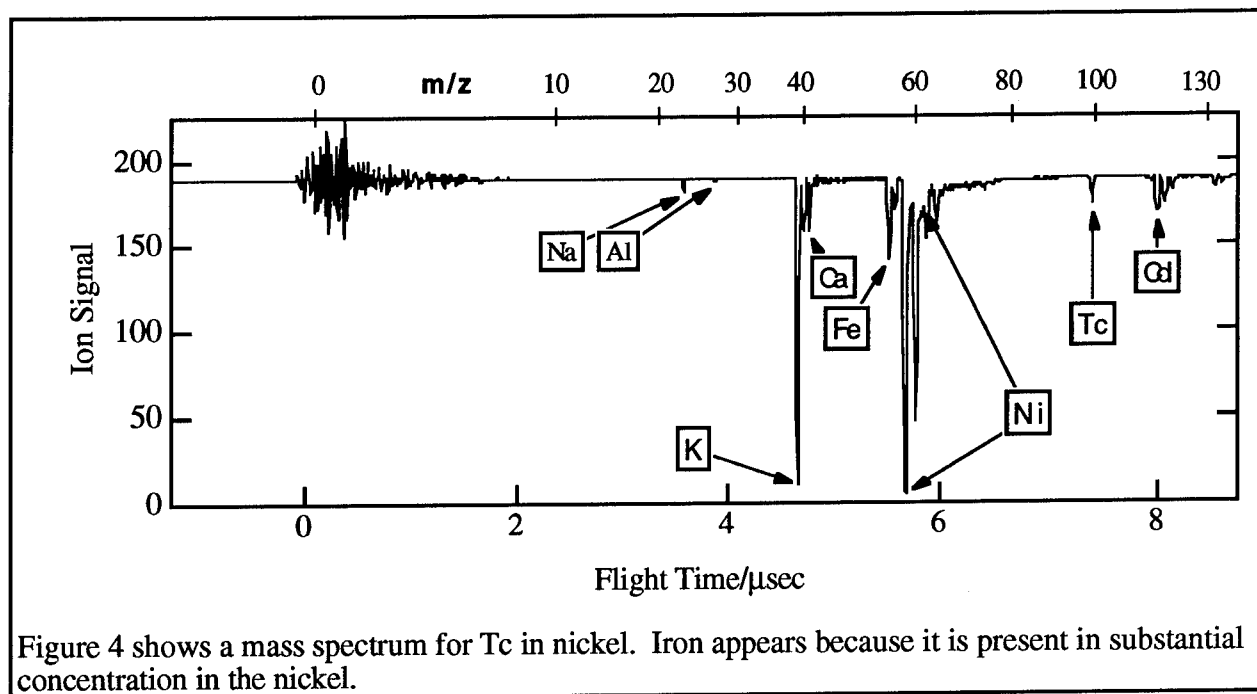


Figure 4 shows a mass spectrum for Tc in nickel. Iron appears because it is present in substantial concentration in the nickel.

In other experiments, the threshold and intensity dependence of the RLA signal were measured. For successive measurements on the same area of the sample, the intensity dependence remained constant,  $\text{signal} \propto I^n$ , with  $n = 4.75 \pm 0.25$ . However, the threshold for production of detectable signal was seen to increase by  $\approx 5\times$ . We tentatively interpret this as indicating that the intensity dependence reflects the physics of the ablation/ionization process, while the threshold reflects the chemical properties (binding energy) of the material being ablated/ionized.

## References

1. N. S. Nogar, R. C. Estler, Laser Desorption/Laser Ablation with Detection by Resonance Ionization Mass Spectrometry, in *Lasers and Mass Spectrometry*, D. M. Lubman, ed., Oxford, New York, (1990) 65.
2. J. Sneddon, P. G. Mitchell, N. S. Nogar, Laser vaporization for sample introduction in atomic and mass spectroscopy, in *Laser Induced Plasmas and Applications*, L. J. Radziemski, D. A. Cremers, Dekker, New York, (1989) 347.
3. C. J. McLean, et al., Resonant laser ablation (RLA), *Int. J. Mass Spectrom. Ion Process.*, **96**, R1 (1990).
4. L. Wang, et al., Observations and analysis of resonant laser ablation of GaAs, *Appl. Phys.*, **B53**, 34 (1991).
5. L. Wang, K. W. D. Ledingham, C. J. McLean, R. P. Singhal, Laser-induced collisional processes in resonant laser ablation of GaAs, *Appl. Phys.*, **B54**, 71 (1992).
6. D. J. Burgess, P. C. Stair, E. Weitz, Calculations of the surface temperature rise and desorption temperature in laser-induced thermal desorption, *J. Vac. Sci. Technol.*, **A4**, 1362 (1986).

# A New Fiber Optic LIF-Sensor for the Detection of Environmental Pollutants

W. Schade, J. Bublit, M. Dickenhausen and M. Grätz

University of Kiel, Olshausenstrasse 40, D-24098 Kiel, Germany

Time-integrated laser-induced fluorescence (LIF) spectroscopy and fiber optics provide a powerful tool for the diagnostics of various environmental pollutants in different media [1]. The method can easily be adapted for practical applications, e.g. in the trace analysis of oil contaminations in the soil or in the water. Since petroleum products are complicated mixtures of poly- and monocyclic aromatic hydrocarbons their time-resolved fluorescence spectra are described by a sum of up to three exponentials with characteristic intensities  $a_i$  and decay times  $\tau_i$ . For excitation in the uv (337 nm) and observation of the fluorescence at 400 nm decay times  $\tau_p \geq 50$  ns are obtained for pure oil samples. However, for the same conditions most water and soil samples show very short fluorescence decay times with typical  $\tau_m \leq 10$  ns [2]. Therefore, time-integrated detection of "early" and "late" fluorescence with respect to the laser pulse can be used very efficient for qualitative and quantitative diagnostics. On the basis of experimental results a computer simulation is developed to show the dependence of the time evolution of the LIF-signals when the concentration of contaminations with long decay times (e.g. polycyclic aromatic hydrocarbons (PAH)) is changed in a polluted water sample [3]. In fig. 1a results of this computer simulation are shown. The left curve corresponds to the fluorescence from dissolved organic matter (DOM) which is always present in natural water. For times  $t > 60$  ns after the laser pulse no fluorescence is obtained. However, when the number density of PAH in the water sample is increased a significant fluorescence signal can be measured for times  $t > 60$  ns. Then, time-integrated detection of fluorescence in the time gates 0 to 100 ns ( $I_1$ ) and 100 to 200 ns ( $I_2$ ) with respect to the laser pulse is very efficient method to measure even very low concentrations of PAH in the oil water mixtures. The ratio  $I_2/I_1$  can be used for qualitative and quantitative diagnostics (refer to fig. 1b).

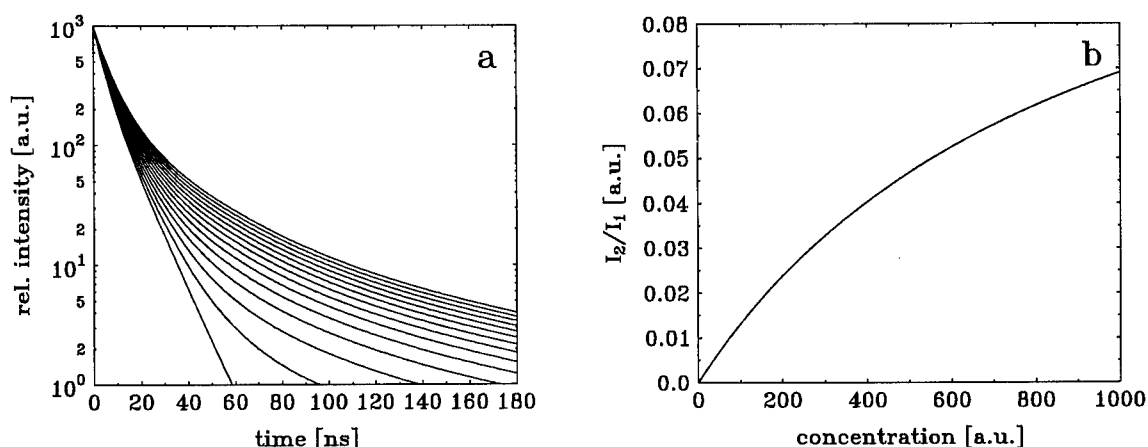


**Figure 1:**

(a) Computer simulations of LIF-decay spectra for a water sample with increasing PAH contaminations.  
 (b) Calculated ratios  $I_2/I_1$  of "late" (100-200 ns) and "early" (0-100 ns) fluorescence intensities of a water sample as function of the PAH concentration.

If a nitrogen laser (337 nm) is used for the excitation and the time-integrated fluorescence intensities  $I_1$  and  $I_2$  are recorded at 400 nm the typical detection limit for PAH contaminations is 0.5 mg/liter in water and 5 mg/kg in soil.

The application of uv-laser lines below 300 nm improves (1) the detection limit and (2) it gives the possibility to select between mono- and polycyclic aromatic hydrocarbons in the sample under investigation. With a KrF-excimer laser and a hydrogen Raman-shifter laser radiation is achieved at 248 nm, 276 nm and 314 nm, respectively. In fig. 2 LIF intensity spectra for pure water (a, b) and oil polluted water samples (c, d) are shown for the excitation wavelengths 248 nm and 337 nm. While in the latter case no significant differences in the intensity spectra are obtained, the differences in the LIF spectra measured for 248 nm excitation can be used for the diagnostics. Contrary to PAH-molecules monocyclic aromatic hydrocarbons like benzene, toluene, xylene and ethylbenzene (BTXE) have efficient absorptions below 300 nm. Therefore, BTXE-fluorescence can be induced by KrF-excimer (248 nm) but not by nitrogen laser (337 nm) radiation. Depending on the concentration of BTXE in the sample self-absorption effects cause a red-shift of the fluorescence. For excitation at 248 nm a decrease of the Raman-scattered laser light at 270 nm (fig. 2b, c) is obtained for the oil polluted water sample. This is explained by the high absorption cross sections of the BTXE for wavelengths below 300 nm. This effect is not obtained for excitation at 337 nm (fig. 2b, d).

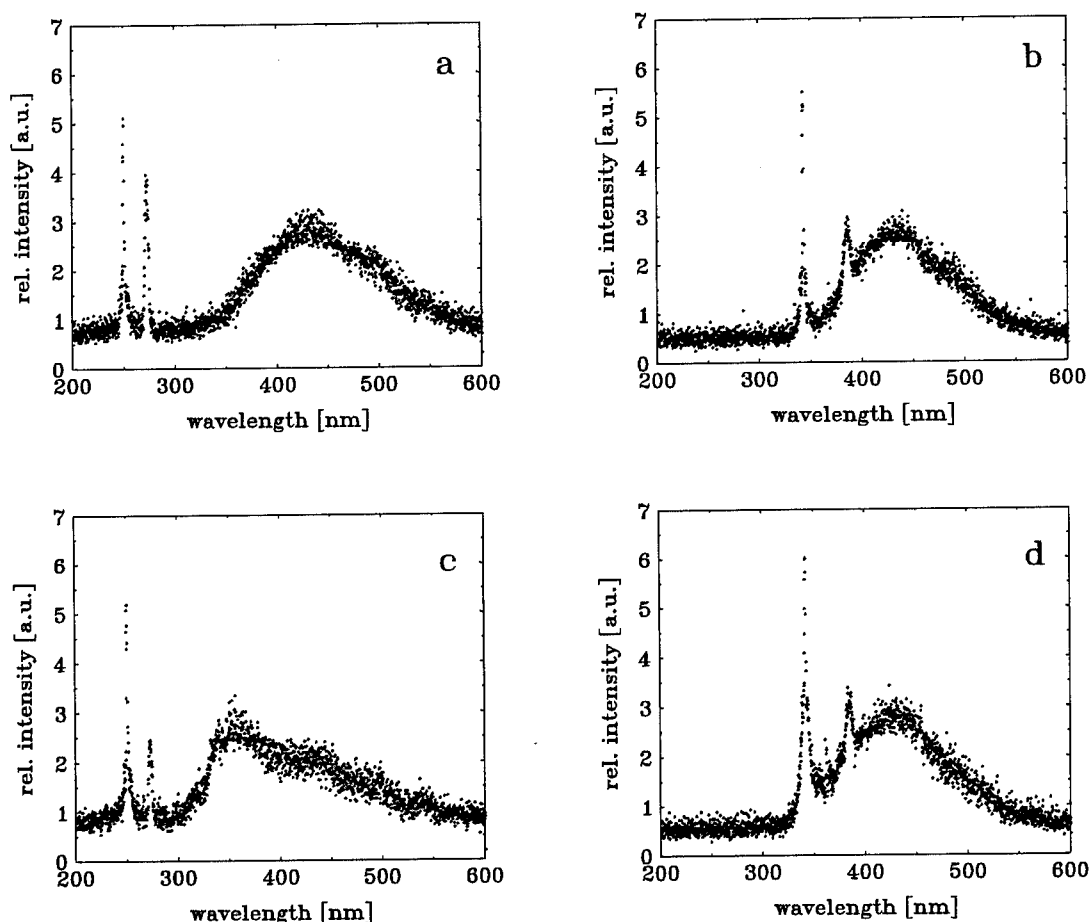


**Figure 2:**

Laser-induced fluorescence spectra of natural water (a, b) and a 10 mg/liter oil water mixture (c, d). The excitation was performed at 248 nm (a, c) and 337 nm (b, d).

For a concentration of 10 mg/liter engine oil in water the maximum of LIF-intensity is found around 350 nm. For the same conditions the fluorescence intensity of an unpolluted water sample is about a factor of 4.5 lower at 350 nm. Therefore, multiwavelength laser excitation and time-integrated fluorescence detection at different positions in the spectrum with proper time gates is an efficient method to measure PAH and BTXE contaminations in water or soil samples with high accuracy.

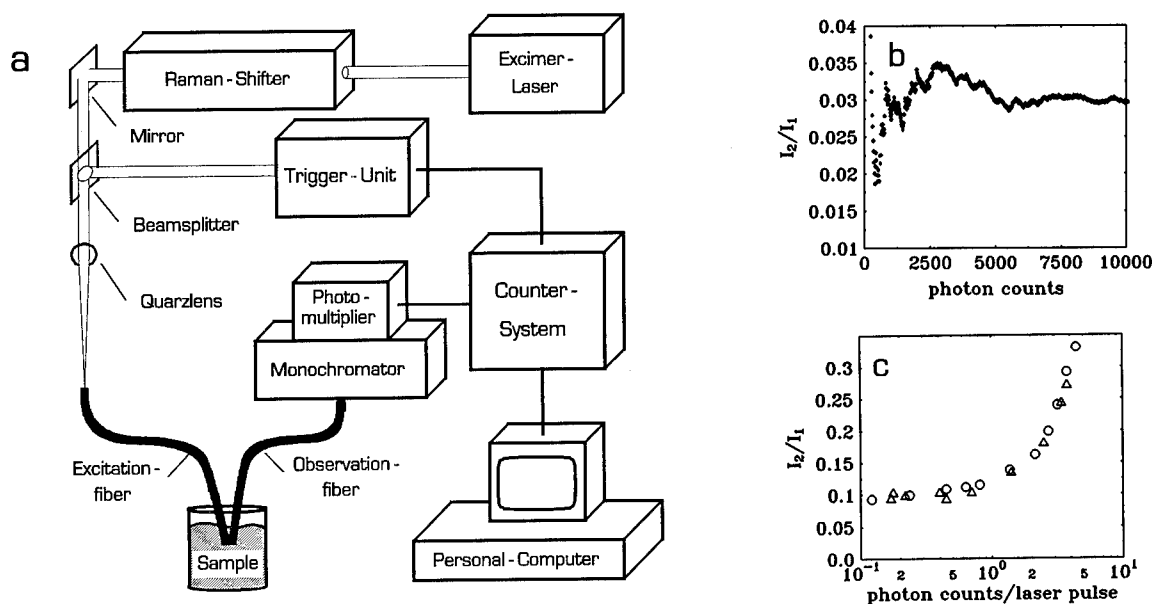


**Figure 3:**

(a) Experimental set-up for time-integrated fluorescence detection of polluted soil and water samples and multiwavelength uv-laser excitation. (b) Accuracy of the ratio  $I_2/I_1$  for an oil polluted water sample (10 mg/liter oil) as function of detected photon counts. (c) Accuracy of the ratio  $I_2/I_1$  as function of ratio of detected photons and laser pulses ( $\Delta$  experimental data, O calculations).

In the present experiment a compact multigas excimer laser, two fiber optics with integrated detection head, a photon counting system for the time-integrated recording of the fluorescence and a personal computer for controlling the system and for data processing are used. Additionally a hydrogen-Raman shifter is applied to produce laser lines at 276 nm and 314 nm when the excimer laser is operated with KrF at 248 nm (refer to fig. 3a). However, in most of the field measurements done so far the excimer laser was operated as a nitrogen laser. The counter system consists of four 100 MHz counters which are gated by the trigger unit and are used to measure the intensities  $I_1$  and  $I_2$  for different conditions. Photon counting is applied because of the very low fluorescence intensities in the "late" time gates in the case of low PAH or BTXE contaminations in the samples under investigation. This signal recording technique implies some problems in the accuracy of the ratio  $I_2/I_1$  which is used for the quantitative diagnostics. An uncertainty of  $I_2/I_1$  better than 5% requires about 6000 counted photons (fig. 3b). On the other hand the ratio  $I_2/I_1$  depends also on the ratio of counted photons to laser pulses, as shown in fig. 3c. Therefore, a laser with a repetition rate up to 100 Hz is applied in these experiments. The typical time for data averaging is two minutes. Then about 6000 photons are detected in individual measurements, and the ratio of counted photons to laser pulses is 1:2.

In fig. 4 an example of the potential of this method for practical applications is

shown. Drillings down to two meter depth have been taken in the area around a leaking diesel gas pump. These soil samples are then analyzed on-line by measuring time-integrated fluorescence intensities  $I_2/I_1$ . The laser excitation was performed at 337 nm and the fluorescence was observed at 400 nm. This gives informations about the sum-PAH contamination of the soil samples under investigation. The arrow in fig. 4 indicates the position of the leaking gas pump and the lines show the distribution of sum-PAH contamination in a vertical soil layer of two meter depth and six meter width. Between the surface and a depth of 1.5 meter the layer consists of sand, followed by a 0.15 m thick area of peat and then clay. Near the surface and the gas pump the highest diesel concentrations of up to 10000 mg/kg soil are found while more in the depth and in the width the diesel concentration decreases down to 100 mg/kg. The peat layer acts like a "natural sealing". In the clay directly below the gas pump only PAH concentrations between 5 and 100 mg/kg soil are detected, and samples from the same depth but more in the width show concentrations below 5 mg/kg.

The advantage of the time-integrated fluorescence detection after uv-laser excitation compared to the chemical laboratory analysis are the on-line detection, the improved spatial resolution and a high sensitivity. While most of the pollutants are complicated mixtures of molecules multiwavelength excitation with uv-laser lines is applied to select between these components. This is shown for PAH and BTXE in oil-polluted water or soil sample.

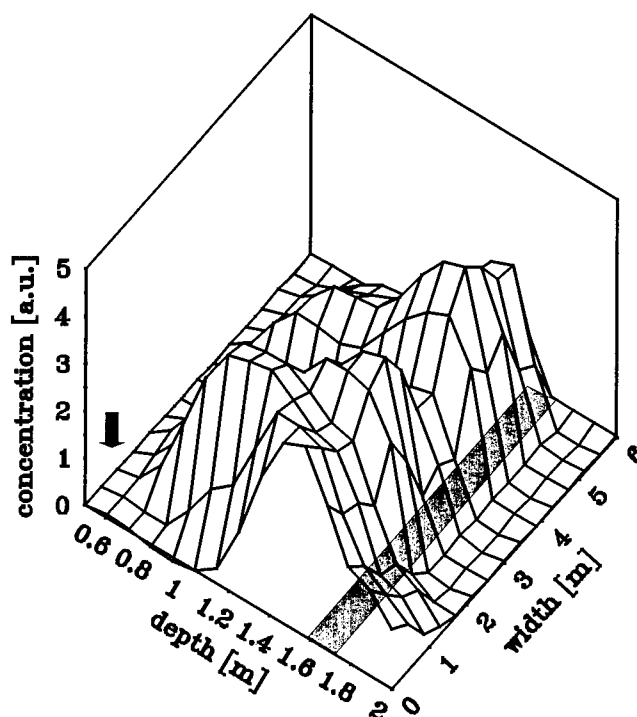


**Figure 4:**  
Distribution of sum-PAH contamination in a vertical soil layer near a leaking diesel gas pump (arrow). The laser excitation was performed at 337 nm and the time-integrated fluorescence was detected at 400 nm.

## References:

1. J.W. Griffin and K.B. Olsen, American Society for Testing and Materials **ASTM STP 1118**, ed. D.M. Nielsen and M.N. Sara, Philadelphia, p. 311 (1992)
2. W. Schade, J. Bublitz, K.-P. Nick and V. Helbig, Laser in Remote Sensing, ed. V. Klein, K. Weber and Ch. Werner (Springer, Berlin), p. 53 (1992)
3. W. Schade and J. Bublitz, Laser und Optoelektronik **25(4)**, 41 (1993)

## Zeeman Laser Interferometry for Detection and Chemical Analysis

Roger G. Johnston  
Chemical Science and Technology Division  
Los Alamos National Laboratory  
MS J565, Los Alamos, NM 87545  
(505) 667-7414

### Zeeman Laser Interferometry

Zeeman laser interferometry [1-3] relies on use of a two-frequency, Zeeman effect laser. This helium-neon laser uses a carefully controlled magnetic field to cause a Zeeman energy level splitting inside the laser plasma tube. As a result, the laser emits two collinear laser lines with orthogonal linear polarizations. The two laser lines have a wavelength near  $\lambda = 632.8$  nm, and differ by only 250 kHz in frequency.

For interferometry, the two laser lines are separated, used as separate arms of the interferometer, then reunited and allowed to interfere on a photodiode, producing a 250 kHz beat frequency. We compare this beat frequency with a reference 250 kHz sine wave generated by the Zeeman laser. A change in the refractive index (RI) of the sample causes a relative phase change given by [1-3]

$$\Delta\phi = 360^\circ (L/\lambda) \Delta RI \quad (1)$$

where  $L$  is the sample pathlength (typically 5 cm). We measure the phase changes with a resolution of  $\Delta\phi = 0.03^\circ$ . This is equivalent to an interferometric resolution of  $\lambda/12000 = 0.5$  Å.

### Zeeman Refractive Index Detector

A refractive index detector [1,4] is an instrument for monitoring a time-varying sample, such as a flowing (or sampled) gas or liquid, for changes in the refractive index (RI). If the temperature and pressure of the flowing sample are held constant, RI changes indicate a change in the

composition or contamination of the sample.

A Zeeman interferometer can be used as an ultrasensitive RI detector. We have shown that RI measurements made in this way are in good agreement with theory [1,3]. Demonstrated resolution is  $\Delta RI = 1 \times 10^{-9}$  for a 5 cm sample pathlength and 19  $\mu$ liter probe volume. Typical sensitivity for compositional changes is parts per million for contaminants in gases and part per billion in liquids.

The average drift for the Zeeman RI detector with a 5 cm sample pathlength is  $\lambda/2100$  per hour ( $\Delta RI = 6 \times 10^{-9}$  per hour); this is while monitoring the RI of a gas flowing through the interferometer at a rate of 300 mliter/min [1,2].

The stability of the Zeeman interferometer is so good, in fact, that a person can pound on the table on which the Zeeman interferometer sits with his/her fist without seriously interfering with the  $\lambda/12000$  measurements. The reasons for this excellent stability include the intrinsic stability of the Zeeman laser, careful temperature control ( $\pm 1$  mK), stable mechanical design, the parallelism of the interferometer arms, use of few optical components, avoidance of conventional beam splitters, and the fact that we measure phase rather than interferometric fringes or light intensity, as in conventional interferometry.

### **Detection for Gel Electrophoresis**

Gel electrophoresis is an important technique for separating fragments of DNA by size [5]. The Zeeman RI detector can be used to detect (in real-time) the presence of DNA bands as they pass through one spot in the gel. It is not necessary to fluorescently stain the DNA, radioactively label it, or make ultraviolet absorption measurements. This eliminates extra processing steps and delays, problems



with handling hazardous materials, changes in the DNA structure and its mobility through the gel, artifacts in quantification, partial loss of sample if the stains or radioactive labels have to be removed from the DNA after electrophoresis, and possible DNA damage [5].

Current sensitivity is 0.2 ng of DNA in the Zeeman probe beam.

This can be improved by better temperature control of the gel.

Proteins and other large macro-molecules can also be detected during gel electrophoresis.

### **Detection of Specific Chemical Species**

RI detectors are universal detectors—they can detect almost any contaminant. They can, however, also be used to detect specific chemical species. To detect a specific contaminant, a second laser or illumination source of an appropriate wavelength is needed. When the chemical of interest is present, it absorbs a portion of the incident wavelength. This may result in an excited species, having a different RI that can be detected by the Zeeman RI detector [6].

Alternately, the absorbed incident light may cause an increase in the sample temperature. The resulting decrease in the RI can again be detected by the Zeeman RI detector. Demonstrated contaminant sensitivity for this type of thermooptic spectroscopy is parts per trillion [2,7].

### **Other Applications**

Micro-Thermometry [3]: Temperature changes from 100  $\mu$ K/sec to over 300 K/sec can be accurately and non-invasively measured in sub- $\mu$ liter volumes.

Polarimetry [8]: Optical rotary dispersion can be continuously measured with 0.03° and 10  $\mu$ sec resolution. The instrument has no moving parts.

Light Scattering [2,9]: The Zeeman effect laser can be used to extract phase and polarization information from elastically scattered light. These measurements are related to elements of the Mueller scattering matrix, but the error analysis is considerably different.

## Acknowledgments

This work was performed under the auspices of the United States Department of Energy and supported in part by LDRD funding from Los Alamos National Laboratory. W. Kevin Grace, Val Bykovsky, Cheryl Lemanski, and A. Rajika Mallawaarachy contributed.

## References

1. R.G. Johnston and W.K. Grace. Refractive index detector using Zeeman interferometry. *Applied Optics* **29**, 4720 (1990).
2. R.G. Johnston, "Zeeman interferometry" in *Optics in Complex Systems*, SPIE **1319**, 222 (1990).
3. R.G. Johnston. Rapid, differential micro-thermometry using Zeeman interferometry. *Applied Physics Letters* **54**, 289 (1989).
4. H.H. Willard, L.L. Merritt, and J.A. Dean. Instrumental Methods of Analysis (Van Nostrand, New York, 1974), pp. 420-435.
5. C. Schafer-Nielsen, Editor. Electrophoresis '88 (VCH Publishers, New York, 1988).
6. G.C. Eiden, P.H. Hemberger, R.G. Johnston, and N.S. Nogar. "Sensing and Characterization Technologies at Los Alamos National Laboratory". *Proceedings, Conference on Environmental Commerce (CONEC '93)*, Chattanooga, TN, October 17-20, 1993 (in press).
7. R.G. Johnston. "Differential Thermo-optic Spectroscopy Using the Two-Frequency, Zeeman Effect Laser". Technical Digest, *1st Topical Meeting on Laser Applications to Chemical Analysis*, (OSA, Washington, D.C., 1987), pp 136-139.
8. R.G. Johnston. "Zeeman interferometry" in *Laser Interferometry*, SPIE **1162**, 344 (1989).
9. R.G. Johnston, S.B. Singham, and G.C. Salzman. Polarized Light Scattering. *Comments on Molecular and Cellular Biophysics* **5**, 171 (1988).

Thursday, March 10, 1994

# Laser Applications to Detection and Analysis of Biological Material

**ThC** 7:00pm–8:40pm  
Grand Room

James Jett, *Presider*  
*Los Alamos National Laboratory*

**Cellular and Biological Applications of Laser Induced Fluorescence.** Larry A. Sklar, Gregory M. Jones\*, Terri Gilbert Houghton\*, National Flow Cytometry Resource, Los Alamos National Laboratory, Los Alamos, NM 87545 and Cancer Center, \*University of New Mexico School of Medicine, Albuquerque, NM 87131

Lasers are widely used in biological applications to detect fluorescent molecules which probe the structure and activities of cells, cellular components, and biomolecules. Dye molecules used in biological systems are often referred to as "probe molecules" or "probes". Lasers are often selected over other excitation sources such as arc lamps because of the power density, the increased intensity when imaging faint or dilute fluorophores and the advantages of monochromatic sources for reducing stray light from turbid biological samples. The applications introduced in this paper include observing molecules and cells in suspension by spectroscopy, flow cytometry, and microscopy.

**Fluorescence Spectroscopy in Solution/Suspension** (1). Fluorescence measurements in solution are generally based on the environmental sensitivity of the emitting molecule. While spectral features may be of interest, often the fluorescence lifetime, polarization, or intensity at one or more wavelengths are observed. A large number of fluorescent molecules are commercially available (2). These include dyes sensitive to pH, divalent cations, and the proximity of other dye molecules. Derivatives are often available for linking to biological molecules such as antibodies and proteins, associating with lipids or other surfaces, or binding to DNA. Many biologically interesting interactions have kinetics that can be followed with rapid mix ("stopped flow") spectrofluorometers that allow analysis of macromolecular assembly and cell activation in the time frame of a few milliseconds.

*Fluorescence lifetime analysis by photon counting and phase sensitive detection.* Measurements of the excited state lifetime permit an evaluation of the environment of both homogenous and heterogeneous populations of probes. For example, each tryptophan in a protein can be in a different site with a unique lifetime and characteristic exposure to the aqueous environment. In contrast, multiple exponential behavior of a single tryptophan in a protein can reflect several conformational "states" of the protein. Lifetime measurements in biological systems were originally made with flash lamps and single photon detection ("time domain method"). Because of low repetition rates, these measurements often took many minutes to hours. In the last decade, the flash lamps have given way to pulsed lasers and the photon counting methods have been supplemented with phase sensitive detection (PSD). The first PSD lifetime devices used a single frequency of modulation. Lifetimes in the "frequency domain" are determined from the phase shift and amplitude demodulation of the emitted light as compared to the exciting light. Multiple lifetime analysis by PSD requires sequential observation of a biological sample at two or three frequencies to obtain multiple lifetimes and their amplitudes. At the present time, PSD analysis uses the multiple harmonic frequency method in which 20 or more frequencies are used; with air-cooled laser powers of 100 mW or less, lifetime analysis on nM dye solutions is made in seconds. In the time domain, turbid control samples are easily evaluated by point by point subtraction from the sample data. In the frequency domain, vector algebra approaches are used to correct for the background of control samples. There has recently been increased interest in non-exponential rather than multiple exponential decay behavior as a way of describing heterogeneity in the probe environment.

*Molecular Mobility/Relaxation Dynamics.* Rotation of macromolecules can be evaluated from steady state analysis of fluorescence anisotropy. In biological systems, it is generally convenient to pick probes with lifetimes comparable to the correlation times of the macromolecular assemblies they sample. When polarization methods are coupled to phase sensitive detection or photon counting, dynamic measurements of fluorescence depolarization can be obtained. This time-resolved fluorescence allows the inspection of molecular flexibility, and relaxation or reorientation processes in solution and membranes.

*Molecular Structure Through Resonance Energy Transfer.* Molecular structure and assembly may be elucidated using fluorescence resonance energy transfer (RET) between donor and acceptor probes. The basic requirement for the donor/acceptor pair is that the acceptor absorbance spectrum overlaps the donor emission spectrum. The donor transfers energy to the acceptor at the expense of donor emission so that the fluorescence quantum yield and lifetime of the donor decrease in the presence of the acceptor. The efficiency of energy transfer depends upon the distance of separation of the two fluorophores according to a  $1/R^6$  dependence. With optimal chromophores, distances up to  $\sim 90$  angstroms can be determined. The donor/acceptor pair of fluorescein and phycoerythrin (a phycobiliprotein containing multiple chromophores) has been used to measure distances in excess of 150 angstroms (3); naphthyl/dansyl pairs have been used to measure distances as small as 10 angstroms. Non-exponential energy transfer between ends of biomolecules has been interpreted in terms of molecular flexibility (4).

**Flow cytometry.** Flow cytometric technology uses one or more lasers to analyze a stream of particles - cells or chromosomes - at rates up to thousands of particles per second (5). Particles are characterized by their size, shape and fluorescent staining. When droplets with individual particles are electrostatically charged, single cell or particle populations can be sorted out of a heterogenous sample for further study. Cell surface markers can be targeted by fluorescently labelled antibodies so that cells can be characterized according to the number and types of protein antigens expressed on the cell surface. DNA can be stained on the basis of the number of base pairs and thus individual chromosomes can be detected and sorted by size. By choosing the fluorescent probes appropriately, several biological characteristics can be measured on a single cell. Flow cytometers can often discriminate between the fluorescence associated with the particle and the medium so that the evaluation of dye binding can often be performed in a heterogeneous sample in which both free and bound dye are present.

*Cell Activation.* Fluorescent probes sensitive to the cell microenvironment are useful in detecting fluctuations in the concentrations of ions inside cells and associated with cell activation. Activated cells can also be distinguished by morphological alterations detected in changes of the "forward" or "side" scatter properties or expression of the number of surface proteins or antigens. Cell-cell interactions are readily detected since cell aggregates differ in size, shape, and protein expression from individual cells (6). Kinetic cytometry is being used to evaluate the interactions of ligands and cell surface receptors (7). Analysis of kinetic data can often provide mechanistic insight into ligand binding events, receptor internalization or other "processing" events or more generally "macromolecular assembly". A flow cytometer coupled to a rapid mix delivery system is presently under development at LANL to improve the kinetic resolution of flow cytometry.

*Clinical diagnostics and rare event detection.* One of the most important applications of the flow cytometer is for blood cell analysis (hematology). Fluorescent molecules that bind to cellular DNA are used to determine the viability of cells, to evaluate the DNA ploidy and the phase of the cell cycle. Studies are currently in progress that can determine whether a cell is undergoing apoptosis - natural cell death - or necrosis, a tool that may enhance the efficiency of chemotherapeutic treatments (8). With the ability to classify cells according to many characteristics simultaneously, it is possible to detect relatively rare events in a mixed cell sample, for example: 1) white blood cells in the presence of 1000 fold excess of red blood cells in blood; 2) cells of fetal origin in a maternal blood sample or cancer cells expressing unique tumor antigens.

*Spectroscopy in flowing systems* (9). Spectroscopic approaches are useful in characterizing the environment of the probe and thus the local structure in biological systems. One can measure several wavelengths of emission or probe depolarization in single cells easily. Moreover, instrumentation has been developed to measure fluorescence lifetime (by phase sensitive detection) and spectra (by Fourier transform interferometric methods) in flow cytometry. Spectroscopic analysis appears to be useful to examine the spatial relationships of molecules on cells by RET.

*Image Cytometry.* Each particle generates a pulse of light scatter and fluorescence as it passes through the laser beam. The pulse shape and width and the angular dependence of the scatter intensity (10) contains information about the size, shape, and morphology of the cell as well as the relative distribution of the probe molecules with which the probe has been stained. Thus, a nuclear stain would exhibit a pulse shape distinct from a surface or a cytosolic stain.

**Microscopy.** Lasers have extended the utility of fluorescence microscopy (11). In addition to creating images, lasers permit both scanning and confocal capabilities. The scanning minimizes stray light and increases lateral resolution while the confocal technique increases axial resolution. Phase sensitive detection analysis of lifetimes has been accomplished in the microscope. Photobleaching of spots, lines, and patterns on cells with high laser power has permitted the analysis of lateral diffusion of molecules, while bleaching with polarized light has permitted analysis of rotational diffusion. Two-photon laser scanning fluorescence microscopy has made it possible to use a visible laser to excite a UV sensitive fluorescent dye by generating high intensities at the focal spot of the delivery optics of the microscope (12). This high intensity is required since excitation of the dye involves the absorption of two photons of the visible light simultaneously. This method appears to avoid two basic problems brought about through the coupling of confocal microscopy with UV sensitive dyes: 1) confocal microscopes deliver and collect light via the same optical path, requiring a high degree of chromatic correction, and 2) morphological changes of the cells in response to UV exposure. Another novel application of lasers with scanning confocal microscopy is RET measurement (13). Using the energy transfer capabilities of the donor/acceptor fluorophores and the axial and lateral precision of the confocal microscope allows localized energy transfer efficiencies of donor/acceptors pairs on single living cells to be measured. Using the high intensity provided by the laser light source photo-bleaching RET (pRET) may be performed in which the rate of bleaching of the donor depends upon the proximity of the acceptor. These measurements provide evidence for the proximity of cell surface receptor complexes (3).

## References

1. Lakowicz, J.R., Principles of Fluorescence Spectroscopy, Plenum Press, 1983
2. Haugland, R. P., Molecular Probes Handbook of Fluorescent Probes and Research Chemicals, 5th Edition, 1992.
3. Szabo Jr. G., Pine, P.S., Weaver, J.L., Kasari, M., Aszalos, A., Epitope Mapping by Photobleaching Fluorescence Resonance Energy Transfer Measurements Using a Laser Scanning Microscope System., *Biophys. J.* 61:661-670, 1992
4. Wu, P., Rice, K.G., Brand, L., Lee, Y.C., Differential flexibilities in three branches of an N-linked triantennary glycopeptide., *Proc. Natl. Acad. Sci. USA*, 88:9355-9359, 1991
5. Clinical Flow Cytometry: Principles and Application, K.D. Bauer, R.E. Duque, and T.V. Shankey (eds.) Williams and Wilkens, Baltimore Maryland, 1993.
6. Simon, S.I., Chambers, J. K., and Sklar, L.A., Flow Cytometric Analysis and Modeling of Cell-Cell Adhesive Interactions: The Neutrophil as a Model. *J. Cell Biol.*, 111:2747-2757, 1990
7. Sklar, L. A., Real-time analysis of ligand-receptor dynamics and binding pocket structure of the formyl peptide receptor, **Cellular and Molecular Mechanisms of Inflammation**, 3:1-23, 1992
8. Darzynkiewicz, Z., Bruno, S., Del Bino, G., Gorczyca, W., Hotz, M.A., Lassota, P., and Traganos, F., Features of Apoptotic Cells Measured by Flow Cytometry, *Cytometry*, 13:795-808, 1992
9. Sklar, L.A. National laboratory provides laser resource in flow cytometry. *Laser Focus World*, August 1991, 1-7.
10. Salzman, G.C., Singham, S.B., Johnston, R.G., and Bohren, C.F., Light Scattering and Cytometry, 81-107, **Flow Cytometry and Sorting**, eds M.R. Melamed, T. Lindmo, and M.L. Mendelson, Wiley-Liss, N.Y.
11. Jovin, T.M. Arndt-Jovin, D.J., Luminescence Digital Imaging Microscopy, *Annu. Rev. Biophys. Biophys. Chem.* 18:271-308, 1989
12. Denk, W., Strickler, J.H., Webb, W.W., Two-Photon Laser Scanning Fluorescence Microscopy, *Science*, 248:73-76, 1990
13. Jovin, M.J., Arndt-Jovin, D.J., FRET Microscopy: Digital Imaging of Fluorescence Resonance Energy Transfer Application in Cell Biology, Cell Structure and Function by Microspectrofluorometry, Academic Press, 1989

# Phase-Sensitive Flow Cytometry: New Technology For Analyzing Biochemical, Functional, and Structural Features in Fluorochrome-Labeled Cells/Particles.

John A. Steinkamp, Life Sciences Division, Mail Stop M888, Los Alamos National Laboratory, Los Alamos, NM 87545. Telephone: 505-667-2756, FAX: 505-665-3024.

Flow cytometry (FCM) instruments rapidly measure biochemical, functional, and cytological properties of individual cells and macromolecular components, e.g., chromosomes, for clinical diagnostic medicine and biomedical and environmental research applications. These measurements are based on labeling cells with multiple fluorochromes for correlated analysis of macromolecules, such as, DNA, RNA, protein, and cell-surface receptors. In addition to utilizing the spectral emission properties of fluorescent markers, i.e., different colors/intensities, to measure specific cellular features, the excited state lifetimes also can provide a means to discriminate among the different fluorochromes. A new FCM approach, based on phase-resolved fluorescence lifetime spectroscopy methods (Vesolova *et al*, 1970, Lakowicz and Cherek, 1981), recently has been developed to provide unique capabilities for separating signals from multiple overlapping emissions in fluorochrome-labeled cells as they pass across a modulated laser excitation source (Steinkamp and Crissman, 1993). In addition, the measurement of fluorescence lifetime (Pinsky *et al*, 1993, Steinkamp *et al*, 1993) also is of importance because it provides information about fluorophore/cell interactions. An important advantage of lifetime measurements is that lifetimes in some case can be considered as absolute quantities. However, the lifetime of fluorophores bound to cellular macromolecules can be influenced by physical and chemical factors near the binding site, such as solvent polarity, cations, pH, energy transfer, excited-state reactions, and quenching. Thus, lifetime measurements can be used to probe the cellular environment, possibly including chemical and structure changes that occur in DNA and chromatin. Table I lists the lifetimes of some typical fluorochromes that are used to quantify cellular DNA, total protein, and antibody-labeling to cellular antigens.

The phase-sensitive flow cytometer is a novel instrument that combines flow cytometry and fluorescence lifetime frequency-domain spectroscopy principles to resolve emission signals from multiple fluorescent probes based on differences in their lifetimes and to measure lifetimes directly. Fluorochrome-labeled cells are analyzed as they intersect an intensity-modulated laser excitation beam consisting of a dc and a high-frequency (sinusoidal) excitation component (see Fig. 1). Fluorescence is measured orthogonal to the laser-beam cell-stream intersection point using a single detector consisting of a collection lens, a longpass barrier filter, and a photomultiplier tube. The fluorescence signals which are shifted in phase ( $\phi$ ) relative to the excitation frequency and amplitude

TABLE I

FLUORESCENT DYE/COMPOUND	EXCITATION WAVELENGTH (nm)	FLUORESCENCE LIFETIME (ns)	PHASE SHIFT* AT 10 MHz (degrees)
Hoechst 33258	uv	3.5	12.4
DAPI (DNA)	uv	~4.0	14.0
Mithramycin	420	3.0	10.7
Propidium Iodide	515	1.2	4.3
Propidium Iodide (Cells)	515	13.0	39.2
Ethidium Bromide	515	1.8	6.5
Ethidium Bromide (Cells)	515	19.0	50.0
Ethidium Bromide (DNA)	515	22.5	54.6
Acridine Orange (Cells)	480	3.0 (Green)	10.7
Acridine Orange (Cells)	480	13.0 (Red)	39.2
Fluorescein	480	4.7	16.4
FITC	480	3.6	12.5
Texas Red-Avidin	530	4.6	16.1
Phycoerythrin-Avidin	530	3.5	12.6

\*Phase shift equals  $\arctan \omega\tau$ , where  $\omega = 2\pi f$  the angular frequency and  $\tau$  = fluorescence lifetime



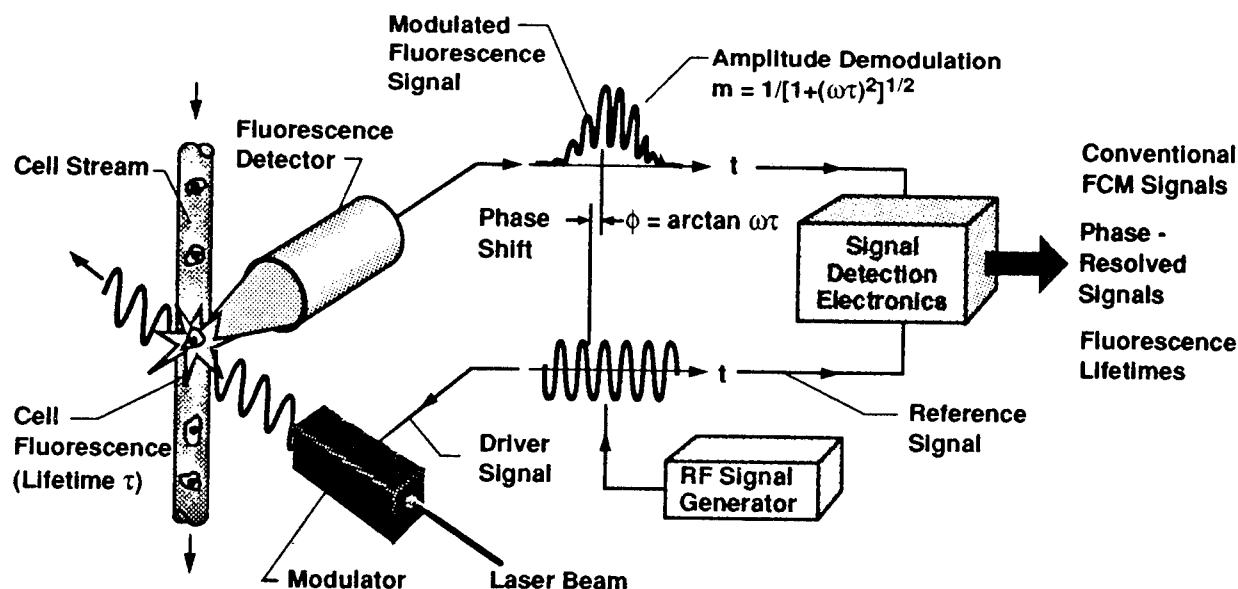


Figure 1. Conceptual diagram of the phase-sensitive flow cytometer illustrating the laser excitation source, modulator, RF signal generator, laser beam-cell stream intersection point in flow chamber (flow chamber not shown), fluorescence detector, and signal detection/processing electronics. The fluorescence signal phase shift ( $\phi$ ) with respect to the reference signal is equal to the  $\arctan \omega\tau$ , where  $\omega$  is the angular frequency ( $2\pi\phi$ ) and  $\tau$  is the fluorescence lifetime.

demodulated, are processed by phase-sensitive signal-detection electronics to resolve signals from heterogeneous fluorescence emissions resulting from differences in their lifetimes and quantify fluorescence lifetimes directly.

The time-dependent fluorescence emission signal  $[v(t)]$  is a high-frequency, Gaussian-shaped, modulated pulse that results from the passage of the cell across the focused laser beam and it can be expressed as:

$$v(t) = V[1 + m \cos(\omega t - \phi)] \cdot e^{-a^2(t-t_0)^2}, \quad (1)$$

where  $V$  is the signal intensity,  $\omega$  is the angular excitation frequency,  $\phi$  and  $m$  are the respective signal phase shift and demodulation terms associated with a single fluorescence decay time ( $t$ ),  $t$  is time, and  $a$  is a term related to the velocity of a cell crossing the laser beam at time  $t_0$ . This equation is derived for cells that are excited by an excitation source with a 100% depth of modulation. A more general expression will take into account the laser excitation depth of modulation factor ( $m_{ex}$ ) which will reduce the high-frequency signal amplitude term. The cw-excited dc signal component is extracted using a low-pass filter to give conventional fluorescence intensity information. The high-frequency signal component, which is shifted in phase ( $\phi$ ) by an amount

$$\phi = \arctan \omega\tau \quad (2)$$

relative to the excitation frequency and demodulated by a factor ( $m$ ), where

$$m = 1/[1 + (\omega\tau)^2]^{1/2}, \quad (3)$$

is processed by a phase-sensitive detector (PSD) consisting of a multiplier and a low-pass filter. A phase shifter is used to shift the phase ( $\phi_R$ ) of the reference signal input to the multiplier with respect to modulated fluorescence signal. The PSD output is a Gaussian-shaped signal that is proportional to fluorescence intensity, the demodulation factor, and the  $\cos(\phi - \phi_R)$  expressed as:

$$v_o(t) = \frac{1}{2} m V \cos(\phi - \phi_R) \cdot e^{-a^2(t-t_0)^2}. \quad (4)$$

The output intensity can thus be made to vary from both positive and negative values depending upon the sign of the  $\phi - \phi_R$  phase shift term.

The principle of phase suppression, as applied to flow, for separating two fluorescence signals having different emission decay times, i.e., phase shifts, by phase-sensitive detection, is illustrated

below. The output of the PSD is expressed (by superposition) as:

$$v_o(t) = \frac{1}{2} m_1 V_1 \cos(\phi_1 - \phi_R) \cdot e^{-a^2(t-t_0)^2} + \frac{1}{2} m_2 V_2 \cos(\phi_2 - \phi_R) \cdot e^{-a^2(t-t_0)^2}, \quad (5)$$

where  $V_1$  and  $V_2$  are the signal intensities,  $m_1$  and  $m_2$  are the demodulation factors, and  $\phi_1$  and  $\phi_2$  are the phase shifts that result when a cell stained with two fluorochromes, each having a different lifetime  $\tau_1$  and  $\tau_2$ , is excited with a modulated excitation source. To resolve either of the two signals the reference phase is shifted by an amount  $\pi/2 + \phi_1$  or  $-\pi/2 + \phi_2$  degrees. This results in one signal being passed and the other being nulled. For example, if the reference phase is adjusted to equal  $-\pi/2 + \phi_2$  degrees, the detector output is expressed as:

$$v_o(t) = \frac{1}{2} m_1 V_1 \sin(\phi_2 - \phi_1) \cdot e^{-a^2(t-t_0)^2}. \quad (6)$$

Similarly, if the reference phase is adjusted to equal  $\pi/2 + \phi_1$  degrees, the output is expressed as:

$$v_o(t) = \frac{1}{2} m_2 V_2 \sin(\phi_2 - \phi_1) \cdot e^{-a^2(t-t_0)^2}. \quad (7)$$

Both signals are resolved, but with a loss in amplitude  $[\sin(\phi_2 - \phi_1)]$ .

Fluorescence lifetime is quantified directly by the two-phase method. A quadrature phase hybrid circuit is used to form two reference signals that are 90 degrees out of phase with each other. These signals are input as references to two PSDs, the outputs which are expressed as:

$$v_{\phi-90}(t) = \frac{1}{2} mV \sin \phi \cdot e^{-a^2(t-t_0)^2} \text{ and } v_{\phi}(t) = \frac{1}{2} mV \cos \phi \cdot e^{-a^2(t-t_0)^2}, \quad (8)$$

where  $\phi$  is the signal phase shift (see Equation 2). The  $v_{\phi-90}(t) / v_{\phi}(t)$  ratio expression results in the  $\tan \phi$  which is directly proportional to the fluorescence decay time expressed as:

$$\tau = \frac{1}{\omega} \tan \phi = \frac{1}{\omega} [V(\phi-90) / V(\phi)]. \quad (9)$$

The signal detection electronics outputs are amplified, integrated, and transferred to a computerized data-acquisition system for display as frequency distribution histograms or as bivariate dot and contour diagrams.

The initial results show signal phase shift and amplitude demodulation recorded on fluorospheres and cells stained for total DNA content using propidium iodide (PI) and ethidium bromide that were excited in a 1 to 30 MHz frequency range; a signal detection limit threshold range of 300 to 500 fluorescein molecules equivalence, compared to 250 molecules equivalence for cw/dc laser excitation; a measurement precision (coefficient of variation measured on frequency distribution histograms) of 1.8% on alignment fluorospheres and 3.6% on cells stained with PI (DNA content); the resolution of fluorescence signals from cells stained in combination with PI and fluorescein isothiocyanate (FITC), based only on differences in their decay lifetimes expressed as phase shifts [see Fig. 2, parts (A) - (E)]; and the direct measurement of nanosecond fluorescence lifetimes on fluorospheres and cells stained with PI and FITC [see Fig. 2(F)]. Of particular significance in the data recorded in Fig. 2(F) is the lifetime measurement linearity (compared to conventional static time-resolved measurements, see Table I) and the uniformity of the fluorescence lifetime histograms compared to the broader integrated fluorescence intensity measurements of total cellular DNA and protein [see Fig. 2(A) and 2(B)].

Like conventional flow cytometers, the phase-sensitive cytometer can analyze fluorochrome-labeled cells or subcellular components for clinical, biomedical, and environmental research applications. However, because this cytometer can electronically separate the signals from two different fluorochrome emissions based on their lifetimes and also make conventional measurements, it has a wide range of technical applications. Of particular importance are fluorescent probes in which the lifetime changes between the bound and unbound (free) state, e.g., calcium indicators. Also of interest are probes, such as, the Hoeschst DNA-binding fluorochromes, in which the lifetime changes as function of energy transfer/quenching by surrounding agents (DNA-incorporated BrdU). Phase-sensitive detection methods also have the potential to reduce background interferences, e.g., cellular autofluorescence and Raman and Rayleigh scatter, that cause decreased measurement sensitivity and precision. In addition, fluorescence lifetime can be used as a spectroscopic probe to study the interaction of fluorochromes with their targets, each other, and the surrounding environment. Alternative methods to resolve multicomponent emissions/lifetimes will require that multifrequency excitation be employed (Jameson *et al*, 1984).

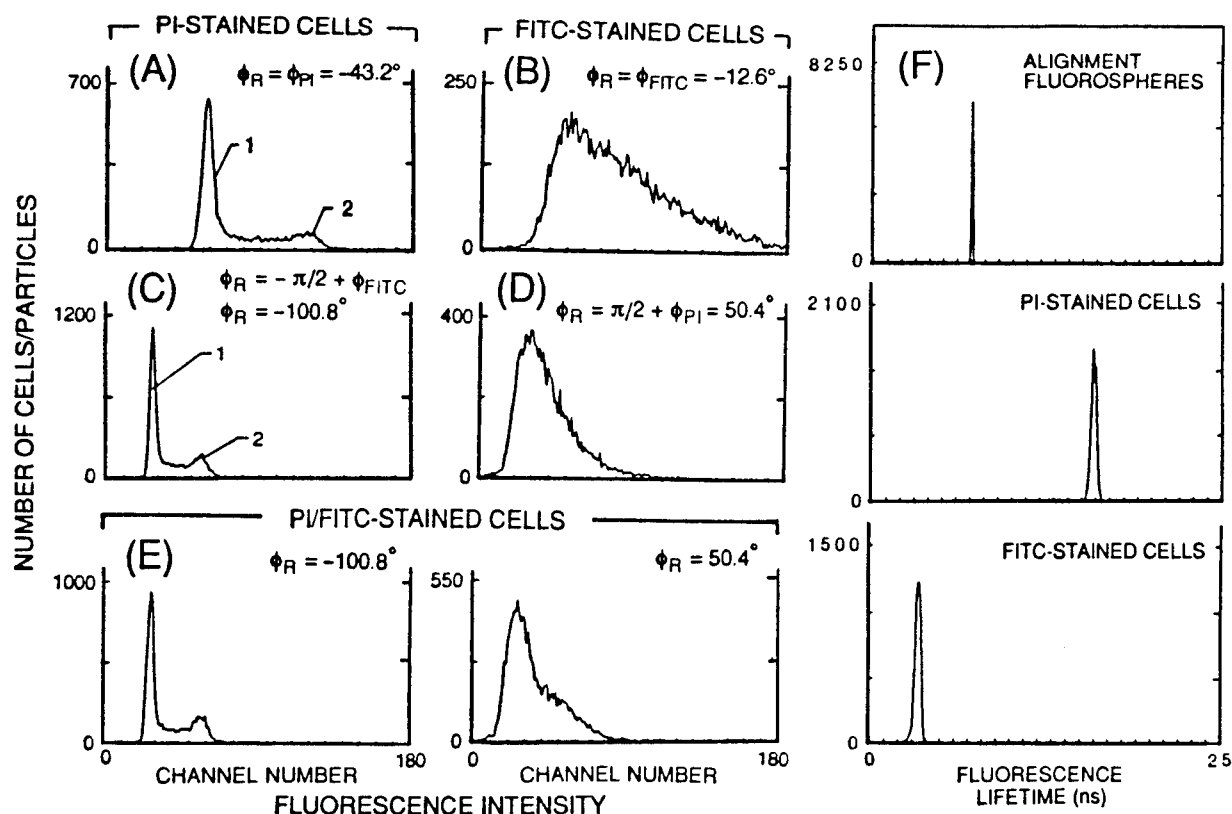


Figure 2, Parts (A) - (E). Frequency distribution histograms of the PSD output signals from line CHO cells stained separately with PI and FITC and in combination and analyzed using a 10 MHz modulation frequency and 488 nm wavelength laser excitation. In parts (A) and (B), the phase of the reference signal was adjusted to maximize the PSD output signals for PI-stained cells ( $\phi_R = \phi_{PI} = -43.2^\circ$ ) and for FITC-stained cells ( $\phi_R = \phi_{FITC} = -12.6^\circ$ ), respectively, and the corresponding histograms were recorded. In part (C), FITC-stained control cells were first analyzed and  $\phi_R$  was adjusted ( $\phi_R = -\pi/2 + \phi_{FITC} = -100.8^\circ$ ) to null the PSD signals. PI-stained cells were then analyzed at the same phase shift and PMT/amplifier gains and the histogram was recorded. Similarly, in part (D), PI-stained cells were analyzed and  $\phi_R$  adjusted ( $\phi_R = \pi/2 + \phi_{PI} = 50.4^\circ$ ) to null the PSD signals. FITC-stained cells were then analyzed at the same phase shift and gain settings and the corresponding histogram was recorded. In part (E), cells stained in combination with PI and FITC were analyzed by first recording the PSD output signal histograms with  $\phi_R = -100.8^\circ$  (PI signals resolved) and then with  $\phi_R = 50.4^\circ$  (FITC signals resolved). Figure 2, Part (F). Fluorescence lifetime frequency distribution histograms recorded on Coulter "DNA Check" alignment fluorospheres and on PI- and FITC-stained line CHO cells analyzed using a 10 MHz modulation frequency, 488 nm wavelength laser excitation, and a ratio module gain of 9.6X.

## REFERENCES

- Jameson, D.M., Gratton, E., and Hall, R.D. (1984). *Appl. Spect. Rev.* 20, 55-106.  
 Lakowicz, J.R. and Cherek, H. (1981). *J. Biol. Chem.* 256, 6348-6353.  
 Pinsky, B.G., Ladasky, J.J., Lakowicz, J.R., Berndt, K., and Hoffman, R.A. (1993). *Cytometry* 14, 123-135.  
 Steinkamp, J.A. and Crissman, H.A. (1993). *Cytometry* 14, 210-216.  
 Steinkamp, J.A., Yohsida, T., and Martin, J. C. (1993). *Rev. Sci. Instrum.* In press.

This work was performed at the Los Alamos National Laboratory, Los Alamos, NM, under the joint sponsorship of the United States Department of Energy; the Los Alamos National Flow Cytometry Research Resource, National Institutes of Health Grant No. P41-RR01315; and the National Institutes of Health Grant No. R01-RR07855.

### **Recent Developments in DNA Fragment Sizing by Flow Cytometry**

Mitchell E. Johnson, Jeffrey T. Petty, Peter M. Goodwin, John C. Martin, W. Patrick Ambrose, Babetta L. Marrone, James H. Jett and Richard A. Keller, Chemical and Laser Sciences Division and Life Sciences Division, Los Alamos National Laboratory, Los Alamos, NM 87545, 505-665-2092

Gel electrophoresis is the most widely accepted technique for analysis and separation of DNA fragments. Standard gel electrophoresis is used for fragment sizes up to approximately 50 kb in length. Larger fragments must be separated by some form of pulsed field electrophoresis (1). Capillary gel electrophoresis (2) and ultrathin slab gel electrophoresis (3) are currently being developed to allow for high speed separation of DNA sequencing ladders for sizes less than 1 kb. No matter what form of electrophoresis is used, the separation is highly non-linear and generally has an upper limit to the size of the DNA that can be analyzed. In addition, conventional gel-based separations may take many hours, depending on required resolution and detection method.

We have recently developed a new approach to sizing DNA fragments (4). The technique is based upon flow cytometry and results in DNA fragment size measurement that is linear with respect to both fragment size and number of fragments measured. Size linearity follows from the fact that fluorescence is measured from stoichiometrically stained individual fragments of DNA as they flow through a laser beam. Counting linearity follows since each fragment is measured individually.

We have demonstrated that large, individual, fluorescently stained DNA fragments can be sized accurately at a rate of approximately 60 fragments per second (4). A histogram of the fluorescence intensities of individual fragments (10 to 50

kbp) in a mixture of lambda phage DNA ( $\lambda$  DNA), a *Kpn* I digest of  $\lambda$  DNA, and an *Apa* I digest of  $\lambda$  DNA was used to demonstrate linear sizing with an accuracy of better than 2% in 164 seconds.

Detection and analysis of individual fluorescently stained DNA fragments in the one millisecond that they are in the laser beam requires sensitive fluorescence detection capabilities. Our apparatus is a modification of the instrumentation we used to detect single dye molecules and to measure their fluorescence lifetimes (5, 6). However, modifications in the single molecule detection apparatus necessary to achieve reasonable resolution in the fragment sizing requires compromises which tend to increase the background. The current method also has limitations related to staining chemistry. In this talk, we will describe efforts to size smaller fragments of DNA, with a view towards absolute size and resolution limits.

Sizing of DNA fragments by flow cytometry should also obviate the upper size range inherent in gel electrophoresis. We will also describe recent efforts to size of large fragments of DNA (> 100 kbp).

1. Schwartz, D. C. and Cantor, C. R. (1984) *Cell*, **37**, 67-75.
2. Swerdlow, H., Zhang, J. Z., Chen, D. Y., Harke, H. R., Grey, R., Wu, S., Dovichi, N. J. and Fuller, C. (1991) *Anal. Chem.*, **63**, 2835-2841.
3. Kostichka, A. J., Marchbanks, M. L., Brumley, R. L., Jr., Drossman, H. and Smith, L. M. (1992) *Bio/Technology*, **10**, 78-81.
4. Goodwin, P. M., Johnson, M. E., Ambrose, W. P., Martin, J. C., Marrone, B. L., Jett, J. H., and Keller, R. A. (1993) *Nucleic Acids Res.*, **21**, 803-806.
5. Shera, E. B., Seitzinger, N. K., Davis, L. M., Keller, R. A. and Soper, S. A. (1990) *Chem. Phys. Lett.*, **174**, 553-557.
6. Wilkerson, C. W., Jr., Goodwin, P. M., Ambrose, W. P., Martin, J. C. and Keller, R. A. (1993) *Appl. Phys. Lett.*, **62**, 2030-2032.

## Morphological Resonances for Multicomponent Immunoassays

W. B. Whitten, M. J. Shapiro, and J. M. Ramsey  
Chemical and Analytical Sciences Division  
Oak Ridge National Laboratory  
Oak Ridge, TN 37831-6142  
(615) 574-4921

B. V. Bronk  
U.S. Army Edgewood RDEC  
Edgewood, MD 21010  
(410) 671-2326

We are developing a multicomponent immunoassay technique in which a small sample can be simultaneously analyzed for a large number of species of microorganisms. Sensitivity is sufficient for the detection and identification of individual organisms. While the present scheme requires manipulation and visual observation by the analyst, the technique could be readily automated.

The identification is based on optical size discrimination of transparent microspheres. Morphology-dependent resonances in elastically or inelastically scattered light can be used to determine the diameter of a microsphere to better than one part in  $10^4$ . This means that we can use the diameter of a microsphere as an identifying label for a type of antibody that might be immobilized on the microsphere surface. Our analysis scheme is to attach antibodies to each targeted microorganism or biomolecule to microspheres of different known size. The spheres can then be mixed together since the antibodies are now effectively labeled. If only a few tens of species are targeted, the microspheres can be purchased or manufactured with the required size distribution. Otherwise, for hundreds of targets, it would probably be necessary to sort the microspheres into size increments before the antibodies were attached. This mixture of sphere-labeled antibodies can then be stored until an analysis is required.

For an analysis, a small quantity of sample suspected to contain targeted species is stained with a fluorescent dye. If the targets are entirely microorganisms, an intercalating dye such as ethidium bromide or the more powerful proprietary dyes could be used. Otherwise, perhaps a dye that attaches indiscriminately to peptides. The unattached dye must then be removed in a separations step if it would attach to the microspheres or antibodies. Incubation of the stained sample with an aliquot of the microsphere mixture should result in selective binding of the stained microbes in the sample with appropriately coated spheres. The mixture can then be examined under a fluorescence microscope to see which spheres have attached microorganisms. Single attached microorganisms can be readily observed in this way. The size of a sphere with attached targeted species can be determined from the frequencies of the morphology-dependent spectral resonances for positive identification.

To test these ideas, we procured two species of dyed inactive bacteria, *E. coli* and *Staph. aureus*, from Molecular Probes, Inc. Antibodies to these organisms were obtained from Biodesigns, International. The antibodies were attached to carboxylated polystyrene spheres by the carbodiimide reaction, with spheres and reagent kit from Polysciences Corporation.

The spheres with one type of antibody were first incubated with a suspension of the appropriate bacteria to see if the microorganism would bind to the spheres. While some bacteria were observed attached to the spheres and single bacteria were easily observed in fluorescence, the microorganisms could be easily detached from the spheres by stirring.

The specificity of the attraction was tested by mixing 6.5- $\mu$ m spheres coated with anti-Staph. aureus and 10- $\mu$ m spheres with anti-E. coli with a suspension of rhodamine-dyed E. coli and Texas Red-dyed Staph. aureus. The results of observations of a large number of spheres show that the binding is indeed selective and therefore mostly due to the antibody-antigen reaction. There is a small amount of nonspecific binding, presumably due to adsorption. Bound to the 10- $\mu$ m spheres, we found 85 E. coli and 9 Staph. aureus. 13 E. coli were bound to the incorrect 6.5- $\mu$ m spheres and 226 Staph. aureus were correctly attached.

This work was supported by the U.S. Army Edgewood Research and Development Engineering Center and by the U.S. Department of Energy, Office of Basic Energy Sciences. Oak Ridge National Laboratory is managed by Martin Marietta Energy Systems, Inc., for the U.S. Department of Energy under Contract DE-AC05-84OR21400.





Thursday, March 10, 1994

## Single Molecule Detection

**ThD** 9:00pm–10:20pm  
Grand Room

Robert P. Lucht, *Presider*  
*University of Illinois at Urbana–Champaign*

## Single-Molecule Detection in Microdroplets

Michael D. Barnes, William B. Whitten, and J. Michael Ramsey,

Chemical and Analytical Sciences Division,  
Mail Stop 6142, Oak Ridge National Laboratory,  
Oak Ridge, Tennessee 37831-6142; mdb@jmrsun2.acd.ornl.gov

### Introduction

Detection of single molecules in condensed phase with high signal-to-noise ratios is important for applications which involve detection of fluorescent tags such as DNA sequencing,<sup>1</sup> fluorescence immunoassay,<sup>2</sup> or hydrology.<sup>3</sup> In addition, observation of photophysical phenomena unique to the interaction of a radiation field with an *isolated* molecule, such as photon antibunching,<sup>4</sup> depends upon having such high sensitivity. As demonstrated by the experiments of Moerner<sup>5</sup> and Orrit,<sup>6</sup> very high sensitivity at the single molecule level can be achieved by probing "guest" molecules in solid hosts at cryogenic temperatures. However, practical applications requiring single molecule detection usually require measurements on liquid phase solutions at room temperature. These demands pose new problems such as solvent dependent quantum yield, finite photochemical lifetime (the number of absorption-emission cycles which occur before irreversible bleaching of fluorescence), and solvent Raman scattering and fluorescence.

Our experimental approach to detecting single dye molecules in solution is based on using levitated microdroplets as the sample medium and employing cw laser excitation and photon-counting detection.<sup>7</sup> Several advantages accrue from this approach. First, the probe volume is defined by the droplet diameter which has been made as small as 35 femtoliters in our experiments. Second, the analyte molecule is confined to the probe volume with no diffusive losses so that every molecule present in a droplet can be interrogated. Third, the laser-analyte interaction time can be extended arbitrarily so that all molecules remain in the interaction region until photolyzed, thus allowing the maximum number of fluorescence photons to be extracted. In addition, we have recently observed a factor of  $\approx 10$  increase in the spontaneous emission rate of R6G due to cavity-QED effects in 4  $\mu\text{m}$  diameter glycerol droplets.<sup>8</sup> These effects can greatly increase the signal-to-noise ratio for single molecule detection both through an increase in the saturated absorption rate and through enhancement of the fluorescence yield per molecule.<sup>9</sup>

Here we show data representing fluorescence detection of single R6G molecules in

micron-sized levitated glycerol droplets with signal-to-noise ratios ranging between 10 - 45. Signals from individual R6G molecules were identified on the basis of both the magnitude of the signal and by the unique time dependence expected for single molecules. In addition, the distribution of measured photocounts for droplets believed to contain single R6G molecules agrees well with the distribution expected for single (1-chromophore) molecules.

## Experimental

The apparatus used to measure fluorescence from levitated droplets is described in Ref. 7. Briefly, droplets are levitated in a three-electrode structure similar to that used in ion trap mass spectrometers. Fluorescence from the droplet was collected from the droplet with an  $f/1$  collection optic mounted in the ring electrode at an angle of  $90^\circ$  with respect to the cw  $\text{Ar}^+$  excitation laser. The laser was polarized in the horizontal direction, and an intensity at the droplet of about  $500 \text{ W/cm}^2$  was used. Light collected from the droplet is spectrally filtered using an interference filter centered at 575 nm with 25 nm bandwidth (Omega Optical 575DF25) and focused onto a cooled photomultiplier (Hamamatsu R943-02) operated in photon-counting mode (1-second integration time). Glycerol droplets containing R6G were produced with a piezoelectric pipet.<sup>10</sup> The droplet diameter was determined by measuring the distance between reflected and refracted glare-spots<sup>11</sup> from He-Ne laser illumination using an eyepiece reticle with rulings that correspond to  $1 \mu\text{m}$ . Uncertainty in the diameter measurement was estimated to be about 10%.

## Results

The exponential photocount distribution for single-chromophore molecules such as R6G implies that the magnitude of a measured signal is not, of *itself*, a good indication of whether *only* a single molecule is present in the probe volume or not. That is, the distribution of measured signals for single R6G molecules, in the case where all the analyte molecules undergo photobleaching, will not be clustered around some central average value as is the case for, say,  $\beta$ -phycoerythrin. Another discriminant which can be employed to determine whether more than one molecule is present, however, is the unique time dependence of the fluorescence signal expected for a single (1-chromophore) molecule. If the excitation rate (and, fluorescence signal) is approximately constant, the molecule will emit photons at a constant rate until photolysis occurs, at which time the signal will stop abruptly. In an ideal case, this will give rise to a "step-function" time dependence of the fluorescence signal for a single molecule. If more than one molecule is present in the

droplet, the molecules will generally photolyze at different times. Thus, the fluorescence signal for 2 or 3 molecules should ideally display a series of steps in time, where the count rate drops abruptly due to the bleaching of a molecule.

Figure 1 shows fluorescence data after mean background subtraction for 2 droplets which are calculated (based on the concentration and droplet diameter) to contain (a) 0.8, and (b) 0.2 molecules respectively. The number of fluorescence counts above background for traces (a) and (b) are 1670, and 60 respectively. The time-dependence and the magnitude of the fluorescence signal shown in trace (a) is characteristic of the presence of only one molecule in the droplet, while no significant signal above background is observed in trace (b). Taking the signal-to-noise ratio to be  $S/B^{1/2}$ , where  $S$  and  $B$  are the total signal and background counts acquired during the photochemical lifetime, the signal-to-noise ratio for (a) is 43.

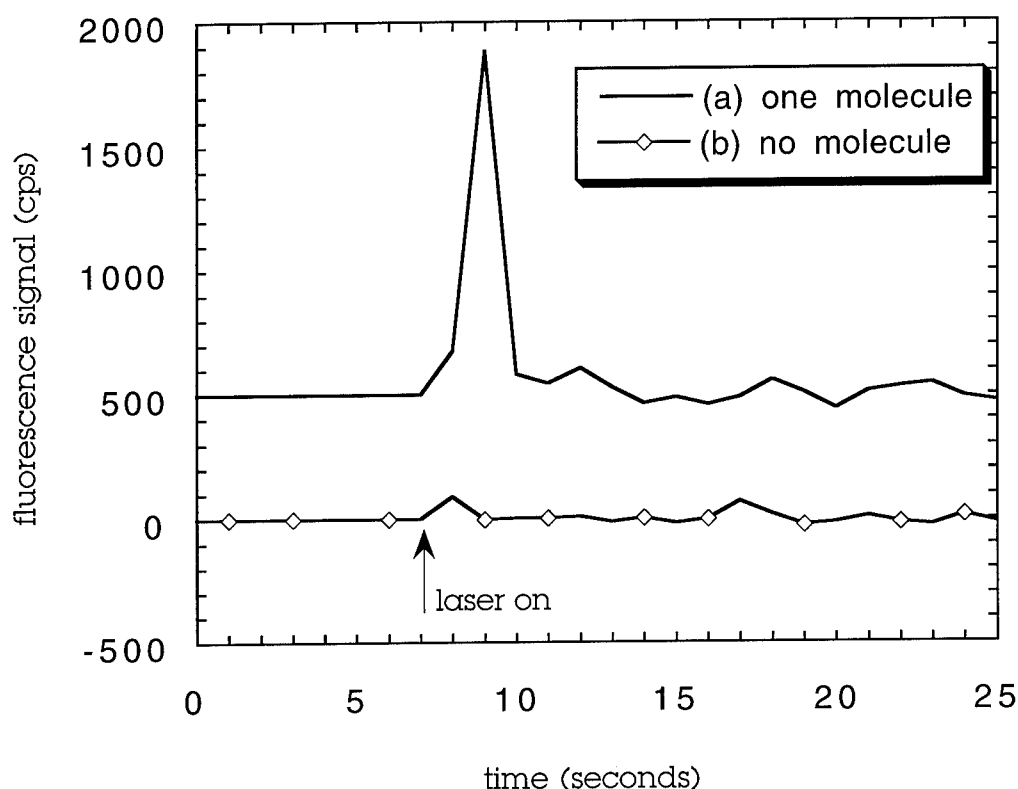


Figure 1. Fluorescence count rate vs. time for droplets containing (a) 1 molecule, and (b) 2 molecules. The number of molecules in droplets (a) and (b) were determined from the size and concentration to be 0.8 and 0.2 respectively.

We have demonstrated detection of single R6G molecules in levitated microdroplets with signal-to-noise ratios ranging between 10 and 50 using cw laser excitation and photon-counting detection. The presence of single molecules has been identified from both the magnitude of the fluorescence signal which agrees well with the average number of photocounts per molecule measured in separate experiments at nanomolar concentrations, and by the unique time-dependence of the fluorescence signal which is significantly different from droplets containing several molecules. In addition, photocount statistics obtained for droplets believed to contain single R6G molecules (from a maximum likelihood analysis) agree well with those expected for single (1-chromophore) molecules. It has previously been shown that, by employing a digital detection approach, much lower concentration detection limits may be obtained than those achievable using conventional detection techniques. The ability to detect single molecules with high signal-to-noise ratios in microdroplets should provide a new approach towards analyzing ultra-dilute solutions.

### References

- (1) Swerdlow, H.; Chen, D. Y.; Harke, H. R.; Grey, R.; Wu, S. L.; Dovichi, N. J.; and Fuller, C. *Anal. Chem.* **1991**, *63*, 2835.
- (2) Saunders, C. G.; Jett, J. H.; and Martin, J. C. *Clin. Chem.* **1985**, *31*, 2020.
- (3) Suijlen, J.; and van Leussen, W. *Coastal and Estuarine Studies*, vol. 3; Michaelis, W. ed.; Springer-Verlag: New York 1990.
- (4) Basché, Th.; Moerner, W. E.; Orrit, M.; and Talon, H. *Phys. Rev. Lett.* **1992**, *69*, 1516.
- (5) Moerner, W. E.; and Kador, L. *Phys. Rev. Lett.* **1989**, *62*, 2535.
- (6) Orrit, M.; and Bernard, J. *Phys. Rev. Lett.* **1990**, *65*, 2716.
- (7) M. D. Barnes, K. C. Ng, W. B. Whitten, and J. M. Ramsey, *Anal. Chem.* **65**, 2360 (1993).
- (8) Barnes, M. D.; Whitten, W. B.; Arnold, S.; and Ramsey, J. M. *J. Chem. Phys.* **1992**, *97*, 7842.
- (9) Barnes, M. D.; Whitten, W. B.; and Ramsey, J. M. *J. Opt. Soc. Am. B* submitted.
- (10) Arnold, S.; Folan, L. M. *Rev. Sci. Instrum.* **1986**, *57*, 2250.
- (11) Ashkin, A.; and Dziedzic, J. M. *Appl. Opt.* **1981**, *20*, 1803.

## Monte Carlo Model of a Single Molecule Counting Experiment

Lloyd M. Davis, Li-Qiang Li,

*University of Tennessee Space Institute, Tullahoma, TN 37388*

### 1. Introduction

In experiments for fluorescence detection of single molecules in solution the background due to unrejected scattered light increases linearly with laser power while the dye molecule fluorescence signal and photodegradation probability saturate. For slow flow rates, a molecule will usually photodegrade before it leaves the sample volume, while the background signal will continue to be accumulated for the integration time, usually taken as the full transit time. These considerations have previously been used to select operating conditions for ultrasensitive detection experiments by maximizing the mean signal-to-noise,  $S/N = n_f/\sqrt{n_b}$ , where  $n_f$  is the mean number of fluorescence counts and  $\sqrt{n_b}$  is the fluctuation in the background count.<sup>1</sup> However, such optimization is not valid for single molecule detection, since it assumes that the fluorescence photon statistics are Poissonian. Maximum  $S/N$  is achieved for laser intensities below saturation and for transit times longer than the photodegradation time, since this gives on average more photons per molecule by extracting considerably more photons from those easy-to-detect "bright" molecules that by chance do not photodegrade.

We have previously solved the equations for excitation and photodegradation as a molecule transits a Gaussian laser profile and have shown that the probability density function of the number of photons expected from a single molecule actually consists of a decaying exponential which terminates at a Poisson-like peak attributable to those molecules that exit the sample volume before photodegradation.<sup>2</sup> An individual molecule will be detected whether the number of photons is well above, or only a little above a preset threshold, which is determined from the probability density function of the background. If we use *the probability of detecting the molecule minus the probability of detecting a background fluctuation* as the optimization criterion, we find that for our experimental parameters best operation is obtained at faster flow velocities and at laser excitation above saturation, despite a smaller mean burst amplitude at these conditions.

### 2. Experiment

Encouraged by the prospect of efficiently detecting single molecules at faster flow rates, we are developing an experiment that uses fast flow velocities to overcome diffusional loss in order to efficiently count individual dye molecules from a sub-microliter sample of ultradilute aqueous solution. We have so far demonstrated high efficiency using Phycoerytherin molecules<sup>3</sup> and are presently completing our measurements using single chromophore molecules. In our experiment, the sample is conveniently loaded into a commercially available capillary which is inserted into our flow cell. As the solution emerges from the sub-micron capillary orifice (see Fig. 1), individual dye molecules pass into the flow stream and are carried downstream through an elliptically focused laser beam. Fluorescence is collected at right angles to the laser beam and to the flow stream. The molecules are then detected using photon burst detection, with the use of time-gated photon detection for discrimination of Raman scattered light originating from the solvent.<sup>4</sup>

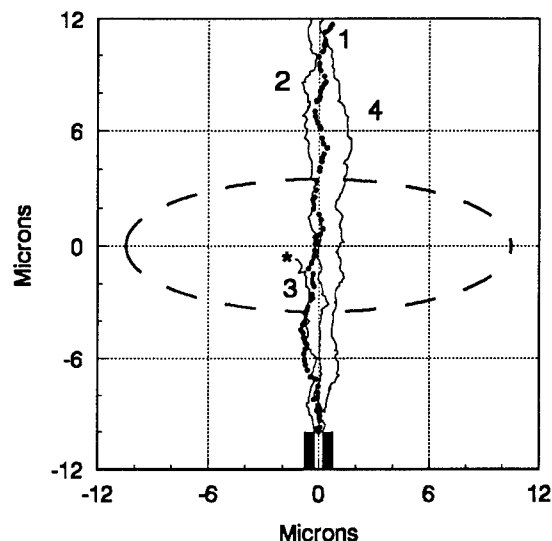


Fig. 1 Geometry of single molecule counting experiment showing simulated molecule trajectories.

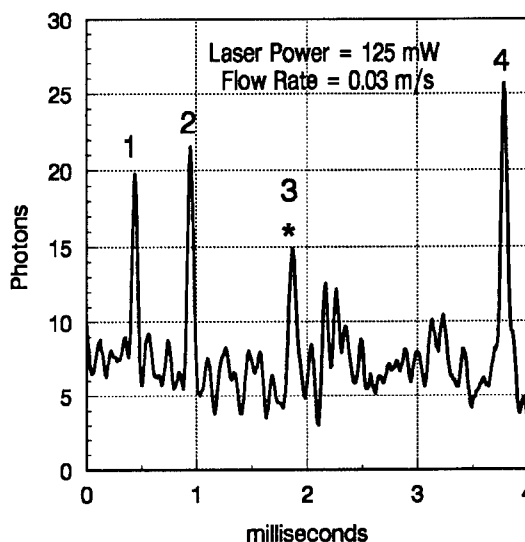


Fig. 2 Weighted sliding sum of photocounts showing bursts due to simulated single molecules of Fig. 1.

The molecules inevitably undergo diffusion in the flow stream. In order to cause all molecules to pass through the laser beam before diffusional spreading becomes significant, the laser waist must be positioned as closely as possible to the capillary tip. The size of the laser beam waist in the direction of the flow stream determines how closely to the capillary the laser waist may be positioned before scattered light from the capillary tip becomes significant. The depth-of-focus for light collection of the high numerical aperture microscope objective that is used to collect light from the sample volume ( $\sim \pm 6\mu\text{m}$ ) determines the maximum useful waist size in the transverse direction. With these restrictions, because of diffusion, all molecules will pass through the sample volume only if the velocity of the flow stream is sufficiently fast. However, if the flow velocity is too fast, the residence time of the molecule within the sample volume will be too short to collect a sufficient number of fluorescence photons for detection of the molecule.

In our experiment, we have taken steps to increase the rate of fluorescence photon detection by increasing the optical collection efficiency and the detector quantum efficiency<sup>5</sup> and by reducing the effects of the dead-time of the electronics in order to avoid signal loss due to pile-up.<sup>3</sup> While these parameters are determined by experimental constraints, we are free to select the laser power and flow velocity to optimize the detection efficiency.

### 3. Monte Carlo Simulation

Since diffusion significantly complicates the calculation of the photon statistics, we have developed a 3-D Monte Carlo model of single molecule detection in solution, which treats the geometry of our experiment as a particular case. The model includes factors important for our experiment which were not included in the previously reported simulation.<sup>4</sup> In particular, the model includes both detector and electronic dead times ( $0.8\mu\text{s}$  and  $5\mu\text{s}$ ), the 3-D laser intensity profile, depth-of-focus of optics, attention to calculation of detailed photon statistics and a more precise treatment of diffusion.

Fig. 1 shows a 2-D projection of the trajectories of several molecules that emerge from the capillary, as generated by the Monte Carlo simulation using molecular parameters for rhodamine 6G.<sup>6</sup> Other parameters used by the simulation have been set at values appropriate for our experiment, and the concentration is such that 99% of the molecules are alone as they pass through the sample volume. Fig. 1 includes the trajectory of a molecule that photodegrades while passing through the laser waist, shown by the ellipse.

The Monte Carlo code simulates our actual experiment by returning a stream of numbers, each of which is the delay in microseconds since the previously detected photon. Thus the simulation is useful as a platform upon which to test the algorithms which are incorporated into our PC-based data acquisition and real-time analysis system. Furthermore, the simulation provides a graphical display of the results of the analysis and it allows experimental parameters to be interactively modified while giving a real time visualization of the effects of the changes. This is useful for exploring the parameter space to come to an appreciation of the limits imposed by pile-up, diffusional-loss, intensity saturation, photodegradation and simultaneous transit of two or more molecules.

We have investigated the use of various filters to process the stream of photon delay times, including linear and non-linear weighted sliding sums with both fixed and dynamically-varying widths. For brevity, here we only discuss the use of a linear weighted sliding sum filter with weights determined from the mean Gaussian profile experienced by a molecule which transits the laser without diffusion or photodegradation. In the Monte Carlo simulation, this Gaussian profile is known *a priori* from the size of the laser and the selected flow rate. In an actual experiment, we use a Gaussian with width equal to the mean residence time of molecules in the sample volume, as obtained from the time-averaged autocorrelation function, which is accumulated directly from the stream of microsecond photon delays.

Fig. 2 shows the results of the weighted sliding sum analysis of the photons generated during the passage of the simulated molecules shown in Fig. 1. Note that in this case, the molecule which has photodegraded has generated a burst which is just below the threshold (15).

#### 4. Detection and Optimization Criteria

In order to count single molecules, specific criteria must be established for detecting photon bursts and discriminating them from noise. Individual bursts will contain fluctuations due to shot noise so that if a simple threshold scheme is employed, a single molecule may be counted more than once due to noise at the leading or trailing edges of the burst. Such multiple counting may be avoided by ignoring fluctuations in the weighted sum below a preset value, hereafter taken to be 1.0 photons.

The Monte Carlo simulation gives prior knowledge of whether a burst is due to the transit of a molecule or to noise, enabling us to collect histograms of the amplitudes of the bursts in each case. The two histograms are shown in Fig. 3 for the operating conditions of Figs. 1 and 2 after 1000 molecules have passed. The optimum threshold for single molecule counting is chosen to be at the valley in the sum of the two histograms. Then the difference between the areas of the histograms above this threshold, normalized by the number of molecules that have passed, defines the *detectability*, i.e., the fraction of molecules correctly counted minus the fraction of false counts.



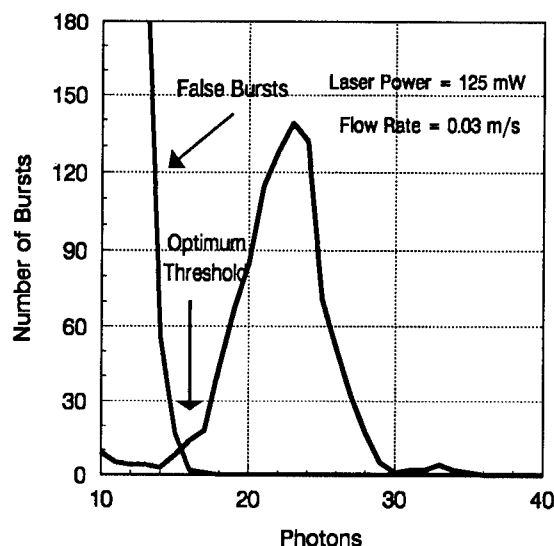


Fig. 3 Histograms of burst amplitudes from 1000 simulated molecules.

Power (mW)	Flow rate $\times 10^{-3}$ ( $\text{ms}^{-1}$ )						
	5	10	15	20	25	30	35
25	.915	.911	.878	.843	.765	.715	.644
	18	10	8	6	5	5	4
50	.915	.924	.913	.910	.897	.878	.854
	34	18	14	11	9	8	7
75	.840	.898	.913	.921	.926	.919	.902
	48	26	19	14	12	10	9
100	.776	.863	.903	.922	.928	.923	.916
	58	30	22	18	15	13	11
125	.769	.886	.896	.912	.913	.927	.899
	63	38	26	21	18	15	13
150	.647	.876	.883	.911	.901	.915	.904
	79	43	29	26	19	17	15

Table 1 Molecule detectability vs. laser power and flow rate.

Table 1 gives the detectability and the optimum threshold for a range of laser powers and flow velocities. Maximum detectability of  $\sim 0.92$  is obtained at a laser power of 125 mW and a flow rate of  $3.0 \times 10^{-2} \text{ms}^{-1}$ , whereas the power for which excitation of a molecule at the origin saturates is 75 mW and the flow rate for which the transit time equals the photodegradation time<sup>1</sup> is  $9.5 \times 10^{-2} \text{ms}^{-1}$ . However, the optimum conditions depend significantly on experimental parameters. If simulations are performed with the assumption of no dead time, optimum detectability of  $\sim 0.97$  occurs at a higher flow rate and larger laser power, whereas if the total collection efficiency is assumed to be smaller than the estimated experimental value of  $7 \times 10^{-3}$ , optimum detectability occurs at lower flow rates and smaller laser powers.

## References

1. R.A. Mathies, K. Peck and L. Stryer, *Anal. Chem.* **62**, 1786–1791 (1990).
2. L.M. Davis, L.Q. Li, E.B. Shera, A. Castro and S.A. Soper, *Opt. Soc. Am. Tech. Dig.* **13**, 70–72 (1992).
3. L.Q. Li and L.M. Davis, *Opt. Soc. Am. Tech. Dig.* **16**, 1 (1993).
4. E.B. Shera, N.K. Seitzinger, L.M. Davis, R.A. Keller and S.A. Soper, *Chem. Phys. Lett.* **174**, 553–557 (1990).
5. L.Q. Li and L.M. Davis, *Rev. Sci. Instrum.* **64**, 1524–1529 (1993).
6. S.A. Soper, E.B. Shera, L.M. Davis, H.L. Nutter and R.A. Keller, *Photochem. and Photobiol.* **57**, 972–977 (1993).

## Electrophoresis of Single Fluorescent Molecules

Alonso Castro and Brooks Shera  
Physics Division, Mail Stop D434  
Los Alamos National Laboratory  
Los Alamos, NM 87545  
Telephone: (505) 667-7264

The fast, efficient detection and separation of minute quantities of biologically important molecules plays a central role in a variety of fields, such as molecular biology, biotechnology, immunology, medical diagnostics, and forensic analysis. It has proven difficult to identify and separate biomolecules at such low concentrations by existing means. Thus, it is of importance to develop methods that are able to probe such low concentrations with adequate sensitivity, resolution and ease. Here, we describe a new method for detecting and identifying individual fluorescent molecules in solution. The technique involves the measurement of electrophoretic velocities of individual molecules in a mixture, and identification by comparison with the electrophoretic velocity known to be characteristic of a particular molecular species. The application of the method to the detection and size identification of DNA restriction fragments in solution at the single molecule level has been demonstrated. In a similar experiment, the electrophoretic velocities of single molecules of the protein phycoerythrin was determined. Although we have focused on the detection and identification of biologically important molecules, the technique has the potential to find applications in organic and inorganic chemical analysis.

In our experiments, the sample consisted of a solution of the molecules under study at a concentration of  $\sim 10^{-14}$  M. The 532 nm output of a mode-locked Nd:YAG laser is split in two beams. These two laser beams were focused into a 100- $\mu$ m square cross section cell to yield 5  $\mu$ m spots, separated by 200  $\mu$ m from each other (Fig. 1).

An external electric field ( $\sim 100$  V/cm) is applied between the ends of the capillary cell, which causes the molecules to migrate towards the cathode or anode, depending on their charge. The individual molecules are detected as they pass through each of the two laser beams. The electrophoretic velocity is then calculated from the time required for each molecule to travel the distance between the two beams.

Single molecules were detected by a modified version of our single-molecule detection apparatus (1). Briefly, as a molecule passes across the laser beam, a fluorescence photon burst is produced, which is collected by

a microscope objective, and detected by a single-photon avalanche photodiode. Each laser beam has a separate time-correlated single-photon detection channel. The detectors reject Raman and Rayleigh scattering by the use of a time-gate window set such that only delayed fluorescence photons were detected. Such parameters as extinction coefficient, photodegradation, quantum yield, and detection efficiency, determine the number of observed fluorescence photons per molecule.

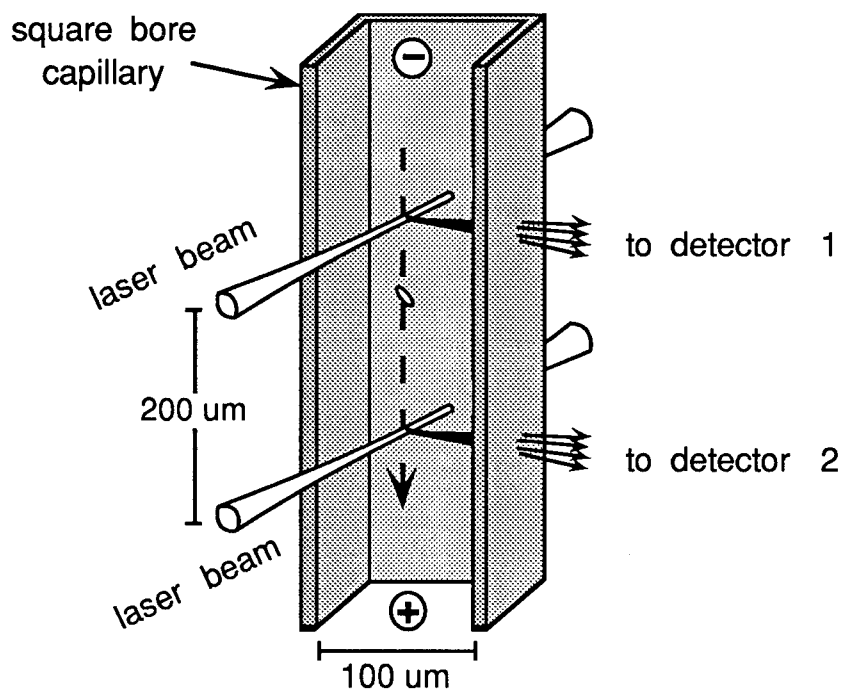


Fig. 1

Since the fluorescence quantum yield of DNA is very small, we intercalated the fluorescent dye TOTO-1 (a dimer of thiazole orange) (2) into DNA. Figure 2. shows the fluorescence bursts observed from the two detection channels for a 10 femtomolar solution of lambda DNA (48,000 base pairs) in TBE buffer to which TOTO-1 was added at a base pair to dye ratio of 5:1.

Every burst on the first detector appears shifted on the second detector by the time taken by a individual molecule to travel the distance between the two laser beams.

To investigate the identification of DNA fragments according to size, we used a mixture of DNA fragments of three different sizes: 38, 24 and 10 Kbp. Since DNA fragments of different sizes experience essentially the same drag-force per unit charge in free solution, no separation would

be possible. We therefore added hydroxy-propyl-methyl-cellulose at a concentration of 0.25% as sieving media (3,4). The time required for each molecule in the mixture to travel the distance between laser beams was recorded. As expected, larger fragments are retarded by the sieving media, whereas smaller fragments travel faster. Figure 3 shows a histogram of these times for the DNA fragment mixture. Three peaks are observed, corresponding to each of the DNA fragment sizes. Experiments are under way to extend the range of fragment sizes, as well as to increase the size resolution. Preliminary experiments have also shown the applicability of the technique to the separation of proteins, and its application to the identification of other molecular species of biological importance is being explored.

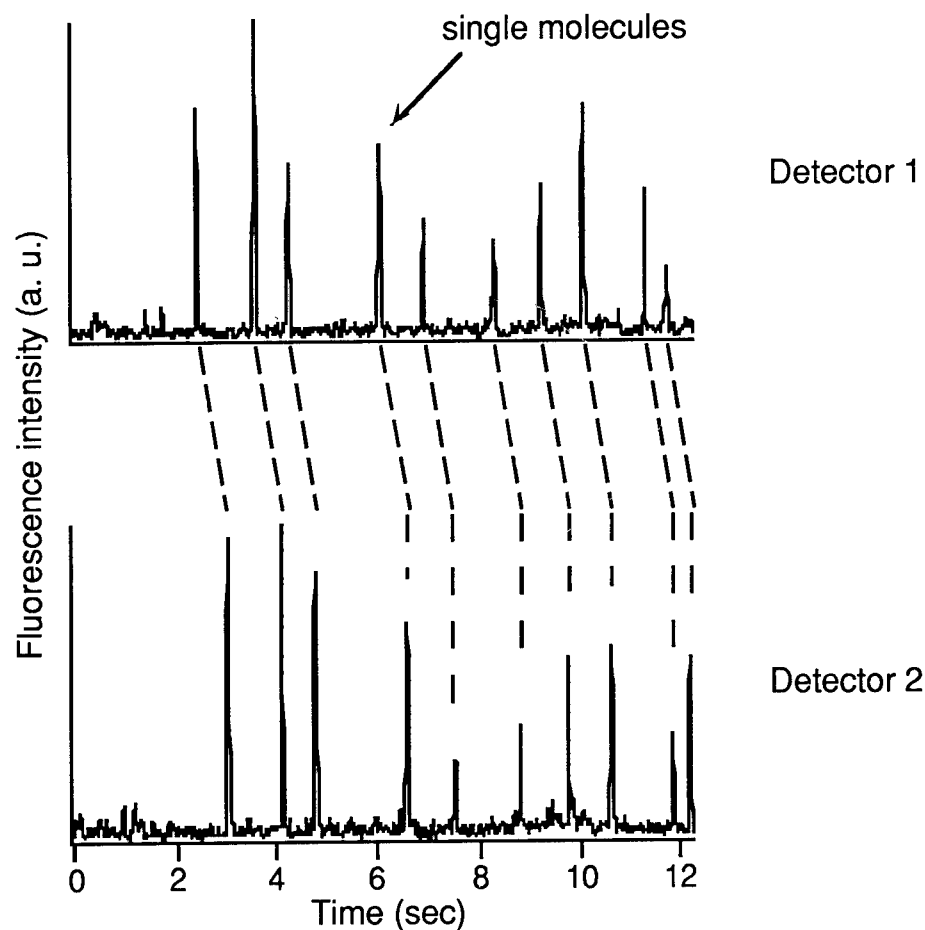


Fig. 2

Thus, a novel method for the measurement of electrophoretic velocities of single molecules has been developed. The use of the method to the detection and size identification of DNA restriction fragments in solution at the single molecule level has been demonstrated.

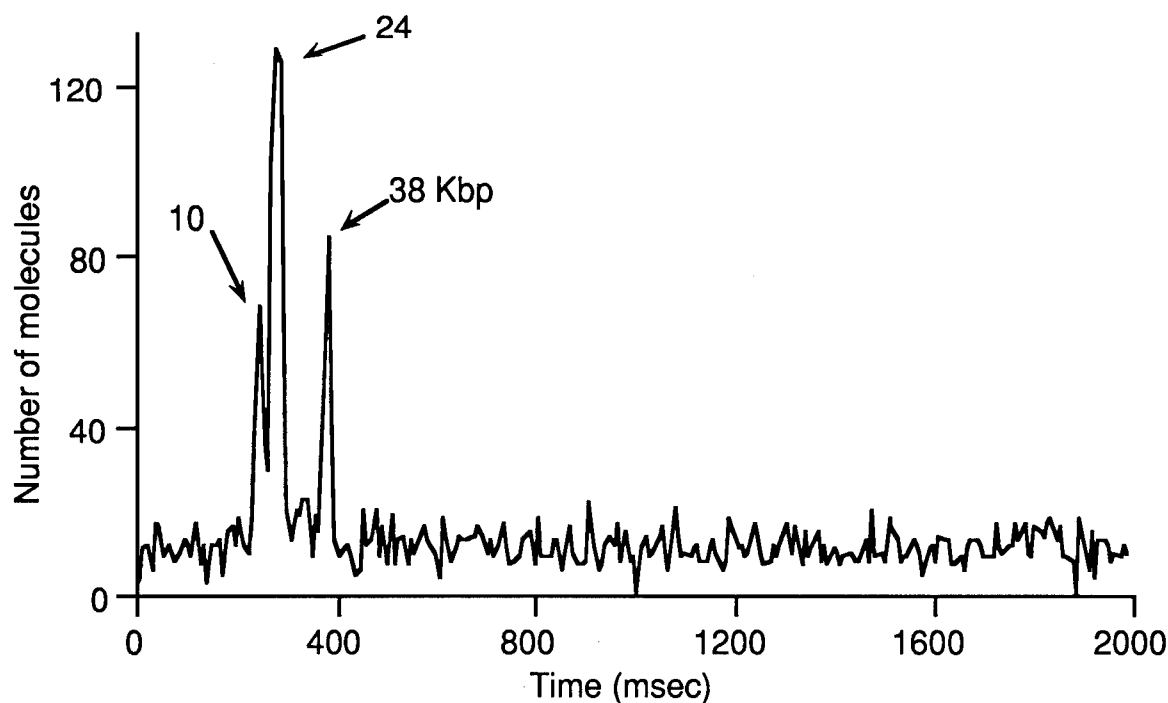


Fig. 3

The technique commonly used for restriction fragment sizing is gel-slab electrophoresis. However, this technique is time consuming, labor intensive, non-quantitative, and does not readily allow automation, whereas this new method promises to combine the advantages of free-resolution capillary electrophoresis (system automation, speed, reproducibility) with the unsurpassed sensitivity of single-molecule detection. An additional advantage over conventional electrophoresis is that the identification process is continuous, rather than batch oriented, and the process is therefore suitable for applications that require rapid, continuous on-line analysis. Furthermore, the extreme sensitivity of the method may open the way to develop fluorescence immunoassay and DNA fingerprinting techniques without the need for extensive DNA amplification using PCR or other methods.

#### References:

1. E. B. Shera, N. K. Seitzinger, L. M. Davis, R. A. Keller, and S. A. Soper, *Chem. Phys. Lett.* **174**, 553 (1990).
2. Molecular Probes, Inc., Eugene, Oregon.
3. M. Zhu, D. L. Hansen, S. Burd, and F. Gannon, *J. Chromatogr.* **480**, 311 (1989).
4. B. Yoshinobu, C. Sumita, K. Hide, N. Ishimaru, K. Samata, A. Tanaka, and M. Tsuchiko, *J. Liq. Chromatogr.* **16**, 955 (1993).

## Fluorescence Spectroscopy on a Single Molecule Basis with a Near-field Spectrometer

X. Sunney Xie, Robert C. Dunn

Pacific Northwest Laboratory<sup>‡</sup>  
Molecular Science Research Center  
P.O. Box 999, Mail Code K2-14  
Richland, WA 99352  
Tel: 509-375-6372

Recent advances in near-field optical microscopy [1] have offered exciting possibilities for conducting molecular spectroscopy at the nanometer dimension. In particular, fluorescence detection of single chromophores and single proteins containing several chromophores have been achieved using this technique[2][3]. For chemical analysis and biological applications, fluorescence measurements with near-field optics will be particularly informative, providing spectroscopic information not accessible with other scanning probe techniques, such as SEM, STM and AFM.

To conduct spectroscopic measurements on a single molecule basis, we have taken special care in designing a near-field microscope with an extremely high fluorescence detection sensitivity. Illumination is provided by an aluminum coated fiber tip probe positioned near the surface using a feedback mechanism to regulate the sample-tip distance based on shear force, similar to that of reference [1]. The optical train is designed such that the emission is collected with high efficiency while the residual excitation light is completely rejected. A photon counting scheme that combines a sensitive avalanche photodiode detector and multichannel counting electronics has been implemented. This scheme results in the fluorescence detection sensitivity required for single molecule spectroscopy.

We report the near-field fluorescence imaging of single photosynthetic proteins allophycocyanin (APC) dispersed on a glass substrate. As shown in Figure 1, single APC trimers have six chromophores covalently bound to the protein. These chromophores give rise to strong absorption and emission bands in the visible peaked at approximately 650 nm and 670 nm, respectively. APC has long been known for the intensity of its fluorescence and its inherent photostability occasioning its use as a test of single molecule sensitivity. Figure 2 shows a  $1\mu\text{m} \times 1\mu\text{m}$  the near-field fluorescence image taken with the near-field microscope. This result demonstrates the ability of the near-field technique to detect and localize single proteins on the nanometer scale. Furthermore, the emission signal sizes that we have measured for single APCs are such that spectroscopic measurements which spread the emission in both the frequency and

time domains are possible allowing one to make spectroscopic and dynamic measurements on single proteins.

One particular advantage of near-field optical microscopy over other scanning probe microscopies is the high time resolution afforded by optical measurements. This will allow the study of fast dynamical processes inaccessible with other techniques. The natural first step is to characterize the temporal behavior of the short light pulses emerging from the aluminum coated fiber tip. The conventional autocorrelation technique using second harmonic generation in nonlinear crystals is difficult for the low photon flux ( $10^{10}$  photon/sec) exiting near-field tips. We have therefore employed a method based on photon correlation techniques[4]. This technique, which does not rely on nonlinear crystals, has several advantages, such as a photon counting sensitivity for weak beams and an unlimited time resolution. Figure 3 shows the photon correlation trace of a picosecond pulse train (76MHz repetition rate, 10ps FWHM autocorrelation) emerging from a) an uncoated and b) an aluminum coated near-field probe. The FWHM of the photon correlation traces are 10ps which is identical to that of the input pulses, indicating that the intensity profile of the picosecond pulses remains unchanged [5].

In conducting fluorescence lifetime measurements with near-field optics, a high repetition rate, low energy picosecond laser system and time-correlated single photon counting electronics are incorporated into our near-field microscope. This enables us to measure fluorescence lifetimes with high temporal resolution (30ps). Dynamical processes such as electron transfer and energy transfer can thus be studied at specific local environments. Moreover, time-resolved capability will enable "fluorescence lifetime imaging" which measures an intrinsic property of the molecular species and is free from complications encountered in near-field intensity imaging.

Progress in collecting emission spectra, conducting polarization spectroscopy and fluorescence life time measurements on single molecules with near-field optics will be reported.

#### References

- [1]. E. Betzig and J. K. Troutman, *Science*, **257** (1992) 189.
- [2]. E. Betzig and R. J. Chichester, *Science*, in press.
- [3]. Robert C. Dunn, Errol V. Allen, Stephen A. Joyce, Gordon A. Anderson, X. Sunney Xie, *J. Ultramicroscopy*, in press
- [4] Y. Miyamoto, T. Kuga, M. Baba, M. Matsuoka, *Optics Lett.*, **18**, (1993) 900.
- [5] Robert C. Dunn and X. Sunney Xie, *J. Ultramicroscopy*, in press

‡ Pacific Northwest Laboratory is operated for the U. S. Department of Energy by Battelle Memorial Institute under Contract No. DE-AC06-76RLO 1830.

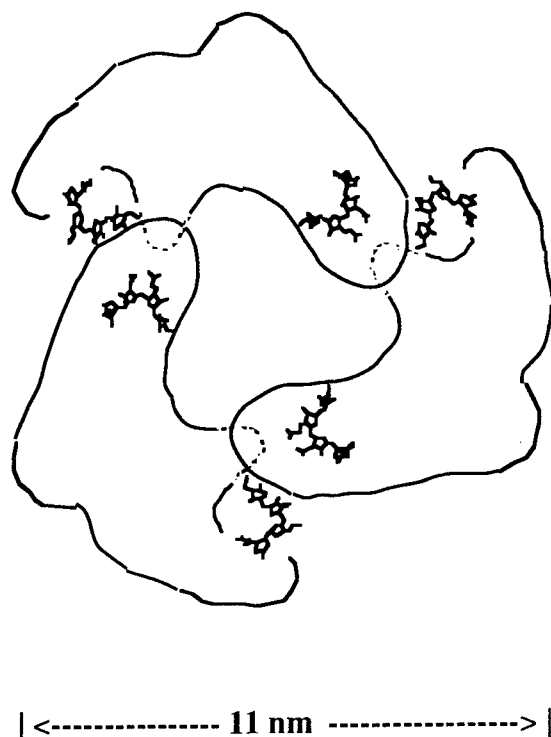


Figure 1. The structure of APC which contains six tetra-pyrrole chromophores and has a disc like structure with 11nm diameter and 3nm thickness..

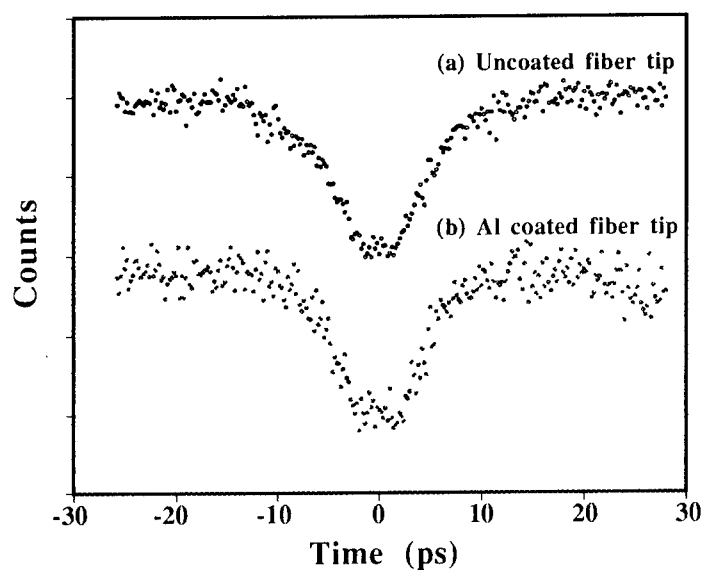


Figure 3. a) Autocorrelation of the pulses emerging from an uncoated fiber tip (1 meter long) and b) an aluminum coated fiber tip using the photon correlation technique. The FWHM of both traces are 10ps, identical to that of the input laser pulses measured with a conventional autocorrelation technique.



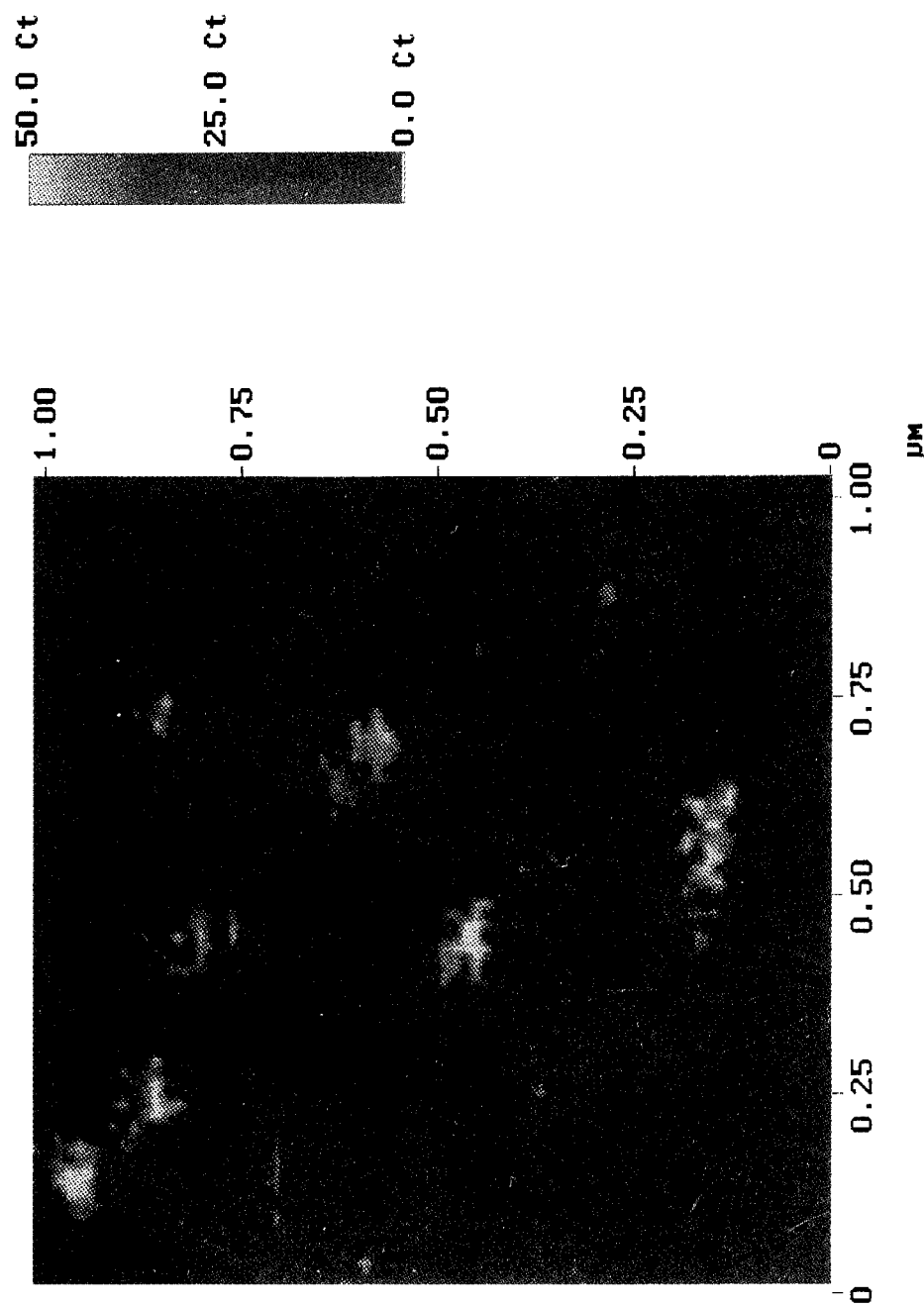


Figure 2. Near-field fluorescence image of single APC trimers dispersed on a glass cover slip. The FWHM of the individual bright spots are 100 nm, due to fluorescence from single APC proteins. The spatial resolution is limited by the diameter of the tip used. The extrapolated signal for positioning the tip above a peak is 5000-10000 counts/sec which is enough to carry out spectroscopic measurements on a single protein basis.



Friday, March 11, 1994

## Gas Phase Spectroscopy

**FA** 8:15am–10:15am  
Grand Room

Andrzej W. Miziolek, *Presider*  
*U.S. Army Ballistic Research Laboratory*

## **Diagnostics for Emission Monitoring for Hazardous Waste Incineration**

Terrill A. Cool

School of Applied and Engineering Physics, Cornell University, Ithaca, NY 14853

The unique attributes of resonance-enhanced multiphoton ionization/time-of-flight mass spectrometry (REMPI/TOFMS) for rapid, ultrasensitive, and selective detection of toxic organics make it a promising new tool for quantitative evaluation of incinerator performance. The spectral selectivity of resonance ionization mass spectrometry, realizable with jet-cooling, eliminates the need for the time-consuming capillary column sample separation of conventional GC/MS analysis. Recent research indicates that real-time repetitive monitoring of a wide class of trace emissions at the part-per-billion level (ppb) is possible with the REMPI/TOFMS method.[1,2] Indeed, REMPI detection capabilities for specific compounds are expected to significantly influence strategies for the use of surrogates for stack gas monitoring.

Numerous surrogate species, chosen to be resistant to destruction under several potential incinerator failure modes, have been suggested. Post flame thermal degradation, under oxygen-starved conditions, of species that penetrate the primary flame zone is thought to be critical to the achievement of high efficiencies for the destruction of many toxic species.[3-9] Monitoring and control of this failure mode, often associated with poor mixing, is a primary consideration in the selection of surrogates.[5,6,9-11]

Perhaps of even greater importance may be the use of surrogates for monitoring the existence of toxic combustion byproducts; polycyclic aromatic compounds are of particular concern because of their carcinogenic properties. Indeed, the most dangerous of these compounds, the polychlorinated dibenzodioxins and dibenzofurans (PCDDs and PCDFs), would have to be controlled at sub part-per-trillion levels to be in compliance

with new regulations proposed for the European Economic Community.[12] Direct continuous emission monitoring of species at such low detection limits is beyond the capabilities of any presently known technique, including the REMPI/TOFMS method. Nevertheless, repetitive on-line incinerator emissions monitoring, at the part-per-billion level, appears to be quite feasible with REMPI/TOFMS and is adequate for control of less hazardous polycyclic aromatics and many of the precursor compounds to the formation of the PCDDs and PCDFs. According to current kinetic models, the chlorinated benzenes, phenols, and biphenyls, at part-per-billion levels, are likely precursors to PCDDs and PCDFs at part-per-trillion concentrations.[4,13-16] Thus the use of the REMPI/TOFMS method for monitoring these precursors may enable reliable upper limits to be placed on the concentrations of PCDDs and PCDFs in real time.

We report here measurements of detection limits for cyanogen and six benzene derivatives: phenol, *p*-chlorophenol, *p*-chlorotoluene, 2,4-dichlorotoluene, *p*-cresol, and aniline. These data complement previous studies of the chloroethylenes, benzene, chlorobenzene, 1,2-dichlorobenzene, 1,4-dichlorobenzene, toluene, naphthalene, and 2-chloronaphthalene.[1,2] Eight of the twenty compounds thus far studied have sub part-per-billion detection limits. Selectivities exceeding  $10^3$  were measured for the detection of these eight molecules in the presence of a complex background of chemically similar interferants likely to be present in incinerator effluent. Constraints on the selection of surrogate compounds arising from the analytical capabilities of the REMPI/TOFMS technique are discussed.

### References

1. Cool, T. A. and Williams, B. A., Combust. Sci. Tech. 82, 67 (1992).
2. Williams, B. A., Tanada, T. N., and Cool, T. A., "Resonance Ionization Detection Limits for Hazardous Emissions", *Twenty-fourth Symposium (International) on Combustion* (The Combustion Institute, Pittsburgh, 1992) p. 1587.
3. Dellinger, B., Torres, J. L., Rubey, W. A., Hall, D. L., Graham, J. L., and Carnes, R. A., Hazard. Waste 1, 137 (1984).
4. Rubey, W. A., Dellinger, B., Hall, D. L., and Mazer, S. L., Chemosphere 14, 1483 (1985).
5. Dellinger, B., Rubey, W. A., Hall, D. L., and Graham, J. L., Hazard. Waste Hazard. Mater., 3, 139 (1986).
6. Dellinger, B., Graham, M. D. and Tirey, D. A., Hazard. Waste. Hazard. Matl., 3, 293 (1986).
7. Graham, J. L., Hall, D. L., and Dellinger, B., Environ. Sci. Technol. 20, 703 (1986).
8. Hall, D. L., Dellinger, B., Graham, J. L., and Rubey, W. A., Hazard. Waste Hazard. Mater. 3, 441 (1986).
9. Taylor, P. H. and Dellinger, B., Environ. Sci. Technol. 22, 438 (1988).
10. Seeker, Wm. R., *Twenty-Third Symposium (International) on Combustion* (The Combustion Institute, Pittsburgh, 1990), p. 867.
11. Taylor, P. H., Dellinger, B. and Lee, C. C., Environ. Sci. Technol. 24, 316 (1990).
12. Acharya, P., DeCicco, S. G., and Novak, R. G., J. Air Waste Manage. Assoc. 41, 1605 (1991).
13. Lustenhouwer, J. W. A, Olie, K., and Hutzinger, O, Chemosphere 9, 501 (1980)
14. Altwicker, E. R., Schonberg, J. S., Konduri, R. K. N. V., and Milligan, M. S., Hazard. Waste Hazard. Mater. 7, 73 (1990).
15. Ritter, E. R. and Bozzelli, J. W., Combust. Sci. Tech. 74, 117 (1990).
16. Frenklach, M., Combust. Sci. Technol. 74, 283 (1990).

## Tunable Diode Laser Study of Premixed Methane/Oxygen Flames Inhibited by Halogenated Compounds

Robert G. Daniel, Kevin L. McNesby, and Andrzej W. Miziolek  
Army Research Laboratory  
AMSRL-WT-PC  
Aberdeen Proving Ground, Maryland 21005-5066  
(410) 278-6157

### Introduction

We are presently conducting experiments in which we obtain both temperature and species concentration profiles of a low pressure, premixed methane/oxygen flame, to which small amounts (0.25 - 1.0 %) of a halogenated methane compound have been added. We are using the method of Two Line Thermometry [1], in which a pair of IR active transitions are recorded by tunable diode laser (TDL) absorption spectroscopy and analyzed to determine the temperature of the flame and the partial pressure of the absorbing species. This method offers a nonperturbing probe of flame characteristics and has the ability to operate over a broad range of elevated temperatures. TDL absorption spectroscopy can be used wherever a line-of-sight configuration is possible and background gas absorptions do not interfere.

Our study is part of a larger program to develop models of flame extinction using Halon alternative compounds. The results are used to aid in the development of computational models for inhibited flames. Once developed and tested, these models will be used to predict the relative flame extinction properties of Halon alternative compounds, as well as predict the possible formation of toxic compounds during their use. The inhibitor compounds utilized in this study are listed in Table I.

---

TABLE I: List of fire suppressant compounds studied

$\text{CF}_4$	$\text{CF}_3\text{Br}$
$\text{CF}_3\text{H}$	$\text{CF}_3\text{I}$
$\text{CF}_2\text{H}_2$	$\text{C}_2\text{F}_5\text{I}$
$\text{CF}_2\text{HCl}$	$\text{C}_3\text{F}_7\text{I}$

---

### Experimental

The experimental apparatus consists of a tunable diode laser (TDL) as an infrared (IR) radiation source, a low pressure flat flame burner, a heated reference cell, an etalon, three LN2 cooled detectors and signal processing electronics. The TDL frequency scan and data collection are controlled by a personal computer. The output of the TDL is passed through two beam splitters before passing through the burner

chamber. One of these split beams passes through a confocal etalon producing Fabry-Perot fringes during the laser scan, the other passes through the heated reference cell. The reference cell contains 16 torr of CO and is kept at a temperature of 160 - 165 °C. This temperature allows transitions from the first excited vibrational state of CO to be observed and collected, which serve as the reference for the laser frequency.

The burner chamber consists of a low pressure flat flame burner (McKenna Corp.) composed of two water cooled concentric circular metal frits mounted on a vertical translation stage. The center circle is 10 cm in diameter and serves as the flame region. A 1 cm diameter torus surrounds this and serves as a shroud for the flame. Argon is used as a shroud gas and serves to reduce interference from the combustion gases. The gases are introduced to the burner via an MKS Model 147B mass flow controller or a Matheson Model 601 Rotameter. The flow controller handles the fuel (CH<sub>4</sub>), oxidizer (O<sub>2</sub> or air), and the inert gas shroud (Ar). The inhibitor is introduced to the flame region of the burner through the rotameter, which has been calibrated with a wet test meter. The burner is located in a vacuum chamber which is maintained at low pressure (20 torr) by a high volume vacuum pump (Sogevac SV100) whose flow is attenuated by the combination of an adjustable butterfly valve and a gas bleed valve. The pressure of the chamber is monitored by a capacitance manometer (MKS Model 390).

The IR radiation source is a Laser Photonics Tunable Diode Laser, and the diode used for the CO spectroscopy lases in the 2040 - 2055 cm<sup>-1</sup> region. The radiation is detected by one of three LN2 cooled HgCdTe or InSb detectors. Three traces are recorded during each scan: a sample, an etalon spectrum, and a reference spectrum. These are stored on the PC for further analysis.

### Two Line Thermometry

To calculate the flame temperature and species concentration we use a method known as Two Line Thermometry. In this method, a spectrum containing two transitions from different vibrational states of a species is collected. In our experiments, the collected spectrum contains transitions of two hot bands of CO. The absorbance of the species is given by the Bouguer-Lambert law:

$$Abs(\nu) = -\ln\left(\frac{I}{I_0}\right) = S_{\nu J}(T) \Phi(\nu - \nu_0) p_{CO} L$$

where  $S_{\nu J}(T)$  is the transition line strength,  $p_{CO}$  is the partial pressure of CO, and  $L$  is the total path length (10 cm), and  $\Phi(\nu - \nu_0)$  is the lineshape function describing the profile of the individual line. A non-linear least squares fitting routine has been written to determine the temperature, partial pressure, and line widths of the two transitions. The transition lineshape is described by either a Voigt or Galatry function. At the flame temperatures under study, collisional narrowing can become important, necessitating the use of the Galatry function. The choice of lineshape profile is determined by the goodness of fit as measured by the Chi Squared test. The line strength, a function of



temperature, is calculated from known relations [2].

$$S = \frac{8\pi^3}{3hc} \mu_1^2 \frac{v+1}{2\alpha} \left( \frac{N_{v,J}}{(2J+1)p} \right) J\omega \left[ 1 - \exp\left(\frac{-hc\omega}{kT}\right) \right]$$

It is the product of several factors which account for the fractional population of the originating state, induced emission from the excited state, and intensity factors for vibrational and rotational state. The fractional population of the state takes into account the temperature of the system in both the energy of the lower state and in the partition function. The computed absorbance of the individual lines are summed to generate a fit to the collected spectrum determining the temperature of the flame and the partial pressure of the absorbing species (CO).

In the present study, we primarily use two pairs of transitions. We avoided using any fundamental transitions as we observed that many of the fundamental transitions are saturated in the flame, thus preventing an accurate determination of the line strength of the transition. Also, fundamental transitions are subject to interference from laboratory air and cooling postflame gases inside the burner chamber. The line pairs used are P18 (2,1) + P12 (3,2) located at approximately 2042.90  $\text{cm}^{-1}$  and the P20 (2,1) + P14 (3,2) at approximately 2034.14  $\text{cm}^{-1}$ . We found no significant differences between these two, or any other, line pairs used in this study. Both transitions in a pair are located within 0.4  $\text{cm}^{-1}$  of each other. Difficulties arise when using greater separation due to the nonlinear output of the diode laser and the nonlinear response of the detectors.

The TDL frequency is calibrated with the heated reference cell. Transitions from both the fundamental and from the first excited state of CO are observed and provide a sufficient number of transitions to unambiguously assign the transitions observed in the flame. Line positions for CO were obtained from literature values [3].

## Results

Typical results from a series of experiments are illustrated in Figure 1. Shown is the flame temperature as a function of height above the flat flame burner surface. It is readily seen that the temperature increases upon addition of the inhibitor, in this case  $\text{CF}_2\text{H}_2$ , even in small quantities (0.25 %) and the temperature also peaks at a greater distance from the burner surface than the uninhibited  $\text{CH}_4/\text{O}_2$  flame, which is the solid line in Figure 1. This phenomenon, observed previously for  $\text{CF}_3\text{Br}$  [4,5], has been attributed to the flame front moving away from the burner surface, reducing heat losses to the cooled burner head. Results vary for the different species in the temperature change and in the distance the peak temperature lies above the burner surface relative to the uninhibited flame. Experiments are continuing at this time and are expanding to include other inhibitor compounds and other combustion species.

We have established and continue to expand a set of experimental data of flame temperature profiles for premixed  $\text{CH}_4/\text{O}_2$  and  $\text{CH}_4/\text{Air}$  flames with small amounts of halogenated compounds as a dopant. This data should prove useful for comparison to the presently developing chemical kinetic models of premixed inhibited flames. In particular, researchers at NIST are developing a reaction model with

fluorinated compounds as the flame dopants [6] and this data appears to be the first such set available for premixed flat flames doped with fluorinated compounds. The current interest in fluorinated compounds stem from the pressing need for replacement compounds for the presently used Halons. Hopefully, this data will further the present flame modeling efforts, and help in the search for alternative fire suppressants.

### References

- [1] R. K. Hanson and P. K. Falcone, *Applied Optics* **17**, 2477-2480 (1978). X. Ouyang and P. L. Varghese, *Applied Optics* **28**, 1538-1545 (1989).
- [2] S. S. Penner, "Quantitative Molecular Spectroscopy and Gas Emissivities," Addison-Wesley, Reading, MA, 1959.
- [3] T. R. Todd, C. M. Clayton, W. B. Telfair, T. K. McCubbin, Jr., and J. Pliva. *Journal of Molecular Spectroscopy* **62**, 201-227 (1976).
- [4] J. C. Biordi, C. P. Lazzara, and J. F. Papp, in "Halogenated Fire Suppressants," ACS Symposium Series 16. American Chemical Society, Washington, D. C., 1975.
- [5] C. K. Westbrook, *Comb. Sci. and Tech.* **34**, 201-225 (1983).
- [6] M. R. Zachariah et al., NIST, private communication.

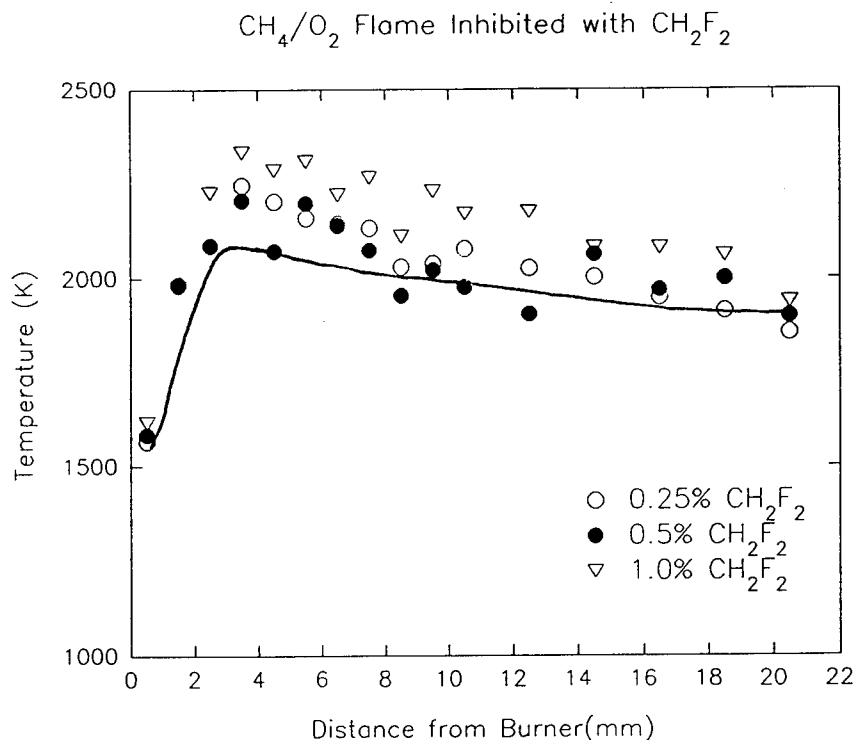


Figure 1. Flame temperature vs. height above burner surface for a stoichiometric  $\text{CH}_4/\text{O}_2$  flame. The solid line is the uninhibited flame. Total pressure is 20 torr.

## Laser-Induced Fluorescence Measurements of CH and C<sub>2</sub> During Diamond CVD

George A. Raiche, Michael S. Brown, and Jay B. Jeffries

Molecular Physics Laboratory  
SRI International  
333 Ravenswood Ave. Menlo Park, CA 94025  
Phone: (415) 859-6341  
Fax: (415) 859-6196

Chemical vapor deposition (CVD) of diamond film has recently been discovered in variety of flame and plasma environments. A gas jet of effluent from a dc-arc plasma has one of the fastest growth rates for high quality diamond film. To improve the yield from such arc-jet plasmas, models of the deposition chemistry and sensors to control the reactive gas jets are needed. Measurements of the gas temperature in the jet and boundary layer above the substrate surface are crucial to develop models of the process chemistry. Laser-induced fluorescence (LIF) measurements of the rotational distribution of diatomic radicals has proven an effective method for non-intrusive determinations of gas temperature in low-pressure flames.<sup>1</sup> In this presentation we discuss LIF observations of CH radicals in a dc-arc-jet reactor during diamond CVD and explore different excitation and detection strategies to determine the optimum method for temperature measurements.

There are significant differences between the gas effluent of a dc-arc-jet plasma and a premixed gas flame. In the arc-jet there is substantial electron impact emission; thus, the arc-jet has considerably more background emission than a flame with similar radical densities. The gas residence time in the arc-jet is quite short which limits the chemical reaction time of the plasma dissociated gases; thus, the arc-jet is much further from chemical equilibrium than the flame. The resulting changes in chemical composition can produce quite different optical interference for the CH LIF. Even though the arc-jet environment is similar to low-pressure flames, the optimum LIF strategy for CH LIF must be re-examined.

CH has been observed in our laboratory by LIF in a variety of flames<sup>1-3</sup> between 5 and 40 Torr which spans the operating range of our dc-arc-jet CVD reactor. Figure 1 schematically shows the arc-jet reactor, the optical collection, and the laser excitation for LIF. Diamond film is grown in this reactor on a water cooled molybdenum substrate from the effluent from a dc-arc plasma. The arc is struck in a mixture of hydrogen and argon between a tungsten cathode and an anode shaped into a converging/diverging nozzle. A small amount (<1%) methane is added to the gas exiting the nozzle. The effluent forms a luminous jet of gas approximately 1 cm in diameter, which impinges on a water cooled substrate approximately 5 cm from the exit plane of the nozzle. A tunable pulsed laser beam is directed through the effluent and the LIF is detected on the axis mutually orthogonal to the laser and effluent beams. The residence time of the reactive gas between the nozzle and boundary layer above the substrate is less than 100 $\mu$ s.

The gas temperature between the nozzle exit and substrate is required to model the chemistry occurring in the gas jet. Gas temperature can be inferred from LIF measurements of the rotational distribution of the diatomic radical. Chemical reactions produce the transient CH with some initial rotational, vibrational, and electronic state distribution. The free radical CH is quite

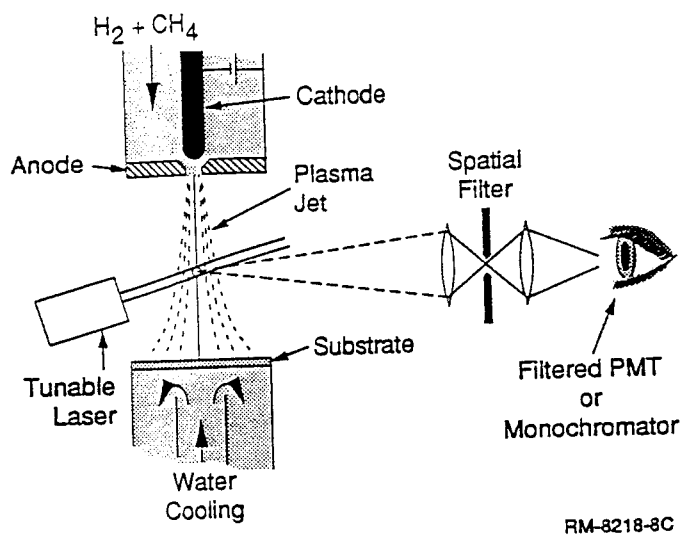


Figure 1

gas temperature in this gas jet which has nearly 50% argon feedstock available for non-reactive collisions.

The care required to determine gas temperature from LIF measurements is described in detail by Rensberger et al.<sup>1</sup> and the method is only briefly discussed here. The wavelength of the excitation laser is varied to excite transitions originating from several different rotational levels in the ground electronic state of the molecule. The amplitude of the signal from each transition is proportional to the population of the lower state, degeneracies, and spectroscopic transition strengths. The rotational level population has a Boltzmann distribution, and thus depends exponentially on gas temperature. Any other rotational dependence of the LIF signal can produce an error in the inferred temperature. Thus, any variation in detector response with excitation transition or rotational level dependence of the collisional quenching must be accounted.

Collisional quenching of excited diatomic hydrides has been shown<sup>4</sup> to depend on rotational level. Thus, transitions to different rotational levels have a variation in quantum yield for fluorescence versus quenching. In the 20 Torr pressure of the arc-jet reactor the fluorescence lifetime is more than 100 ns. Therefore, time gated detection of only the first 10 ns of the fluorescence mitigates any variation of quantum yield with rotational level.

The variation of detector response with excited rotational level has been shown for OH in a flame to perturb the inferred temperature as much as 1500 K from a temperature of 2300 K and at the same time the distribution appeared Boltzmann.<sup>1</sup> When the laser excites a transition only a single quantum level in the excited state is populated; from that level we observe the P, Q, and R branch fluorescence. Even though rotational energy transfer (RET) collisions redistribute the excited state population, the RET collisions compete with quenching collisions which tend to freeze the population in the initially excited level. For flame OH, more than 30% of the total LIF comes from the initially excited level.<sup>5</sup> The time gating of the signal to the first few ns of the fluorescence exacerbates this problem. Thus, we require a uniform detector response over the entire set of P, Q, and R branch transitions for the level excited.

reactive in this environment and after a few collisions reacts to produce other species, predominately with  $H_2$  and  $H$  to form  $CH_2$  and atomic carbon, respectively. Thus, the CH radical only has a few collisions to relax from the nascent rotational distribution to a thermal distribution reflecting the gas temperature. CH is produced by the  $CH_2 + H \rightarrow CH + H_2$  reaction which is only 3.5 kcal/mole exothermic; thus, the nascent product CH is not expected to have a rotational distribution significantly different than thermal. The small amount of excess energy available in CH rotations above the thermal energy should be removed in one or two gas collisions. We therefore expect the CH rotational distribution to reflect the

Since the arc-jet effluent has such bright emission, we must filter the fluorescence to select the wavelength of the LIF. Thus to measure temperature, the detector must be able to isolate the fluorescence from a specific vibrational band, yet have flat response over the rotational transitions in that band. For CH that requires a bandwidth in excess of 15 nm with flat response. We obtain such a detector bandwidth by using a monochromator with a narrow front slit, a wide back slit, and an end-on photomultiplier with uniform response over a large (several cm radius) area. This provides a detector whose response versus wavelength has a trapezoidal shape, and the center wavelength can be tuned by the monochromator grating.

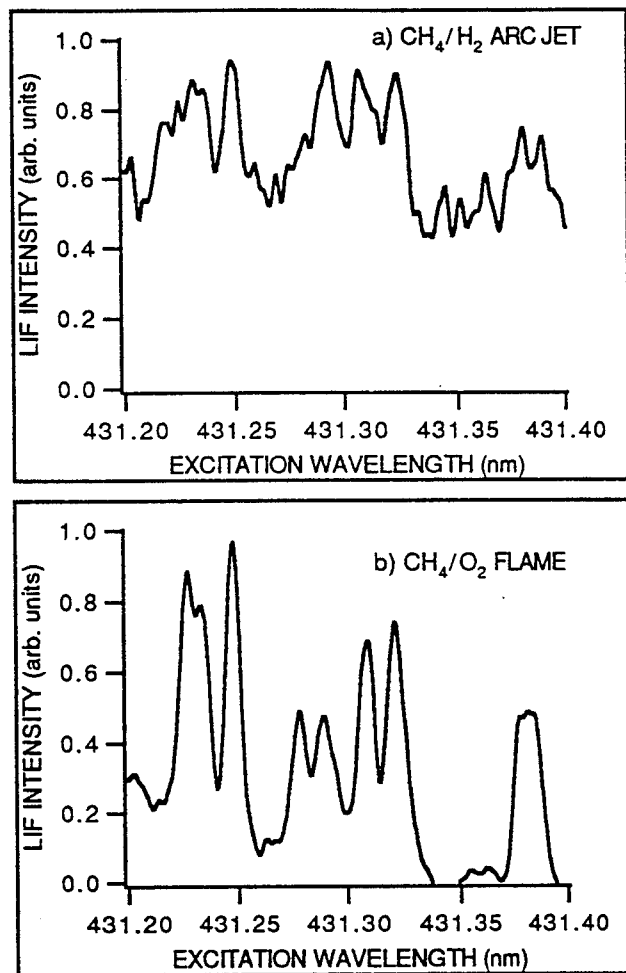


Figure 2

we obtained CH gas temperature measurements in 200 Torr arc-jet plasmas using this scheme.<sup>6</sup> If we excite the weaker transition the smaller line strength can be overcome with more laser intensity; however, the thermal population in  $v''=1$  is lower by a factor of ten at 2000 K. An example of this detection scheme is shown in Figure 3 for both the arc-jet and laboratory flame. Here, the background LIF is minimized and even though the signal is reduced from Figure 2 by a factor of ten, the signal to noise is significantly improved.

LIF of CH with the B-X electronic transitions has also been observed in the arc-jet. The Franck-Condon factors of 0.9 and 0.1 for the 0-0 and 0-1 bands provide a better situation for off diagonal excitation. Unfortunately, excitation at 390 and 432 nm produces interference LIF from

Gas temperature measurement using CH LIF has a clear trade-off between line-strengths, Franck-Condon factors, and scattered light. Since the detector has uniform response over an entire vibrational band, the detector is very sensitive to scattered laser light if the same vibrational band is used for excitation and detection. Figure 2 shows a portion of the CH A-X 0-0 band excitation in both the dc-arc-jet and a laboratory flame. Note that the LIF in the arc-jet rides has a large background present with the laser wavelength both on and off resonance. This is present even with a detector bandwidth which is less than that required for LIF temperatures. The large background in the arc-jet is a combination of scattered laser light and interference LIF discussed below.

The scattered light problem can be avoided if a band different from the one excited is detected. The CH A-X transition is quite diagonal; the 0-0 and 0-1 bands have Franck-Condon factors of 0.996 and 0.003, respectively. Thus, exciting 0-0 and observing 0-1 will reduce the signal by a factor of 300; even with this loss of signal

another species in the arc-jet effluent. This interference provides a non-zero background and degrades the signal to noise. Data from each of the four CH LIF schemes and characterization of the interference will be discussed.

This research is supported by ARPA on contract with the Naval Research Laboratory

Dr. George Raiche's permanent address is: Department of Chemistry, Hamilton College, Clinton, New York. Dr. Brown's current address is: Metro-Laser, Irvine, California.

## References

1. K. J. Rensberger, J. B. Jeffries, R. A. Copeland, K. Kohse-Höinghaus, M. L. Wise, and D. R. Crosley, *Appl. Opt.* **28**, 3556 (1989); D. R. Crosley and J. B. Jeffries, *Temperature: Its Measurement and Control in Science and Industry*, J. F. Schooley, ed., (American Institute of Physics, New York, 1992) p. 702.
2. K. J. Rensberger, M. J. Dyer, and R. A. Copeland, *Appl. Opt.* **27**, 3679 (1988).
3. D. E. Heard, J. B. Jeffries, G. P. Smith, and D. R. Crosley, *Comb. Flame* **88**, 137 (1992).
4. R. A. Copeland, M. J. Dyer, and D. R. Crosley, *J. Chem. Phys.* **82**, 4022 (1985); N. L. Garland and D. R. Crosley, *Twenty-first Symp. (Int.) on Combustion* (Combustion Institute, Pittsburgh, PA, 1986) p. 1693.
5. J. B. Jeffries, K. Kohse-Höinghaus, G. P. Smith, R. A. Copeland, and D. R. Crosley, *Chem. Phys. Lett.* **152**, 160 (1988).
6. G. A. Raiche and J. B. Jeffries, *Appl. Opt.* **32**, 4629 (1993).

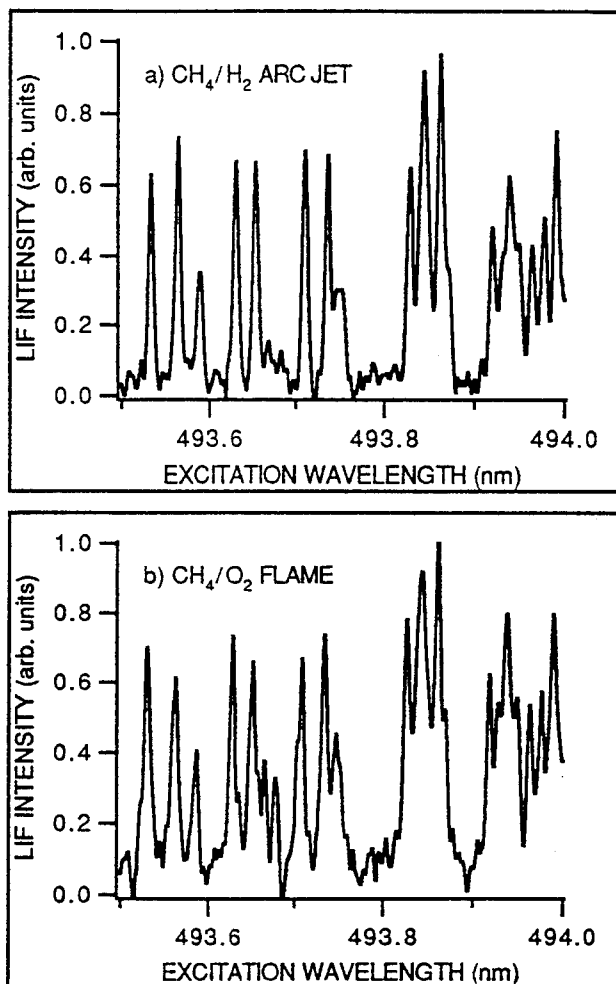
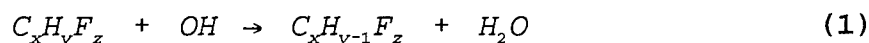


Figure 3

## Structure Matters: Detection of Difluoromethyl and Difluoroethyl Radicals by Resonance Enhanced Multiphoton Ionization Spectroscopy

Jeffrey W. Hudgens, Jeffrey L. Brum, Russell D. Johnson III, David V. Dearden, Chemical Kinetics and Thermodynamics Division, Chemical Science and Technology Laboratory, National Institute of Standards and Technology, Gaithersburg, MD 20899 (Tel. 301-975-2512)

The link between anthropogenic chlorofluorocarbon (CFC) release and stratospheric ozone depletion now appears well established. Several fluorinated methanes and ethanes are among the hydrofluorocarbons (HFCs) currently being investigated as replacements for the chlorine containing congeners that have traditionally found use as refrigerants, fire extinguishers, and in more specialized applications. In recent years significant effort has focused on the tropospheric degradation pathways available to HFCs initiated by H atom abstraction by a hydroxyl radical. For alternate CFC's the generic initiating reactions are:



Although an impressive amount of mechanistic and kinetic information concerning these pathways has been gathered recently, much remains to be learned about the fluorinated methyl and ethyl radicals which represent the first intermediates of the degradation process.

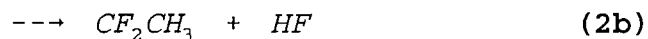
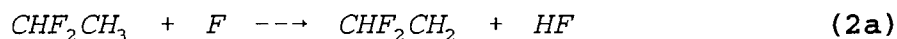
In this regard we have investigated the radicals produced by H atom abstraction from difluoromethane (HFC-32) and 1,1-difluoroethane (HFC 152a) using resonance enhanced multiphoton ionization (REMPI) spectroscopy. We report the first electronic spectra of the  $CHF_2$  and  $CF_2CH_3$  radicals. The spectrum of  $CF_2CH_3$  represents the first observation of a vibrationally resolved electronic excited state of a substituted ethyl radical.

The experimental apparatus used in these studies consisted of a tunable dye laser, flow reactor, time-of-flight mass spectrometer, and computer data acquisition system. Radicals

were generated in a flow reactor which operated at 250-400 Pa (2-3 torr) by hydrogen abstraction from  $\text{CH}_2\text{F}_2$  (or  $\text{CD}_2\text{F}_2$ ) using F atoms produced in a microwave discharge. The radicals effused from the flow reactor into the ionization region of a time-of-flight mass analyzer. The estimated radical density in the ionization region is  $10^{10} \text{ cm}^{-3}$ . Radicals were ionized with the focused output of a pulsed dye laser (energy = 10-20 mJ/pulse; bandwidth =  $0.2 \text{ cm}^{-1}$ , FWHM; focal length = 150 mm). The ions were mass resolved, and the intensities of the mass peaks of interest were monitored with a gated integrator and averaged and recorded with a computer data-acquisition system, as a function of laser wavelength.

The electronic spectra of  $\text{CHF}_2$  and  $\text{CDF}_2$  radicals appeared between 330-430 nm. Both spectra span nearly  $11000 \text{ cm}^{-1}$  and exhibit about 70 distinct vibrational bands. Analyses reveal that the spectra arise from two-photon resonances with planar Rydberg states. A third laser photon ionized the radicals. Spectroscopic constants were found for the  $\tilde{\text{F}}(3\text{p})$  Rydberg state of the  $\text{CHF}_2$  radical ( $\nu_{00} = 49312(10) \text{ cm}^{-1}$ ,  $\nu'_2$  (C-F str) =  $1365(8) \text{ cm}^{-1}$ ,  $\nu'_3$  ( $\text{CF}_2$  scissors) =  $660(20) \text{ cm}^{-1}$ ,  $\nu'_4$  (OPLA) =  $1022(1) \text{ cm}^{-1}$ ) and of the  $\text{CDF}_2$  radical ( $\nu_{00} = 49323(10) \text{ cm}^{-1}$ ,  $\nu'_2$  (C-F str) =  $1300(21) \text{ cm}^{-1}$ ,  $\nu'_3$  ( $\text{CF}_2$  scissors) =  $650(15) \text{ cm}^{-1}$ ,  $\nu'_4$  (OPLA) =  $864(2) \text{ cm}^{-1}$ ). The REMPI spectra exhibited  $\nu''_4 = 1-5$  hot bands of the  $\tilde{\text{X}}^2\text{A}'$  radical. Modeling of these hot bands with a quartic double-well potential gives the inversion barrier,  $B_{\text{inv}} = 2800(500) \text{ cm}^{-1}$ , and the out-of-plane angle,  $\Phi_{\text{m}} = 49(6)^\circ$ .

The reaction used to produce difluoroethyl radicals



may produce two difluoroethyl isomers,  $\text{CF}_2\text{CH}_3$  and  $\text{CHF}_2\text{CH}_2$ . The branching ratio of (2) is unknown. The products of reaction (2) produce  $m/z$  65 REMPI signal between 335 and 475 nm. Most of this spectrum is a congested continuum; however, between 420 and 462 nm a



progression of nine distinct vibrational bands protrudes through the underlying continuum.

*Ab initio* calculations at the MP2/6-31G\*, G1, and G2 theory levels of  $\text{CF}_2\text{CH}_3$ ,  $\text{CF}_2\text{CH}_3^+$ ,  $\text{CHF}_2\text{CH}_2$ , and  $\text{CHF}_2\text{CH}_2^+$  enable a fairly complete analysis. The  $m/z$  65 REMPI spectrum originates from two photon resonances with a 3p Rydberg state of  $\text{CF}_2\text{CH}_3$  radicals. A third laser photon ionized the radicals. The electronic origin is tentatively assigned at  $\nu_{00}=43275\text{ cm}^{-1}$  and the vibrational progression is assigned as the  $\nu_9'(-\text{CF}_2\text{ wag})=530\text{ cm}^{-1}$ . The continuous REMPI spectrum arises from the overlap of many vibrational combination bands within the 3p Rydberg state. Starting near 412 nm one or more 3d Rydberg states may also add to the congested spectrum.

*Ab initio* calculations also predict that the  $\text{CHF}_2\text{CH}_2$  isomer may also contribute to the spectrum above  $\sim 362\text{ nm}$ . Because the Rydberg states of  $\text{CHF}_2\text{CH}_2$  rapidly isomerize into the  $\text{CF}_2\text{CH}_3$  structure, this REMPI spectrum of  $\text{CHF}_2\text{CH}_2$  radicals should appear as a featureless continuum.

$\text{CHF}_2$  and  $\text{CF}_2\text{CH}_3$  radicals are similar to the extent that both radicals exhibit 3p Rydberg spectra that span  $\sim 11000\text{ cm}^{-1}$ . The expanses of these spectra arise from the substantial geometry changes between the radical and cation-like Rydberg structures. But the differences are significant. While the vibrational bands of  $\text{CHF}_2$  are discrete, the vibrational bands of  $\text{CF}_2\text{CH}_3$  overlap to form a continuum.  $\text{CHF}_2$  radicals can be photoionized with good selectivity from complex gas-phase mixtures. But the selectivity available from photoionization schemes for  $\text{CF}_2\text{CH}_3$  radicals is limited.

The spectral congestion exhibited by  $\text{CF}_2\text{CH}_3$  radicals arises from fundamental properties of haloethyl radicals and cations. These properties include substantial geometry changes, a greater density of available upper vibrational levels, and the potential for isomerization. Using *ab initio* results, we will explain the present spectra and show that these results apply to the REMPI detection of other haloethyl radicals.

## Computation of Synthetic Diatomic Spectra

J. O. Hornkohl, C. Parigger, and J. W. L. Lewis  
 University of Tennessee Space Institute  
 B. H. Goethert Parkway  
 Tullahoma, TN 37388  
 (615) 393-7491

### 1. Introduction

Comparisons of measured spectra to synthetic spectra have become commonplace in both pure and applied spectroscopy. For example, the comparison might be made as part of the evaluation of the accuracy of the molecular parameters, or the comparison might be made for determination of the temperature or population density of the spectroscopically active molecule. Numerous computer programs have been written for the computation of synthetic diatomic spectra. Many of these apply only to a specific type of transition. Some apply only to specific bands of a certain molecule. One starting on a new molecule faces the task of writing a new computer program for computation of the synthetic spectra. The following describes a series of computer programs that can be applied to any diatomic molecule.

### 2. Diatomic Line Positions and Line Strengths

The prediction of a spectrum requires the line positions and line strengths. The line positions, customarily given in vacuum wavenumbers, are the term value differences

$$\tilde{\nu}(n'v'J', n''v''J'') = T_{n'v'J'} - T_{n''v''J''}, \quad (1)$$

where  $J$  is the total angular momentum quantum number,  $v$  is the vibrational quantum number,  $n$  denotes all other required quantum numbers,  $T_{nvJ}$  is a term value, a single prime denotes the upper states, and a double prime the lower. The diatomic line strength can be expressed as the product

$$S(n'v'J', n''v''J'') = |\langle n'v' | R_e(r) | n''v'' \rangle|^2 S(J', J'') = |a_0 + a_1 r_1(v', v'') + \dots|^2 q(v', v'') S(J', J'') \quad (2)$$

in which  $R_e(r)$  is the electronic transition moment (a function of the internuclear distance  $r$ ),  $S(J', J'')$  is the Hönl-London or rotational line strength factor,  $q(v', v'')$  is the Franck-Condon factor,

$$q(v', v'') = \langle v' | v'' \rangle, \quad (3)$$

and  $\bar{r}_i(v', v'')$  is the  $i$ -th  $r$ -centroid,

$$\bar{r}_i(v', v'') = \frac{\langle v' | r^i | v'' \rangle}{\langle v' | v'' \rangle}. \quad (4)$$

The measurement of spectral line positions is notably accurate while the measurement of spectral intensities is notably inaccurate. Thus, Eqs. (1) and (2) apply at two quite different levels of approximations. Typically, the Born-Oppenheimer approximation is inadequate for line positions, Eq. (1), but is acceptable for line strengths, Eq. (2).

Traditionally, the Born-Oppenheimer approximation separates the total diatomic eigenfunction into electronic and nuclear parts. The nuclear part is further separated into vibration of the nuclei and rotation of the nuclei. The separation of the diatomic eigenfunction

into its *angular momentum*, *vibrational*, and *other* parts is more useful. For Hund's case *a* coupling this type of separation for a molecule having  $\mathcal{N}$  electrons gives

$$\langle \mathbf{r}_1, \mathbf{r}_2, \dots, \mathbf{r}_{\mathcal{N}}, \mathbf{r} | nJM\Omega S\Sigma \rangle = \sqrt{\frac{2J+1}{8\pi^2}} \langle X'_e r | n \rangle |S\Sigma\rangle D_{M\Omega}^{J*}(\alpha\beta\gamma), \quad (5)$$

where  $\mathbf{r}_1, \mathbf{r}_2, \dots, \mathbf{r}_{\mathcal{N}}$ , are the lab-fixed spatial coordinates of the  $\mathcal{N}$  electrons,  $\mathbf{r}$  is the lab-fixed internuclear vector,  $D_{M\Omega}^J(\alpha\beta\gamma)$  is an element of the rotation matrix,  $\alpha$ ,  $\beta$ , and  $\gamma$  are the Euler angles,  $|S\Sigma\rangle$  is the total electronic spin ket,  $X'_e$  is a symbol denoting  $3\mathcal{N}-1$  rotated electronic coordinates ( $\gamma$  is the remaining electronic coordinate),  $M$  is the quantum number for the lab-fixed component of the total angular momentum, and  $\Omega$  is the quantum number for the internuclear component of the total angular momentum. Because the Hund's case *a* eigenfunction declares that both  $M$  and  $\Omega$  are good quantum numbers, the case *a* eigenfunction is *not* an angular momentum state since no two components of angular momentum commute. A manifestation of this is that these eigenfunctions have a peculiar behavior under the raising and lowering operators. The case *a* eigenfunction is, nevertheless, a complete orthonormal basis.

Hönl-London factors for  $a \leftrightarrow a$  transitions are given by

$$S(J', J'') = (2J'' + 1) \langle J''\Omega''k, \Omega' - \Omega'' | J'\Omega' \rangle^2 \delta(S', S'') \delta(\Sigma', \Sigma'') \quad (6)$$

in which  $\langle J''\Omega''k, \Omega' - \Omega'' | J'\Omega' \rangle$  is a Clebsch-Gordon coefficient, and  $k$  is the order of the transition (i.e.,  $k = 1$  for electric dipole,  $k = 2$  for two-photon,  $k = 2$  for Raman, and so forth).

The relationships between the electric dipole line strength, the Einstein coefficients  $A_{nm}$ ,  $B_{nm}$ , and  $B_{mn}$ , and the oscillator strength  $f_{mn}$  and  $f_{nm}$  hold, without modification, for all quantum systems including the diatomic molecule. The equation which defines the line strength for a dipole transition between states  $|n'j'm'\rangle$  and  $|n''j''m''\rangle$ ,

$$S_{n'j', n''j''} = \sum_{m'=-j'}^{j'} \sum_{m''=-j''}^{j''} |\langle n'j'm' | \mathbf{d} | n''j''m'' \rangle|^2, \quad (7)$$

fully accounts for the degeneracy of the upper and lower states. The equation from statistical thermodynamics,

$$N_{nj} = \frac{g_{nj}}{Q} e^{-E_{nj}/kT}, \quad (8)$$

in which  $g_{nj}$  is the statistical weight,  $E_{nj}$  is the energy eigenvalue,  $Q$  is the partition function,  $k$  is Boltzmann's constant, and  $T$  is the absolute temperature, also fully accounts for the degeneracy of the upper and lower states. The equations which relate the Einstein coefficients and the oscillator strengths to the electric dipole line strength each contains  $g_{nj}$  in the denominator which is canceled by the  $g_{nj}$  in the numerator of Eq. (8). Thus, a simplicity is achieved if one writes the equations directly in terms of the line strength.

Established methods exist for computation of the vibrational eigenfunctions (e.g., RKR potential curves and Numerov integration of the radial Schroedinger equation). *Ab initio* calculations often provide the most reliable electronic transition moment,  $R_e(r)$ . Thus, the following concentrates on the line positions and Hönl-London factors.

### 3. Computation of the Line Positions and Hönl-London Factors

The algorithm for determining accurate line positions and Hönl-London factors follows the basic methods of Zare,<sup>1</sup> et al.

1. Trial values of the molecular parameters (e.g.,  $B$ ,  $A$ ,  $\epsilon$ ,  $\gamma$ , etc.) are assumed, and an experimental table of vacuum wavenumbers is read.

2. For given values of  $J'$  and  $J''$  rotational Hamiltonians for the upper and lower states are computed in the Hund's case  $a$  basis.

$$\langle a_i | H | a_j \rangle = \langle a_i | H(B, A, \epsilon, \gamma, \dots) | a_j \rangle \quad (9)$$

Fine structure terms and  $\Lambda$ -doubling terms are included. Computation of the Hamiltonian is made applicable to any type of diatomic state by making the quantum numbers and molecular parameters program variables. An electronic state can be mixed with a number of other electronic states.

3. The Hamiltonians are diagonalized,

$$T_{nm} = \sum_i \sum_j U_{ni}^T H_{ij} U_{jm}, \quad (10)$$

by the Jacobi method. The diagonal elements,  $T_{nn}$  are the term values in the intermediate representation.

4. Each submatrix in the Hamiltonian is subjected to the same orthogonal transformation that diagonalized the total Hamiltonian. For example, for the spin-orbit fine structure term

$$\mathcal{H}_{nm}^{\text{SO}} = \sum_i \sum_j U_{ni}^T H_{ij} U_{jm}. \quad (11)$$

5. Selection rules are applied to determine which of the many combination differences represent allowed spectral lines. The angular momentum selection rules are much easier to apply in a general way than the parity selection rules. The angular momentum selection rules are applied by computing the Hönl-London factors,

$$S_{nm}(J', J'') = \left| \sum_{\Omega'} \sum_{\Omega''} U_{n\Omega'}^T \langle J'', \Omega'', 1, \Omega' - \Omega'' | J' \Omega' \rangle U_{\Omega''m} \right|^2, \quad (12)$$

where  $U_{n\Omega}$  are elements of the orthogonal matrix  $\mathbf{U}$  determined in step 2. A non-vanishing sum represents an allowed transition, while a vanishing sum represents a forbidden transition.

6. For each theoretically predicted spectral line, the experimental table is searched to find a line having the same wavenumber to within a specified tolerance (typically  $0.1 \text{ cm}^{-1}$ ), with the same  $J'$  and  $J''$  that has not already been identified with a previously computed theoretical spectral line.

7. A *derivative matrix* is computed. When completed, this matrix will be used to compute corrections to the trial values of the molecular parameters. Computation of the derivative matrix proceeds as follows: For each theoretical line which is accepted in step 6 the error in the theoretical wavenumber is computed,

$$\Delta \tilde{\nu}_j = \tilde{\nu}_{\text{theory}} - \tilde{\nu}_{\text{exper}}, \quad (13)$$

and the contribution of each molecular parameter in the model to this error is computed,

$$\Delta \tilde{\nu}_j = \sum_p \frac{\partial \tilde{\nu}_j}{\partial c'_p} \Delta c'_p - \sum_q \frac{\partial \tilde{\nu}_j}{\partial c''_q} \Delta c''_q, \quad (14)$$

where the symbol  $c'_p$  denotes one of the parameters for the upper state and  $c''_q$  denotes one of the parameters for the lower state.

$$\frac{\partial \tilde{\nu}_j}{\partial c'_p} = \frac{\partial T_n(c'_p)}{\partial c'_p} = \frac{\partial}{\partial c'_p} \sum_{k,l} U_{nk}^T H_{kl} U_{ln} = \sum_{k,l} \left[ \frac{\partial U_{nk}^T}{\partial c'_p} H_{kl} U_{ln} + U_{nk}^T \frac{\partial H_{kl}}{\partial c'_p} U_{ln} + U_{nk}^T H_{kl} \frac{\partial U_{ln}}{\partial c'_p} \right] \quad (15)$$

It can be shown that the first and third terms cancel to give

$$\frac{\partial \tilde{\nu}_j}{\partial c'_p} = \sum_{k,l} U_{nk}^T \frac{\partial H_{kl}}{\partial c'_p} U_{ln} = \sum_{k,l} U_{nk}^T \mathcal{H}_{kl}^{(p)} U_{ln} \quad (16)$$

where the last step holds since  $H_{kl}(c'_p) = c'_p \mathcal{H}_{kl}^{(p)}$ . This result is reason for the computation described in step 4. For the lower states the corresponding result is

$$\frac{\partial \tilde{\nu}_j}{\partial c''_q} = - \sum_k \sum_l U_{nk}^T \mathcal{H}_{kl}^{(q)} U_{ln}. \quad (17)$$

Notice the minus sign on the right side of this equation.

The derivative matrix has a column for each of the molecular parameters and a row for each experimental line for which a theoretical line has been found. For a given experimental line, the above two equations are used to fill out a row of the derivative matrix.

8. Steps 2-7 are repeated for all values of  $J'$  and  $J''$  for which there are experimentally measured line positions. At the conclusion of this step, one has collected the information required to solve for  $\Delta \mathbf{C}$  in the equation

$$\Delta \tilde{\nu} = \mathbf{D} \Delta \mathbf{C} \quad (18)$$

where  $\Delta \tilde{\nu}$  is the column matrix composed of  $\tilde{\nu}_{\text{theory}} - \tilde{\nu}_{\text{exper}}$ ,  $\mathbf{D}$  is the derivative matrix described above, and  $\Delta \mathbf{C}$  is the column matrix composed of corrections to the upper and lower molecular parameters. The method of least squares solution of this equation is as follows:

$$\mathbf{D}^T \Delta \tilde{\nu} = \mathbf{D}^T \mathbf{D} \Delta \mathbf{C} \quad (19)$$

$$[\mathbf{D}^T \mathbf{D}]^{-1} \mathbf{D}^T \Delta \tilde{\nu} = \Delta \mathbf{C}. \quad (20)$$

The variance in the line position is computed,

$$\sigma_{\tilde{\nu}}^2 = \sum_j \frac{(\tilde{\nu}_{\text{theory}} - \tilde{\nu}_{\text{exper}})^2}{N} \quad (21)$$

where the sum is carried over all experimental lines for which a matching theoretical line was found, and  $N$  is the number of molecular parameters. The variance-covariance matrix is computed as

$$V = \sigma_{\tilde{\nu}}^2 [\mathbf{D}^T \mathbf{D}]^{-1}. \quad (22)$$

The diagonal elements of  $V$  are variances (i.e., error estimates) for the parameters. The off-diagonal elements are the covariances of the parameters.

9. The corrections  $\Delta \mathbf{C}$  are made to the coefficients.

10. Steps 2-10 are repeated until the corrections  $\Delta \mathbf{C}$  become negligibly small.

In a typical analysis not all of the parameters are varied.

<sup>1</sup>R. N. Zare, A. L. Schmeltekopf, W. J. Harrop, and D. L. Albritton, J. Mol. Spectrosc. **46**, 37 (1973).



Friday, March 11, 1994

## Four Wave Mixing Spectroscopy

**FB** 10:30am–12:10pm  
Grand Room

Jay B. Jeffries, *Presider*  
*SRI International*

## Degenerate Four-Wave Mixing for Quantitative Diagnostic Measurements

R. L. Farrow, P. H. Paul and E. J. Friedman-Hill  
 Combustion Research Facility, Sandia National Laboratories  
 P.O. Box 969, Livermore, CA 94551-0969  
 (510) 294-3259

P. M. Danehy  
 High Temperature Gasdynamics Laboratory, Stanford University  
 Stanford, CA 94305-3032  
 (415) 723-1823

We report theoretical and experimental studies of the effects of collisional quenching and the contributions of thermal gratings in degenerate four-wave mixing (DFWM).<sup>1</sup> Using single-mode laser radiation, peak signal intensity measurements were performed on an isolated line in the A-X transition of NO. By using appropriate mixtures of N<sub>2</sub> and CO<sub>2</sub> as buffer gases, we varied the collisional quenching rate over several orders of magnitude while maintaining a fixed total collisional dephasing rate. The varying quenching rate also had the effect of varying the heat

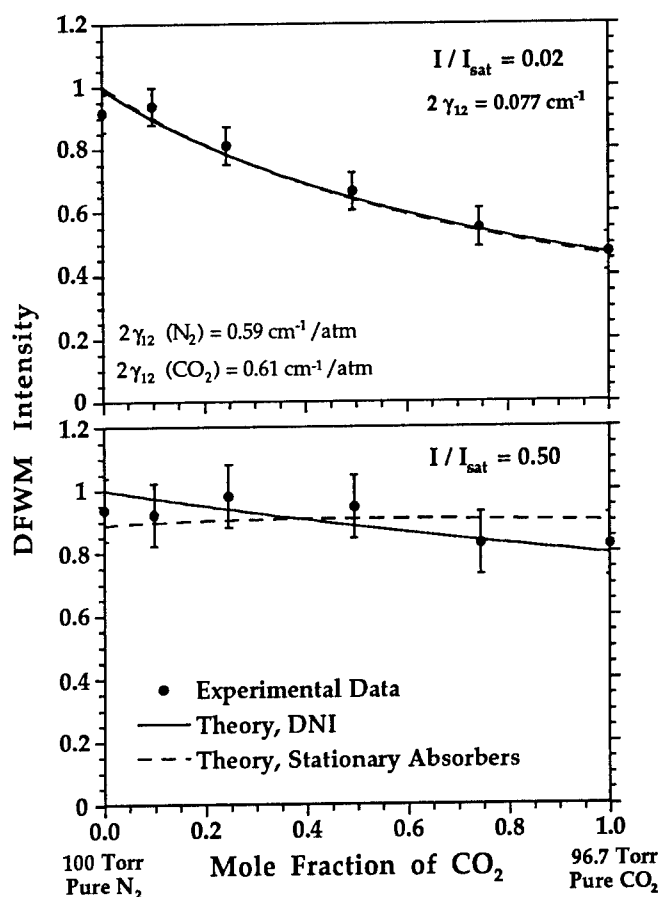


Fig. 1

Experimental and theoretical DFWM intensities of NO plotted against mole fraction of CO<sub>2</sub> in an N<sub>2</sub> / CO<sub>2</sub> mixture, for a fixed laser intensity. The NO quench rate increases by a factor of 10<sup>4</sup> from left to right, while the collisional broadening  $\gamma_{12}$  is held fixed. DNI refers to direct numerical integration of the velocity-dependent density matrix equations.<sup>2</sup> Stationary absorber refers to the two-level DFWM theory of Abrams *et al.*<sup>3</sup> The relative partial pressures of N<sub>2</sub> and CO<sub>2</sub> were chosen to maintain a constant dephasing rate, and the similarity of this rate for both buffer gases (see figure) resulted in a nearly constant total pressure.



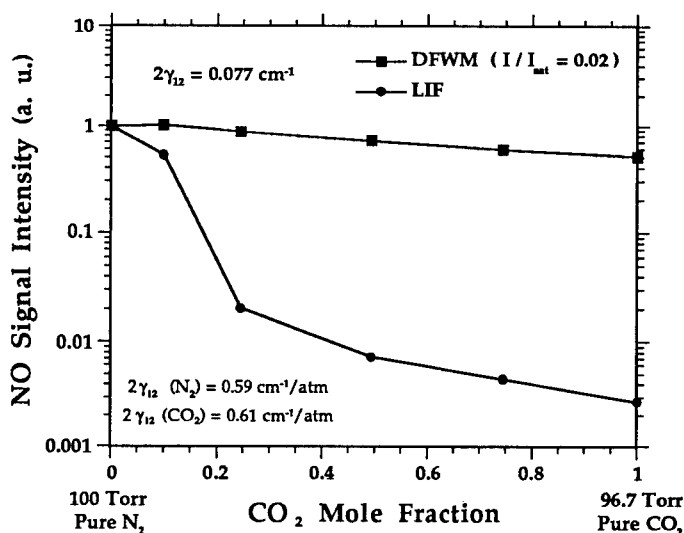


Fig. 2

Nearly unsaturated experimental DFWM (circles) and LIF (squares) signal intensities versus mole fraction of CO<sub>2</sub> in an N<sub>2</sub> / CO<sub>2</sub> mixture. The data are normalized to 1.0 at the left axis and are connected by straight lines to guide the eye.

released by population gratings to form thermal gratings, permitting detailed comparisons of signal intensities from both mechanisms.

The experimental setup used a phase-conjugate geometry and was similar to that described in Ref. 1. The laser source was a single-longitudinal-mode, pulse-amplified ring-dye laser, frequency-doubled and mixed with the Nd:YAG fundamental to obtain ~1.0 mJ pulses tunable near 226 nm. The pulses had a bandwidth of 0.004 cm<sup>-1</sup> and a duration of 10 ns. We typically used 12 - 300 μJ per pulse for each pump beam and one-fourth as much energy for the probe beam. All beams were collimated to a diameter of ~2.5 mm and had vertical polarization. Measurements were performed on ~30 mTorr of NO in mixtures of N<sub>2</sub> and CO<sub>2</sub> contained in a static cell. A total gas pressure of 100 Torr was chosen for the quenching study to minimize thermal-grating contributions, while higher pressures were used to study thermal gratings. DFWM and LIF signal intensities were simultaneously detected using photomultiplier tubes. In all measurements, we probed a well-isolated satellite line, O<sub>12</sub>(2), of the A<sup>2</sup>Σ<sup>+</sup>(v'=0) ← X<sup>2</sup>Π(v''=0) band. The LIF signals were detected through a 10-nm bandpass interference filter centered at 250 nm, corresponding to emission from the A<sup>2</sup>Σ<sup>+</sup>(v'=0) → X<sup>2</sup>Π(v''=2) band.

Shown in Fig. 1 are the results of DFWM intensity measurements (filled symbols) for various mixtures and for two different pump-beam intensities, corresponding to  $I/I_{\text{sat}} = 0.02$  (upper panel) and  $I/I_{\text{sat}} = 0.5$  (lower panel). (Saturation values are given for the 1:1 mixture, since  $I_{\text{sat}}$  increases by approximately 50% from left to right in Fig.1.) The measurements at the left side of the plot correspond to 100 Torr of pure N<sub>2</sub> while those at the right side correspond to 96.6 Torr of pure CO<sub>2</sub>. For both values of  $I/I_{\text{sat}}$  the signal intensity is observed to fall with increasing CO<sub>2</sub> mole fraction, *i.e.*, with increasing quenching. However, the signal decrease is significantly smaller for the more strongly saturated case, approximately 15% compared to 50%. This result confirms a previous suggestion<sup>4</sup> that strongly saturated DFWM intensities are relatively insensitive to quench rate.

Simultaneously measured LIF intensities were observed to vary much more dramatically with quench rate than DFWM intensities. Nearly unsaturated DFWM and LIF measurements for several mixtures of CO<sub>2</sub> and N<sub>2</sub> are indicated by symbols in Fig. 2. The experimental conditions are identical to those previously discussed, with  $\gamma_{12}$  held constant. Note that the DFWM

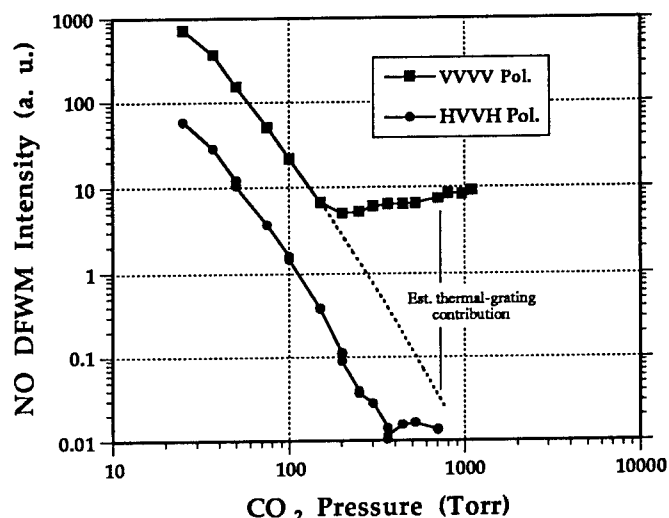


Fig. 3

DFWM intensity of the  $O_{12}(2)$  transition for various  $\text{CO}_2$  buffer pressures and different beam polarizations; solid lines connect the data points. The broken line is an extrapolation of the VVVV dependence at low pressures, indicating the relative contributions of thermal and population gratings.

measurements appear nearly constant on this log plot, while the LIF measurements are severely attenuated as quenching increases from left to right. In fact, the LIF intensity is attenuated by a factor of 370, while the DFWM intensity decreases by a factor of 2. DFWM is clearly less sensitive to quench rate than LIF under these conditions.

For higher pressures of  $\text{CO}_2$ , diffraction by thermal gratings (TG) formed from heat released via quenching began to compete with population-grating diffraction. This effect is more important at higher buffer-gas pressures mainly because the latter decreases rapidly with pressure,<sup>1</sup> while the former is expected to vary slowly with pressure under these conditions. TG diffraction can be conveniently detected by measuring the peak DFWM intensity as a function of buffer-gas pressure. As seen in Fig. 3 the DFWM intensity for vertically polarized beams (VVVV) exhibits an initial steep decline with increasing pressure until ~200 Torr, when it reverses and increases slightly at higher pressures. In contrast, for a horizontally polarized probe beam (HVVH) the signal continues to drop with pressure until the stray-light level is observed. Here, the absence of TG diffraction results from the fact that intensity gratings necessary to generate TG's are not produced by crossed-polarized fields.<sup>5</sup>

TG diffraction can also be studied by using an independently timed laser for the backward pump beam. By stepping the relative delay, the backward pump traces out the time-dependent diffraction efficiency of gratings formed by the forward-propagating beams. As seen in Fig. 4, a delay scan using 100 Torr of  $\text{CO}_2$  buffer results in a signal centered at zero delay (defined as the time for maximum overlap), with a width approximately equal to the convolution of the forward and backward pulses. This signal is generated mainly by a population grating, whose lifetime is sub-nanosecond and therefore follows the excitation pulse. However, at higher  $\text{CO}_2$  pressures the peak of the signal is delayed by ~7 ns and pronounced beats with a period of ~17 ns are observed. Here, the signal is dominated by TG diffraction; the initial delay results from the time required to develop the density fluctuations characteristic of TG's, and the modulation results from beating between two counter-propagating acoustic waves launched by rapidly released heat from the population gratings. The beat period can be related to the grating fringe spacing divided by the speed of sound in the medium. Since the latter depends on the gas temperature, time-resolved measurements of TG diffraction can potentially be used for thermometry. The absence of beats in

the trace measured with N<sub>2</sub> buffer is not yet fully understood, but may result from a dramatically slower rate of heat release associated with inefficient N<sub>2</sub> quenching.

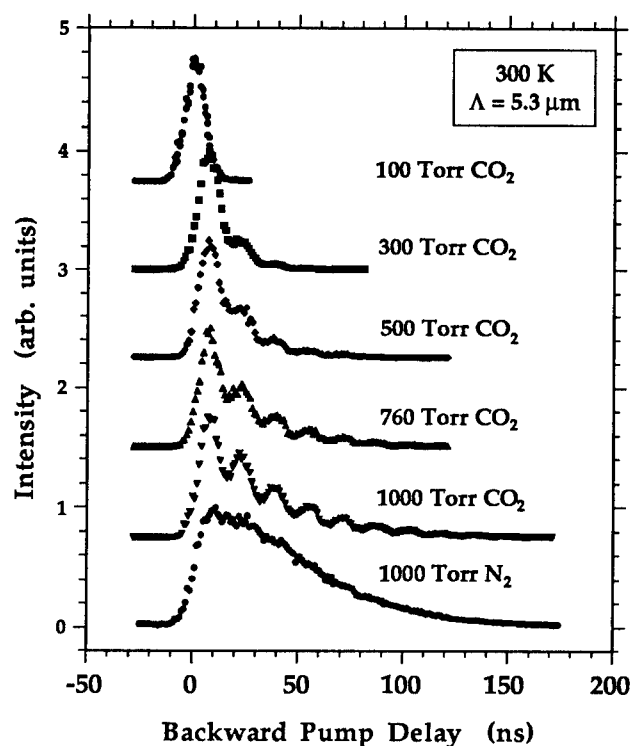


**Fig. 4**

DFWM intensity of the  $O_{12}(2)$  transition as a function of backward pump pulse delay, for various buffer gases and pressures. The trace for 100 Torr of CO<sub>2</sub> is dominated by population-grating diffraction; the other CO<sub>2</sub> traces are dominated by thermal-grating diffraction.

This work was supported by the U.S. Department of Energy, Office of Basic Energy Sciences, Division of Chemical Sciences and the Office of Industrial Technologies, Division of Advanced Industrial Concepts. Partial support for PMD was provided by the Air Force Office of Scientific Research, Aerospace Sciences Directorate, and for RLF by the California Institute for Energy Efficiency.

1. For a review of recent diagnostic applications of DFWM, see R. L. Farrow and D. J. Rakestraw, *Science* **257**, 1894-1900 (1992) and references therein.
2. R. P. Lucht, R. L. Farrow, and D. J. Rakestraw, *J. Opt. Soc. Am. B* **10**, 1508 (1993).
3. R. L. Abrams, J. F. Lam, R. C. Lind, D. G. Steel and P. F. Liao, "Phase conjugation and high-resolution spectroscopy by resonant degenerate four-wave mixing," in *Optical Phase Conjugation*, R. A. Fisher, ed. (Academic, New York, 1983) pp. 211-284.
4. T. Dreier and D. J. Rakestraw, *Opt. Lett.* **15**, 72-74 (1990).
5. H. J. Eichler, P. Günter, and D. W. Pohl, *Laser-Induced Dynamic Gratings* (Springer-Verlag, New York, 1986) p. 18.

## Effects of Doppler Broadening and Unequal Pump Intensities in Saturated Degenerate Four-Wave Mixing Spectroscopy

**Robert P. Lucht**, Department of Mechanical and Industrial Engineering, University of Illinois, Urbana, IL 61801. (Phone 217-333-5056)

**Michael S. Brown**, MetroLaser, 18006 Skypark Circle, Suite 1008, Irvine, CA 92714. (Phone 714-553-0688)

**Larry A. Rahn**, Combustion Research Facility, Sandia National Laboratories, Livermore, CA 94450. (Phone 510-294-2091)

**INTRODUCTION:** Degenerate four-wave mixing (DFWM) is a technique that shows great promise for sensitive measurements of transient gas-phase species, and diagnostic applications of DFWM are being pursued actively at laboratories throughout the world. Applications of DFWM as a combustion diagnostic and as a tool for molecular spectroscopy are reviewed in a recent article by Farrow and Rakestraw (1992). However, significant questions remain regarding strategies for quantitative concentration measurements using DFWM.

In this paper we discuss recent results from a theoretical investigation of saturated DFWM. The effects of Doppler broadening on strategies for concentration measurements and the influence of unequal pump intensities on DFWM line shapes are investigated. DFWM signal intensities and line shapes are calculated for a nondegenerate two-level resonance interacting with high intensity pump and/or probe beams. The time- and space-dependent density matrix equations for a two-level system irradiated by two pump beams and a probe beam are given by (Boyd, 1992)

$$\frac{\partial \rho_{11}(z,t)}{\partial t} = -\frac{i}{\hbar} (V_{12}\rho_{21} - \rho_{12}V_{21}) + \Gamma_{21} \rho_{22}, \quad (1)$$

$$\frac{\partial \rho_{21}(z,t)}{\partial t} = -\rho_{21} (i\omega_{21} + \gamma_{21}) - \frac{i}{\hbar} V_{21} (\rho_{11} - \rho_{22}), \quad (2)$$

where the diagonal matrix elements  $\rho_{11}$  and  $\rho_{22}$  are proportional to the populations of level 1 and 2 and the off-diagonal matrix element  $\rho_{21}$  describes the coherence between levels 1 and 2. In Eqns. (1) and (2)  $\hbar$  is Planck's constant,  $\Gamma_{21}$  is the population transfer rate from level 2 to level 1,  $\omega_{21}$  is the resonance frequency, and  $\gamma_{21}$  is the coherence dephasing rate. Assuming that all the laser beams are linearly polarized and the polarizations are parallel, the interaction term  $V_{21}$  is given by

$$V_{21} = -\bar{\mu}_{21} \cdot \vec{E}(z,t) = -\mu_{21} [E_b(z,t) + E_f(z,t) + E_{pr}(z,t)] \quad (3)$$

where  $\bar{\mu}_{21}$  is the electric dipole matrix element,  $\mu_{21}$  is its projection in the direction of the laser polarization,  $E_b(z,t)$  is the backward-propagating pump field,  $E_f(z,t)$  is the forward-propagating pump field, and  $E_{pr}(z,t)$  is the probe field. The electric fields  $E_n(z,t)$  are assumed to be infinite plane waves. Equations (1) and (2) are integrated directly for a two-level system irradiated by

single-mode laser radiation (the amplitudes  $A_n(t)$  are modeled as Gaussian in time with FWHMs of 5 nsec). The density matrix equations are integrated independently at 500-1000 grid points to obtain  $\rho_{21}(z,t)$ . A spatial Fourier transform is then performed on  $\rho_{21}(z,t)$  to obtain the amplitude of the DFWM signal at time  $t$  in the phase-matched direction. Doppler effects are included by solving the equations for numerous closely-spaced velocity groups.

In a recent paper, Lucht et al. (1993) compared the results of these two-level model calculations with measurements of DFWM line shapes and signal intensities for NO in a buffer gas of He over a wide range of He pressure. The calculated line shapes and the pressure dependence of the NO DFWM signal intensity were found to be in excellent agreement with experiment. The major conclusion of this two-level, single-mode laser study was that for pump laser intensities approximately equal to the saturation intensity, the pressure dependence of the DFWM signal is reduced greatly compared to the unsaturated case. For minimal dependence on total collision rate, operation with pump laser intensities approximately equal to twice the saturation intensity is optimal [ $I_{\text{pump}} = 2 I_{\text{sat}}$ ;  $I_{\text{sat}} = (nc \hbar^2 / 8\pi)(\gamma_{21}\Gamma_{21}/\mu_{21}^2)$ ]. All calculations were performed with the probe intensity equal to 1/4 of the pump beam intensity ( $I_{\text{pr}} = 0.25 I_{\text{pump}}$ ), and with equal forward and backward pump intensities ( $I_f = I_b = I_{\text{pump}}$ ); these were the values used experimentally.

**DOPPLER EFFECTS:** For pump laser intensities approximately equal to the saturation intensity, the dependence of the DFWM signal intensity on collisions is minimized. One obvious strategy for quantitative concentration measurements using DFWM would be to operate with the pump laser intensities approximately equal to the saturation intensity. However, signal generation efficiency is still very dependent on the ratio of collisional to Doppler broadening for resonances where the collisional width is comparable to or less than the Doppler width. Although it is often stated that phase-conjugate DFWM is a Doppler-free technique, it is more correctly termed a sub-Doppler technique. As the pressure decreases, the ratio of Doppler to collisional broadening increases and the lasers will couple effectively with a smaller fraction of molecules, leading to a decrease in signal level. When the collisional width is much smaller than the Doppler width, only those molecules with velocities near zero will be able to interact effectively with the pump and probe beams in the phase conjugate geometry.

This is illustrated in Fig. 1, where the calculated DFWM signal intensity is plotted versus the ratio of collisional to Doppler broadening. For the calculations shown, the Doppler width was held constant ( $0.1 \text{ cm}^{-1}$ ) and the collisional width was varied. The laser intensities were adjusted so that pump laser intensities were equal to the collision-rate-dependent saturation intensity [ $I_{\text{sat}} \propto (\Delta\omega_C)^2 \propto \gamma_{21}\Gamma_{21} \propto P^2$ ] for each value of  $\Delta\omega_C$ ; the saturation intensity  $I_{\text{sat}}$  does not depend on the Doppler width. For these excitation conditions, the DFWM signal intensity increases very rapidly as the ratio of collisional to Doppler width increases. For collisional widths larger than the Doppler width, however, the rate of increase of the signal intensity slows substantially, and may approach an asymptotic limiting value for  $\Delta\omega_C \gg \Delta\omega_D$ .

**EFFECTS OF UNEQUAL PUMP INTENSITIES:** Brown et al. (1992) performed high-resolution measurements of non-saturated (low laser intensity) DFWM line shapes for OH in an atmospheric pressure flame. They also performed measurements of line shapes under saturating conditions, and explored the effects of unequal pump intensities, but did not publish the saturated line shapes. A comparison of calculated and experimental line shapes is shown in Fig. 2; the numerical calculations are in excellent agreement with experimental results. The very different line

shapes that occur for the three different cases of pump excitation are predicted well, and in each case the theoretical and measured laser intensities agree to a factor of two or better. This excellent comparison with measured OH line shapes and accurate prediction of the effects of unequal pump intensities is further validation of the DNI technique for modeling the DFWM process.

**FUTURE WORK:** The DNI technique will be used to investigate possible strategies for concentration measurements using DFWM that minimize the dependence of the signal intensity on both Doppler and collisional broadening. Calculations will be performed for picosecond DFWM, and multiple-level models will be investigated.

**ACKNOWLEDGMENTS:** This work was supported by the United States Department of Energy, Office of Basic Energy Sciences, Division of Chemical Sciences.

## REFERENCES

- R. W. Boyd (1992), *Nonlinear Optics*, (Academic Press, Boston), p. 191.  
 M. S. Brown, L. A. Rahn, and T. Dreier (1992), "High-Resolution Degenerate Four-Wave Mixing Spectral Profiles for OH," *Opt. Lett.* **17**, 76-78.  
 R. L. Farrow and D. J. Rakestraw (1992), "Detection of Trace Molecular Species Using Degenerate Four-Wave Mixing," *Science* **257**, 1894-1899.  
 R. P. Lucht, R. L. Farrow, and D. J. Rakestraw (1993), "Saturation Effects in Gas-Phase Degenerate Four-Wave Mixing Spectroscopy," *J. Opt. Soc. Am. B* **10**, 1508-1520.

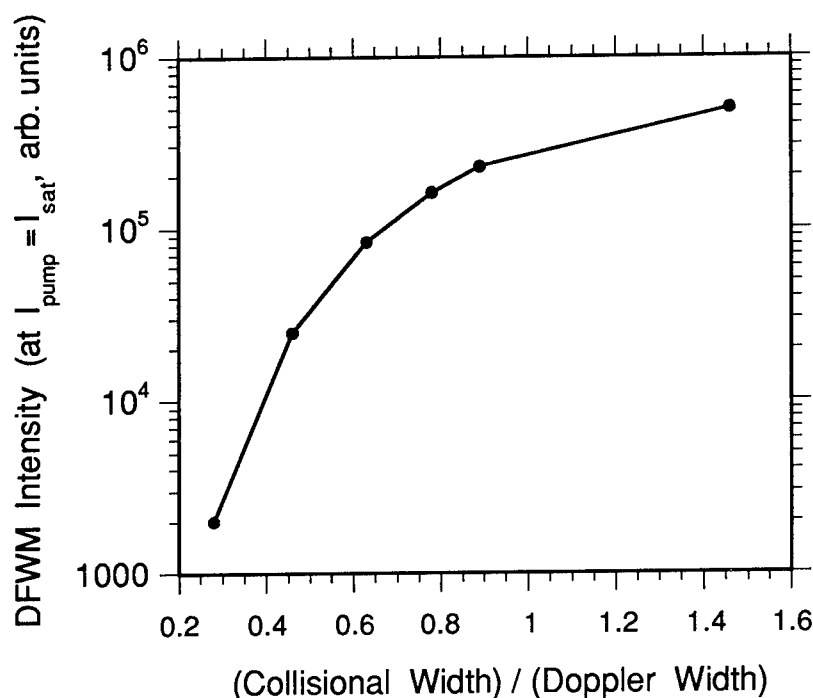


Fig. 1. Dependence of DFWM signal intensity on ratio of collisional to Doppler width.

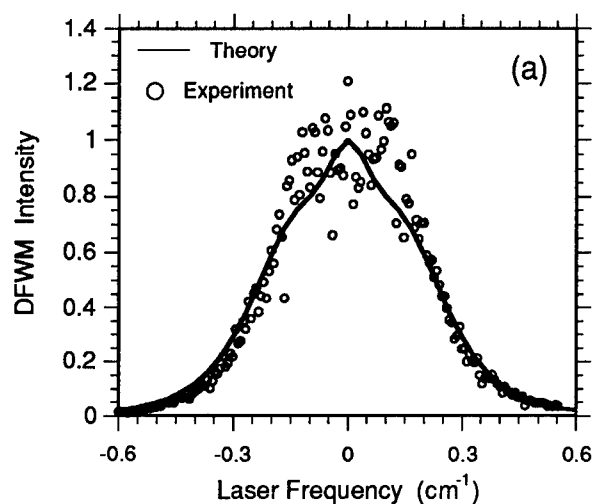
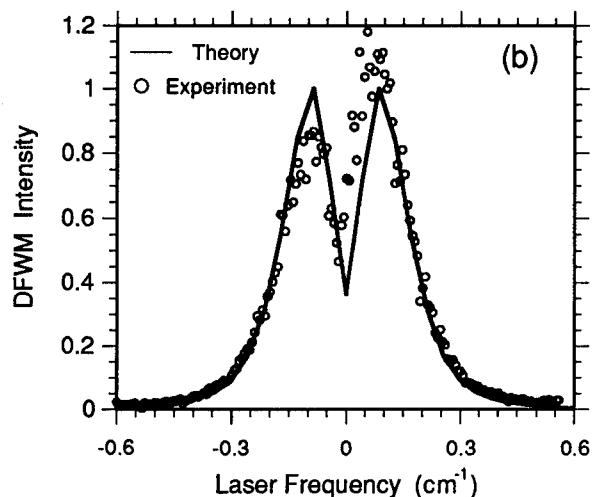


Fig. 2. Comparison of experimentally measured and calculated lineshapes for saturated OH DFWM.

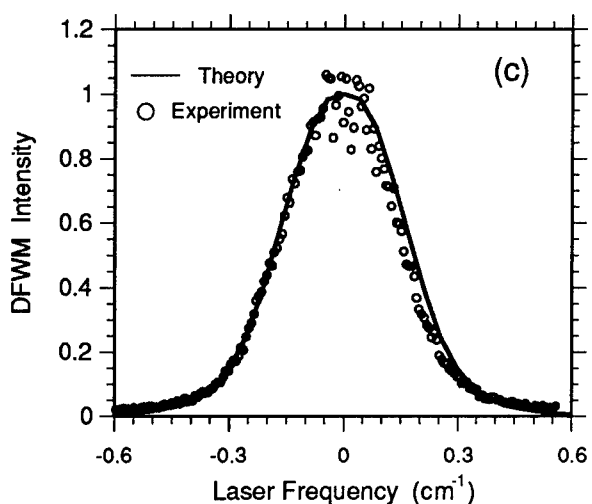
(a) Equal pump intensities:

	Expt	Theor
$I_f / I_{\text{sat}}$	8.3	6.7
$I_b / I_{\text{sat}}$	8.2	6.7
$I_{\text{pr}} / I_{\text{sat}}$	0.2	0.17



(b) Strong backward pump:

	Expt	Theor
$I_f / I_{\text{sat}}$	0.9	0.4
$I_b / I_{\text{sat}}$	11	4.6
$I_{\text{pr}} / I_{\text{sat}}$	0.2	0.08



(c) Strong forward pump:

	Expt	Theor
$I_f / I_{\text{sat}}$	7.6	4.9
$I_b / I_{\text{sat}}$	2.4	1.5
$I_{\text{pr}} / I_{\text{sat}}$	0.09	0.12

## Degenerate Four-Wave Mixing in a Methane/Air Flame Using a Regeneratively Mode-Locked Ti:Sapphire Laser

M.A. Linne

Division of Engineering, Colorado School of Mines  
Golden, CO 80401  
(303) 273-3609

G. J. Fiechtner

Center for Combustion Research, University of Colorado  
Boulder, CO 80309-0427

The potential of resonant Degenerate Four-Wave Mixing (DFWM) for measurements of major and minor species concentrations and temperature in reacting flows has been established by several groups<sup>1</sup>. Spatial resolution has been demonstrated, as has two-dimensional planar imaging. Perhaps most significantly, large signals have been observed at moderately high pressures (1100 Torr)<sup>2</sup>, establishing the potential for measurements inside practical combustion systems. As a result, a good deal of research is currently devoted to understanding the fundamental physical aspects of the technique.

Degenerate Four-Wave Mixing is a third order nonlinear optical process. Three beams at the same wavelength (and typically from the same laser) are overlapped in space, according to phase matching constraints, and a fourth signal beam is produced. The nonlinear polarization of the medium is expressed in terms of a third order susceptibility  $[X^{(3)}]$  together with the vector interactions of the 3 input waves <sup>3</sup>  $E_1$ ,  $E_2$ , &  $E_p$  :

$$P_{NL} = 1/2 \{ A (E_1 \cdot E_p^*) E_2 + B (E_2 \cdot E_p^*) E_1 + C (E_1 \cdot E_2) E_p^* \} + c.c. \quad (1).$$

The three input beams are labeled "pump beam 1", "pump beam 2", and the "probe beam". The coefficients A, B and C are related to tensor components of the susceptibility  $X^{(3)}$ .  $E_p^*$  is the complex conjugate of  $E_p$ . The nonlinear polarization represented in equation (1) is then used as a source term in the wave equation. Phase matching between the four wave vectors in the form :  $k_1 + k_2 = k_p + k_c$  { $k_c$  = the signal (conjugate) wave vector} is required in order to couple the nonlinear polarization into the electric fields. A portion of the first term in equation (1),  $A (E_1 \cdot E_p^*)$ , describes a spatial interference pattern which is imprinted upon the medium via the susceptibility-related term "A". It could be due, for example, to the Kerr effect, or to absorption (resonant DFWM). The imprinted interference pattern is thus a standing, sinusoidal material grating. The remaining portion of the first term in equation (1),  $E_2$ , then represents scattering of pump beam 2 from the grating. The second term in equation (1) is similar to the first, and the third term does not contribute to resonant, single-photon DFWM.

There is a strong resonant enhancement of the DFWM signal when the laser is tuned to an atomic or molecular absorption. For the case of broadband excitation (as we have used in this work), the laser creates both a population (amplitude) grating at line center, and a dispersive (phase) grating in the wings of the line. Farrow et al<sup>4</sup> have extended the Abrams and Lind<sup>5</sup> perturbative, steady-state, two-level model to the case for low intensities (relative to the saturation intensity) and for broadband excitation (integrated over the absorption profile). Their result predicts that resonant DFWM signals, for the assumptions involved, will be proportional



to number density squared. If we assume that the three input beams are of equal intensity, then the signal should scale with intensity cubed.

Recent studies in cells at various pressures and with various collision partners, using pulsed lasers (nanosecond widths), have shown that line broadening arguments can not always account for the observed collisional effects on DFWM signals<sup>6,7</sup>. It is generally agreed that  $X^{(3)}$  wave mixing does occur, but energy can be transferred by collisional processes from population fringes into both temperature and pressure waves, giving rise to a strong thermal (phase) grating<sup>8</sup>. Signal interference from a thermal grating can make it very difficult to relate signal levels to number density. Detailed measurements, therefore, require the elimination of thermal grating interferences when they do occur. It has been known for some time that thermal gratings can be avoided by pumping with crossed polarization<sup>9,10</sup>. Rakestraw<sup>10</sup> has also pointed out that thermal gratings can be avoided by using picosecond pulses. Gasdynamic effects in flames of interest occur over several hundred picoseconds, so a measurement at about 50 ps or less would not be subject to thermal grating interferences. This is one of several reasons for doing DFWM the picosecond regime.

Our experimental layout is depicted in Fig. 1. The burner was a Perkin-Elmer aspirating unit fitted with a Meeker type burner head, operated near stoichiometric fuel/air ratios in this case. Various solutions of KCl in water were aspirated into the flow in order to provide controlled, reproducible levels of atomic potassium in the flame.

We used a Spectra-Physics regeneratively mode locked Ti:Sapphire laser, equipped with a 2 ps Gires-Tournois interferometer<sup>11</sup>. This laser produced about 900 mW of output when pumped with 7 W from an Ar:Ion laser, with autocorrelation pulse-widths around 1.4 ps (assuming a  $\text{sech}^2$  pulse shape). The transform limited bandwidth is about 0.5 nm. The laser was tuned to the  $4^2S_{1/2} - 4^2P_{1/2}^o$  transition in atomic potassium at 769.9 nm.

Referring to figure 1a, about 450 mW arrived at the DFWM setup. The two beam splitters transmit 70% and reflect 30% of the laser intensity. Adjustable delay lines were inserted into all three beams by retro-reflection from roof prisms mounted on translation stages. Roof prism rp2 offset the beam downward, and mirror m2 was stationed below the probe beam. Pump beam number 2 was considered the reference beam for alignment. It was mechanically chopped at about 1 kHz and it was fitted with a set of roof prisms capable of up to 530 ps delay. We collimated and aligned all three beams in the far-field using drilled masks, and then directed them through a lens to the flame position. Temporal alignment was verified by simultaneous, static autocorrelation in KDP at the lens focus. The lens has a 7.5 cm focal length and gives a measured  $1/e^2$  focal diameter of 116  $\mu\text{m}$ . Focusing offers several advantages: the three beams are immediately overlapped in the same location, giving excellent spatial resolution in the transverse direction, it makes the pulse autocorrelation scheme simple to perform, and the intensities at the spot are then near the saturation intensity<sup>5</sup>.

Power levels in the three beams at the focal spot were  $P(1) = 40$  mW,  $P(2) = 39$  mW, and  $P(P) = 60$  mW. This gave an estimated ratio at line center around  $I / I_{\text{sat}} \approx 3 - 4$ . This is not an accurate representation of saturation in this experiment, however, because the laser bandwidth spans the entire line. Saturation in the wings of the line is more difficult to achieve<sup>12</sup>.

The all-forward geometry we used is similar to BOXCARS (Fig. 1b). The DFWM phase matching condition dictates that the signal scattered by pump beam 2 off of a grating formed by pump beam 1 and the probe beam should exit at the fourth corner of the box. We used a confocal arrangement with a second, matched lens. The array of beams could thus be re-collimated

through the drilled masks and the signal beam can be roughly located in space. We filtered spurious scatter using an array of apertures. The signal was detected with a photomultiplier tube (PMT), and the PMT output was directed to a lock-in amplifier. We simultaneously monitored fluorescence at 90 degrees to the beam overlap region.

This DFWM arrangement gave maximum signal levels around 140 mV with background scatter levels of 1 - 2 mV. In comparison, our fluorescence signal levels were around 100  $\mu$ V with a 30  $\mu$ V background.

Initial saturation results indicate that a best-fit to the data gives a power law dependence of  $I_{\text{signal}} \propto I^3$ , consistent with expectations. We did not reach full saturation, likely because of laser bandwidth. Solutions of varying KCl concentration were used to acquire sensitivity curves. An absorption measurement using a tungsten filament lamp was then performed to calibrate the data. The same KCl solutions were used, and the flow rates of fuel, air and solution were carefully matched between the DFWM experiment and the calibration. A curve fit to the data does not produce a quadratic signal dependence on concentration, as one would expect. This is most likely due to beam absorption at higher concentrations<sup>13,14</sup>. If the high number density data are ignored, the remaining low concentration data fit a quadratic well. An important conclusion is that the measurement offers good sensitivity, limited primarily by the interference of laser scatter.

Finally, we mounted a small audio loud speaker on the fuel / air line, and we drove it at 50 Hz with a frequency synthesizer. This induced a known disturbance in an otherwise laminar flame. The output of the lock-in amplifier was directed to a PC based A/D system with an FFT board. The FFT's generated (see Fig. 2) clearly show the 50 Hz modulation. This simple experiment demonstrates the utility of an effectively cw based system for detection of turbulence statistics. The noise level represents A/D noise caused by low signal levels. A high quality instrumentation amplifier would improve the signal/noise ratio considerably.

#### References:

1. R.L. Farrow & D.J. Rakestraw, *Science*, **257**, (9/25, 1992).
2. R.L. Vander Wal, R.L. Farrow & D.J. Rakestraw, 24th Symposium (International) on Combustion / the Combustion Institute, Pittsburgh, PA, (1992).
3. D.M. Pepper & A. Yariv, in Optical Phase Conjugation, R.A. Fisher, Ed., Academic Press Inc., San Diego, (1983).
4. R.L. Farrow, D.J. Rakestraw & T. Drier, *J. Opt. Soc. Am. B*, **9**, No. 10, (1992).
5. R.L. Abrams, J.F. Lam, R.C. Lind, D.G. Steel & P.F. Liao, in Optical Phase Conjugation, R.A. Fisher, Ed., Academic Press Inc., San Diego, (1983).
6. R.L. Vander Wal, B.E. Holmes, J.B. Jeffries, P.M. Danehy, R.L. Farrow & D.J. Rakestraw, *Chem. Phys. Lett.*, **191**, (1992).
7. P.M. Danehy, E.J. Friedman-Hill, R.P. Lucht & R.L. Farrow, sub. to *Appl. Phys. B*, (1993).
8. P.H. Paul, private communication.
9. R. Trebino, C.E. Barker & A.E. Siegman, *IEEE J. Q.E.*, **QE-22**, No. 8, (1986).
10. D.J. Rakestraw, L.R. Thorne & T. Drier, 23rd Symposium (International) on Combustion / the Combustion Institute, Pittsburgh, PA, (1990).
11. J.D. Kafka, M.L. Watts & J.-W. J. Pieterse, *IEEE J. Q. E.*, **QE-28**, No. 10, (1992).
12. S. Williams, D.S. Green, S. Sethuraman & R.N. Zare, *J. Am. Chem. Soc.*, **114**, (1992).
13. P. Ewart, P. Snowden & I Magnusson, *Opt. Lett.*, **14**, No. 11, (1989).
14. B.A. Mann, S.V. O'Leary, A.G. Astill & D.A. Greenhalgh, *Appl. Phys. B*, **54**, (1992).

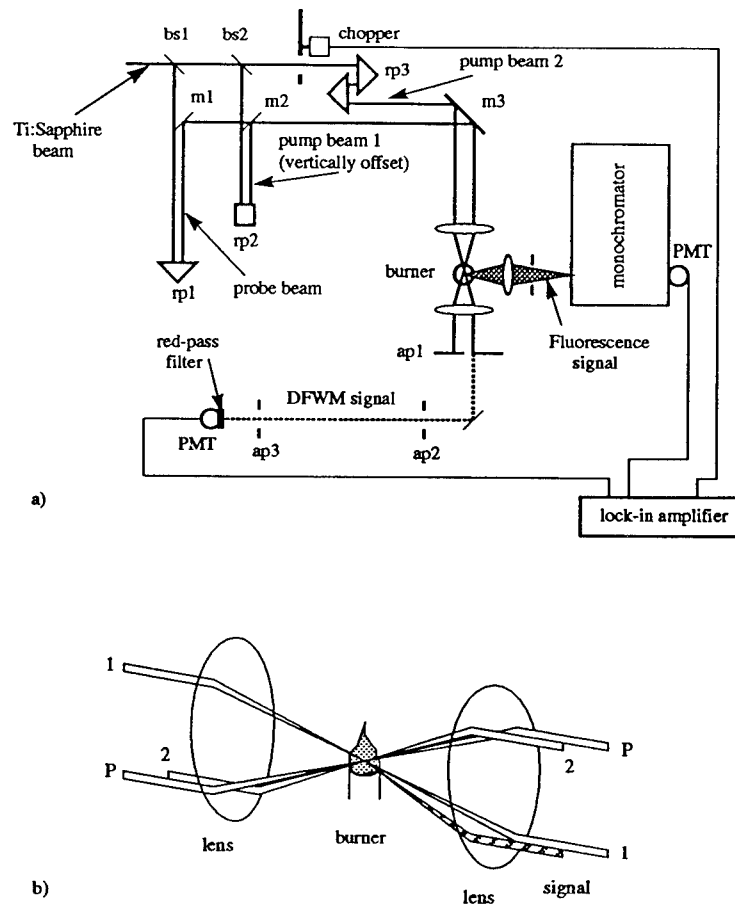


Figure 1. DFWM layout.

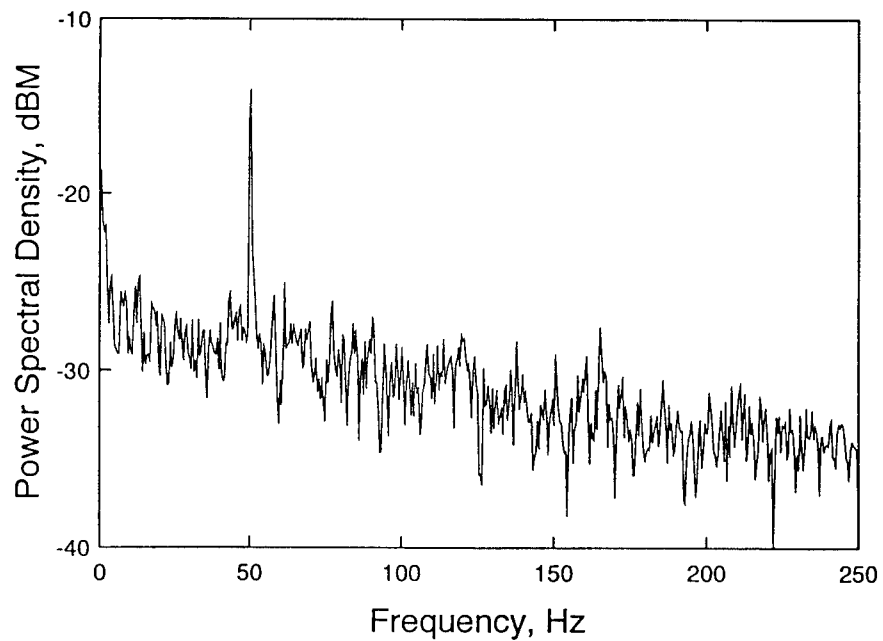


Figure 2. Frequency spectrum of 50 Hz modulated flame.

## A 30 Hz CARS System for Concentration and Temperature Measurements in Supersonic, Turbulent, H<sub>2</sub>/Air Combustion

M. W. Smith [NASA LaRC, MS 170, Hampton VA, USA (804) 864-6261], A. D. Cutler [George Washington U.], M.W. Millard [Metro-Laser], G. B. Northam [NASA LaRC]

### Introduction

CARS has become perhaps the most common non-intrusive laser diagnostic technique used for the analysis of reacting gas flows.<sup>1-4</sup> This paper describes the design and calibration of a dual broadband CARS system assembled to measure single-point, single-shot, temperature and species concentration in a simulated hydrogen-fueled scramjet (Supersonic Combustion RamJET) engine model. No scramjet data are included in this paper. However, the optical system design features driven by the scramjet engine test environment are discussed. During calibration, temperatures and relative concentrations of N<sub>2</sub> were derived by fitting single-shot CARS spectra acquired at 30 Hz. This optical system was derived in part from a previous 10 Hz system designed for thermometry only.<sup>5</sup> Since N<sub>2</sub> concentrations were found by spectral fitting, they were not subject to problems of beam steering, or beam attenuation. These problems, common in situations with high turbulence levels and windows, interfere with concentration measurement strategies that depend on acquiring absolute CARS signal intensities. In fuel-rich conditions, single-shot temperatures were also found independently by fitting H<sub>2</sub> CARS spectra.

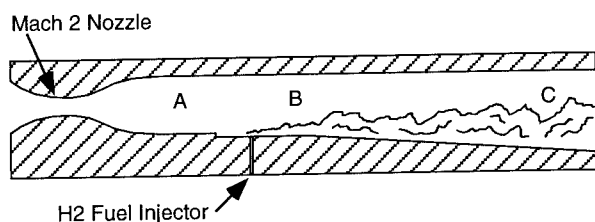


Figure 1

Flow conditions vary along the internal path of a scramjet duct. Figure 1 is a schematic of a test rig. At a typical operating point, H<sub>2</sub>-combustion-heated air flows into the duct at Mach 2,  $T_{\text{static}}=800$  K, and  $P_{\text{static}}=1$  atm. (station A). As a by-product of combustion heating, this "air" contains as much as 35 percent water vapor. In the fuel injection zone (B) the pressure rises to as much as 3 atm. and the temperature rises to as much as 2400 K due to heat addition. This flow is highly turbulent with temperature fluctuations of 1000 K as well as high fluctuations of H<sub>2</sub>, O<sub>2</sub>, and H<sub>2</sub>O species fraction. Downstream (C), the temperature and turbulence levels remain high as the fuel jet mixes and continues to burn, depleting O<sub>2</sub> and producing H<sub>2</sub>O. The pressure drops to about 0.25 atm. at the end of the expansion duct.

Broadband CARS allows the acquisition of a complete spectrum in each laser shot. Single-shot spectra would be required for the scramjet flow because of the fluctuations of fluid properties due to turbulence. Histograms, as well as mean values of temperature and relative concentration of the resonant species (N<sub>2</sub> or H<sub>2</sub>), could be found by fitting these spectra.

Since the anticipated facility run time was only about 10 seconds, the highest possible data rate was desired. On the basis of the fastest available YAG laser and camera, 30 Hz was chosen.

### Hardware

A Spectra-Physics GCR-4 frequency-doubled YAG (30 Hz, 400 mJ/pulse @532 nm, 1 cm<sup>-1</sup>) was used as the pump laser. It was mounted, inverted, to the bottom of a 4'x8' Super Invar optical table. The dye lasers and pitch/catch optics were mounted on the table top. Because the test facility was not climate-controlled, this thermally stable structure was required to maintain precise spatial overlap of the CARS beams. The table structure was mounted via 3-point suspension to a frame designed to attach it to a 1-axis traverse system in the facility. The pitch/catch optics on the table top were mounted on a 2-axis translation system, thus system allowing the positioning of the measurement volume in all three dimensions.

Axially-pumped home-built broadband dye lasers were employed for both species. Rhodamine 640 dye in methanol was used for the N<sub>2</sub> laser and a 1:1 mixture of LDS-698 and DCM in DMSO was used for the H<sub>2</sub> laser.

Planar BOXCARS<sup>6</sup> was used since optical access to the scramjet duct could then be reduced to a slit. Parallel beam polarizations maintained spectral sensitivity to species concentration. Air-purged, recessed windows were employed to make the duct airtight. With planar BOXCARS, a multi-pass dichroic cell<sup>7</sup> was needed to split the signal beam from the residual pump prior to coupling it to a 50  $\mu$ m multi-mode fiber optic cable. The fiber was used to deliver the signal to the remotely located 1 m spectrometer which was fitted with a Peltier-cooled single-intensified photodiode array (P-46 phosphor). A dynamic-ranging splitter<sup>8</sup> was inserted in front of the camera to avoid clipping of spectra at low temperatures.

Spectra were acquired using a PARC model 1461 controller and downloaded after each run to a DECStation 5000 UNIX workstation for processing. Two Mbytes of onboard controller memory allowed 33 seconds worth of data (1000 shots) to be acquired before downloading was necessary.

### Data Processing

A unique feature of this CARS system was its capability to measure the relative concentration of N<sub>2</sub> from single-shot spectra over a wide range of temperature and N<sub>2</sub> mole fraction. Temperature sensitivity in the CARS N<sub>2</sub> Q branch is derived from a dramatic increase in width of the "fundamental band" with temperature up to about 1000K and the rise of the "hot band" at higher temperatures. Relative concentration sensitivity, on the other hand, relies on a much smaller shift in intensity, on the "pedestal" that arises along the wings of the spectrum when the contributions of the non-resonant susceptibility of the buffer gas ( $\chi_{\text{nr,buf}}$ ) become discernible. This effect is more noticeable at flame temperatures, where the buffer gas

fraction is high, and  $\chi_{nr,buf}$  is high due to the presence of  $H_2O$ . In ambient air, conversely, this pedestal is very small, producing only 10 or 20 digitization counts in 10,000. The current work shows, however, that with careful experimental technique, this sensitivity can be exploited even near STP.

Several system/procedural modifications were required to produce spectra that could be fit for concentration:

1. "Background" files had to be taken immediately after each run. Normally a 100 shot background file (dye laser off) was taken immediately after a 100 shot data file. These frequent background files were required because the base level of the photo-diode array wandered up and down in a 10 or 20 count range over a several minute period, presumably as the Peltier cooler activated/deactivated in response to its thermostat. It was also discovered that at least 90 minutes of cool-down time was required before the detector became stable in this 10-20 count range.

2. The dynamic range splitter had to be relocated in the optical train. Previously, the splitter was located before the spectrometer input slit, thus providing two images of a spectrum at the output plane where the camera was located. However, nothing prevented the tail of the right channel spectrum from superimposing on the left channel spectrum, or vice-versa. Although not noticeable in  $N_2$  thermometry, this effect mimicked the "pedestal" from which concentration sensitivity is derived. So the splitter was moved from the front of the spectrometer to the front of the camera so an image mask could be added at the spectrometer output plane to clip the offending "tails" of the spectra prior to splitting. A doublet relay lens was then required between the mask and the splitter/camera assembly to re-image the spectra. This arrangement eliminated the cross talk between channels.

3. Image persistence caused by the P-20 phosphor in the original camera was so severe at 30 Hz, that even thermometry fitting was adversely effected<sup>9</sup>. Concentration fitting would have been impossible. A P-46 rare earth phosphor was substituted, and although it greatly reduced the influence of image persistence, it did not eliminate it. Therefore, the detector was scanned at 90 Hz for an acquisition rate of 30 Hz. For each laser shot there were three scans, a clearing scan that was not stored, a "pre-scan" that was stored, and a data scan that was also stored. The decay characteristics of the phosphor were analyzed and it was found that the latent image decayed nearly uniformly by a factor of 0.6 from the time of the pre-scan to the time of the data scan. Thus 0.6 times each pre-scan was subtracted from each data frame to remove the effect of persistence.

4. Accurate dye laser gain curves were also required. After each calibration run, the measurement volume was bathed in freon and the resulting CARS spectra (corresponding to dye laser gain curves mapped to the anti-Stokes) were recorded on the same detector used for the  $N_2$  spectra. A 100 shot average gain curve was used to normalize the  $N_2$  CARS spectra, accounting for the non-uniform pumping by the dye laser in frequency space, as well as normalizing any non-uniformities introduced by the spectrometer, imaging system, or detector.

## Calibration Data Analysis and Reduction

A flat-flame porous-plug burner was used to calibrate the CARS system. CARS temperature and concentration measurements were made in a 1 atm.  $H_2$ /air flame from  $\Phi=0.2$  to  $\Phi=6$ , ( $\Phi$ =fuel/air equivalence ratio). Calibration data were also taken in room temperature air and in air heated by an electric furnace.

The calibration process involved calculating the temperature and concentration in the measurement volume and comparing it to the temperature and concentration derived by selecting the "best fit" of an experimental CARS spectrum to a library of theoretical CARS spectra. In the case of a perfect/complete model for generating theoretical CARS spectra, this would actually be a "validation" rather than a "calibration" process. There would be no parameters to vary. For  $N_2$  and  $H_2$  temperature, this was the case, but for  $N_2$  concentration, values of  $\chi_{nr}$  for the buffer gas constituents had to be adjusted (within the limits of published values) to get the best fits over the burner operating range.

The flowrates of air and  $H_2$  through the burner, and the heat loss to the burner cooling water were measured, then the measurement volume temperature and gas fractions were calculated using an equilibrium chemistry code.<sup>10</sup> For the furnace data the temperature was measured with a thermocouple; gas fractions were 0.78  $N_2$  and 0.21  $O_2$  since ambient air was used.

Theoretical spectra were generated using the CARSFT code from Sandia<sup>11</sup>. For  $H_2$ , a 1-D library of spectra was generated over temperature in 50 K increments, each element being the product of a CARSFT run. A 2-D library was generated for  $N_2$ ; one dimension was temperature as before, the second dimension the mole fraction of  $N_2$ .

A special curve-fitter/comparator routine was written to find the best library entry for each experimental spectrum. Originally the fitter took the square root of the data spectrum ( $\chi$  rather than  $\chi^2$ ) and searched the library for the area-normalized entry with the minimum square error. Although fitting  $\chi$  rather than  $\chi^2$  produced better concentration fits, it was discovered that at low signal-to-noise, taking the square root of the data produced a bias in the concentration fits. Pedestal had been inadvertently introduced on the wings of each spectrum by taking the square root of a noisy signal. A two-pass fitter was therefore developed that first found the best fit to intensity ( $\chi^2$ ), then used this smooth theoretical spectrum as a weighting function to a second pass fit. Thus  $\chi$  could effectively be fit without taking the square root of the data spectrum.

The probe function (a.k.a. optical transfer function, instrument function, "slit" function) required to generate broadband spectra in CARSFT was measured by imaging a line from a Xenon lamp through the fiber optic/spectrometer/camera system. The shape of the transfer function was dominated by the finite spot size delivered by the fiber optic and by the broad wings introduced by the camera intensifier. Both temperature and concentration accuracy were very sensitive to errors in the shape of this transfer function.

Figure 2 shows the flat-flame burner temperatures derived from  $N_2$  CARS and  $H_2$  CARS measurements compared to the temperatures derived from the burner gas flowrates. Each point represents the average of 100 spectral fits (not a fit of an aver-

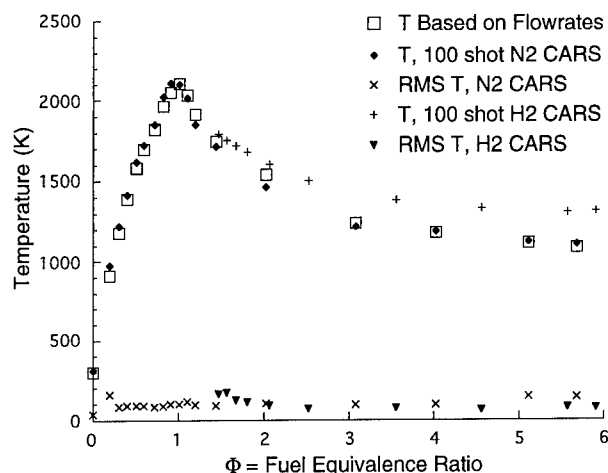


Figure 2

aged spectrum). The rms temperature values are also shown. Fluctuations in the CARS fits were almost completely due to dye laser spectral noise which varied shot-to-shot. Note the rms  $N_2$  CARS temperatures are approximately 100 K over the entire  $\Phi$  range. Above  $\Phi=2$ , where the  $H_2$  CARS was no longer affected by shot noise, the  $H_2$  fits show a lower rms temperature (about 70 K). Under the assumption that the burner flame temperature was constant, these rms values represent the CARS temperature random errors. An unresolved systematic disagreement of about 120 K between the  $H_2$  and  $N_2$  temperatures appears above  $\Phi=2.5$ . It was impossible to take simultaneous  $H_2$  and  $N_2$  spectra since only one imaging system was available, thus this systematic error may have been due to differing burner conditions between the  $N_2$  and  $H_2$  runs.

Ideally,  $N_2$  mole fraction ( $X_{N_2}$ ) would be derived from a CARS spectrum by finding a best fit theoretical spectrum. The theoretical spectrum would be found by floating the appropriate parameters—in this case, temperature, and the mole fractions  $X_{N_2}$ ,  $X_{O_2}$ ,  $X_{H_2}$ , and  $X_{H_2O}$ . This is an ill-posed problem, however, since for a given spectral shape, there is not a

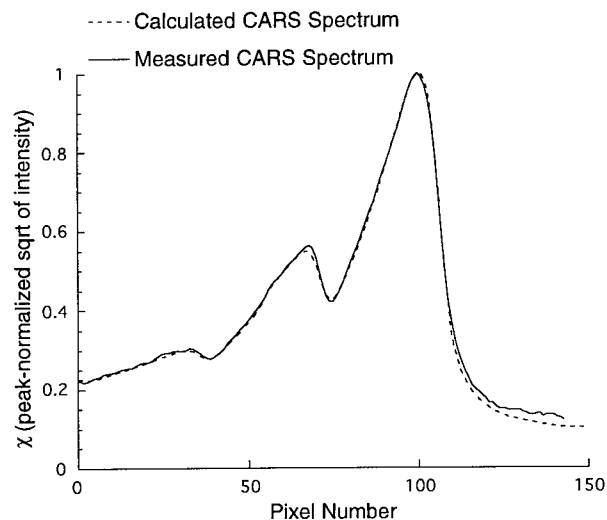


Figure 3

corresponding unique combination of mole fractions. Thus a 2-D library of theoretical CARS spectra was generated to use as a standard for quantitative comparisons. One library dimension was temperature, the other was relative concentration, arbitrarily defined as the mole fraction of  $N_2$  in a binary mixture of  $N_2$  and buffer gas (where  $\chi_{nr,buf}$  was a constant  $8.5 \times 10^{-18} \text{ (cm}^3/\text{erg)}/\text{amagat}$ ). The  $N_2$  CARS relative concentrations were found by comparing experimental CARS spectra to the 2-D library; calculated relative concentrations were found by comparing theoretical spectra to the same library. For the flat-flame burner, CARSFT was used to generate a "correct" theoretical spectrum at each  $\Phi$  by entering the known values for  $X_{N_2}$ ,  $X_{O_2}$ ,  $X_{H_2}$ , and  $X_{H_2O}$ . The corresponding best  $\chi_{nr}$  values were found by trial and error ( $N_2=8.5$ ,  $O_2=11.4$ ,  $H_2O=18.5$ ,  $H_2=8.5$  were used).<sup>12,13</sup> A theoretical  $N_2$  Q-branch spectrum calculated for  $\Phi=1$  with the known  $X$ 's and best  $\chi$ 's is compared to its corresponding experimental spectrum (100 shot average) in fig. 3.

This concentration comparison procedure assumes that a good fit can be made between the theoretical spectrum generated with the correct buffer gas  $X$ 's and  $\chi$ 's and an entry in the theoretical library generated with arbitrary buffer gas properties. In fig. 4, spectrum E ("correct" spectrum with 65%  $N_2$ , 34%  $H_2O$ ) and spectrum D (library entry with 37%  $N_2$ , 63% buffer gas) are superimposed to demonstrate that this assumption is good for the  $\Phi=1$  (2100 K) case. Similar fit quality was found over the full  $\Phi$  range.

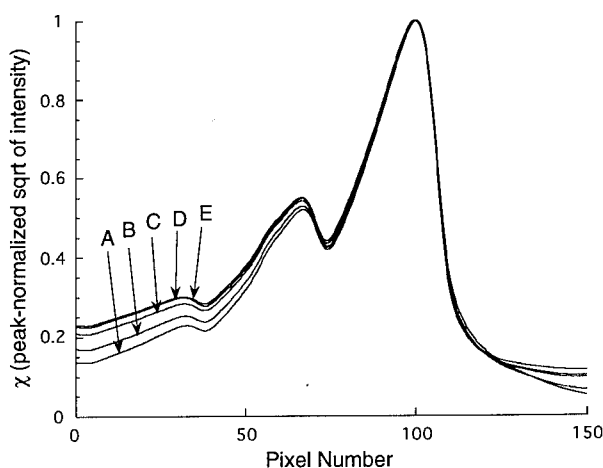


Figure 4

Spectra A, B, and C in fig. 4 are included to demonstrate the effects of buffer gas composition on the pedestal from which the relative concentration sensitivity is derived. Spectrum A was calculated for 2100 K, 100%  $N_2$ , and shows the effect of ignoring the presence of the buffer gas. Ignoring the buffer gas (using a 1-D library over temperature) produced a 200 K error in fitted temperature at 2100 K, as the fitter sought to replace concentration "pedestal" with "hot-band" to get the best fit. Spectrum B was calculated for 2100 K, 65%  $N_2$ ,  $\chi_{nr,buf}=8.5$ , and demonstrates the effect of using the wrong  $\chi_{nr,buf}$ . Spectrum C was calculated for 2100 K, 65%  $N_2$ ,  $\chi_{nr,buf}=18.5$ , which includes the correct  $\chi_{nr,buf}$  for water which is the primary buffer

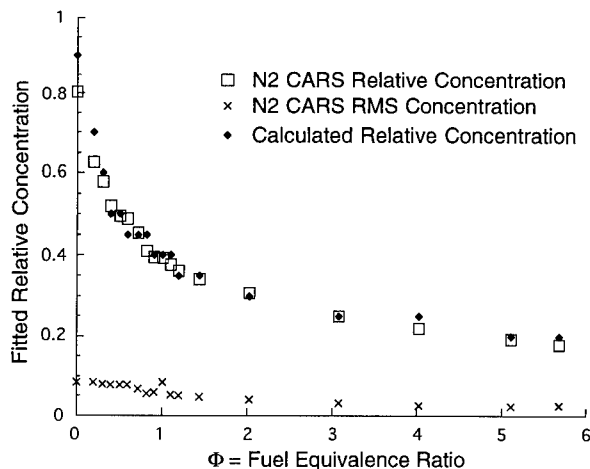


Figure 5

gas, but neglects the effect of foreign gas broadening by water on the  $N_2$  spectrum. A foreign gas broadening model for  $H_2O$  on  $N_2$  was included in the "exponential gap" lineshape model that was used in CARSFT. The minimal j-level dependence of this foreign gas broadening is the reason that spectra D (63% buffer gas, no  $H_2O$ ) and E (34%  $H_2O$ ) are so similar.

In fig. 5, the  $N_2$  CARS experimental relative concentrations are compared to the calculated relative concentrations over the burner  $\Phi$  range. The rms values for the 100 shot CARS data are also shown. Note that the rms concentration increases as  $\Phi$  decreases (as  $N_2$  fraction increases). When the resonant species fraction is high, the concentration sensitivity of the CARS signal is small, thus the high rms values indicate an increased influence of shot-to-shot dye laser noise.

In a scramjet, the buffer gas fraction and composition would be unknown, thus quantitative  $N_2$  mole fraction measurements would not be possible. However, quantitative code-validation comparisons could be made by using CARSFT to generate spectra for each point in a computed flow-field solution and making relative concentration comparisons as was done in fig. 5 for the calibration data. Water production is a key indicator

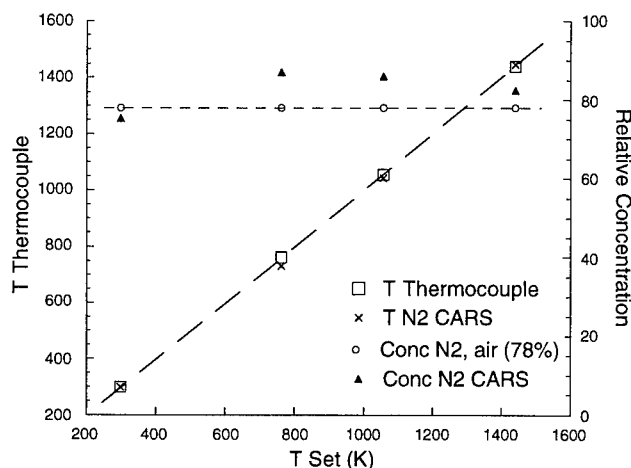


Figure 6

of performance in a scramjet, thus it is advantageous that this concentration comparison approach is most sensitive to  $H_2O$  fraction. This high sensitivity is due both to the high  $\chi_{nr}$  for  $H_2O$  and the simultaneous foreign gas broadening of the  $N_2$  spectrum in the presence of  $H_2O$  (see fig. 4).

CARS data taken in air in an electrically heated furnace were also fit using the same 2-D library. The results shown in fig. 6, demonstrate the proper temperature and relative concentration sensitivities for dry air at temperatures up to 1400 K. Note that the concentration remains nearly constant at 80% (the library was in increments of 10%) over the full temperature range. The furnace calibration confirms the accuracy of the system at conditions outside of the flat-flame burner operating envelope.

Finally, it should be reiterated that all calibrations described above were for 1 atm. For the measurements in the scramjet pressure to be encountered, since the concentration pedestal is strongly influenced by pressure (at 2100 K the height of the wing changes about a factor of 2 moving from 1 to 3 atm.). Facility wall pressures would be used in practice.

## References

1. B. Attal-Tretout, P. Bouchardy, P. Magre, M. Pealat, and J.P. Taran, "CARS in Combustion: Prospects and Problems," *Applied Physics B* 51, 17-24, 1990.
2. S. Fujii and M. Gomi, "Fast Temperature Determination by Nitrogen Coherent Anti-Stokes Raman Spectroscopy," *AIAA Journal*, Vol. 26, No. 3, March 1988.
3. T. J. Anderson and A. C. Eckbreth, "Simultaneous Measurements of Temperature and  $H_2$ ,  $H_2O$  Concentrations in Hydrogen-Fueled Supersonic Combustion," *AIAA 28th Aerospace Sciences Meeting*, Reno, NV, 1990.
4. F. Y. Yueh and E. J. Beiting, "Simultaneous  $N_2$ ,  $CO_2$ , and  $H_2$  Multiplex CARS Measurements in Combustion Environments Using a Single Dye Laser," *Applied Optics*, Vol. 27, No 15, August 1988.
5. M. W. Smith, O. Jarrett Jr., R. R. Antcliff, G. B. Northam, A. D. Cutler, D. J. Taylor, "Coherent Anti-Stokes Raman Spectroscopy Temperature Measurements in a Hydrogen-Fueled Supersonic Combustor," *AIAA Journal of Propulsion and Power*, Vol. 9, No 2, March-April 1993, p 163-168.
6. A. C. Eckbreth, *Laser Diagnostics for Combustion and Species*, Abacus Press, 1988.
7. S. Fujii, M. Gomi, Y. Jin, "Instantaneous CARS Thermometry in Turbulent Flames," *Comb. and Flame*, 48: 232-240, 1980.
8. A. C. Eckbreth, "Optical Splitter for Dynamic Range Enhancement of Optical Multichannel Detectors," *Applied Optics*, Vol. 22, No. 14, July 1983.
9. D. R. Snelling, G. J. Smallwood, and T. Parameswaran, "Effect of Detector Nonlinearity and Image Persistence on CARS Derived Temperatures," *Applied Optics* Vol 26, No.1, Jan. 1987.
10. S. Gordon and B. J. McBride, "Computer Program for Calculation of Complex Chemical Equilibrium Compositions, Rocket, Performance, Incident and Reflected Shocks, and Chapman-Jouget Detonations," NASA SP-273, 1971.
11. R. E. Palmer, "The CARSFT Computer Code for Calculating Coherent Anti-Stokes Raman Spectra: User and Programmer Information," Sandia Report, SAND89-8206-UC-13.
12. L. Farrow, R. P. Lucht, and L. A. Rahn, "Measurements of the Non-resonant Third-Order Susceptibilities of Gases Using Coherent Anti-Stokes Raman Spectroscopy," *JOSA B*, Vol. 4, No.8, 1987.
13. Lundeen, S.Y. Hou, J. W. Nibler, "Nonresonant Third Order Susceptibilities for Various Gases," *J. Chem. Phys.* 79 (12), 1983.









Ambrose, W. Patrick — ThC3  
Anderson, J. E. — ThB3

Barnes, Michael D. — ThD1  
Barshick, C. M. — WB3  
Beeson, Michelle D. — ThA5  
Bermudez, German — TuB4  
Bischel, William K. — TuA1  
Bisson, Scott E. — WC2  
Blanchard, G. J. — WA4  
Bohn, P. W. — WA4  
Bomse, David S. — WB1  
Bondarenko, D. B. — WD2  
Bronk, B. V. — ThC4  
Brown, Michael S. — FA3, FB2  
Brum, Jeffrey L. — FA4  
Bublitz, J. — ThB4  
Budni, P. A. — TuA2

Carson, P. G. — ThA2  
Castro, Alonso — ThD3  
Chaturvedi, S. K. — TuB9  
Chen, Yud-Ren — WD10  
Cheo, P. K. — WD3  
Chicklis, E. P. — TuA2  
Chien, Ring-Ling — TuB11  
Chin, R. P. — TuA3  
Chou, Nee-Yin — WD10  
Christiansen, David E. — TuB6  
Chuang, T. J. — TuA3  
Chung, S. H. — WD6  
Cisper, M. E. — WD9  
Cool, Terrill A. — FA1  
Cutler, A. D. — FB4

Dale, J. M. — ThA3  
Danehy, Paul M. — WD4, FB1  
Daniel, Robert G. — FA2  
Davis, E. James — ThA4  
Davis, Lloyd M. — ThD2  
Dearden, David V. — FA4  
Deka, C. — WD11  
Dharamsi, A. N. — TuB9  
Dickenhausen, M. — ThB4  
Dolotov, S. M. — WD2  
Drummond, James R. — WB2  
Duncan, M. D. — WA3  
Dunn, Robert C. — ThD4

Eckbreth, Alan C. — WA  
Edmondson, Ricky — ThB1  
Eiden, G. C. — WD9, ThB3

Farrow, Roger L. — WD4, FB1  
Fiechtner, G. J. — FB3  
Fister, Julius C. — WA5  
Fried, Alan — WB2  
Friedman-Hill, Ernest J. — WD4, FB1  
Frost, A. E. — WA3

Garrett, A. W. — WD9  
Gettemy, Donald J. — TuB6

Gillig, Kent — ThB1  
Goldsmith, J. E. M. — WC2  
Goodwin, Peter M. — ThC3  
Gratz, M. — ThB4  
Groll, H. — WB4

Hahn, J. W. — WD6  
Hargis, P. J. — TuB5  
Harris, Joel M. — WA5  
Hemberger, P. H. — WD9  
Hemmerling, B. — WD5  
Henry, Bruce — WB2  
Hornkohl, James O. — TuB2, FA5  
Houghton, Terri Gilbert — ThC1  
Hovde, D. Christian — WB1  
Huang, J. Y. — TuA3  
Hubschmid, W. — WD5  
Hudgens, Jeffrey W. — FA4

Jackson, A. D. — TuB9  
Jeffries, Jay B. — FA3, FB  
Jett, James H. — ThC, ThC3  
Johnson, Mitchell E. — ThC3  
Johnson, III, Russell D. — FA4  
Johnston, M. V. — TuB8, ThA2  
Johnston, Roger G. — ThB5  
Jones, Gregory M. — ThC1

Kane, Daniel J. — WB1  
Kang, K. T. — WD6  
Keller, Richard A. — ThC3  
Kinsel, Gary R. — ThB1  
Knights, M. G. — TuA2  
Koldunov, M. F. — WD2  
Kuritsyn, Y. — WB4

Langford, Andrew O. — WC3  
Leavitt, E. D. — TuB8  
Lewis, J. W. L. — TuB2, TuB3, FA5  
Li, Li-Qiang — ThD2  
Linne, M. A. — FB3  
Liu, Huiying — WD8  
Lu, W. — WA4  
Lucht, Robert P. — ThD, FB2

Mack, Jr., Larry H. — TuB7  
Mansoori, B. A. — ThA2  
Marrone, Babetta L. — ThC3  
Martin, John C. — ThC3  
McCarthy, J. C. — TuA2  
McNesby, Kevin L. — FA2  
Mehuys, David G. — WC1  
Meier, Ulrich E. — WB  
Millard, M. W. — FB4  
Miziolek, Andrzej W. — FA, FA2  
Montaser, Akbar — WD8  
Murphy, D. M. — ThA1  
Murray, Kermit K. — ThA5

Neubauer, K. R. — ThA2  
 Ng, C. K. — TuB10  
 Ngo, Dat — WA2  
 Niemax, Kay — WB4, ThA  
 Nogar, N. S. — WD9, ThB3  
 Northam, G. B. — FB4

Oh, Daniel B. — WB1

Parigger, Christian — TuB2, TuB3, FA5  
 Park, S. N. — WD6  
 Patel, V. — TuB10  
 Paul, P. H. — FB1  
 Petty, Jeffrey T. — ThC3  
 Pfefferle, Lisa — TuB4  
 Pinnick, R. G. — WA2  
 Plemmons, David H. — TuB2, TuB3  
 Pollak, T. M. — TuA2  
 Ponomarenko, E. P. — WD2  
 Preppernau, B. L. — TuB5  
 Proffitt, Michael H. — WC3

Rahn, Larry A. — FB2  
 Raiche, George A. — FA3  
 Ramsey, J. Michael — TuA, WB3, ThA3, ThC4, ThD1  
 Rassat, Scot D. — ThA4  
 Rob, Mohammad A. — TuB7  
 Rodriguez, R. — WD7  
 Ross, P. L. — TuB8  
 Russell, David H. — ThA5, ThB1

Sappey, Andrew D. — TuB1, ThB, ThB2  
 Schade, W. — ThB4  
 Schnurer-Patschan, C. — WB4  
 Schunemann, P. G. — TuA2  
 Seaton, Colin — WC  
 Seaver, Mark — WA3  
 Seki, H. — TuA3  
 Sewell, Scott — WB2  
 Shapiro, M. J. — ThC4  
 Shaw, Robert W. — WB3  
 Shen, Y. R. — TuA3  
 Shera, Brooks — ThD3  
 Silver, Joel A. — WB1  
 Singh, B. — TuB10  
 Sitnikov, N. M. — WD2  
 Sklar, Larry A. — WD11, ThC1  
 Smith, M. W. — FB4  
 Song, Q. — WA4  
 Stampanoni-Panariello, A. — WD5  
 Stanton, Alan C. — WB1  
 Startsev, A. V. — WD2  
 Steinkamp, John A. — WD11, ThC2  
 Steinkruger, Fred J. — TuB6  
 Sun, H. C. — TuB10

Taylor, David J. — TuB6  
 Tulaikova, T. V. — WD2

Van Bramer, S. E. — TuB8

Wang, Qi — WD1  
 Wells, F. V. — WD7  
 Wexler, A. S. — ThA2  
 Whittaker, Edward A. — TuB10  
 Whitten, William B. — ThA3, ThC4, ThD1  
 Winter, Michael — WA1

Xie, X. Sunney — ThD4  
 Xu, Z. — WA4

Yang, M. — ThA3  
 Young, J. P. — WB3

Zerkle, David K. — TuB1, ThB2  
 Zhou, Y. — WD3  
 Zybin, A. — WB4

# **LASER APPLICATIONS TO CHEMICAL ANALYSIS**

*Sponsored by*  
**Optical Society of America**

**POSTDEADLINE PAPERS**

**MARCH 8–11, 1994  
JACKSON HOLE, WYOMING**

## **LASER APPLICATIONS TO CHEMICAL ANALYSIS POSTDEADLINE PAPERS**

<b>PD1</b>	<b>Study of the Energetics and Dynamics of Hydrogen Bond Formation in Carboxylic Acids, A. Winkler and P. Hess . . . . .</b>	<b>265</b>
<b>PD2</b>	<b>Laser-induces Thermal Acoustical (LITA): Simple, Accurate Single-shot Gas Measurements, E. B. Cummings . . . . .</b>	<b>266</b>
<b>PD3</b>	<b>Single Particle Raman Analysis of Coal-fired Power Plant Stack Effluent, C. D. Masters, D. K. Hutchins, M. K. Hudson, and A. J. Adams . . . . .</b>	<b>270</b>
	<b>Postdeadline Author Index . . . . .</b>	<b>274</b>

**"STUDY OF THE ENERGETICS AND DYNAMICS OF HYDROGEN BOND FORMATION  
IN CARBOXYLIC ACIDS "**

A. Winkler and P. Hess

Institute of Physical Chemistry  
University of Heidelberg  
Im Neuenheimer Feld 253  
D-69120 Heidelberg

**ABSTRACT**

Dissociation rates of dimeric formic, acetic and propionic acid in the gas phase were measured by resonant photoacoustic spectroscopy. Consistent sets of kinetic and thermodynamic data were obtained from the pressure dependence of the resonance frequency and broadening of the resonance profile of the first radial mode of a cylindrical resonator. The standing acoustic waves were excited by resonant absorption of modulated CO<sub>2</sub> laser radiation.

The energetics is very similar for the three carboxylic acids with an enthalpy of dissociation of about 60 kJ/mol, a dissociation entropy of about 150 J/mol,K and an activation energy of about 32 kJ/mol. This implies a stepwise dissociation of the cyclic dimer into an open dimer with one H-bond in a slow rate determining process and a subsequent fast decay of the chain dimer into two monomers.

The rate constants measured for the dissociation process are very different and indicate that the dynamics depends sensitively on the structure of the molecule.

The results clearly show that the present measurements performed in the frequency domain with a modulated cw laser are more accurate and provide more information than previous temperature-jump experiments using pulsed lasers.

## Laser-induced thermal acoustics (LITA): simple, accurate single-shot gas measurements

E.B. Cummings

GRADUATE AERONAUTICAL LABORATORIES

CALIFORNIA INSTITUTE OF TECHNOLOGY

Pasadena, CA 91125

Laser-induced thermal acoustics (LITA) is a time-resolved four-wave mixing technique for sensitive nonintrusive measurement of the sound speed, thermal diffusivity, acoustic damping rate, and complex susceptibility of a gas. In LITA, acoustic gratings induced by laser electrostriction and rapid laser heating evolve hydrodynamically, modulating an acousto-optically scattered signal beam that is detected and recorded in time. A simple expression derived from the equations of linear hydrodynamics and scattering accurately describes the signal. Sound speeds accurate to 0.5% and transport properties accurate to 30% have been measured in atmospheric conditions in a single-shot without calibration using "garden variety" lasers. LITA "spectra" have been taken of weak spectral lines of  $\text{NO}_2$  in concentrations less than 50 ppb. Signal reflectivities up to  $10^{-4}$  predicted by the theoretical expression have been observed experimentally. The hydrodynamic nature of the LITA interaction suggests interesting applications beyond those already performed.

Laser-Induced Thermal Acoustics (LITA) is new time-resolved four-wave mixing technique for point measurement of sound speed (thereby temperature), thermal diffusivity, and acoustic damping (thereby viscosity) of a gas<sup>1</sup>. The LITA signal arises from the acousto-optic effect and the opto-acoustic effects of electrostriction and absorption with thermalization. A similar technique has been used to measure sound speeds in crystals<sup>2</sup> and liquids<sup>3</sup>. The temperature of the laboratory air was measured within 0.5% with uncalibrated single-shot LITA, limited by air composition and beam geometry uncertainties. The thermal diffusivity and acoustic damping coefficient were measured within 15% of published values, limited by finite beam-size and thermalization-rate effects, which were ignored in the signal analysis. Much better accuracy is expected when improved models are completed. With this caveat, the absolute amplitude and time-history of LITA signals are accurately represented by a simple analytical expression derived from the linearized equations of light scattering and hydrodynamics. The signals arising from electrostriction and thermalization, proportional to the real and imaginary gas susceptibility respectively, have different signatures. Thus LITA can measure the complex gas susceptibility, which was demonstrated using weak visible transitions of the laboratory-air trace-species  $\text{NO}_2$  (less than 50 ppb.) LITA benefits from strong excited-state energy quenching and thus has advantages over other techniques<sup>4</sup> where quenching rates are high, as in many flows of aerothermochemical interest where high density is needed for fast chemistry. Analysis and experiment have shown that LITA signals rival those of LIF (laser-induced fluorescence) or DFWM signals in intensity when comparable lasers are used.

In LITA, light from a short-pulse "driver" laser (e.g., 1 - 1000 mJ, 1 - 10 ns) generates acoustic waves by two opto-acoustic effects, electrostriction and rapid thermalization. Electrostriction, the tendency of polarizable molecules to move toward regions of high optical electric field intensity<sup>5</sup>, is proportional to the real part of the gas susceptibility. Thermalization is a collisional process proportional to the imaginary part of the gas susceptibility: molecules of the gas absorb driver laser energy; inelastic collisions convert excited-state energy to molecular kinetic or rotational energy; finally, elastic molecular collisions equilibrate the velocities of the molecules, raising the temperature. Acoustic waves are produced when the drop in gas density accompanying thermalization sharply lags that of equilibration. The density-perturbation field of the acoustic waves generates a susceptibility-perturbation field that scatters light from a long-pulse or CW "source" laser, forming the LITA signal.

The driver laser is split into two beams which cross at a small angle (0.5 - 5 degrees) in the gas, where the beams interfere to form an ellipsoidal electric-field intensity grating. This grating generates acoustic structures with modulation depths from 0.01% to 5% via opto-acoustic effects. Electrostriction forms two traveling acoustic wavepackets (phonons) and a weak isobaric density grating (thermon), each with the wavelength of the electric field grating. Thermalization generates similar acoustic structures but the "thermon" is dominant. The phonons counterpropagate in the direction parallel to the grating vector and decay by acoustic damping, while the thermon decays by heat conduction. Light scattered from the source laser by the acoustic grating structures adds coherently and emerges in a coherent beam when the source laser is incident at the Bragg angle of the gratings. Light scattered by the phonons have Doppler shifts relative to light scattered by the thermon of  $\pm\omega_B = c_s q$ , the "Brillouin frequency" where  $c_s$  is the sound speed and  $q$  is the electric-field intensity-grating vector magnitude. Beating between the light scattered by these structures modulates the detected signal, which bears three frequency components (neglecting damping): a DC component; a component at the Brillouin frequency, caused by phonon/thermon signal beating; and a component at twice the Brillouin frequency, caused by beating of signals generated by the conjugate phonons. It is noteworthy that LITA signals also contain Doppler shifts from convection



which may be extracted by beating the LITA signal against the unscattered source beam. In this way, LITA should be a very capable velocimeter. LITA velocimetry experiments are currently under construction.

An analytical expression for the amplitude and time history of the LITA signal has been derived from the linearized equations of hydrodynamics and light scattering<sup>6</sup> allowing *a priori* estimation the magnitude of LITA signals and interpretation of actual LITA signals<sup>1</sup>, with very good experimental agreement. A simple analytical result for the signal intensity,  $I(t)$ , is obtained for short-duration Gaussian driver beams, infinite-extent, monochromatic source beam, and single-rate-dominated thermalization:<sup>1</sup>

$$I(t) \propto (A \exp\{-D_T q^2 t\} + B \cos\{c_s q t + \Phi\} \exp\{-\Gamma q^2 t\})^2,$$

where  $D_T$  is the thermal diffusivity,  $\Gamma$  is the acoustic damping coefficient, and  $A$ ,  $B$ , and  $\Phi$  are simple algebraic functions of gas and laser beam parameters. When the approximations listed above are not valid, spatial and temporal convolutions of laser-beam profiles and thermalization behavior augment the analysis. These parameters are readily measured except the thermalization rates, which may be inferred from LITA data or estimated from published data. The assumption of flat source-beam intensity caused the largest deviation from experiment. Analysis refinements including a Gaussian source beam are in progress. The ratio of signal beam to source beam intensity is of the order  $10^{-4}$  for room air with a thermal modulation depth of 1% in a two-millimeter-long sample volume, without resonant enhancement at the source-laser wavelength<sup>1</sup>.

Fig. 1 is a schematic diagram of the experimental apparatus used in these LITA experiments. The driver laser is a pulsed dye laser with a noise bandwidth of about 2 GHz. When pumped by a Q-switched, frequency-doubled Nd:YAG laser (Continuum, model YG-660) at 150 mJ/pulse, the dye laser emits about 40 mJ of light tuned between 587 nm and 592 nm in approximately 5 ns pulses. Three-millimeter-wide driver beams are formed from the dye laser emission by a 50% beamsplitter ( $B.S.$ ) and a mirror  $m_1$ . The driver beams intersect at the focus of the 400 mm lens where they approximate finite plane waves about 200  $\mu\text{m}$  in diameter. The beam-crossing angle is set by the distance between the parallel beams, which is adjusted using micrometer translation stages under mirrors  $m_2$  and  $m_3$ . BOXCAR geometries<sup>4</sup> with crossing angles ranging from  $1.0^\circ$  to  $2.3^\circ$  were used in these experiments. Detection of the driver beam pulse by a silicon PIN photodiode,  $p_1$  (Thor labs, model DET-2SI), triggers the acquisition of the LITA signal. The source laser is a 1W CW argon ion laser operating at 488 nm (Spectra Physics Model 165). A two-lens system adjusts the source beam diameter, which ranged from about 200  $\mu\text{m}$  to 2 mm. Phase-matching adjustments are made using a micrometer-driven translation stage under  $m_4$ . A silicon PIN photodiode,  $p_2$ , monitors the intensity of the source beam.

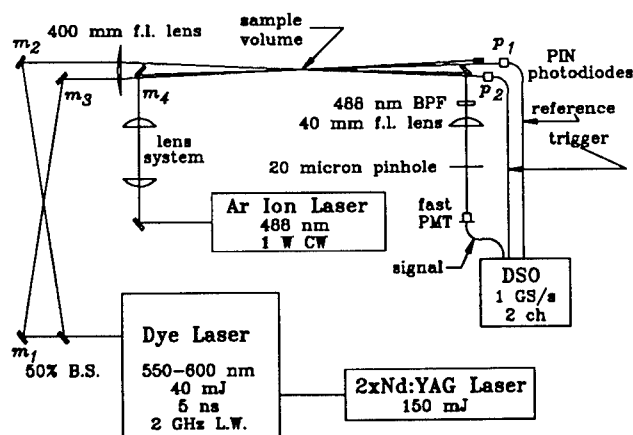


Fig. 1. Schematic diagram of the LITA experiment setup.

The detection system consists of a fast photomultiplier tube (PMT) (Hamamatsu model OPTO-8) with at least a 500 MHz signal bandwidth and optical filters to prevent signal contamination, including a 10 nm interference filter at 488 nm and a 40 mm lens/20  $\mu\text{m}$  pinhole spatial filter. The LITA signal path-length to the detector is about 2.5 m. The PMT power supply (Fluke 412B) was carefully filtered to eliminate RF noise. Data are recorded using a 1 GS/s, eight-bit, two-channel digital storage oscilloscope (DSO) (HP 54510A). This records typically 500-to-2000-sample time histories of signals from the PMT and  $p_2$ .

In early LITA experiments using laboratory air, the signal arising from nonresonant electrostriction was roughly 30 photons per nanosecond (reflectivity of  $\sim 10^{-8}$  with the 1 W source beam). A sample signal is plotted as the dotted curve in Fig. 2. The frequency of the modulation is about 26 MHz, twice the Brillouin frequency, yielding a sound speed accurate within the uncertainty of the knowledge of the laboratory sound speed ( $\sim 0.5\%$ ). The resonantly-enhanced signal recorded near a weak line of  $\text{NO}_2$  appears as a dashed curve and the signal recorded near the peak of the absorption line is the solid curve plotted in Fig. 2. On the solid curve

the dominant modulation is at the Brillouin frequency, caused by interference between the signals scattered by the phonons and the thermon. All curves are 256-shot ensemble averages. LITA's good sensitivity is demonstrated since the ambient air contained less than 50 ppb of  $\text{NO}_2$  according to the Southern California Air Quality Management District.

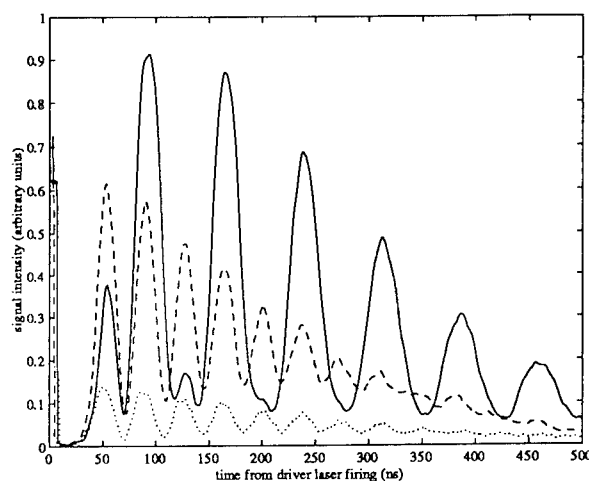


Fig. 2. Nonresonant (dotted curve), near-resonant (dashed curve), and resonant LITA signal (solid curve).

A LITA "spectrum" of trace  $\text{NO}_2$  appears in Fig. 3. The spectrum is built from 256-shot averages of signals with driver laser scanning in 12 GHz steps. In the foreground the signal comes primarily from resonantly-enhanced electrostriction; in the background, the signal is characteristic of resonance (thermalization). The structure between consists of unresolved lines because of the large frequency step; however, the possibility of recording complex susceptibility spectra via LITA is demonstrated. Quantitative spectroscopic surveys are planned when automation of laser scanning, data acquisition, and signal analysis is complete.

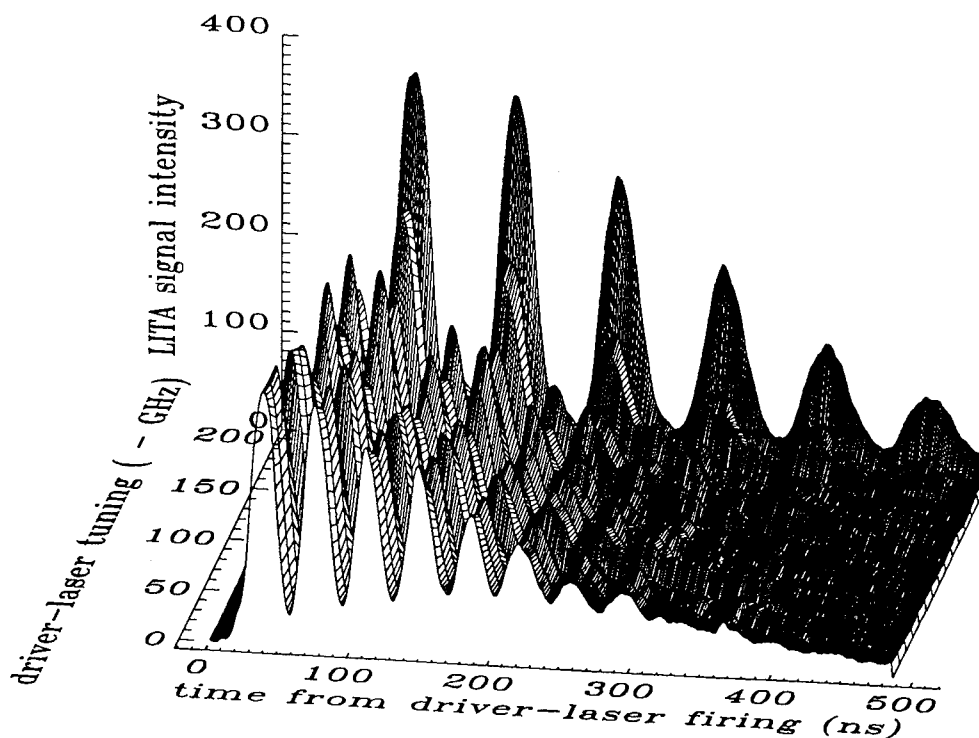


Fig. 3. LITA "spectrum" of trace  $\text{NO}_2$  taken by scanning driver laser in 12 GHz steps.

Seeding the gas with  $\text{NO}_2$  provided LITA signals that were several orders of magnitude stronger than the signals obtained from room air, with estimated reflectivities around  $10^{-4}$ . A sample single-shot LITA signal and theoretical fit using published values of transport properties and calculated sound speed appear in Fig. 4(a). The driver beam crossing angle was  $1.04^\circ$ , yielding a grating wavelength of  $32.3 \mu\text{m}$  and a Brillouin frequency of 10.7 MHz. At high concentration of absorbing species, the thermalization effect swamps the electrostrictive effect. The theoretical fit becomes progressively worse with time as the phonons "walk off" the finite source beam. Fig. 4(b) shows a four-shot average of the LITA signal obtained when the beam crossing angle was widened to  $2.3^\circ$  (grating wavelength of,  $14.5 \mu\text{m}$ ; Brillouin frequency of 23.9 MHz.) In Fig. 4(b) the theoretical LITA signal shows better agreement with experiment because the shorter-wavelength phonons are damped before they leave the source beam. In these experiments, thermalization is resolved so the single-rate model of thermalization is replaced by the superposition of two single-rate thermalizations: a fast  $\sim 10$  ns process and a slow  $\sim 100$  ns process. A better fit to the data could be obtained by adopting a more accurate thermalization model and source-beam-profile model (a top-hat profile is assumed) and including the effect of source-beam phase noise.

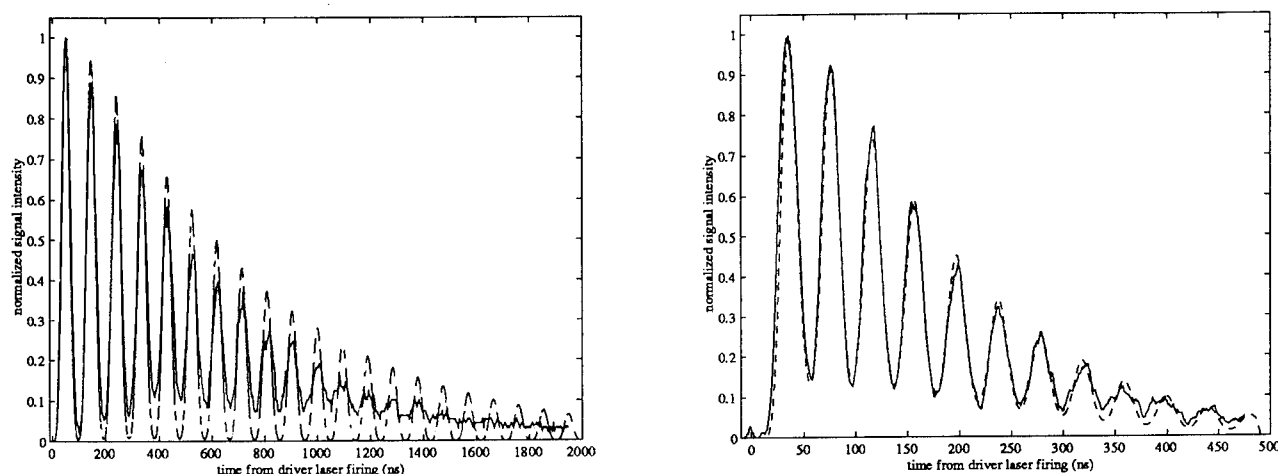


Fig 4. (a) Single-shot LITA signal of  $\text{NO}_2$ -seeded air and theoretical fit (dashed curve), grating wavelength  $32.3 \mu\text{m}$ . (b) Four-shot average LITA signal of seeded air and theoretical fit, grating wavelength  $14.5 \mu\text{m}$ .

In conclusion, LITA has demonstrated excellent potential in the first round of experiments. LITA is capable of filling application gaps left by other laser diagnostics. For example, LITA excels where quenching rates are high. LITA does not require knowledge of energy-transfer rates or energy level information about the target species. Indeed, the technique has been performed entirely nonresonantly. The very first nonresonant LITA signals provided the laboratory sound speed within the uncertainty of independent measurements. In both magnitude and time-history, the LITA signal is well represented by a simple analytical expression derived from the linearized equations of hydrodynamics and light scattering. Future extensions of this work include performing LITA velocimetry and spectroscopy and the signal analysis to include finite source-beam size effects, source-laser noise effects, and more realistic thermalization models.

The author gratefully acknowledges the support of the University Research Initiative (URI) in aerothermochemistry sponsored by the AFOSR. The author is also indebted to the ONR for their support of his graduate education through their fellowship program.

## References

1. E.B. Cummings, GALCIT report FM 92-2, CIT, Pasadena, CA, (1992).
2. K. A. Nelson, M. D. Fayer, *J. Chem. Phys.* **72** 5202, (1980).
3. R.J.D. Miller, R Casalegno, K. A. Nelson and M. D. Fayer, *Chem. Physics* **72**, 371 (1982).
4. A.C. Eckbreth, *Laser Diagnostics for Combustion Species and Temperature*, Abacus Press, Cambridge, MA (1988).
5. R.W. Boyd, *Nonlinear Optics*, Academic Press, New York, NY (1992).
6. B.J. Berne, R. Pecora, *Dynamic Light Scattering*, John Wiley and Sons, New York,

## Single Particle Raman Analysis of Coal-fired Power Plant Stack Effluent

C. D. Masters, D.K. Hutchins, M.K. Hudson, and A.J. Adams

Submit correspondence for all authors to:  
Department of Electronics and Instrumentation  
E.T.A.S. Building  
University of Arkansas at Little Rock  
2801 South University Avenue  
(501) 569-8000

### Introduction

The 1990 Clean Air Act requires commercial power plants to monitor environmental emissions. Present instrumentation on power plant stacks is being used to spot check combustion gas levels. Power plant furnaces fired by natural gas emit combustion byproducts such as  $\text{NO}_x$  and  $\text{SO}_2$ . While these gases are of environmental concern, the instrumentation needed to monitor them is relatively straightforward and is available commercially. Coal-fired furnaces, on the other hand, produce tons of particulate matter known as fly ash, most of the which is removed by electrostatic precipitators. However, smaller, lighter aerosols remain in the exhaust air as it exits the stack. The identification and characterization of fine particulate matter is a difficult task. There is a need for analytical instrumentation which monitors particulate matter in the stack and provides real time information to plant operators. Particulates leaving the stack consist mainly of metal oxides in various oxidation states. One study, using standard laboratory techniques, identified thirty-six different oxides.<sup>1</sup> Fortunately, most of the emitted particulates are not environmentally dangerous. Therefore, instruments can be optimized to detect only those components considered detrimental. Particle Raman spectroscopy has the potential to make the required measurements under the conditions mentioned above.

Raman spectroscopy has proven effective in the identification and characterization of organic compounds and some inorganic salts, but little information exists in the literature concerning Raman analysis of metal oxides. Oxides present in fly ash that are also thought to be dangerous to the environment include compounds of chromium, arsenic, and nickel. The problem is made more complex by the fact that some metals are found in a number of oxidation states. Chromium, for example, forms the compounds  $\text{Cr}_2\text{O}_3$  (chromium III) and  $\text{CrO}_3$  (chromium VI). The former is considered harmless while the latter is thought to act as a carcinogen. Another concern in particle Raman spectroscopy is the possibility of particle pyrolyzation. Since Raman scatter is generally a weak effect, the signal from a single aerosol particle is diminishingly small. The intense laser radiation needed to produce a measurable amount of Raman scatter often heats the particle to the point of decomposition. For these reasons, we decided that a single particle Raman system should be developed in which a particle could be trapped indefinitely and studied using Raman or other analytic techniques. In this way, laboratory-prepared compounds and eventually particulate material from a stack could be analyzed in controlled situations so optimum excitation and detection methods for a final instrument design can be determined. The focus of present work is the design and construction

of a single particle Raman spectroscopic system which would be able to identify and speciate different types of environmentally hazardous metal oxides.

Several different methods of trapping aerosol particles appear in the literature. Perhaps the most common is the "quadrupole cell" consisting of two hyperbolic end caps and a central toroidal electrode.<sup>2</sup> A particle can be held indefinitely providing the voltages have been adjusted properly. We have not chosen this type of trap for two reasons. First, the charge to mass ratio of the particle being trapped must be within a small range determined by the frequency of the alternating voltage applied to the center electrode and the dc end cap potential. In a sample with a wide size distribution only a small percentage of particles could be trapped with a single setting. Secondly, the nature of the experiment requires that as much signal as possible is recovered from the particle. The central electrode encircles the particle. Therefore, holes must be drilled in the central electrode so that light scattered from the particle can be collected. A hole large enough to obtain a signal from a sub-micron particle would compromise trap integrity.

We have chosen instead, a modified Milikan cell shown schematically in Figure 1. This trap is characterized by flat end cap electrodes used to create an electric field to offset gravity. Horizontal stabilizing forces are provided by an insulated center pin in the lower plate (with polarity opposite that of the plate).<sup>3</sup> The modified Milikan cell provides a 360 degree view around the suspended particle, thus making room for collection optics, control signal optics and, a micro-telescope. Trapping depends on the charge to mass ratio, but the usable range is much broader than a quadrupole cell. This trap has been shown to capture particles ranging from 1 to 10  $\mu\text{m}$ .<sup>4</sup>

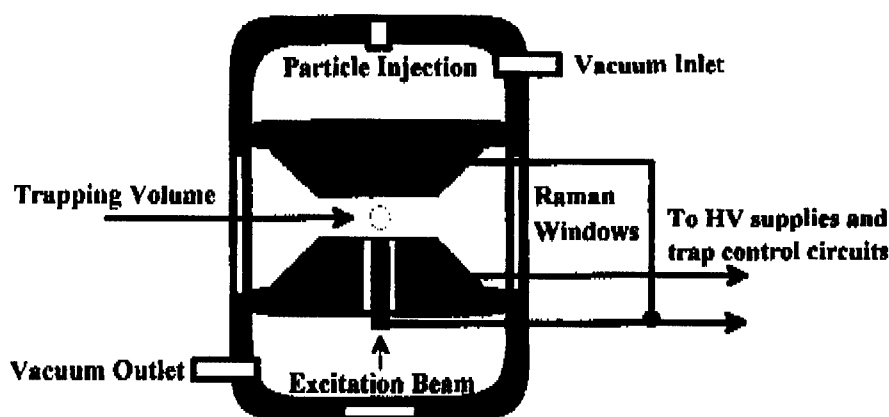


Figure 1: Single Particle Trap

### Experimental System

One of the problems addressed is that of injecting single particles into the trap. Although several different methods exist for generating aerosols, none are suited to single particle experiments. Particulates in the stack exist as dry powders and are surrounded by a hot, dry atmosphere. Nebulization produces many particles in a moist atmosphere. Dust generators produce dry particles but in vast numbers. The presence of many charged particles in the trapping volume must be avoided in order for the trap to operate properly. A spring loaded hypodermic syringe has proven effective in placing as few as 3 or 4 particles into the trap at a time. These particles are manipulated through manual control of the electric fields until only

one remains in the trapping volume. The trap is then switched to automatic control. An optoelectronic feedback loop is used to hold the particles automatically by monitoring the light scattered from the particle, which is illuminated for trapping purposes by a 5mW HeNe laser beam. The optical system layout appears in Figure 2. The Argon-ion laser is the excitation source. This laser has a power output of 12 watts in 6 lines, which are isolated using a prism and beam dumps. The single line power available varies from 4 watts at 514.5 nm to 200mW at 472.7nm. The excitation beam is directed vertically upward from beneath the trap. Because Raman lines are often obscured by fluorescence peaks, one of the first goals of the single particle system will be the determination of an optimum wavelength for excitation. This wavelength will be chosen to offer minimum interference from fluorescence while providing maximum possible Raman signal amplitude.

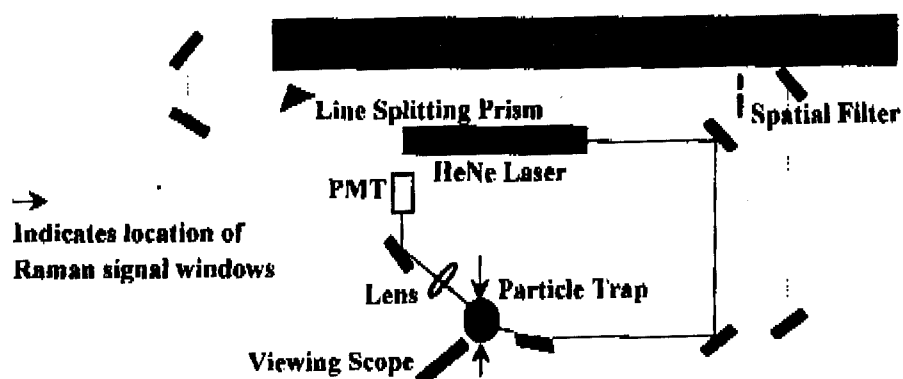


Figure 2: Single Particle System Optical Layout

### Experimental Work and Plans

The chromium oxide system mentioned earlier has been chosen as the first subject of study. This system is representative of the degree of complexity which the final instrument must be able to handle. Characteristics of the two chromium species are:

1. Both compounds are non-white (one is red the other green), i.e. absorptive heating must be addressed.
2.  $\text{CrO}_3$  has a low melting point ( $196^\circ\text{C}$ ) compared with  $\text{Cr}_2\text{O}_3$  ( $2435^\circ\text{C}$ ).
3. Multiple oxidation states of the same metal exist.

Raman spectra of  $\text{Cr}_2\text{O}_3$  are available from bulk studies carried out on surfaces and from large single crystals, but Raman spectra for most other heavy metal oxides have are not available. This is attributed to the lack of interest in Raman analysis of these compounds until recently. Results of work with similar metal oxide compounds used as catalysts in industrial processes may be useful in single particle applications as well.<sup>7</sup>

In preliminary work, we have been able to trap Chromium (III) oxide particles approximately  $10\mu\text{m}$  in diameter and reference PLS particles as small as  $1\mu\text{m}$ . A study to determine the particle size trapping range is underway. Studies to determine the optimum method and wavelength for excitation of the particles are planned. If the argon laser

wavelengths prove unsatisfactory, an eximer pumped dye may be used. We plan to investigate use of a chopped beam or a pulsed laser in order to avoid heating and particle decomposition.

Raman spectroscopy shows potential as an analytic tool for the real time identification and speciation of particulate matter in coal-fired power plant smoke stacks. A single particle trap has been constructed to determine optimum parameters for a final instrument design. In addition to a study of the chromium oxides, this system will also be used to study the Raman spectra of other heavy metal oxides for the first time. Results of this work are pertinent to the commercial power industry and environmental impact investigations alike.

## References

1. Headlee, A.J.W., Hunter, R.G., *Ind. Eng. Chem.*, **45**, 548 (1953); West VA Geol. Survey, Bull. No. 13A, 36 (1955).
2. Frickel, R.H., et al, AD/A 056 236 (National Technical Information Service, U.S. Dept. of Commerce, Springfield, VA).
3. Fletcher, H., *Phys. Rev.*, **4**, 440 (1914).
4. Hutchins, D.K., private communication (1993).
5. Brown, D.A., Cunningham, D., Glass, W.K., *Spectrochimica Acta.*, 965 (1968).
6. Beattie, I.R., Gilson, T.R., *J. Chem. Soc. (A)*, 197, 980 (1971).
7. Wachs, I.E., Hardcastle, F.D., Chan, S.S., *Spectroscopy*, **1** No. 8, 30 (1987).

*Postdeadline Author Index*

**A**adams, A. J. - 270

**C**ummings, E. B. - 266

**H**ess, P. - 265

Hudson, M. K. - 270

Hutchins, D. K. - 270

**M**asters, C. D. - 270

**W**inkler, A. - 265



## TECHNICAL PROGRAM COMMITTEE

**Mary Wirth, Chair**  
*University of Delaware*

**Alan C. Eckbreth, Chair**  
*United Technologies Research Center*

**Jay B. Jeffries, Program Chair**  
*SRI International*

**J. Michael Ramsey, Program Chair**  
*Oak Ridge National Laboratory*

**Sarah Cohn**  
*Potomac Photonics*

**Alan Fried**  
*National Center for Atmospheric Research*

**James H. Jett**  
*Los Alamos National Laboratory*

**Murray V. Johnston**  
*University of Delaware*

**Robert P. Lucht**  
*University of Illinois*

**Ulrich E. Meier**  
*DLR EN-CV, Germany*

**Andrzej W. Miziolek**  
*U.S. Army Ballistic Research Laboratory*

**Kay Niemax**  
*Institute für Spektrochemie und Angewandte Spektroskopie, Germany*

**Andy Sappey**  
*Los Alamos National Laboratory*

**Colin Seaton**  
*Coherent Laser Group*